THE UNIVERSITY OF CHICAGO

SURFACE-MEDIATED INTERACTIONS AND SELF-ASSEMBLY PATHWAYS OF COLLOIDAL NANOCRYSTALS

A DISSERTATION SUBMITTED TO
THE FACULTY OF THE DIVISION OF THE PHYSICAL SCIENCES
IN CANDIDACY FOR THE DEGREE OF
DOCTOR OF PHILOSOPHY

DEPARTMENT OF CHEMISTRY

BY

AHHYUN JEONG

CHICAGO, ILLINOIS

AUGUST 2026

© 2026 by Ahhyun Jeong.

Table of Contents

List of Tables

List of Figures

Acknowledgements

This thesis is the culmination of a journey that I could not have undertaken alone. I am deeply indebted to the mentors, collaborators, colleagues, friends, and family who have guided, supported, and inspired me along the way.

First and foremost, I would like to express my profound gratitude to my advisor, Prof. Dmitri V. Talapin. His insight, creativity, and unwavering support have shaped not only this thesis but also the scientist and person I have become. His consistent positivity and patience gave me the confidence to keep pushing forward and explore new ideas. I would also like to thank my committee members, Prof. John Anderson and Prof. Philippe Guyot-Sionnest, for their guidance and encouragement.

This thesis would not exist without the insight and generosity of my collaborators. I am especially grateful to Prof. Naomi Ginsberg and her group members, including Dr. Christian Tanner, Vivian Wall, and John Davis, for their invaluable support in the measurement and interpretation of beamtime experiments. The many days and nights we spent working at beamlines across the world are among my fondest memories. I am thankful to the beamline scientists, including Dr. Byeongdu Lee and Dr. Burak Guzelturk, whose technical expertise and advice were essential for successful experimental setups and data analysis. I would like to thank those who made STEM imaging possible, including Dr. Xiaoben Zhang in Prof. Junhong Chen's group and Saghar Rezaie in Prof. Sadegh Yazdi's group, for their help and careful work. I am also grateful to Dr. Aditya N. Singh from Prof. David T. Limmer's group for his simulation efforts, which provided crucial theoretical context to our experiments. I greatly appreciate Dr. Shengsong Yang, Dr. Chang Liu, and Dr. Sungsu Kang from Prof. Paul Alivisatos's group for countless scientific advice and discussions.

The University of Chicago has provided an exceptional scientific environment, supported by outstanding facilities and staff. I am deeply thankful to Dr. Alex Filatov for training and always keeping the X-ray facility in excellent shape. I would like to thank Dr. Justin Jureller and Dr. Sarah Brown for their guidance and careful maintenance of MRSEC instruments, and to express my appreciation to Dr. Shengsong Yang, Dr. Chang Liu, Dr. Sungsu Kang, Yimei Chen for their support with TEM experiments. I am also thankful to Dr. Philip Griffin for his guidance and maintenance of Soft Matter Characterization instruments.

I have been extraordinarily fortunate to work alongside remarkable colleagues in the Talapin group. They have been both collaborators and friends. I am especially grateful to Dr. Josh Portner, who mentored me early on, and to Zehan Mi, who has been a steadfast partner in our self-assembly work throughout my Ph.D. journey. I would also like to thank my undergraduate mentee, Youssef Tanzoui, for nearly four years of dedicated effort and major contributions to our scientific progress. I am indebted to Dr. Justin C. Ondry, Dr. Zirui Zhou, Dr. Chenkun Zhou, Dr. James Cassidy for their scientific advice, stimulating discussions, and collaborations. I would also like to thank all the former Talapin group members: Dr. Wooje Cho, Dr. Aritrajit Gupta, Dr. Haoqi Wu, and Dr. Di Wang, Alex Hinkle, as well as current members: Dr. Jun Hyuk Chang, Dr. Yuan Liu, Dr. Yufang Kou, Ruiming Lin, Young-Hwan Kim, Isak Jatoi, Noah Mason, Tanya Chen, Yi-Chun Liu, Marley Downes, York Chu, Yuezhou Chen, Helen Qin, Sarah Bachrach, and Cyd Kennard for their discussions and the supportive group atmosphere we shared. I am especially grateful to Dr. Andrew Nelson for his administrative and technical support, as well as his scientific advice, all of which played a crucial role in making this Ph.D. possible.

I would also like to thank the mentors who supported me during my undergraduate research, Prof. Artem A. Bakulin and Prof. Kwang-Seob Jeong, whose guidance made it possible for me to

begin my Ph.D. journey and whose advice continues to shape my scientific thinking. I am thankful to Dr. Thomas R. Hopper from Prof. Bakulin's group, and Dr. Dongsun Choi and Dr. Gahyeon Kim from Prof. Jeong's group, for their mentorship and for helping me build the foundational skills that carried me into graduate school.

Beyond the laboratory, I have benefited from mentors and colleagues who enriched my teaching and outreach experiences. I would like to thank Dr. Meishan Zhao and Dr. Britni Ratliff for their guidance during my first-year general chemistry teaching assistantships. I am grateful to Dr. Christin Ahn for inviting me to participate in numerous outreach activities that were both enjoyable and rewarding, reminding me of the broader impact of science. I also wish to thank Dr. Vera Dragisich for her administrative and emotional support in her role as graduate student director, and Melinda Moore and Aram Sarkisian for their administrative assistance.

My journey has been made immeasurably richer by friends who brought balance, joy, and perspective beyond the scientific journey. I am deeply thankful to my climbing friends: Dr. Zirui Zhou, Yuwei Zhou, Jacky Yao, Suin Choi, Haibei Zhang, Ben Epley, and Wen Li, for the climbs, conversations, and shared challenges that helped me reset and recharge. I would also like to thank the UChicago Kendo Club members: Saul Meyer-Feng, Fabricio Wei, Haotian Wang, Wenzhong Long, Yuchen Jin, Robin Luo, Athena Roscoe, Minerva Roscoe, Yunyi Xing, for the fun we shared together. I am grateful to my table tennis mates: Dr. Zirui Zhou, Dr. Chang Liu, and Xiaolong Zhu for teaching me, practicing with me, and making countless evenings lighter and more enjoyable. I would also like to extend my heartfelt thanks to my friends Spela Kunstelj, Yeji Kim, Matthew Bousquet, Chen-Yu Lien, Kwanghoon Jeong, Sheila Keatings, Sam Knights, Alvin Huang, Jose Guerra, Taemin Kim, and Nayoon Kim, whose friendship and support. I would like to express my

gratitude to my boyfriend, Dr. Zirui Zhou, for his encouragement throughout this journey; his presence has been a constant source of strength and comfort.

Finally, I owe my deepest gratitude to my family. Their love, patience, and unwavering belief in me have sustained me through every high and low of this journey. Their support has been the foundation on which all of this work rests. To my family: thank you for always being there, for your encouragement from near and far, and for giving me the strength to pursue this path.

Abstract

Colloidal nanocrystals (NCs) stabilized by compact, inorganic ligands offer a promising route toward strongly coupled, electronically functional superlattices. However, despite their potential, the colloidal behavior and interparticle interactions of electrostatically stabilized sub-10 nm NCs remain poorly understood, limiting the rational design of their assemblies. In this dissertation, I investigate the dispersion thermodynamics, interparticle forces, and self-assembly pathways of PbS NCs functionalized with thiostannate metal chalcogenide complex (MCC) ligands (PbS-$Sn_2S_6^{4-}$). Using small-angle X-ray scattering (SAXS), I show that these NCs exhibit pronounced deviations from ideal solution behavior, governed by long-range electrostatic repulsion that contrasts sharply with the short-range steric interactions of oleate-capped PbS NCs. Screening these interactions with multivalent electrolytes reduces the repulsive length scale, enabling controlled transitions from amorphous films to crystalline domains during drying and spin-coating. Second virial coefficients extracted from SAXS measurements quantify how ligand chemistry, solvent environment, and NC size shape the pair potentials that ultimately dictate colloidal stability and assembly.

Building on this understanding of interparticle interactions, I demonstrate that PbS NCs capped with strongly charged MCC ligands ($Sn_2S_6^{4-}$, AsS_4^{3-} etc.) self-assemble into all-inorganic superlattices with both long-range translational order and atomic-lattice orientational alignment. Structural characterization reveals an unexpected edge-to-edge configuration of NCs, and numerical simulations show that this orientational order is thermodynamically stabilized by many-body ion correlations within the dense electrolyte environment. Remarkably, these superlattices exhibit reversible oriented attachment, where unwashed PbS-$Sn_2S_6^{4-}$ NC superlattices containing incorporated K_3AsS_4 can be fully disassembled back into their original

colloidal NCs, preserving their size and shape distributions. Partial removal of the incorporated electrolyte during washing induces permanent lattice contraction and epitaxial neck formation, rendering the assemblies irreversible. This behavior highlights a delicate interplay between ligand chemistry, electrolyte incorporation, and lattice mechanics that governs the transition between reversible and permanent oriented attachment.

Together, these findings advance the fundamental understanding of electrostatically stabilized NCs and establish a framework for designing nanocrystal solids with tunable order, coupling, and reversibility. The discovery of atomically aligned yet reconfigurable superlattices opens new opportunities for dynamic, stimuli-responsive, and defect-correcting materials with potential applications in adaptive optoelectronics, self-healing architectures, and next-generation nanostructured devices.

1. Chapter 1: Introduction

1.1. Colloidal nanocrystals and their applications

Colloidal nanocrystals (NCs) represent a versatile class of nanomaterials composed of an inorganic crystalline core stabilized by a shell of ligands.[1] Their hybrid structure enables solution-phase synthesis, purification, and processing, distinguishing them from bulk materials and enabling scalable fabrication routes. Over the past several decades, colloidal NCs have emerged as technologically significant because their optical, electronic and magnetic properties can be precisely tuned through control of size, composition, shape, and surface chemistry.[2]

A particularly important subset of colloidal nanocrystals is semiconductor NCs whose diameters are comparable to or smaller than the exciton Bohr radius.[3] In this regime, carriers experience spatial confinement, giving rise to discrete energy levels and size-dependent band gaps.[3] These quantum-confined NCs, commonly referred to as quantum dots (QDs), exhibit tunable photoluminescence, enhanced oscillator strengths, and unique electronic structures that can be engineered for specific functions. As a result, QDs have found broad application in areas such as light-emitting diodes, photodetectors, photovoltaics, biological imaging, and quantum information technologies (Figure 1.1.1).[1–4]

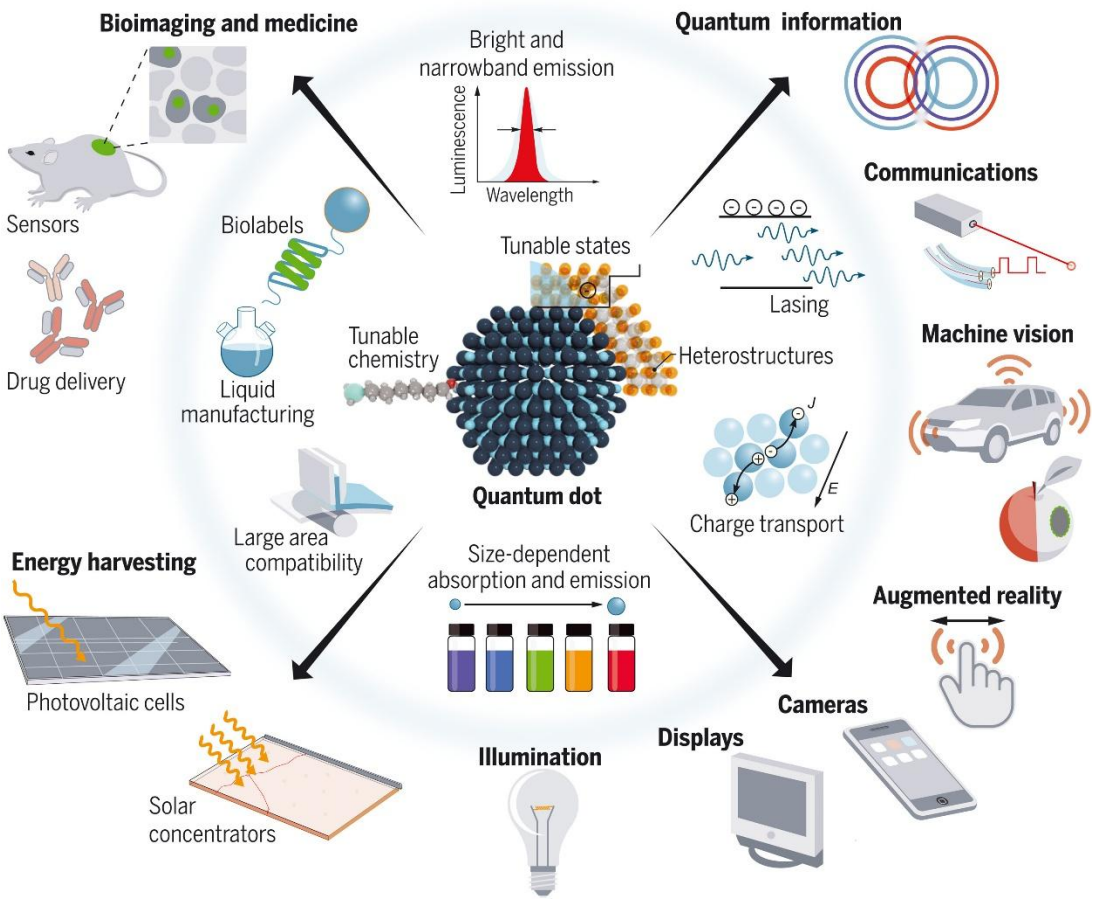

Figure 1.1.1: Technological applications of quantum dots.

Schematics of technological applications of quantum dots. Reprinted with permission from ref.[2] © 2021 American Association for the Advancement of Science.

Among the various QD materials, lead sulfide (PbS) occupies a central role in this thesis. PbS is a classical IV–VI semiconductor with a narrow band gap and a large exciton Bohr radius (~18 nm), making it particularly well-suited for infrared optoelectronic applications.[5] PbS QDs have been widely explored for next-generation solution-processed solar cells and infrared photodetectors,[6–8] and for use in field-effect transistors,[9] light-emitting diodes,[8] and thermoelectric devices.[9] Their synthesis is typically achieved through a hot-injection approach, in which a sulfur precursor is rapidly injected into a hot solution of a lead precursor in the

presence of long-chain organic ligands such as oleic acid.[6] This method enables precise control over nucleation and growth, yielding monodisperse nanocrystals with tunable sizes and well-defined surface chemistries.

1.2. Organic and inorganic ligands on nanocrystal surfaces

In a colloidal solution, nanocrystals (NCs) stay separated from each other by repulsive pair potentials, which prevent unwanted NC aggregation.[10] The repulsive pair potentials can be introduced by attaching organic ligands with long flexible chains, molecules such as oleic acid (OA), oleylamine (OAm), and dodecylthiol (DDT), to the NC surface, thus leading to steric repulsion between NCs.[10] These ligands contain a functional headgroup (carboxylic acid, carboxylate, amine, thiol etc.) that binds directly to surface metal sites, while the extended hydrocarbon chain provides steric repulsion that prevents nanocrystals from aggregating in solution.[10] This steric stabilization is highly effective, enabling the synthesis of monodisperse nanocrystals and their dispersion in nonpolar solvents.

However, the long-chain organic ligands that ensure colloidal stability also act as electrically insulating barriers.[11] Their low dielectric constant and large spatial footprint hinder electronic coupling between adjacent nanocrystals, severely limiting charge transport. This becomes a critical bottleneck for optoelectronic applications such as solar cells and photodetectors, where efficient carrier mobility is essential for device performance.[11] Early strategies to address this challenge focused on replacing bulky ligands with shorter organic molecules. For example, researchers have explored exchanging native ligands with short-chain carboxylates or amines containing only a few carbon atoms.[12] While such ligand exchanges can

improve electronic coupling, they often compromise colloidal stability. Nanocrystals capped with short organic ligands tend to aggregate or precipitate before film deposition, leading to non-uniform or defective films that degrade device performance.[13]

Another widely used approach is to first deposit nanocrystal films and then remove the long-chain ligands post-deposition.[10,11] Guyot-Sionnest *et al.* reported the first example of solid-state ligand exchange in NC thin films, showing that chemical treatment of CdSe films with dithiols and diamines could impart Ohmic conductivity.[14] Building on this work, a broad range of post-deposition chemical treatments, such as exposure to hydrazine,[15] halide salts,[16,17] and other short-chain dithiols or diamines,[18,19] have been developed to strip or replace bulky organic ligands. Although these methods can enhance interparticle coupling, they also introduce significant drawbacks. Removing bulky ligands creates voids between nanocrystals, reducing packing density and introducing pathways for charge recombination.[12] In some cases, nanocrystals may fuse or sinter, destroying quantum confinement and altering the material's optoelectronic properties.[13,15] Film cracking and irreversible aggregation are common challenges associated with aggressive ligand-removal strategies.[20]

An alternative method to tackle the problem is to use inorganic ligands, such as halides,[21,22] pseudohalides,[22] chalcogenides,[20,22] oxides,[23] and metal chalcogenide complexes,[24–27] that are only one or a few atoms in size. Unlike organic ligands that stabilize nanocrystals sterically, inorganic ligands stabilize them electrostatically through surface charge.[10] This charge-based stabilization allows nanocrystals to remain colloidally stable while achieving much shorter interparticle distances. Films prepared from inorganic-ligand-capped nanocrystals typically exhibit higher packing densities and significantly improved charge transport, enabling advances in infrared photodetectors, field-effect transistors, and photovoltaics.[28–30]

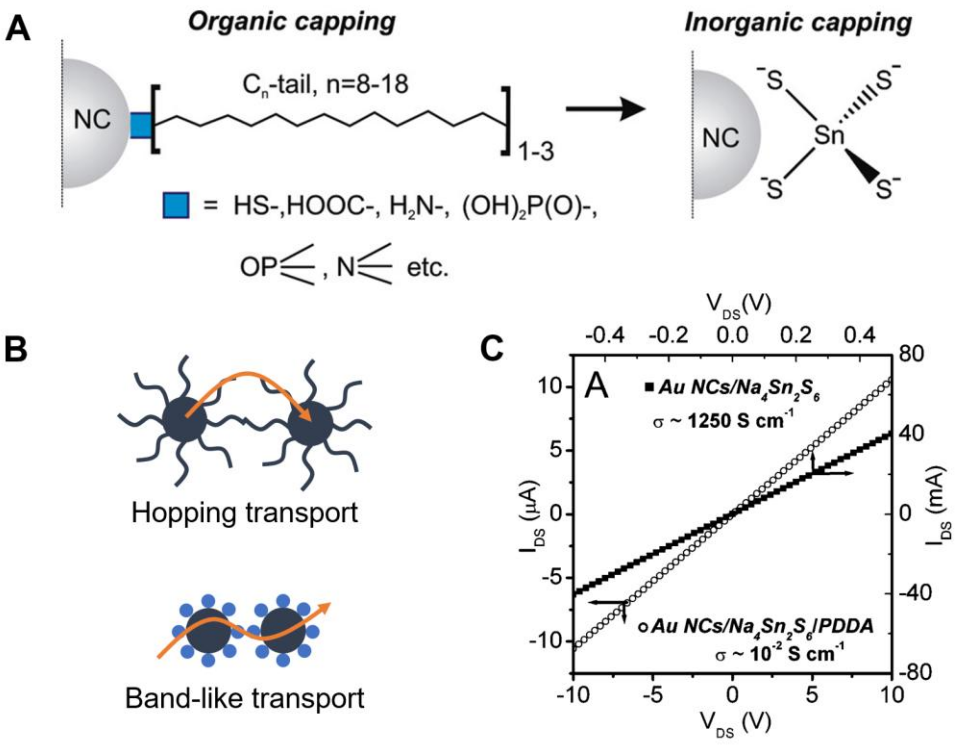

Figure 1.2.1: Comparison of organic and inorganic capping ligands.
(A) Illustration of organic and inorganic capping ligands. **(B)** Illustration of hopping transport and band-like transport in NCs capped with organic and inorganic ligands. **(C)** I-V curve of Au NCs with organic/inorganic ligands. Au NCs with inorganic ligands show higher conductivity. Adapted with permission from ref.[25] © 2010 American Chemical Society.

Within the family of inorganic ligands, this thesis focuses specifically on metal chalcogenide complex (MCC) ligands. Their compact size and high charge density enable nanocrystals to self-assemble into highly ordered superlattices.[31] Such superlattices are attractive not only because they maximize packing density and enhance electronic coupling, but also because they may support emergent collective phenomena that do not arise in disordered assemblies.[13]

1.3. Self-assembly of nanocrystals into strongly coupled superlattices

Self-assembly of nanocrystals (NCs) provides a powerful bottom-up route for constructing complex materials from well-defined nanoscale building blocks. Over the past two decades, researchers have demonstrated an impressive variety of NC-based architectures, including close-packed superlattices, multicomponent crystalline and quasi-crystalline arrangements, and chiral assemblies.[32–34] When NCs pack into ordered superlattices with long-range periodicity, they can exhibit emergent collective behavior not present in isolated particles. For example, enhanced electronic coupling can increase charge mobility,[35,36] cooperative optical responses such as superfluorescence and superradiance,[37,38] and magnetic coupling such as exchange-spring effect (Figure 1.3.1).[39] In addition, theoretical models predict that strong electronic coupling could potentially rise to miniband formation, enabling precise band engineering.[40–42] These collective phenomena broaden the functional potential of NC materials, enabling new opportunities in optoelectronics, quantum information, and nanoscale sensing.

Self-assembly of nanocrystals (NCs) provides a powerful bottom-up route for constructing complex materials from well-defined nanoscale building blocks. Over the past two decades, researchers have demonstrated an impressive variety of NC-based architectures, including close-packed superlattices, multicomponent crystalline and quasi-crystalline arrangements, and chiral assemblies.[32–34] When NCs are organized into superlattices with long-range periodic order, they can exhibit collective behaviors through optical, electronic or magnetic coupling (Figure 1.3.1).

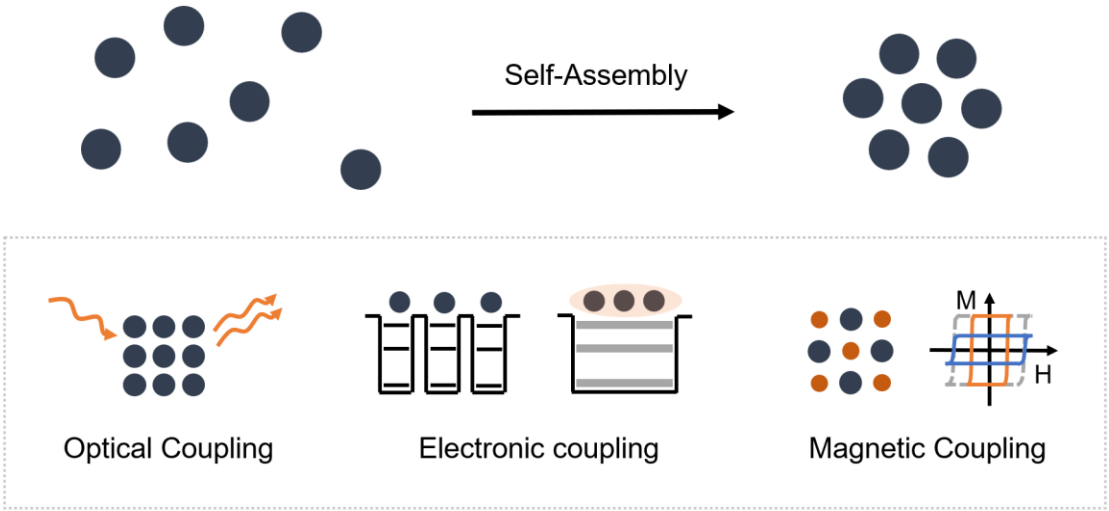

Figure 1.3.1: Coupling behaviors of self-assembled superlattices.
Illustration of the coupling behaviors of self-assembled superlattices.

Conventional strategies for directing NC self-assembly rely on tailoring surface ligands to modulate interparticle potentials, control phase behavior, or introduce external responsiveness (Figure 1.3.2). Adjusting the length, density, or chemistry of organic ligands allows access to a range of superlattice symmetries,[43–45] while DNA-based functionalization has enabled programmable assembly with high structural precision.[46–49] Stimuli-responsive ligands that can be activated chemically, thermally, or photochemically further allow reversible assembly and disassembly.[50,51]

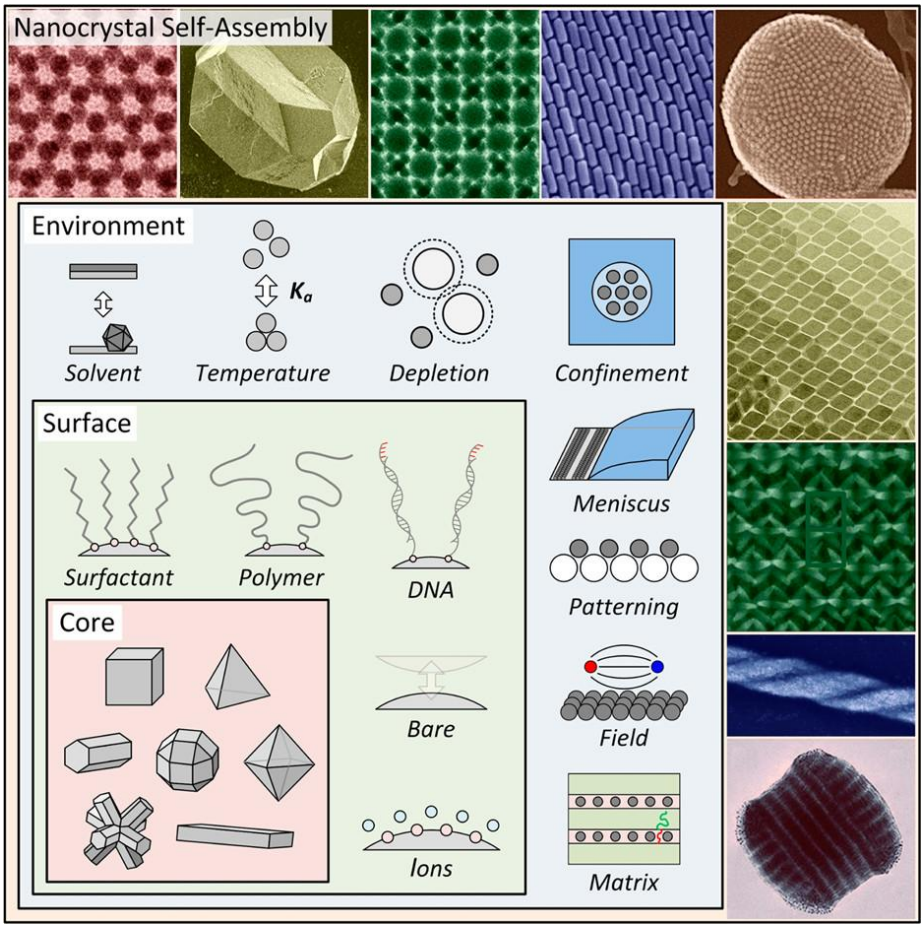

Figure 1.3.2: Diverse range of parameters that influence self-assembly.
Illustration of diverse range of parameters that influence self-assembly. Reprinted with permission from ref.[13] © 2016 American Chemical Society.

Although these ligand systems provide excellent colloidal stability and structural control, their insulating nature suppresses electronic coupling within the resulting superlattices. Attempts to shorten or remove organic ligands can improve coupling but often lead to irreversible aggregation, oriented attachment, or loss of long-range order, limiting the ability to form high-quality, electronically connected NC solids.[19] These limitations highlight the need for alternative surface-chemistry approaches that support both strong interparticle coupling and controlled, reversible assembly.

A promising route involves replacing bulky organic ligands with compact inorganic species (Figure 1.3.3). Such ligands dramatically reduce interparticle spacing, enabling stronger electronic communication and potentially unlocking new collective regimes. Because inorganic ligands stabilize NCs electrostatically rather than sterically, their assembly pathways differ fundamentally from those of organic-capped NCs.[31] Recent work from our group has shown that MCC–capped NCs require the addition of multivalent electrolytes, such as K_3AsS_4, to screen their strong surface charges before assembly can proceed.[31] Once screened, these NCs can be self-assembled into highly ordered superlattices with exceptional packing density and long-range order by altering the solvent environment. Such self-assembly method offers a promising platform for exploring strongly coupled NC solids and the emergent properties that arise from them.

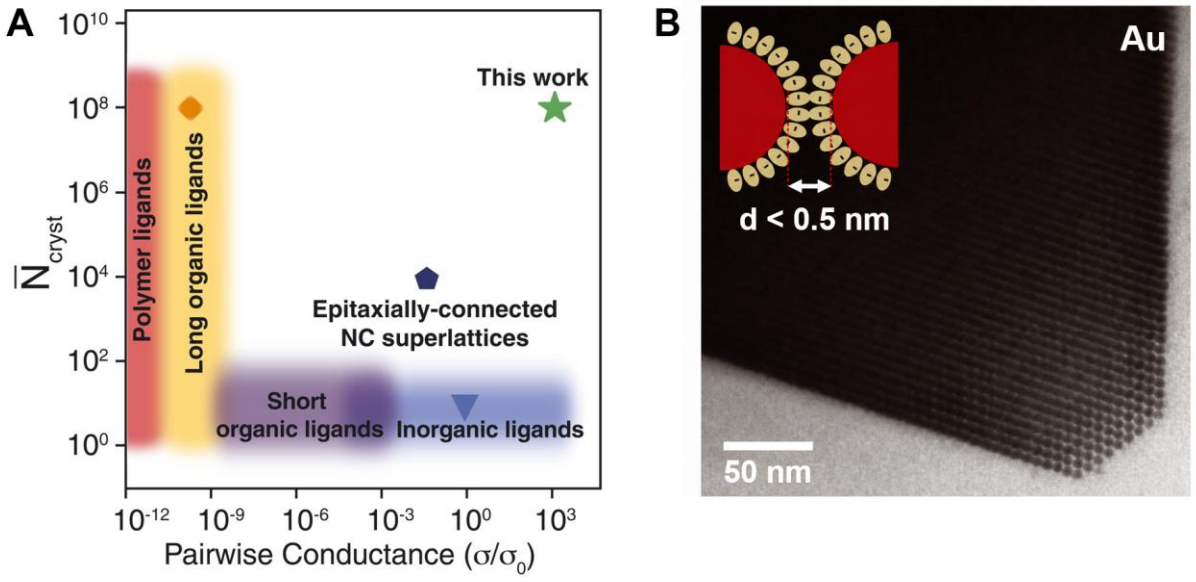

Figure 1.3.3: Self-assembly of all-inorganic nanocrystals to strongly coupled superlattices. **(A)** Order-coupling diagram, showing that superlattice of MCC-capped NCs exhibit both high degree of order and strong electronic coupling. $\overline{N}_{cryst}$ indicates the average number of NCs in a superlattice domain. **(B)** TEM image of $Sn_2S_6^{4-}$-capped Au NC superlattice. Adapted with permission from ref. [31] © 2021 American Association for the Advancement of Science.

1.4. Small-angle X-ray scattering for nanocrystal research

Small-angle X-ray scattering (SAXS) is a powerful characterization technique for probing nanoscale structure in colloidal systems.[52] In a typical SAXS experiment, a collimated X-ray beam is directed onto a sample, and the scattered intensity is collected on a two-dimensional detector at small scattering angles. The resulting pattern contains information about the size, shape, and spatial arrangement of nanoparticles within the sample.

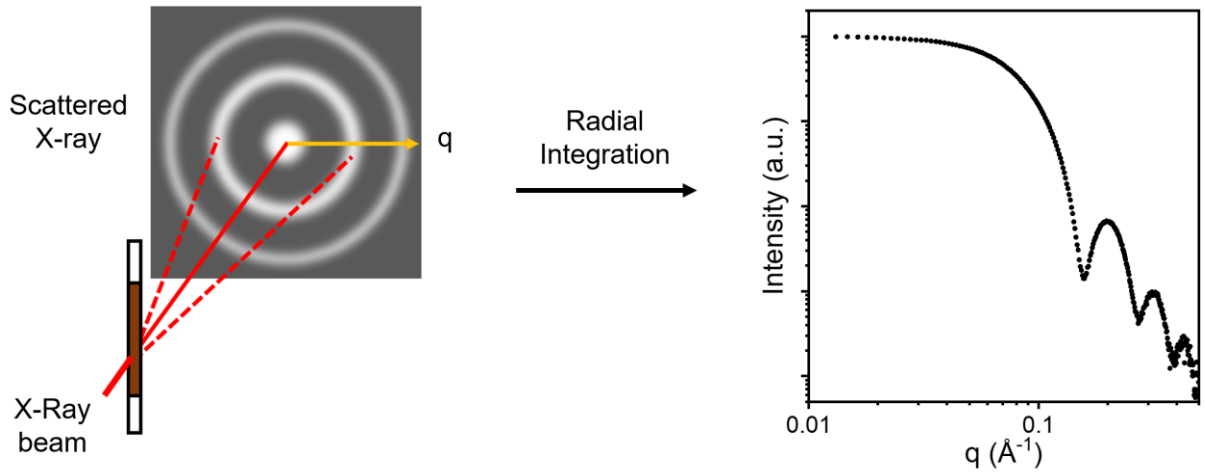

Figure 1.4.1: Small-angle X-ray scattering measurements.
Illustration of SAXS measurement (left) and a representative SAXS pattern of colloidal nanocrystals (right).

Figure 1.4.1 shows a representative SAXS pattern obtained from colloidal PbS nanocrystals (NCs) capped with oleic acid (PbS–OA NCs) with an average core diameter of 5.8 nm. The two-dimensional scattering image is radially integrated to produce a one-dimensional intensity profile, $I(q)$, where $q$is the magnitude of the scattering vector. This 1D SAXS curve forms the basis for structural analysis.

For a single nanocrystal material, the SAXS intensity can be expressed as the product of two contributions: the form factor, $P(q)$, and the structure factor, $S(q)$.[52]

$$I(q) = A\,P(q)\,S(q)$$

The form factor intensity can be modelled as the following, where $F(q,R)$ is the form factor amplitude, $s(R)$ is the size distribution of NCs, q is scattering vector and R is the radius of the NCs:

$$P(q) = \int s(R)\,\langle |F(q,R)|^2 \rangle\,dR$$

$$F(q,R) = \frac{3\big(\sin(qR) - qR\cos(qR)\big)}{(qR)^3}$$

The form factor reflects intrinsic properties of the individual nanocrystals, including their size, shape, and polydispersity.[52] It typically features a low-q Guinier region, where the intensity is nearly flat and sensitive to the overall particle size, followed by an oscillatory decay at high q, known as the Porod region, which contains information about particle shape and surface sharpness.

The structure factor, in contrast, captures how nanocrystals are spatially arranged relative to one another.[52] For a dilute dispersion of well-separated nanocrystals with no positional correlations, the structure factor approaches unity across all q (Figure 1.4.2B). Disordered aggregates exhibit oscillatory features in $S(q)$, reflecting short-range correlations between particles (Figure 1.4.2C).[53] When nanocrystals assemble into ordered superlattices, the structure factor displays sharp Bragg peaks whose positions and intensities reveal the lattice symmetry, periodicity, and degree of long-range order (Figure 1.4.2C).[52]

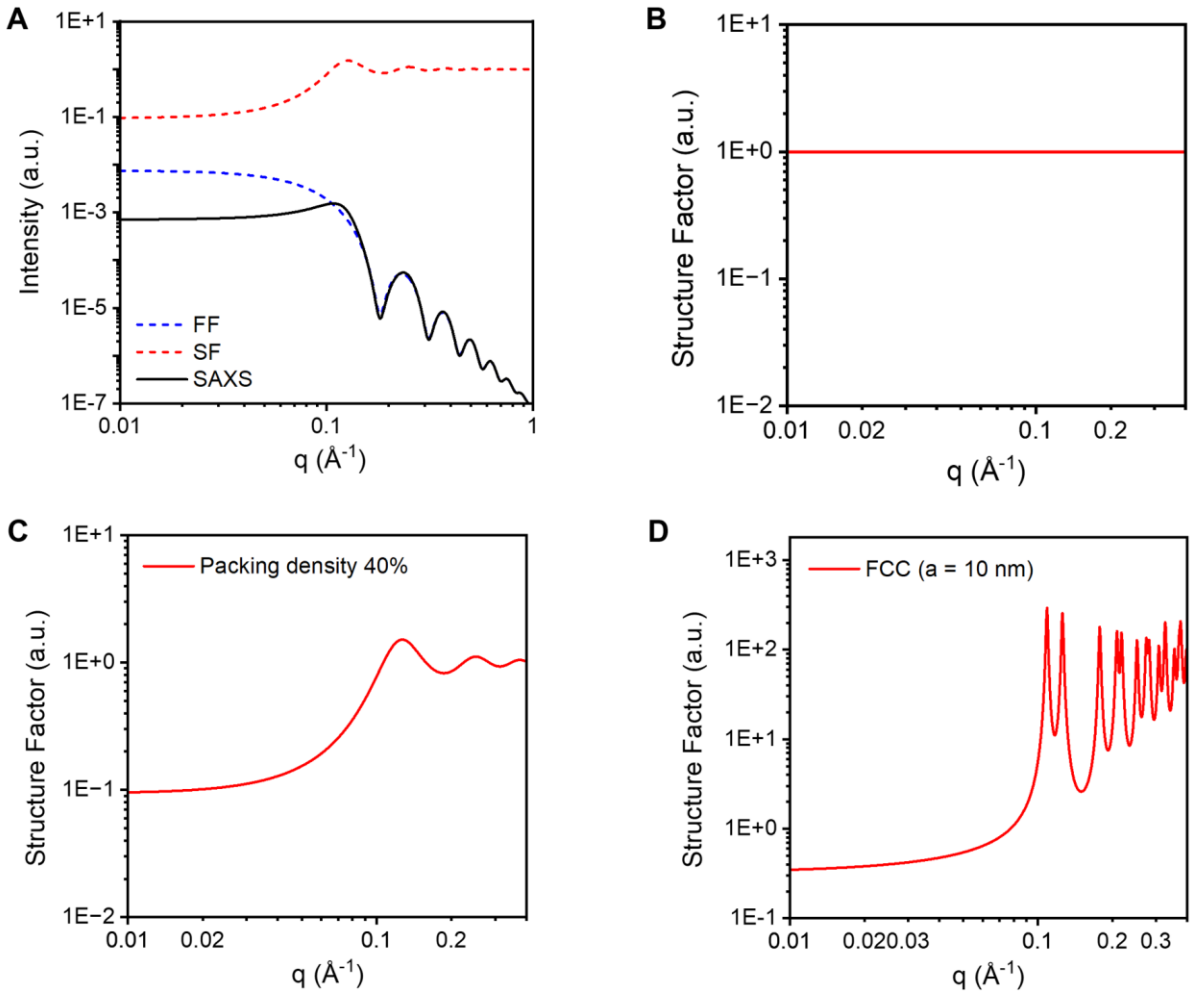

Figure 1.4.2: Structure factor of small-angle X-ray scattering patterns.

(A) Calculated SAXS pattern of a disordered aggregate with a packing density of 40%. Form factor (FF) and structure factor (SF) are shown as dashed lines. **(B)** Structure factor of disordered aggregates. **(C)** Structure factor of an ordered material.

By analyzing both the form factor and structure factor, SAXS provides a comprehensive picture of nanocrystal systems. It enables quantitative extraction of size and shape distributions, assessment of colloidal dispersion quality,[54] and detailed characterization of spatial organization in solution or in solid films.[55] As such, SAXS is an essential tool for understanding how surface

chemistry, interparticle interactions, and assembly conditions shape the structural landscape of colloidal nanocrystals.

1.5. Chapter 1 bibliography

(1) Liu, M.; Yazdani, N.; Yarema, M.; Jansen, M.; Wood, V.; Sargent, E. H. Colloidal Quantum Dot Electronics. *Nat. Electron.* **2021**, *4* (8), 548–558. https://doi.org/10.1038/s41928-021-00632-7.

(2) García De Arquer, F. P.; Talapin, D. V.; Klimov, V. I.; Arakawa, Y.; Bayer, M.; Sargent, E. H. Semiconductor Quantum Dots: Technological Progress and Future Challenges. *Science* **2021**, *373* (6555), eaaz8541. https://doi.org/10.1126/science.aaz8541.

(3) Efros, A. L.; Brus, L. E. Nanocrystal Quantum Dots: From Discovery to Modern Development. *ACS Nano* **2021**, *15* (4), 6192–6210. https://doi.org/10.1021/acsnano.1c01399.

(4) Li, P.; Kim, S.; Tian, B. Beyond 25 Years of Biomedical Innovation in Nano-Bioelectronics. *Device* **2024**, *2* (7). https://doi.org/10.1016/j.device.2024.100401.

(5) Moreels, I.; Lambert, K.; Smeets, D.; De Muynck, D.; Nollet, T.; Martins, J. C.; Vanhaecke, F.; Vantomme, A.; Delerue, C.; Allan, G.; Hens, Z. Size-Dependent Optical Properties of Colloidal PbS Quantum Dots. *ACS Nano* **2009**, *3* (10), 3023–3030. https://doi.org/10.1021/nn900863a.

(6) Carey, G. H.; Abdelhady, A. L.; Ning, Z.; Thon, S. M.; Bakr, O. M.; Sargent, E. H. Colloidal Quantum Dot Solar Cells. *Chem. Rev.* **2015**, *115* (23), 12732–12763. https://doi.org/10.1021/acs.chemrev.5b00063.

(7) Wu, Z.; Ou, Y.; Cai, M.; Wang, Y.; Tang, R.; Xia, Y. Short-Wave Infrared Photodetectors and Imaging Sensors Based on Lead Chalcogenide Colloidal Quantum Dots. *Adv. Opt. Mater.* **2023**, *11* (1), 2201577. https://doi.org/10.1002/adom.202201577.

(8) Kim, J.; Song, S.; Kim, Y.-H.; Park, S. K. Recent Progress of Quantum Dot-Based Photonic Devices and Systems: A Comprehensive Review of Materials, Devices, and Applications. *Small Struct.* **2021**, *2* (3), 2000024. https://doi.org/10.1002/sstr.202000024.

(9) Balazs, D. M.; Loi, M. A. Lead-Chalcogenide Colloidal-Quantum-Dot Solids: Novel Assembly Methods, Electronic Structure Control, and Application Prospects. *Adv. Mater.* **2018**, *30* (33), 1800082. https://doi.org/10.1002/adma.201800082.

(10) Boles, M. A.; Ling, D.; Hyeon, T.; Talapin, D. V. Erratum: The Surface Science of Nanocrystals. *Nat. Mater.* **2016**, *15* (3), 364–364. https://doi.org/10.1038/nmat4578.

(11) Kagan, C. R.; Murray, C. B. Charge Transport in Strongly Coupled Quantum Dot Solids. *Nat. Nanotechnol.* **2015**, *10* (12), 1013–1026. https://doi.org/10.1038/nnano.2015.247.

(12) Morgan, N. Y.; Leatherdale, C. A.; Drndić, M.; Jarosz, M. V.; Kastner, M. A.; Bawendi, M. Electronic Transport in Films of Colloidal CdSe Nanocrystals. *Phys. Rev. B* **2002**, *66* (7), 075339. https://doi.org/10.1103/PhysRevB.66.075339.

(13) Boles, M. A.; Engel, M.; Talapin, D. V. Self-Assembly of Colloidal Nanocrystals: From Intricate Structures to Functional Materials. *Chem. Rev.* **2016**, *116* (18), 11220–11289. https://doi.org/10.1021/acs.chemrev.6b00196.

(14) Guyot-Sionnest, P.; Wang, C. Fast Voltammetric and Electrochromic Response of Semiconductor Nanocrystal Thin Films. *J. Phys. Chem. B* **2003**, *107* (30), 7355–7359. https://doi.org/10.1021/jp0275084.

(15) Talapin, D. V.; Murray, C. B. PbSe Nanocrystal Solids for N- and p-Channel Thin Film Field-Effect Transistors. *Science* **2005**, *310* (5745), 86–89. https://doi.org/10.1126/science.1116703.

(16) Panthani, M. G.; Kurley, J. M.; Crisp, R. W.; Dietz, T. C.; Ezzyat, T.; Luther, J. M.; Talapin, D. V. High Efficiency Solution Processed Sintered CdTe Nanocrystal Solar Cells: The Role of Interfaces. *Nano Lett.* **2014**, *14* (2), 670–675. https://doi.org/10.1021/nl403912w.

(17) Abelson, A.; Qian, C.; Salk, T.; Luan, Z.; Fu, K.; Zheng, J.-G.; Wardini, J. L.; Law, M. Collective Topo-Epitaxy in the Self-Assembly of a 3D Quantum Dot Superlattice. *Nat. Mater.* **2020**, *19* (1), 49–55. https://doi.org/10.1038/s41563-019-0485-2.

(18) Sandeep, C. S. S.; Azpiroz, J. M.; Evers, W. H.; Boehme, S. C.; Moreels, I.; Kinge, S.; Siebbeles, L. D. A.; Infante, I.; Houtepen, A. J. Epitaxially Connected PbSe Quantum-Dot Films: Controlled Neck Formation and Optoelectronic Properties. *ACS Nano* **2014**, *8* (11), 11499–11511. https://doi.org/10.1021/nn504679k.

(19) Cimada daSilva, J.; Balazs, D. M.; Dunbar, T. A.; Hanrath, T. Fundamental Processes and Practical Considerations of Lead Chalcogenide Mesocrystals Formed via Self-Assembly and Directed Attachment of Nanocrystals at a Fluid Interface. *Chem. Mater.* **2021**, *33* (24), 9457–9472. https://doi.org/10.1021/acs.chemmater.1c02910.

(20) Nag, A.; Kovalenko, M. V.; Lee, J.-S.; Liu, W.; Spokoyny, B.; Talapin, D. V. Metal-Free Inorganic Ligands for Colloidal Nanocrystals: S^{2-}, HS^{-}, Se^{2-}, HSe^{-}, Te^{2-}, HTe^{-}, TeS_3^{2-}, OH^{-}, and NH_2^{-} as Surface Ligands. *J. Am. Chem. Soc.* **2011**, *133* (27), 10612–10620. https://doi.org/10.1021/ja2029415.

(21) Dirin, D. N.; Dreyfuss, S.; Bodnarchuk, M. I.; Nedelcu, G.; Papagiorgis, P.; Itskos, G.; Kovalenko, M. V. Lead Halide Perovskites and Other Metal Halide Complexes As

Inorganic Capping Ligands for Colloidal Nanocrystals. *J. Am. Chem. Soc.* **2014**, *136* (18), 6550–6553. https://doi.org/10.1021/ja5006288.

(22) Zhang, H.; Jang, J.; Liu, W.; Talapin, D. V. Colloidal Nanocrystals with Inorganic Halide, Pseudohalide, and Halometallate Ligands. *ACS Nano* **2014**, *8* (7), 7359–7369. https://doi.org/10.1021/nn502470v.

(23) Huang, J.; Liu, W.; Dolzhnikov, D. S.; Protesescu, L.; Kovalenko, M. V.; Koo, B.; Chattopadhyay, S.; Shenchenko, E. V.; Talapin, D. V. Surface Functionalization of Semiconductor and Oxide Nanocrystals with Small Inorganic Oxoanions (PO_4^{3-} , MoO_4^{2-}) and Polyoxometalate Ligands. *ACS Nano* **2014**, *8* (9), 9388–9402. https://doi.org/10.1021/nn503458y.

(24) Kovalenko, M. V.; Scheele, M.; Talapin, D. V. Colloidal Nanocrystals with Molecular Metal Chalcogenide Surface Ligands. *Science* **2009**, *324* (5933), 1417–1420. https://doi.org/10.1126/science.1170524.

(25) Kovalenko, M. V.; Bodnarchuk, M. I.; Zaumseil, J.; Lee, J.-S.; Talapin, D. V. Expanding the Chemical Versatility of Colloidal Nanocrystals Capped with Molecular Metal Chalcogenide Ligands. *J. Am. Chem. Soc.* **2010**, *132* (29), 10085–10092. https://doi.org/10.1021/ja1024832.

(26) Jin, H.; Choi, S.; Xing, G.; Lee, J.-H.; Kwon, Y.; Chong, W. K.; Sum, T. C.; Jang, H. M.; Kim, S. SnS_4^{4-} , SbS_4^{3-} , and AsS_3^{3-} Metal Chalcogenide Surface Ligands: Couplings to Quantum Dots, Electron Transfers, and All-Inorganic Multilayered Quantum Dot Sensitized Solar Cells. *J. Am. Chem. Soc.* **2015**, *137* (43), 13827–13835. https://doi.org/10.1021/jacs.5b05787.

(27) Choi, S.; Jin, H.; Kim, S. SnS_4^{4-} Metal Chalcogenide Ligand, S^{2-} Metal Free Ligand, and Organic Surface Ligand Toward Efficient CdSe Quantum Dot- Sensitized Solar Cells. *J. Phys. Chem. C* **2014**, *118* (30), 17019–17027. https://doi.org/10.1021/jp5005242.

(28) Liu, W.; Lee, J.-S.; Talapin, D. V. III–V Nanocrystals Capped with Molecular Metal Chalcogenide Ligands: High Electron Mobility and Ambipolar Photoresponse. *J. Am. Chem. Soc.* **2013**, *135* (4), 1349–1357. https://doi.org/10.1021/ja308200f.

(29) Bederak, D.; Balazs, D. M.; Sukharevska, N. V.; Shulga, A. G.; Abdu-Aguye, M.; Dirin, D. N.; Kovalenko, M. V.; Loi, M. A. Comparing Halide Ligands in PbS Colloidal Quantum Dots for Field-Effect Transistors and Solar Cells. *ACS Appl. Nano Mater.* **2018**, *1* (12), 6882–6889. https://doi.org/10.1021/acsanm.8b01696.

(30) Lee, J.-S.; Kovalenko, M. V.; Huang, J.; Chung, D. S.; Talapin, D. V. Band-like Transport, High Electron Mobility and High Photoconductivity in All-Inorganic Nanocrystal Arrays. *Nat. Nanotechnol.* **2011**, *6* (6), 348–352. https://doi.org/10.1038/nnano.2011.46.

(31) Coropceanu, I.; Janke, E. M.; Portner, J.; Haubold, D.; Nguyen, T. D.; Das, A.; Tanner, C. P. N.; Utterback, J. K.; Teitelbaum, S. W.; Hudson, ¸ Margaret H.; Sarma, N. A.; Hinkle, A. M.; Tassone, C. J.; Eychmüller, A.; Limmer, D. T.; Olvera De La Cruz, M.; Ginsberg, N.

S.; Talapin, D. V. Self-Assembly of Nanocrystals into Strongly Electronically Coupled All-Inorganic Supercrystals. *Science* **2022**, *375* (6587), 1422–1426. https://doi.org/10.1126/science.abm6753.

(32) Ye, X.; Zhu, C.; Ercius, P.; Raja, S. N.; He, B.; Jones, M. R.; Hauwiller, M. R.; Liu, Y.; Xu, T.; Alivisatos, A. P. Structural Diversity in Binary Superlattices Self-Assembled from Polymer-Grafted Nanocrystals. *Nat. Commun.* **2015**, *6* (1), 10052. https://doi.org/10.1038/ncomms10052.

(33) Talapin, D. V.; Shevchenko, E. V.; Bodnarchuk, M. I.; Ye, X.; Chen, J.; Murray, C. B. Quasicrystalline Order in Self-Assembled Binary Nanoparticle Superlattices. *Nature* **2009**, *461* (7266), 964–967. https://doi.org/10.1038/nature08439.

(34) Zhou, S.; Li, J.; Lu, J.; Liu, H.; Kim, J.-Y.; Kim, A.; Yao, L.; Liu, C.; Qian, C.; Hood, Z. D.; Lin, X.; Chen, W.; Gage, T. E.; Arslan, I.; Travesset, A.; Sun, K.; Kotov, N. A.; Chen, Q. Chiral Assemblies of Pinwheel Superlattices on Substrates. *Nature* **2022**, *612* (7939), 259–265. https://doi.org/10.1038/s41586-022-05384-8.

(35) Whitham, K.; Yang, J.; Savitzky, B. H.; Kourkoutis, L. F.; Wise, F.; Hanrath, T. Charge Transport and Localization in Atomically Coherent Quantum Dot Solids. *Nat. Mater.* **2016**, *15* (5), 557–563. https://doi.org/10.1038/nmat4576.

(36) Talapin, D. V.; Engel, M.; Braun, P. V. Functional Materials and Devices by Self-Assembly. *MRS Bull.* **2020**, *45* (10), 799–806. https://doi.org/10.1557/mrs.2020.252.

(37) Rainò, G.; Becker, M. A.; Bodnarchuk, M. I.; Mahrt, R. F.; Kovalenko, M. V.; Stöferle, T. Superfluorescence from Lead Halide Perovskite Quantum Dot Superlattices. *Nature* **2018**, *563* (7733), 671–675. https://doi.org/10.1038/s41586-018-0683-0.

(38) Chang, W. J.; Roman, B. J.; Paul, T.; Sakotic, Z.; Vora, P.; Kim, K.; Hurst, L. E.; Wasserman, D.; Truskett, T. M.; Milliron, D. J. Ultrastrong Coupling by Assembling Plasmonic Metal Oxide Nanocrystals in Open Cavities. *ACS Nano* **2025**, *19* (12), 12332–12344. https://doi.org/10.1021/acsnano.5c01913.

(39) Chen, J.; Ye, X.; Oh, S. J.; Kikkawa, J. M.; Kagan, C. R.; Murray, C. B. Bistable Magnetoresistance Switching in Exchange-Coupled $CoFe_2O_4$ –Fe_3O_4 Binary Nanocrystal Superlattices by Self-Assembly and Thermal Annealing. *ACS Nano* **2013**, *7* (2), 1478–1486. https://doi.org/10.1021/nn3052617.

(40) Jiang, C.-W.; Green, M. A. Silicon Quantum Dot Superlattices: Modeling of Energy Bands, Densities of States, and Mobilities for Silicon Tandem Solar Cell Applications. *J. Appl. Phys.* **2006**, *99* (11), 114902. https://doi.org/10.1063/1.2203394.

(41) Lazarenkova, O. L.; Balandin, A. A. Miniband Formation in a Quantum Dot Crystal. *J. Appl. Phys.* **2001**, *89* (10), 5509–5515. https://doi.org/10.1063/1.1366662.

(42) Talapin, D. V.; Lee, J.-S.; Kovalenko, M. V.; Shevchenko, E. V. Prospects of Colloidal Nanocrystals for Electronic and Optoelectronic Applications. *Chem. Rev.* **2010**, *110* (1), 389–458. https://doi.org/10.1021/cr900137k.

(43) Boles, M. A.; Talapin, D. V. Binary Assembly of PbS and Au Nanocrystals: Patchy PbS Surface Ligand Coverage Stabilizes the CuAu Superlattice. *ACS Nano* **2019**, *13* (5), 5375–5384. https://doi.org/10.1021/acsnano.9b00006.

(44) Boles, M. A.; Talapin, D. V. Many-Body Effects in Nanocrystal Superlattices: Departure from Sphere Packing Explains Stability of Binary Phases. *J. Am. Chem. Soc.* **2015**, *137* (13), 4494–4502. https://doi.org/10.1021/jacs.5b00839.

(45) Coropceanu, I.; Boles, M. A.; Talapin, D. V. Systematic Mapping of Binary Nanocrystal Superlattices: The Role of Topology in Phase Selection. *J. Am. Chem. Soc.* **2019**, *141* (14), 5728–5740. https://doi.org/10.1021/jacs.8b12539.

(46) Kahn, J. S.; Gang, O. Designer Nanomaterials through Programmable Assembly. *Angew. Chem.* **2022**, *134* (3), e202105678. https://doi.org/10.1002/ange.202105678.

(47) Liu, W.; Halverson, J.; Tian, Y.; Tkachenko, A. V.; Gang, O. Self-Organized Architectures from Assorted DNA-Framed Nanoparticles. *Nat. Chem.* **2016**, *8* (9), 867–873. https://doi.org/10.1038/nchem.2540.

(48) Tian, Y.; Lhermitte, J. R.; Bai, L.; Vo, T.; Xin, H. L.; Li, H.; Li, R.; Fukuto, M.; Yager, K. G.; Kahn, J. S.; Xiong, Y.; Minevich, B.; Kumar, S. K.; Gang, O. Ordered Three-Dimensional Nanomaterials Using DNA-Prescribed and Valence-Controlled Material Voxels. *Nat. Mater.* **2020**, *19* (7), 789–796. https://doi.org/10.1038/s41563-019-0550-x.

(49) Tian, Y.; Zhang, Y.; Wang, T.; Xin, H. L.; Li, H.; Gang, O. Lattice Engineering through Nanoparticle–DNA Frameworks. *Nat. Mater.* **2016**, *15* (6), 654–661. https://doi.org/10.1038/nmat4571.

(50) Grzelczak, M.; Liz-Marzán, L. M.; Klajn, R. Stimuli-Responsive Self-Assembly of Nanoparticles. *Chem. Soc. Rev.* **2019**, *48* (5), 1342–1361. https://doi.org/10.1039/C8CS00787J.

(51) Bian, T.; Gardin, A.; Gemen, J.; Houben, L.; Perego, C.; Lee, B.; Elad, N.; Chu, Z.; Pavan, G. M.; Klajn, R. Electrostatic Co-Assembly of Nanoparticles with Oppositely Charged Small Molecules into Static and Dynamic Superstructures. *Nat. Chem.* **2021**, *13* (10), 940–949. https://doi.org/10.1038/s41557-021-00752-9.

(52) Li, T.; Senesi, A. J.; Lee, B. Small Angle X-Ray Scattering for Nanoparticle Research. *Chem. Rev.* **2016**, *116* (18), 11128–11180. https://doi.org/10.1021/acs.chemrev.5b00690.

(53) Hayter, J. B.; Penfold, J. An Analytic Structure Factor for Macroion Solutions. *Mol. Phys.* **1981**, *42* (1), 109–118. https://doi.org/10.1080/00268978100100091.

(54) Saunders, A. E.; Korgel, B. A. Second Virial Coefficient Measurements of Dilute Gold Nanocrystal Dispersions Using Small-Angle X-Ray Scattering. *J. Phys. Chem. B* **2004**, *108* (43), 16732–16738. https://doi.org/10.1021/jp047153j.

(55) Weidman, M. C.; Smilgies, D.-M.; Tisdale, W. A. Kinetics of the Self-Assembly of Nanocrystal Superlattices Measured by Real-Time in Situ X-Ray Scattering. *Nat. Mater.* **2016**, *15* (7), 775–781. https://doi.org/10.1038/nmat4600.

2. Chapter 2: Methods for synthesis and characterization of nanocrystals

Reprinted with permission from *ACS Nano* 2024, 18, 50, 33864–33874. Copyright © 2024 American Chemical Society.

Reprinted with permission from *J. Am. Chem. Soc.* 2026, 148, 25, 25480–25490. Copyright © 2026 American Chemical Society.

2.1. Synthesis of nanocrystals

This section outlines the synthetic procedures used throughout this thesis to prepare colloidal nanocrystals (NCs), with a particular focus on PbS nanocrystals stabilized by oleic acid ligands.

2.1.1 Synthesis of PbS nanocrystals

PbS nanocrystals (NCs) are commonly prepared using a hot-injection method in which a sulfur precursor is rapidly introduced into a hot solution containing a lead precursor and coordinating ligands in a nonpolar organic solvent. In this work, I employ a procedure adapted from the Jon Owen group, where substituted thioureas serve as the sulfur source and lead oleate provides both the lead ions and the native ligand environment.

Preparation of lead oleate

Preparation of lead oleate follows the method developed by Owen's group.[1] Lead oleate was synthesized as follows. In a 100 mL round-bottom flask, PbO (10.0 g) was suspended in acetonitrile (20 mL, 15.27 g) and cooled in an ice bath. While stirring, trifluoroacetic acid (1.043 g) and trifluoroacetic anhydride (9.368 g) were added dropwise. Because this reaction is highly

exothermic, additions were paused whenever acetonitrile reflux was observed. The mixture gradually transitioned from an orange-yellow suspension to a clear, colorless solution. Separately, oleic acid (25.437 g), triethylamine (10.246 g), and isopropanol (180 mL) were combined in a 1 L conical flask. The solution from the 100 mL flask was then transferred into this mixture while stirring. A white precipitate initially formed, partially dissolved, and eventually remained as the solution reached saturation. After stirring for an additional 30 minutes, the mixture became a thick white suspension.

The suspension was heated on a hot plate at 200 °C until most solids dissolved, then cooled overnight in a refrigerator. The resulting white solid (lead oleate) was collected by vacuum filtration with methanol washing, transferred into several 40 mL vials, and dried overnight in a vacuum oven. The final product was a free-flowing white powder.

Preparation of thiourea

Thiourea derivatives were synthesized via a click-type reaction between an isothiocyanate and an amine.[1] For example, *N*-phenyl-*N*′-*n*-dodecylthiourea was prepared by suspending n-dodecylamine (11.56 g) in toluene (20 mL) in a 500 mL round-bottom flask. A separate suspension of phenyl isothiocyanate (8.44 g) in toluene (20 mL) was added, and the mixture was stirred for ~30 minutes. The reaction mixture evolved from a white suspension to a clear, pale-yellow solution. Toluene was removed by rotary evaporation, and the remaining solids were dried overnight in a vacuum oven, yielding a white to pale-yellow powder. Other substituted thiourea precursors can be prepared using a similar method, using different combinations of isothiocyanates and amines.

Synthesis of 5.8 nm PbS-OA nanocrystals

Synthesis of PbS-OA NCs follows method developed by Owen's group.[1] To prepare 5.8 nm PbS NCs capped with oleic acid (PbS-OA NCs), $Pb(OA)_2$ (5.544 g, 7.2 mmol) and 1-octene (60 mL) were loaded into a three-neck 250 mL round-bottom flask under nitrogen. The mixture was heated to 120 °C. A solution of *N*-phenyl-*N*′-*n*-dodecylthiourea (1.923 g, 6 mmol) in diglyme (2 mL) was then injected. After 10 minutes, the reaction was quenched and transferred into a glovebox. Nanocrystals were precipitated using methyl acetate, redispersed in hexane, and centrifuged to remove insoluble residues. Purification consisted of four cycles of precipitation with methyl acetate followed by redispersion in hexane. The final product was stored in anhydrous hexane under nitrogen. The experimental setup can be found in Figure 2.1.1.

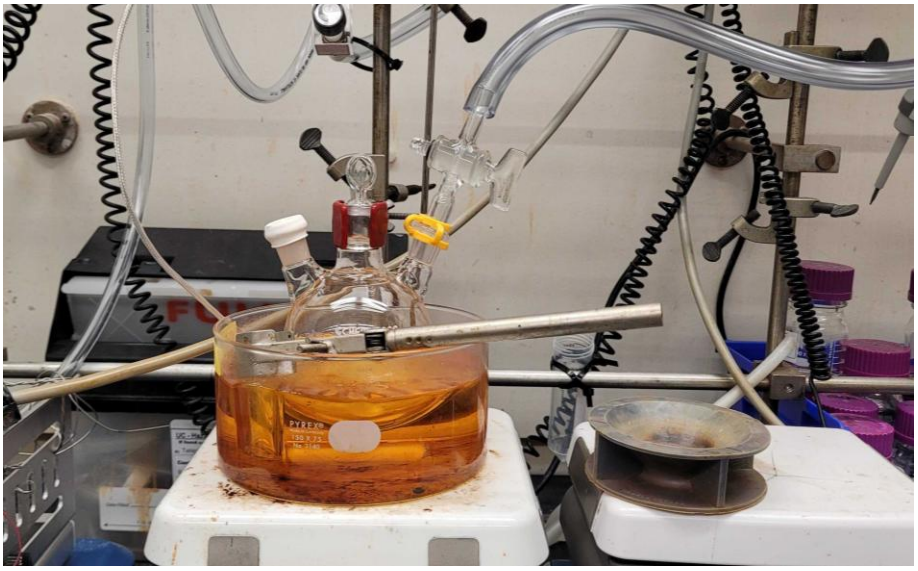

Figure 2.1.1: Experimental setup for PbS-OA NC synthesis by hot injection of substituted thiourea.

Photograph of experimental setup for PbS-OA NC synthesis by hot injection of substituted thiourea. The photograph was taken right before the hot injection.

Size control of PbS-OA nanocrystals

The size of PbS-OA nanocrystals can be systematically tuned by modifying either the thiourea precursor or the reaction solvent.[1] In general, substituted thioureas bearing electron-withdrawing substituents activate more rapidly during hot injection, leading to faster nucleation and ultimately smaller nanocrystals, whereas electron-donating substituents slow precursor activation and yield larger particles. Solvent choice also plays a key role: replacing 1-octene with the more viscous octadecene (ODE) slows reaction kinetics and promotes the growth of larger nanocrystals. Using these principles, different sizes of PbS-OA NCs were synthesized by varying precursor identity and solvent.

For example, 4.0 nm NCs were obtained by injecting *N*-(p-(trifluoromethyl)phenyl)-*N*′-dodecylthiourea (2.331 g, 6 mmol) mixed with diglyme (2 ml) into $Pb(OA)_2$ (5.544 g, 7.2 mmol) in 1-octene (60 ml) at 120 °C, while 7.2 nm NCs were produced by injecting *N*-phenyl-*N*′-*n*-dodecylthiourea (1.923 g, 6 mmol) mixed with diglyme (5 ml) into $Pb(OA)_2$ (5.544 g, 7.2 mmol) in ODE (60 ml) at the same temperature. Increasing both the electron-donating character of the thiourea and the reaction temperature yielded even larger particles, such as 8.3 nm NCs synthesized by injecting *N*-hexyl-*N*′-dodecylthiourea (1.972 g, 6 mmol) with diglyme (2 ml) into $Pb(OA)_2$ (5.544 g, 7.2 mmol) in ODE (60 ml) at 150 °C. All samples were purified using identical precipitation-redispersion cycles to ensure consistent ligand coverage and colloidal quality. The UV-Vis spectra and TEM images of the PbS-OA NCs are shown in Figure 2.1.2.

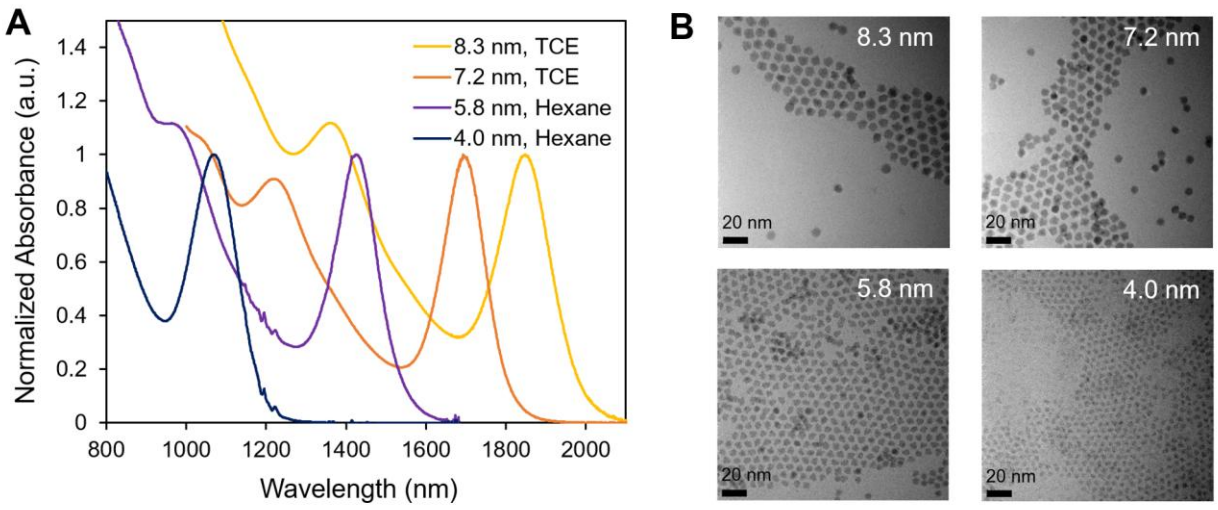

Figure 2.1.2: PbS-OA NCs from substituted thiourea method.

(A) UV-Vis spectra and **(B)** TEM images of PbS-OA NCs synthesized by hot injection of substituted thiourea.

Synthesis of PbS-OA NCs by hot injection of $(TMS)_2S$

An alternative route for synthesizing PbS NCs involves injecting bis(trimethylsilyl)sulfide ($(TMS)_2S$) into a solution of lead oleate that is prepared *in situ* by degassing a mixture of lead oxide and oleic acid at elevated temperature.[2] This method represents the conventional approach for producing PbS NCs. In a typical synthesis, PbO (0.45 g, 2 mmol), oleic acid (15 g), and octadecene (ODE, 10 g) are combined in a 100 mL flask and degassed under vacuum at 95 °C for 30 minutes. After degassing, the atmosphere is switched to nitrogen. Separately, a solution containing $(TMS)_2S$ (210 µL, 1 mmol) and ODE (5 ml) is prepared inside a glovebox and loaded into a syringe fitted with a needle. The syringe is then removed from the glovebox, and the precursor solution is swiftly injected into the lead oleate mixture. Immediately after injection, the heat source is removed, and the reaction mixture is allowed to cool naturally to room temperature.

The crude PbS nanocrystals are transferred to a nitrogen-filled glovebox and precipitated by adding ethanol in a 1:1 volume ratio. The product is washed once more by redissolving in hexane and reprecipitating with ethanol. Finally, the purified PbS-oleate (PbS-OA) NCs are redispersed in hexane and stored under nitrogen. This procedure yields monodisperse PbS-OA NCs with an average diameter of 5.4 nm. The particle size can be tuned by adjusting the amount of oleic acid used in the reaction: 3.5 nm when 2 g of oleic acid is added, 4.0 nm with 5 g, and 5.0 nm with 10 g. The UV-Vis spectra and TEM images of the PbS-OA NCs are shown in Figure 2.1.3.

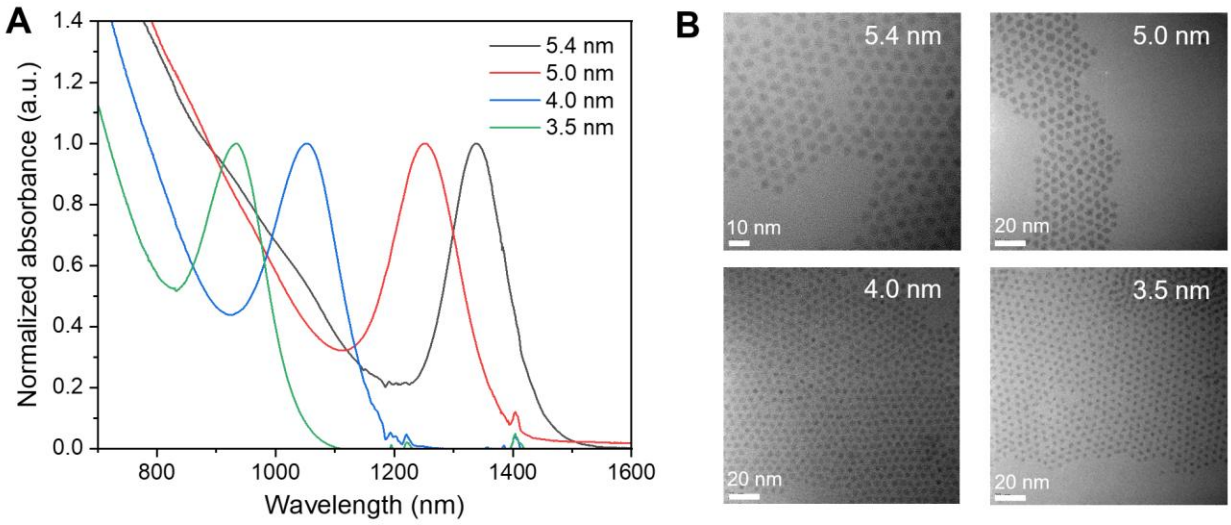

Figure 2.1.3: PbS-OA NCs from $(TMS)_2S$ method.

(A) UV-Vis spectra and **(B)** TEM images of PbS-OA NCs synthesized by hot injection of $(TMS)_2S$.

2.1.2 Synthesis of CdSe nanocrystals

Cadmium selenide (CdSe) nanocrystals (NCs) are another classical class of quantum dots widely employed in optoelectronic devices, including light-emitting diodes and photodetectors. In this work, CdSe NCs were synthesized following a heat-up method adapted from the

procedure developed by Charles Cao and co-workers.[3] In this approach, a mixture of cadmium myristate and selenium dioxide is dispersed in oleic acid and octadecene (ODE) and heated to initiate nucleation and growth. The nanocrystal size is primarily controlled by the reaction time, with shorter reaction durations yielding smaller NCs. Cadmium myristate was prepared in-house, while selenium dioxide was obtained commercially.

Preparation of cadmium myristate

Cadmium myristate was synthesized via a metathesis reaction between sodium myristate and cadmium nitrate.[3] In a 2 L conical flask, NaOH (1.2 g, 30 mmol), myristic acid (6.852 g, 30 mmol), and methanol (500 g) were combined and stirred overnight to ensure complete dissolution and formation of sodium myristate. Separately, $Cd(NO_3)_2 \cdot 4H_2O$ (3.084 g, 10 mmol) was dissolved in methanol (10 mL) and added dropwise to the reaction flask. The mixture initially turned milky and subsequently formed a white precipitate corresponding to cadmium myristate. The solid was collected by vacuum filtration, washed thoroughly with methanol, and dried overnight in a vacuum oven before use.

Synthesis of CdSe nanocrystals

Synthesis of CdSe NCs follows the method developed by Charles Cao's group.[3] To synthesize 5.2 nm CdSe-oleate (CdSe-OA) NCs, cadmium myristate (1.701 g, 3 mmol), selenium dioxide (333 mg, 3 mmol), and ODE (75 g) were loaded into a 250 mL round-bottom flask. The mixture was degassed at 100 °C under vacuum for 1 h and then heated to 240 °C under nitrogen. Approximately 3 min after the temperature reached 230 °C, oleic acid (3 mL) was added dropwise to promote growth and surface passivation. The reaction was quenched 90 min

after reaching 240 °C by removing the heat source and introducing air. Notably, quenching at any time between 5 and 90 min produced NCs of similar size, indicating a narrow growth window under these conditions. Once the mixture cooled below 150 °C, oleylamine (2 mL) and toluene (20 mL) were added. The CdSe-OA NCs were precipitated by adding acetone and ethanol, redispersed in hexane, and subjected to a second precipitation with ethanol before final redispersion in hexane for storage.

Smaller CdSe NCs can be synthesized using the same procedure but except quenching the reaction earlier. However, since the CdSe NC size reaches maximum (5.4 nm) within about 5 minutes, size control by this method is usually very difficult and not reproducible. The UV-Vis spectrum and TEM image of 5.4 nm CdSe NCs are shown in Figure 2.1.4.

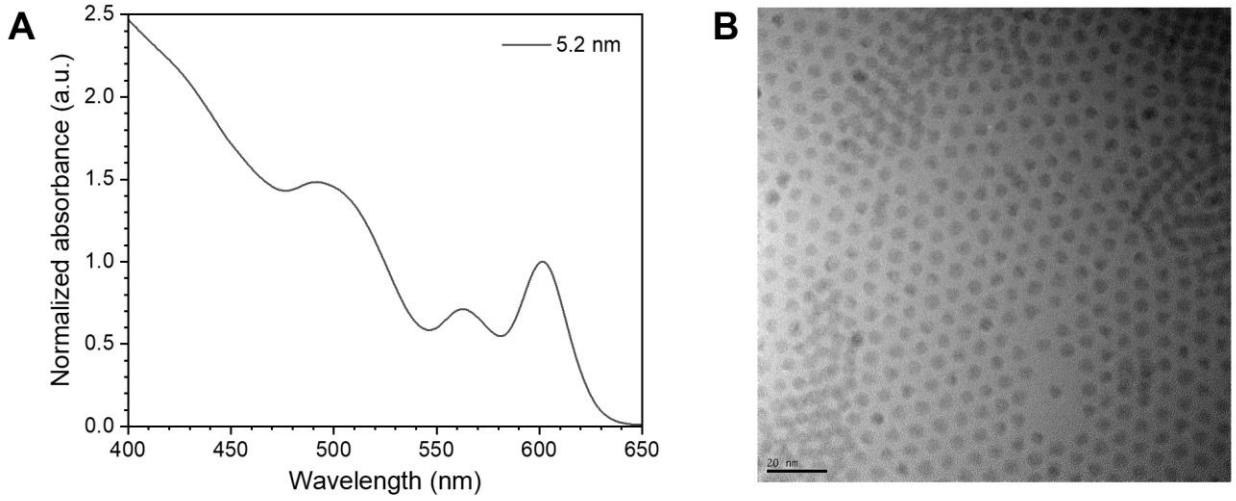

Figure 2.1.4: CdSe-OA/OAm NCs from heat-up method.
(A) UV-Vis spectrum and **(B)** TEM image of 5.4 nm CdSe NCs with a mixture of oleic acid and oleylamine ligands.

2.1.3 Synthesis of Au nanocrystals

Synthesis of 4.0 nm Au NCs

Gold nanocrystals (Au NCs) were synthesized by rapid reduction of Au(III) precursors in the presence of long-chain organic ligands.[4] For the preparation of 4.0 nm Au NCs, 100 mg of $HAuCl_4 \cdot 3H_2O$ was dissolved in a mixture of 15 mL oleylamine (OAm) and 5 mL *n*-hexane. The reaction mixture was cooled to 15 °C using an ice-water bath. Separately, a reducing solution was prepared by dissolving 0.080 g of tetrabutylammonium borohydride (TBAB) in 1 mL OAm and 0.5 mL *n*-hexane. Because TBAB does not fully dissolve under these conditions, the solution was filtered prior to injection. Upon rapid injection of the TBAB solution into the Au precursor mixture, the color changed from golden yellow to dark purple within seconds, indicating the formation of Au NCs. The nanocrystals were precipitated by adding ethanol and subsequently redispersed in hexane. This synthetic method consistently produced Au NCs with diameters between 3.5 and 4.0 nm, largely independent of reaction temperature, solvent composition, or precursor concentration. The TEM image of the Au NC is shown in Figure 2.1.5A.

Synthesis of 5.4 nm Au NCs

To synthesize larger Au NCs (5.4 nm),[5] 124 mg of $AuPPh_3Cl$ and 125 μL of dodecanethiol (DDT) were dissolved in 20 mL of decane. The reaction mixture was heated to 115 °C, after which a reducing solution containing 43 mg TBAB in 2 mL benzene was injected. The solution turned from colorless to dark purple within seconds, confirming rapid nucleation and growth of Au NCs. After stirring for approximately 30 minutes, the reaction mixture was cooled to room temperature, and the nanocrystals were precipitated with ethanol. This procedure

reliably produced Au-DDT NCs with diameters in the range of 5.0 – 5.5 nm. The TEM image of the Au NC is shown in Figure 2.1.5B.

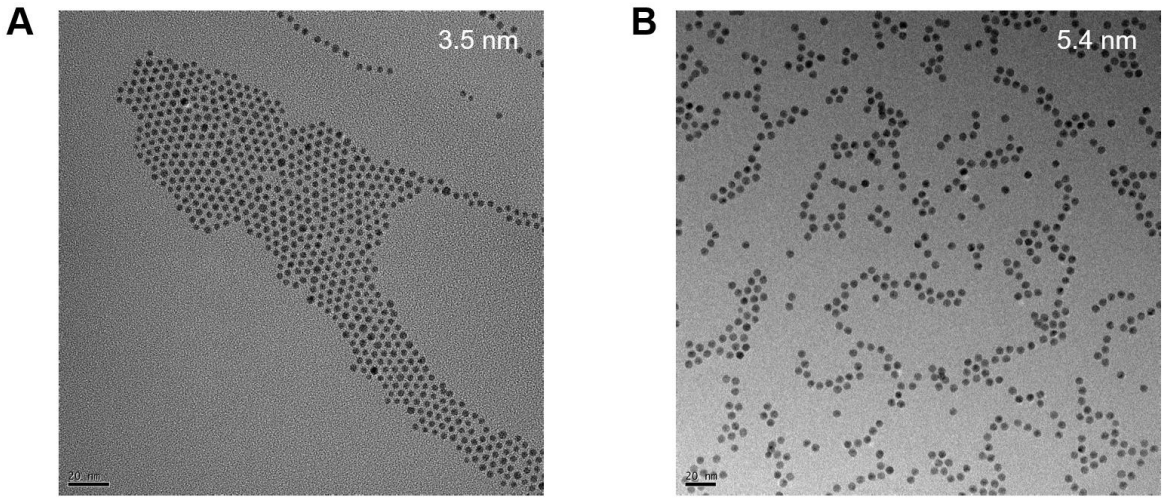

Figure 2.1.5: Au-OAm and Au-DDT NCs from injection of TBAB method.
TEM images of **(A)** 3.5 nm Au-OAm NCs and **(B)** 5.4 nm Au-DDT NCs.

2.2. Ligand exchange of NCs to metal chalcogenide ligands

2.2.1 Experimental procedure for ligand exchange

Ligand exchange of colloidal nanocrystals (NCs) with metal chalcogenide complexes (MCCs) is achieved through a biphasic transfer process in which hydrophobic, organically capped NCs are driven from a nonpolar solvent into a polar medium containing multivalent, anionic ligands.

Distillation of NMF

N-methylformamide (NMF) was purified by vacuum distillation to remove residual impurities and moisture. In a typical procedure, approximately 300 mL of crude NMF was placed in a 500 mL round bottom flask and distilled into a 100 mL round bottom flask to collect the first fraction. After about 30 mL of NMF is collected, the 100 mL round bottom flask was replaced with 250 mL one neck receiving flask, which conveniently fits into a small glovebox antechamber. The distilled NMF was then transferred to glovebox and dried over activated molecular sieves overnight. During distillation, it is crucial to maintain a sufficiently low temperature to prevent thermal decomposition of NMF. The temperature recorded on the thermometer should remain between 40 °C and 50 °C, which can typically be achieved by setting the hotplate to around 150 °C and adjusting as needed. A strong vacuum (< 300 mmTorr) is essential to avoid overheating; insufficient vacuum can lead to decomposition, which is recognizable by the appearance of a pale-yellow color in the distilled NMF.

Although calcium hydride (CaH_2) is recommended as a drying agent, satisfactory results were obtained even without its use. To use CaH_2 as a drying agent, solid chunks of CaH_2 were filled to about half of 40 ml centrifuge tube, and then poured into crude NMF in air. The NMF distillation setup was then fully assembled, and the NMF was stirred with CaH_2 overnight under N_2 flow overnight. The distillation was then carried out like described above. The photograph of the setup can be found below.

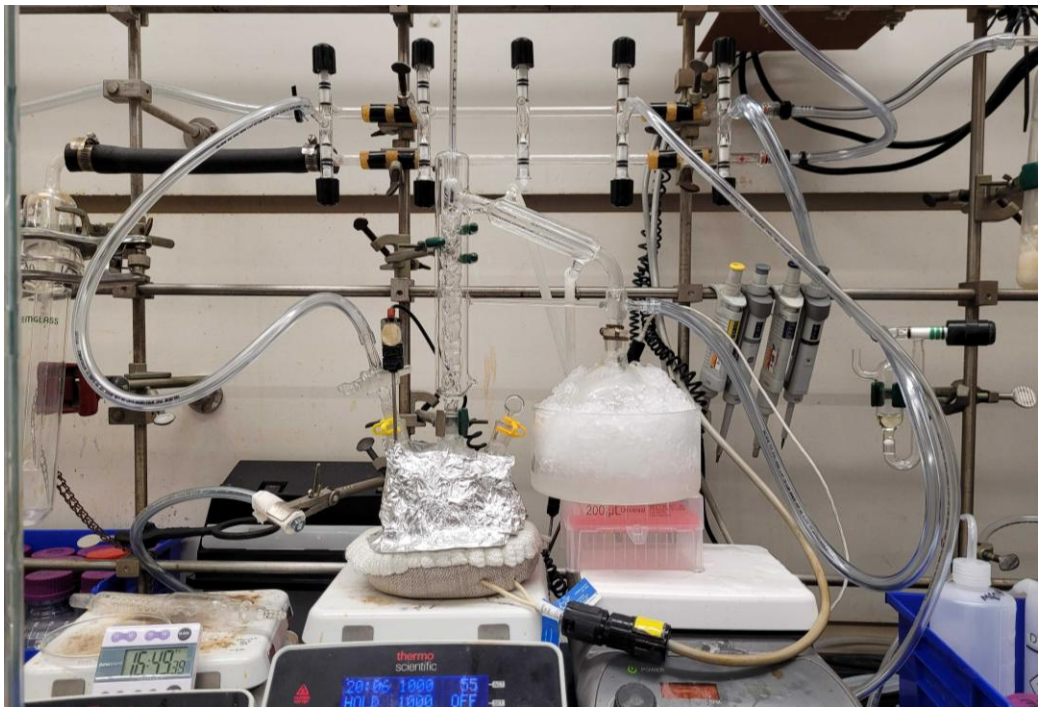

Figure 2.2.1: NMF distillation setup.
Photograph of N-methylformamide (NMF) distillation setup.

Preparation of metal chalcogenide ligand solutions

MCC ligand solutions were prepared by dissolving alkali metal chalcogenide salts in NMF in stoichiometric ratios.[6,7] For example, a 0.16 M $K_4Sn_2S_6$ solution was obtained by combining K_2S (397 mg, 3.6 mmol), SnS_2 (731 mg, 4 mmol), and 10 mL of distilled NMF in a 20 mL vial and stirring the mixture overnight. The initially turbid orange–brown suspension gradually became homogeneous as the salts dissolved. The solution was then purified by centrifugation to remove insoluble white solids that precipitated at the bottom of the tube. After removal of these residues, the supernatant appeared as a clear orange–brown solution. Larger-scale preparations followed the same procedure, though larger vessels (100–250 mL) were required. Because SnS_2 has limited solubility in NMF, it was added in slight excess to minimize the presence of unreacted K_2S, which is known to etch PbS NCs. ICP-OES analysis

confirmed that the resulting solution contained 0.16 M $K_4Sn_2S_6$, indicating that the salts only partially dissolve under these conditions. The dissolution process is exothermic, and care must be taken during scale-up to prevent localized overheating or boiling of NMF.

Other MCC ligand solutions were prepared analogously. A 0.5 M K_3AsS_4 solution was obtained by mixing K_2S (827 mg, 7.5 mmol) and As_2S_5 (775 mg, 2.5 mmol) in NMF, while a 0.2 M K_4GeS_4 solution was prepared from K_2S (323 mg, 4 mmol) and GeS_2 (274 mg, 2 mmol). After overnight stirring, both solutions were purified by centrifugation to remove undissolved solids, yielding clear, light-yellow solutions. Except for SnS_2, which was synthesized in-house, all salts were obtained from commercial suppliers.

Biphasic ligand exchange procedure

The ligand exchange of PbS-OA NCs with MCC ligands followed a previously reported biphasic protocol.[8] In a typical exchange, 4 mL of 25 mM $K_4Sn_2S_6$ in distilled NMF was combined with 8–10 mL of anhydrous hexane and approximately 100 mg of PbS-OA NCs dissolved in hexane in a 20 mL vial. The biphasic mixture was stirred for approximately 4 hours, during which the NCs transferred completely from the upper hexane layer to the lower NMF layer, indicating successful replacement of hydrophobic ligands with anionic $Sn_2S_6^{4-}$ ligands. To remove residual organic ligands and unbound MCC species, the hexane phase was replaced with fresh hexane three times, with 30 minutes of stirring between each replacement. The MCC-capped PbS NCs were then precipitated from the NMF phase using acetonitrile as a nonsolvent, collected, and redispersed in fresh 25 mM $K_4Sn_2S_6$ solution. A second round of biphasic purification was performed following the same procedure. After the final precipitation, the NCs were redispersed in distilled NMF and filtered through a 0.22 μm PVDF membrane. All

steps were conducted in a dry N_2 glovebox to prevent moisture-induced degradation of the MCC ligands.

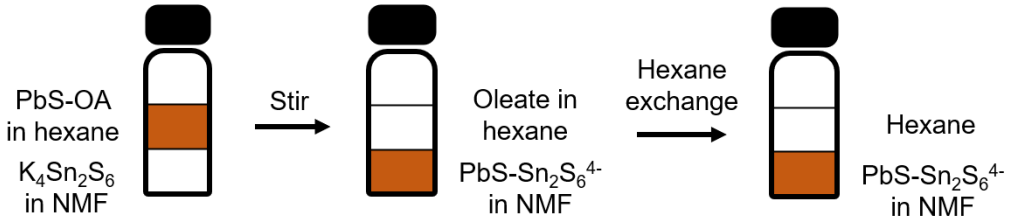

Figure 2.2.2: Ligand exchange.
Schematics of ligand exchange procedure.

Ligand exchange of PbS NCs with other MCC ligands (K_3AsS_4 and K_4GeS_4) followed the same general procedure. For CdSe NCs, higher ligand concentrations (50 mM) and significantly longer exchange times (2–3 nights) were required to achieve complete transfer. Ligand exchange of Au NCs proceeded similarly to that of PbS.

2.2.2 Spectroscopic and colloidal evidence of successful ligand exchange

Following ligand exchange, the nanocrystal (NC) powder exhibits a clear visual change. Figure 2.2.3 presents the photograph of PbS-OA and PbS-$Sn_2S_6^{4-}$ NC powders, prepared by adding a nonsolvent (methyl acetate or acetonitrile, respectively), removing the supernatant, and evaporating residual solvent under vacuum. The photograph shows that the NCs transition from a dull brown/black powder to a shiny, reflective black material after exchange. This change in appearance indicates that the PbS NCs evolve from electronically uncoupled particles into a more strongly coupled, bulk-like solid upon replacement of the long-chain oleate ligands.

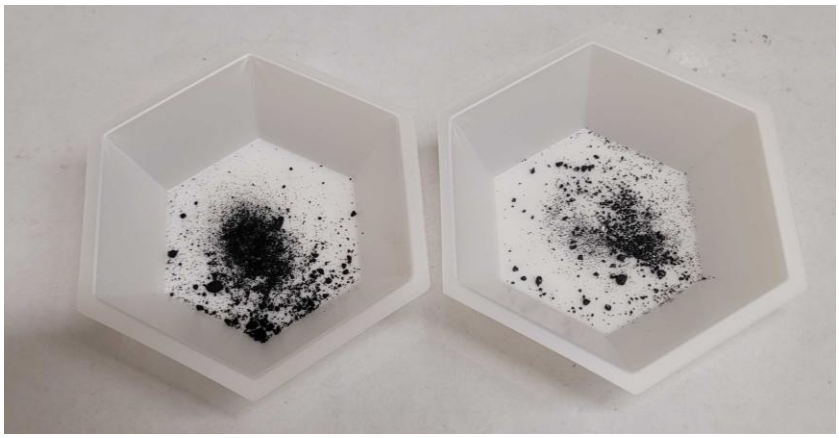

Figure 2.2.3: Photograph of PbS NCs with oleate and thiostannate ligands.

Photograph 6.0 nm PbS NCs before (PbS-OA, left) and after (PbS-$Sn_2S_6^{4-}$, right) the ligand exchange. PbS-OA NC powders are dull, whereas PbS-$Sn_2S_6^{4-}$ NC powders are shiny.

Optical spectroscopy further confirms successful ligand exchange. UV–Vis absorption spectra of 5.8 nm PbS NC solutions showed a red-shift in the first excitonic peak after exchange with $Sn_2S_6^{4-}$ ligands (Figure 2.2.4A). This attributes to the relaxation of quantum confinement, because the carriers to extend into the $Sn_2S_6^{4-}$ ligand layer. The UV-Vis of 5.2 nm CdSe does not exhibit noticeable red-shift after ligand exchange, indicating that the S atoms on $Sn_2S_6^{4-}$ ligands attached at the surface of CdSe NCs do not contribute to relaxation of quantum confinement, indicating that the carriers do not extend into the $Sn_2S_6^{4-}$ ligand layer (Figure 2.2.4B). This observation is consistent with previous literature.[7]

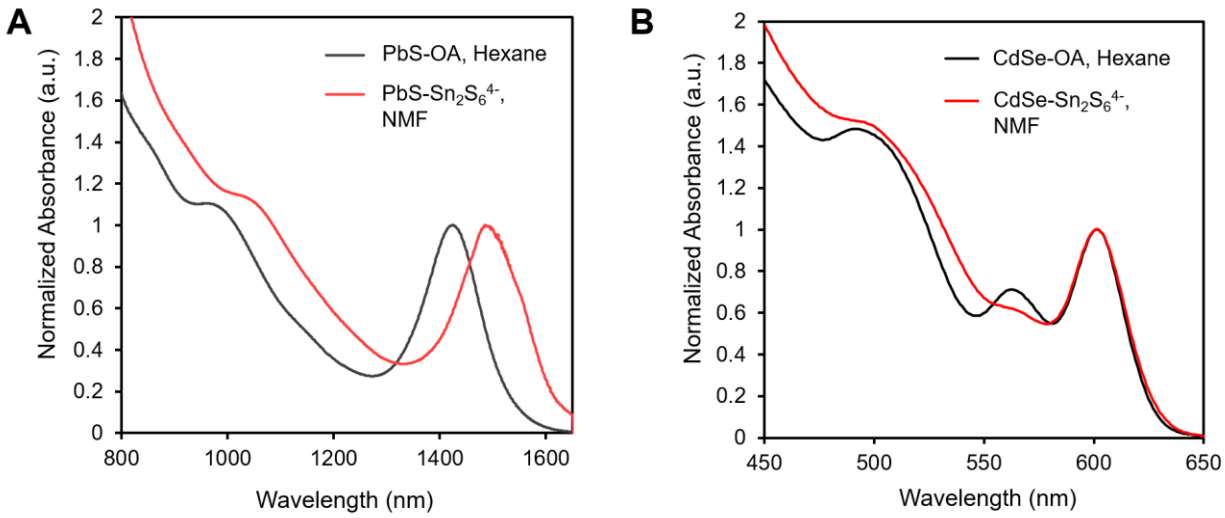

Figure 2.2.4: UV-Vis spectra of PbS and CdSe NCs with oleate and thiostannate ligands. UV-Vis spectra of **(A)** 5.8 nm PbS and **(B)** 5.2 nm CdSe NCs with oleate (OA) ligands and thiostannate ($Sn_2S_6^{4-}$) ligands.

Fourier-transform infrared (FTIR) spectroscopy further confirmed ligand replacement. Figure 2.2.5 shows the FTIR spectra of 6.0 nm PbS-OA and PbS-$Sn_2S_6^{4-}$ NCs, measured in powdered form (like shown in Figure 2.2.3). The FTIR pattern was then background-subtracted, and baseline-corrected using a fifth-order polynomial function (automated function fit, Peak Spectroscopy Software). The characteristic C–H stretching modes associated with oleate ligands disappeared after exchange, indicating significant removal of organic surface species.

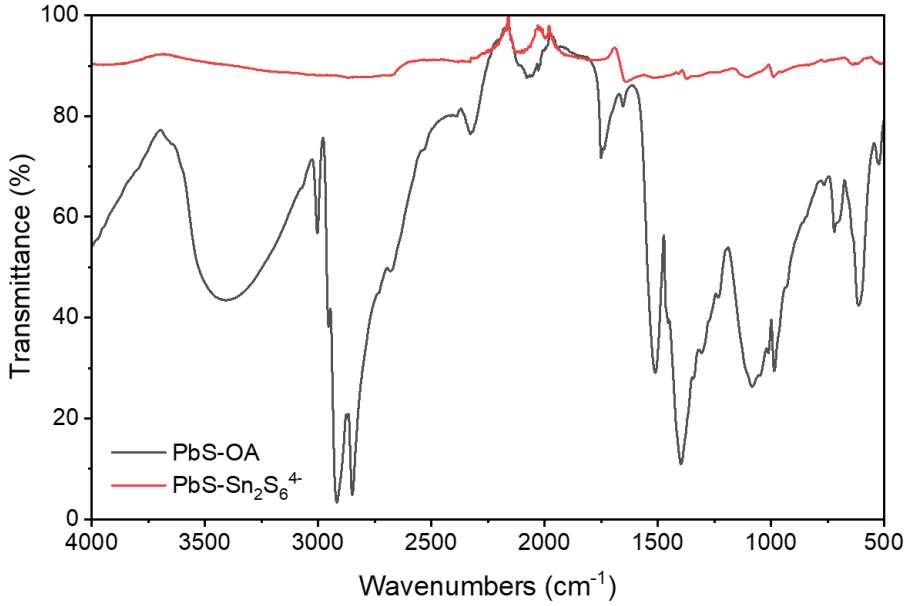

Figure 2.2.5: IR spectra of PbS NCs with oleate and thiostannate ligands.
IR spectra 6.0 nm PbS NCs before (PbS-OA, orange line) and after (PbS-$Sn_2S_6^{4-}$, blue line) the ligand exchange. Lack of C-H stretch vibrations in the 2800-3300 cm^{-1} indicate that oleic acid was removed from the surface. The IR spectra were background subtracted and baseline corrected.

Zeta potential measurements provided an additional confirmation (Table 2.1). Following ligand exchange, the NCs exhibited strongly negative zeta potentials, consistent with the presence of multivalent anionic MCC ligands on the NC surface. The increased surface charge also contributed to improved colloidal stability in polar solvents such as NMF.

Table 2.1: Zeta potential of thiostannate-capped nanocrystals.

NC type	Solvent	Zeta potential
4.0 nm PbS-$Sn_2S_6^{4-}$	NMF	-21.0 mV
5.8 nm PbS-$Sn_2S_6^{4-}$	NMF	-26.1 mV
7.2 nm PbS-$Sn_2S_6^{4-}$	NMF	-25.9 mV

2.3. Self-assembly of nanocrystals

Self-assembly experiments in this work were performed primarily on thiostannate-capped PbS nanocrystals (PbS-$Sn_2S_6^{4-}$ NCs), unless otherwise noted. In general, self-assembly of metal chalcogenide ligand (MCC)-capped NCs was induced by introducing a multivalent electrolyte (e.g., K_3AsS_4, $K_4Sn_2S_6$) followed by either the addition of a nonsolvent or controlled solvent evaporation. The procedures below describe the standard methods used for screening, structural characterization, and film fabrication.

Screening procedure for self-assembly

To rapidly assess whether a given PbS NC sample was capable of self-assembly, a small-volume screening protocol was used. In a typical experiment, 4 μL of a concentrated PbS

NC stock solution (50–100 mg/mL), 8 μL of 0.50 M K_3AsS_4 in NMF, and 8 μL of *N,N*-dimethylformamide (DMF) were combined in a 2 mL centrifuge tube. The mixture was vortexed or pipette-mixed thoroughly and immediately transferred into a glass capillary for SAXS measurement. This procedure enabled rapid evaluation of interparticle ordering under a controlled electrolyte concentration and solvent environment.

Preparation of superlattice powder for structural analysis

For structural characterization by transmission electron microscopy (TEM), scanning transmission electron microscopy (STEM), or SAXS, the self-assembly process was carried out more slowly to increase superlattice grain size and improve sample quality. In a typical preparation, 20 μL of a PbS NC stock solution (50–100 mg/mL) was mixed with 40 μL of DMF. A 500 mM K_3AsS_4 solution was then added incrementally in 5 μL aliquots at one-minute intervals under continuous stirring, until a total of 40 μL had been added. The mixture was stirred for an additional 20 minutes, during which ordered superlattice domains formed as a suspension in the NMF/DMF solvent mixture.

The suspension was centrifuged for 60 seconds to collect the superlattice material, and the supernatant was removed. The resulting pellet was resuspended in 5–10 μL of acetonitrile (MeCN) and drop-cast onto TEM grids for imaging or Kapton tape for SAXS measurements.

Preparation of "washed" superlattice powder for structural analysis

Throughout this thesis, the effect of "washing" superlattices is discussed, as this treatment influences the reversibility and stability of the assembled structures. Washed superlattices were prepared by resuspending the collected superlattice pellet in ~1 mL of MeCN,

followed by centrifugation and removal of the supernatant. This washing step was repeated twice. The final washed superlattice was resuspended in 5–10 μL of MeCN for transfer to a TEM grid for TEM/STEM measurement or Kapton tape for SAXS measurement.

Film fabrication for morphology analysis

Film fabrication procedures differed depending on whether the NCs were capped with organic (oleate) or inorganic ($Sn_2S_6^{4-}$) ligands. Below are the procedures for preparing samples for SEM measurement. For SAXS measurement of the films, a thinner boron-doped Si wafer with a thickness of 50-75 μm to maximize the transmission of X-ray.

For PbS-OA films, a 525 μm thick nitrogen-doped Si wafer with a 300 nm dry-grown thermal oxide layer was cleaned by sonicating sequentially in hexane, acetone, deionized water, and isopropanol for 5 minutes each. The wafer surface was then treated by spin-coating hexamethyldisilazane (HMDS) at 3000 rpm for 45 seconds, followed by annealing at 150 °C for 30 minutes. A solution of PbS-OA NCs in methylcyclohexane (MCH) was drop-cast onto the wafer and allowed to dry under ambient conditions. During solvent evaporation, the wafer was tilted by approximately 10°, achieved by resting one edge on a glass microscope slide, to promote directional solvent flow and improve film uniformity.

For PbS-$Sn_2S_6^{4-}$ NCs, the same wafer cleaning procedure was used, but instead of HMDS treatment, the wafer was exposed to oxygen plasma (Harrick Plasma Cleaner PDC-001) for 15 minutes. The wafer was then transferred into a dry N_2 glovebox. A solution of PbS-$Sn_2S_6^{4-}$ NCs with 0-90 mM K_3AsS_4 in NMF was drop-cast onto the wafer and dried under vacuum. As with PbS–OA films, the wafer was tilted by ~10° during evaporation.

2.4. Measurement and analysis of small-angle X-ray scattering

2.4.1 SAXS measurement and size analysis of colloidal nanocrystal solution

SAXS measurement

Small-angle X-ray scattering (SAXS) measurements were performed primarily on nanocrystal (NC) samples dispersed in solution or on superlattice powders suspended in solvent. For solution-phase measurements, 20–40 μL of the sample was loaded into glass capillaries with an inner diameter of 0.9 mm and a wall thickness of 0.1 mm. The samples were transferred into the capillaries and both ends were sealed by briefly melting the glass under ambient atmosphere prior to measurement. For samples that are highly air-sensitive, or when working with extremely volatile or flammable solvents such as hydrazine, the capillaries can instead be sealed using a UV-curable glues. This approach enables sealing inside a glovebox, ensuring that the samples remain completely oxygen- and moisture-free.

Colloidal stability

Evaluating the colloidal stability of NCs is essential for predicting their ability to self-assemble into high-quality superlattices, as well as for determining whether they can be stored for extended periods and used to produce reproducible inks for solution-processed printing. Visual inspection is a useful first step. Large aggregates or visible clusters immediately indicate instability, but this approach cannot detect micro-scale clustering. Such subtle aggregation may persist unnoticed for hours or even weeks before ultimately leading to precipitation, and also can prevent the NCs from forming ordered superlattices.

Dynamic light scattering (DLS) is a classical method for assessing colloidal stability, but its reliability is limited by the large number of floating parameters required to fit a single

autocorrelation function. As a result, DLS often fails to provide an accurate picture of early-stage aggregation in NC dispersions.

Small-angle X-ray scattering (SAXS) offers a more intuitive and robust means of evaluating colloidal stability. When plotted on a log-log scale, a stable NC dispersion exhibits a characteristic SAXS profile: a nearly flat Guinier region at low q, followed by a steep intensity decay in the Porod region at high q (further discussed in Chapter 3).[9] Well-defined Bessel oscillations are typically observed for monodisperse NCs with size distributions narrower than ~10%. In contrast, unstable dispersions show a pronounced upturn in the low-q region, where the Guinier regime becomes a straight line whose slope reflects the dimensionality of the aggregates (e.g., three-dimensional clusters, sheets, or chains). Most commonly, NCs form three-dimensional aggregates, producing an $I(q) \propto q^{-4}$ dependence at low q.[9] This behavior arises from the superposition of form factors spanning the entire size range from individual NCs to bulk-like clusters. Representative examples of these scattering patterns are shown in Figure 2.4.1.

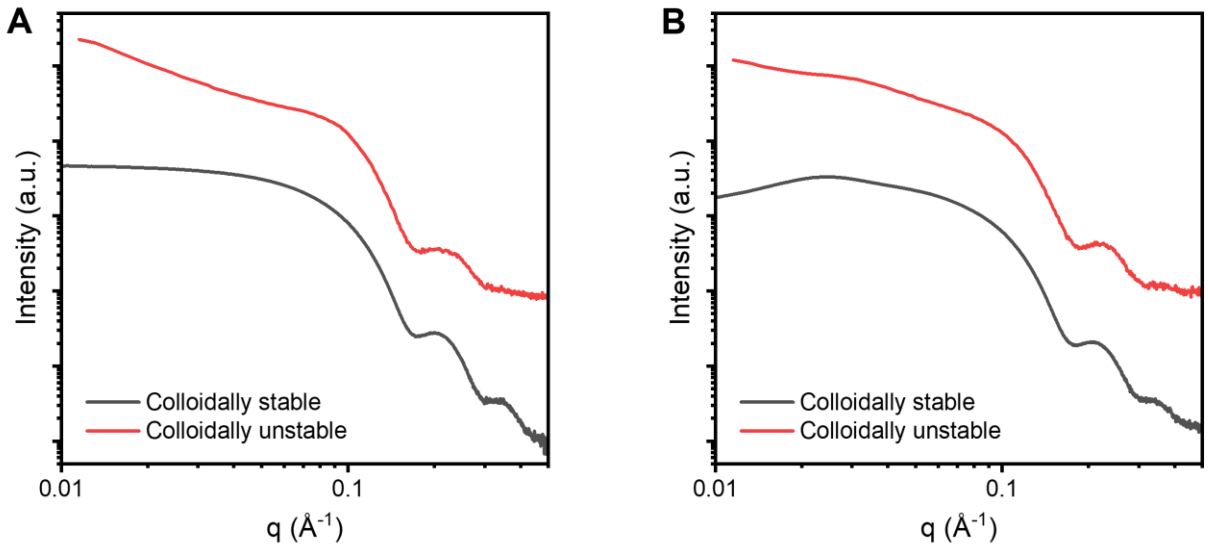

Figure 2.4.1: SAXS patterns of colloidally stable and unstable CdSe NCs.
SAXS patterns of colloidally stable and colloidally unstable 5.2 nm CdSe NCs with **(A)** oleate (OA) ligands and **(B)** thiostannate ($Sn_2S_6^{4-}$) ligands.

Size distribution analysis

The size distribution of PbS-$Sn_2S_6^{4-}$ NCs was determined indirectly by analyzing SAXS patterns of the corresponding oleate-capped PbS NCs. Direct extraction of size information from PbS-$Sn_2S_6^{4-}$ NC SAXS patterns was avoided because the $Sn_2S_6^{4-}$ ligands contain relatively heavy elements that scatter X-rays strongly, artificially inflating the apparent NC diameter.

For size analysis, the SAXS pattern of the oleate-capped NCs was first background-subtracted using the scattering profile of an empty solvent-filled capillary. The corrected intensity profile was then fitted using the size-distribution fitting tools in the Irena package implemented in Igor Pro 9. The fitting region was selected near the transition between the Guinier and Porod regimes (typically $2.0 < qR < 4.5$), where the scattering is most sensitive to particle size and polydispersity (Figure 2.4.2A).

Size distributions were obtained using the maximum entropy method, yielding both number-weighted and volume-weighted distributions (Figure 2.4.2B). The reported NC diameter corresponds to the peak position of the volume-weighted distribution. The size polydispersity (standard deviation) was determined by fitting the volume distribution to a Gaussian function and extracting the corresponding standard deviation. The SAXS patterns and volume distribution of PbS-OA NCs are shown in Figure 2.4.2C and D.

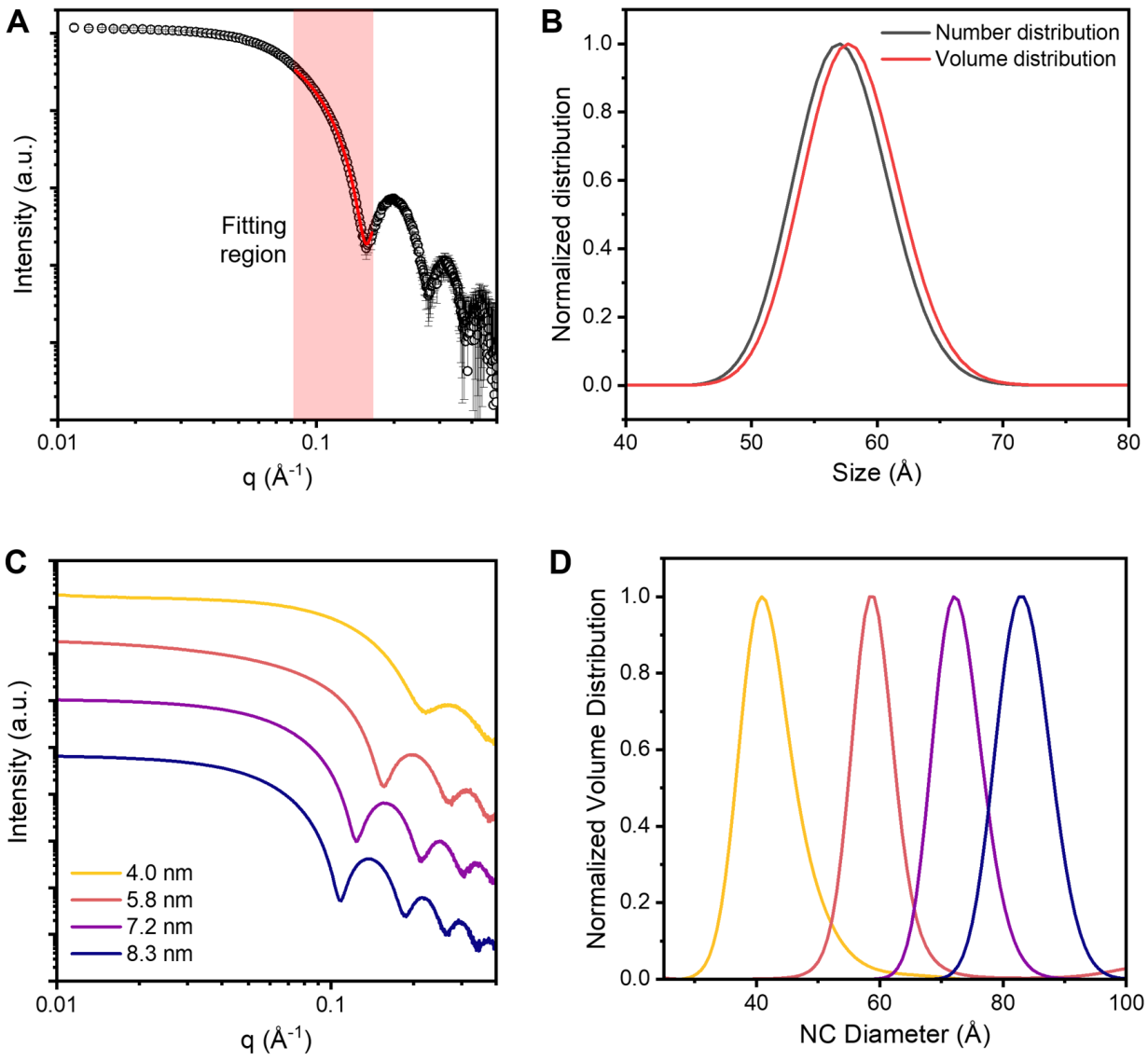

Figure 2.4.2: Size analysis of colloidal nanocrystals using SAXS.

(A) Illustration of size fitting of 5.8 nm PbS-OA NCs. Black circles with error bars are experimental SAXS intensity. Red line is the fitted SAXS pattern using IgorPro9. **(B)** Number and volume distribution of the 5.8 nm PbS-OA NCs. **(C)** SAXS patterns and **(D)** size distributions of 10 mg/ml solutions of PbS-OA NCs in MCH. The size distribution was obtained by analyzing the form factor of SAXS pattern.

2.4.2 Small-angle X-ray scattering of solids and structural analysis

SAXS measurement

For powdered samples, a concentrated NC suspension was drop-cast onto the adhesive side of Kapton tape. A second piece of Kapton tape was placed on top to encapsulate the sample, forming a sealed sandwich structure suitable for SAXS analysis.

Drop-cast or spin-coated NC films were also prepared on thin Si substrates for SAXS measurements. These films were deposited onto boron-doped Si wafers with a thickness of 50–75 μm, which provided sufficient X-ray transparency for transmission-mode measurements.

Bragg peak analysis

Observation of Bragg peaks in the SAXS pattern provides clear evidence that the NCs have self-assembled into an ordered superlattice. The positions of these peaks can be analyzed to determine the crystal structure adopted by the superlattice. To do this, an initial lattice type is assumed, and Miller indices are assigned to each Bragg peak according to the reflection rules for common lattices.

Table 2.2: Reflection rules for common lattices.

Unit Cell	Allowed Reflections
Simple Cubic	Any $h, k\ l$
BCC	$h+k+l$ is even
FCC	$h, k\ l$ all odd or all even
FCC Diamond	h, k, l all odd or $4n$
HCP	l even, and $h+2k \neq 3n$

Once tentative Miller indices are assigned, the scattering vector of each Bragg peak, q_{max}, is compared to the expected value based on the relationship:

$$q_{\max} = \frac{2\pi}{a}\sqrt{h^2 + k^2 + l^2}$$

where a is the cubic lattice constant.[10] If the indices are assigned correctly, a plot of q_{max} versus $\sqrt{h^2 + k^2 + l^2}$ yields a straight line passing through the origin, with a slope equal to $2\pi/a$. The Miller index assignments are refined iteratively until a linear relationship is obtained. If no such line can be produced, the assumed lattice type is rejected and a different structure is tested. After a consistent assignment is found, the lattice constant is extracted from the slope and evaluated for physical reasonableness. Although this method provides a rapid way to identify the superlattice structure, it is not fully conclusive; cross-validation with complementary techniques such as TEM, SEM, or electron diffraction is recommended.

Figures 2.4.3A and C show the plot of q_{max} versus $2\pi\sqrt{h^2 + k^2 + l^2}$ for the Miller indices that best match the experimental peak positions of 7.2 nm PbS NCs, and the corresponding peak assignments are shown in Figures S2.4.3B and D. Some reflections are not visible due to suppression of peak intensity by the form-factor contribution. From this SAXS analysis, we conclude that superlattices formed from 7.2 nm PbS-OA NCs adopt an FCC structure with a lattice constant of 13.2 nm, while 7.2 nm PbS-$Sn_2S_6^{4-}$ NCs also form an FCC superlattice but with a smaller lattice constant of 11.0 nm.

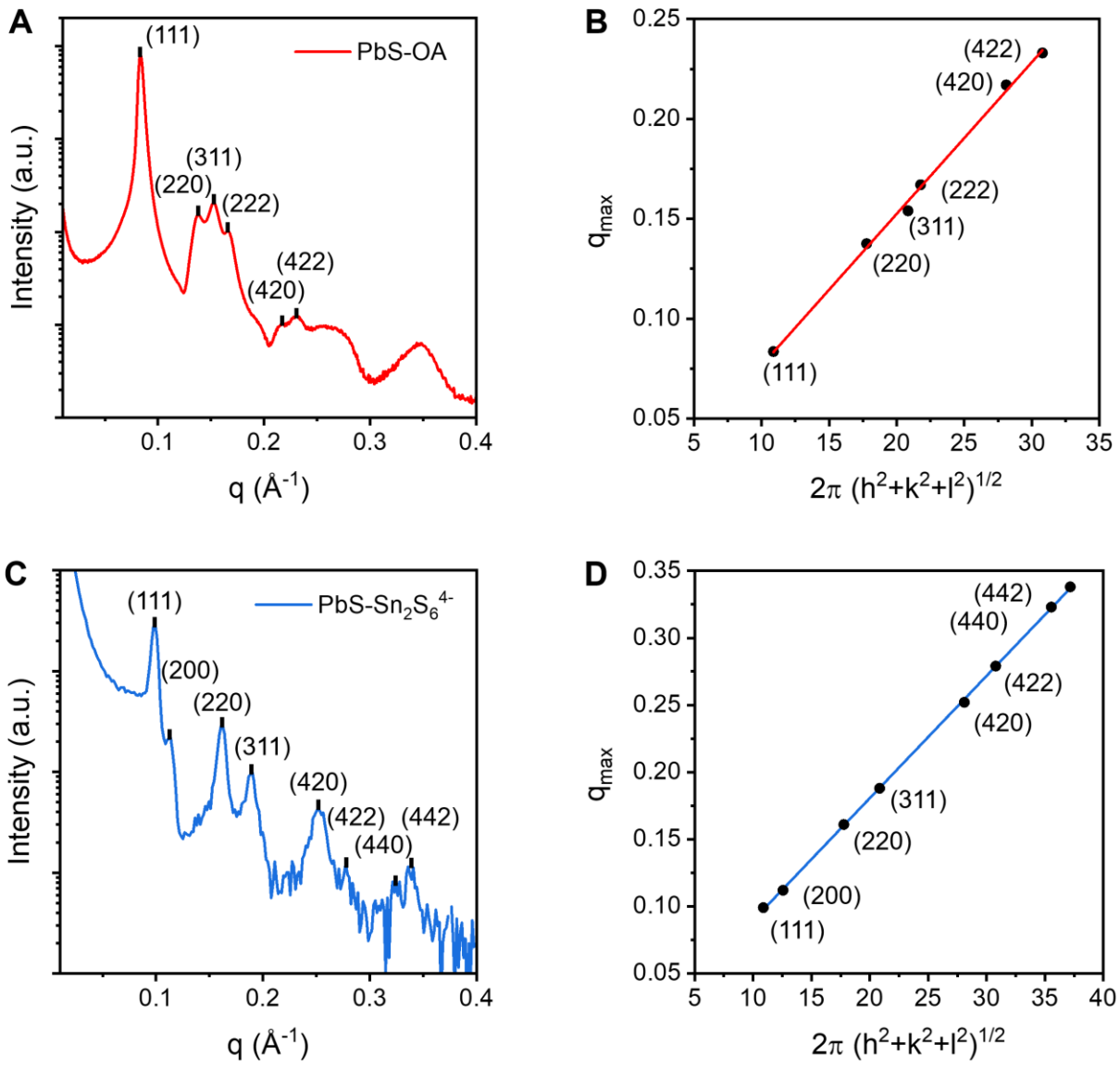

Figure 2.4.3: Structural analysis of superlattices using SAXS.

(A, C) The log-linear plots of SAXS patterns and **(B, D)** the plots of $q_{\max}$ against $2\pi(h^2 + k^2 + l^2)^{1/2}$ of the superlattices of 7.2 nm PbS-OA (red) and 7.2 nm PbS-$Sn_2S_6^{4-}$ (blue) NCs.

2.5. Instrumentation and standard characterization techniques

SAXS: For rapid screening measurements, small-angle X-ray scattering (SAXS) collected using a SAXSLAB Ganesha Instrument with a Cu K-alpha source. Small-angle X-ray (SAXS) data for quantitative analysis are collected at beamline 12-ID-B, Advanced Photon Source (APS) in Argonne National Laboratory. The beam energy was 12.7 keV and the beam size was ~0.5 mm.

UV-Vis-NIR Absorption: UV-Vis-NIR absorption spectra were collected on a Shimadzu UV3600 Plus spectrophotometer.

TEM: Transmission electron microscopy (TEM) images were collected using FEI Tecnai G2 F30 X-TWIN at an accelerating voltage of 300 kV. Samples were prepared by drop-casting a dilute solution of nanocrystals (NCs) onto 400 mesh copper grids with amorphous carbon support (Ted Pella).

TEM-SAED: Transmission electron microscopy selected area electron diffraction (TEM-SAED) images were collected using FEI Tecnai G2 F30 X-TWIN at an accelerating voltage of 300 kV. The method for sample preparation was identical to TEM.

HAADF-STEM: High-angle annular dark field scanning transmission electron microscopy (HAADF-STEM) images were acquired in an aberration-corrected Thermo Fisher Scientific (TFS) Titan Themis operated at an accelerating voltage of 300 kV. The imaging was performed with the convergence semi-angle of 25 mrad, a HAADF detector collection angle range of 52-200 mrad, a beam current of 41 pA, and a dwell time of 2 μsec per pixel. Samples were prepared

by depositing dry powder on TEM grids (Ted Pella, Prod#01824; ultrathin carbon film on lacey carbon support film, 400 mesh, Cu). A TFS low background double-tilt TEM holder was used to tilt superlattices along the desired zone-axis.

SEM: Scanning electron microscopy (SEM) images were collected using a Zeiss Merlin scanning electron microscope with 10 kV accelerating voltage.

STEM-EDS: STEM-EDS mapping were conducted under 300 kV using the Analytical PicoProbe Electron Optical Beam Line, a prototype of the ThermoFisher Spectra UltraX Illiad located at Argonne National Laboratory. Microanalysis measurements of the elemental distribution were obtained using the X-ray Perimeter Array Detector (XPAD) with a capability over 4.5 sR was equipped, guaranteeing the ultrahigh sensitivity for elemental analysis.[11] For elemental mapping, Pb-L lines and Sn-L lines were used to map Pb and Sn, respectively.

DLS-PALS: The zeta potentials of NCs were determined by dynamic light scattering (DLS) and phase analysis light scattering (PALS) technique, using Mobius (Wyatt Technology, WMOB-07) coupled with Atlas Size and Zeta Potential Analyzer (Wyatt Technology). The laser operated at a wavelength of 532 nm, and the detector angle was set at 163.5º. The PALS measurement was operated at an oscillating electric field with 10 V potential and 20 Hz frequency.

ICP-OES: The concentration of NCs were obtained from inductively coupled plasma optical emission spectroscopy (ICP-OES) measurements, which were collected using an Agilent 700

Series instrument or Agilent 5110 Synchronous Vertical Dual View (SVDV). The NCs and ligand solutions were digested according to a previously established protocol.

FTIR absorption: Fourier Transform Infrared (FTIR) absorption spectroscopy data were collected on a Nicolet iS50 FT-IR spectrometer (Thermo Scientific), using ATR (attenuated total reflectance) mode on diamond substrate.

2.6. Chapter 2 bibliography

(1) Hendricks, M. P.; Campos, M. P.; Cleveland, G. T.; Jen-La Plante, I.; Owen, J. S. A Tunable Library of Substituted Thiourea Precursors to Metal Sulfide Nanocrystals. *Science* **2015**, *348* (6240), 1226–1230. https://doi.org/10.1126/science.aaa2951.

(2) Zhang, J.; Crisp, R. W.; Gao, J.; Kroupa, D. M.; Beard, M. C.; Luther, J. M. Synthetic Conditions for High-Accuracy Size Control of PbS Quantum Dots. *J. Phys. Chem. Lett.* **2015**, *6* (10), 1830–1833. https://doi.org/10.1021/acs.jpclett.5b00689.

(3) Chen, O.; Chen, X.; Yang, Y.; Lynch, J.; Wu, H.; Zhuang, J.; Cao, Y. C. Synthesis of Metal–Selenide Nanocrystals Using Selenium Dioxide as the Selenium Precursor. *Angew. Chem.* **2008**, *120* (45), 8766–8769. https://doi.org/10.1002/ange.200804266.

(4) Peng, S.; Lee, Y.; Wang, C.; Yin, H.; Dai, S.; Sun, S. A Facile Synthesis of Monodisperse Au Nanoparticles and Their Catalysis of CO Oxidation. *Nano Res.* **2008**, *1* (3), 229–234. https://doi.org/10.1007/s12274-008-8026-3.

(5) Zheng, N.; Fan, J.; Stucky, G. D. One-Step One-Phase Synthesis of Monodisperse Noble-Metallic Nanoparticles and Their Colloidal Crystals. *J. Am. Chem. Soc.* **2006**, *128* (20), 6550–6551. https://doi.org/10.1021/ja0604717.

(6) Kovalenko, M. V.; Scheele, M.; Talapin, D. V. Colloidal Nanocrystals with Molecular Metal Chalcogenide Surface Ligands. *Science* **2009**, *324* (5933), 1417–1420. https://doi.org/10.1126/science.1170524.

(7) Kovalenko, M. V.; Bodnarchuk, M. I.; Zaumseil, J.; Lee, J.-S.; Talapin, D. V. Expanding the Chemical Versatility of Colloidal Nanocrystals Capped with Molecular Metal Chalcogenide Ligands. *J. Am. Chem. Soc.* **2010**, *132* (29), 10085–10092. https://doi.org/10.1021/ja1024832.

(8) Coropceanu, I.; Janke, E. M.; Portner, J.; Haubold, D.; Nguyen, T. D.; Das, A.; Tanner, C. P. N.; Utterback, J. K.; Teitelbaum, S. W.; Hudson, ¸ Margaret H.; Sarma, N. A.; Hinkle, A. M.; Tassone, C. J.; Eychmüller, A.; Limmer, D. T.; Olvera De La Cruz, M.; Ginsberg, N. S.; Talapin, D. V. Self-Assembly of Nanocrystals into Strongly Electronically Coupled All-Inorganic Supercrystals. *Science* **2022**, *375* (6587), 1422–1426. https://doi.org/10.1126/science.abm6753.

(9) Li, T.; Senesi, A. J.; Lee, B. Small Angle X-Ray Scattering for Nanoparticle Research. *Chem. Rev.* **2016**, *116* (18), 11128–11180. https://doi.org/10.1021/acs.chemrev.5b00690.

(10) Ye, X.; Zhu, C.; Ercius, P.; Raja, S. N.; He, B.; Jones, M. R.; Hauwiller, M. R.; Liu, Y.; Xu, T.; Alivisatos, A. P. Structural Diversity in Binary Superlattices Self-Assembled from Polymer-Grafted Nanocrystals. *Nat. Commun.* **2015**, *6* (1), 10052. https://doi.org/10.1038/ncomms10052.

(11) Zaluzec, N. First Light on the Argonne PicoProbe and the X-Ray Perimeter Array Detector (XPAD). *Microscopy and Microanalysis* **2021**, *27* (S1), 2070–2074.

3. Chapter 3: Surface-mediated interactions of electrostatically stabilized nanocrystals

Reprinted with permission from *ACS Nano* 2024, 18, 50, 33864–33874. Copyright © 2024 American Chemical Society.

3.1. Introduction

Colloidal nanocrystals (NCs) stabilized with long-chain organic ligands have been extensively studied as model systems for self-assembly, giving rise to a rich library of ordered superlattices with diverse symmetries.[1–4] In contrast, nanocrystals capped with compact, charged inorganic ligands have historically resisted long-range ordering.[5] Instead of forming superlattices, these electrostatically stabilized NCs typically precipitate as amorphous aggregates or form disordered films upon deposition.[5] Only recently have systematic efforts begun to uncover conditions under which inorganic-ligand-capped NCs can be coaxed into forming ordered assemblies.[6]

This clear difference in assembly behavior originates from the fundamentally different stabilization mechanisms at play. Organic ligands maintain colloidal stability through steric hindrance: their extended hydrocarbon chains physically prevent NCs from approaching closely enough to aggregate. Inorganic ligands, by contrast, stabilize NCs through electrostatic repulsion arising from their high surface charge.[5,7] These two mechanisms generate qualitatively different interparticle potentials and therefore distinct self-assembly pathways. Understanding these differences is essential, because the NC superlattices with high packing density and strong electronic coupling are best achieved using short, compact inorganic ligands rather than bulky organic ones.[8,9] To design such materials rationally, we must first understand how steric and

electrostatic stabilization influence interparticle forces and how these forces dictate the structural organization of NCs in solution.

Small-angle X-ray scattering (SAXS) provides a powerful means to probe these interactions directly. By measuring the structure factor of NC dispersions, SAXS reveals how particles are spatially correlated in solution.[10] Because the structure factor is related to the radial distribution function through a Fourier transform, it encodes information about interparticle distances, the range of repulsive forces, and the presence or absence of ordering. In this way, SAXS allows us to compare the effective interactions of sterically and electrostatically stabilized NCs under identical solvent conditions, offering insight into how their surface chemistry shapes their collective behavior.

In this chapter, we use SAXS to investigate the colloidal interactions of sub-10 nm PbS NCs stabilized either by oleate ligands (PbS-OA NCs) or by highly charged $Sn_2S_6^{4-}$ ligands (PbS-$Sn_2S_6^{4-}$ NCs). We show that PbS-$Sn_2S_6^{4-}$ NCs exhibit long-range electrostatic repulsions that extend far beyond the ligand shell, leading to complex spatial correlations in solution. In contrast, PbS-OA NCs display only short-range steric repulsion limited to the full ligand length. We further demonstrate that adding a multivalent electrolyte effectively screens the electrostatic repulsion between PbS-$Sn_2S_6^{4-}$ NCs, collapsing their long-range interactions into short-range repulsions similar to those of sterically stabilized NCs. These insights reveal how electrostatic and steric forces govern the structure of NC dispersions and, importantly, identify a strategy for enabling the self-assembly of inorganic-ligand-capped PbS NCs into densely packed, strongly coupled superlattices.

3.2. Interactions of sterically vs. electrostatically stabilized nanocrystals in solution

SAXS patterns of sterically and electrostatically stabilized NCs

Figure 3.2.1 presents representative SAXS patterns of sterically and electrostatically stabilized PbS, CdSe, and Au nanocrystals (NCs). Sterically stabilized NCs refer to particles capped with long-chain organic ligands, such as oleic acid (OA), oleylamine (OAm), or dodecylthiol (DDT), dispersed in nonpolar solvents. In contrast, electrostatically stabilized NCs are capped with multivalent metal chalcogenide complex (MCC) ligands, including $Sn_2S_6^{4-}$, AsS_4^{3-}, GeS_4^{4-}, and are dispersed in polar solvents such as *N*-methylformamide (NMF).

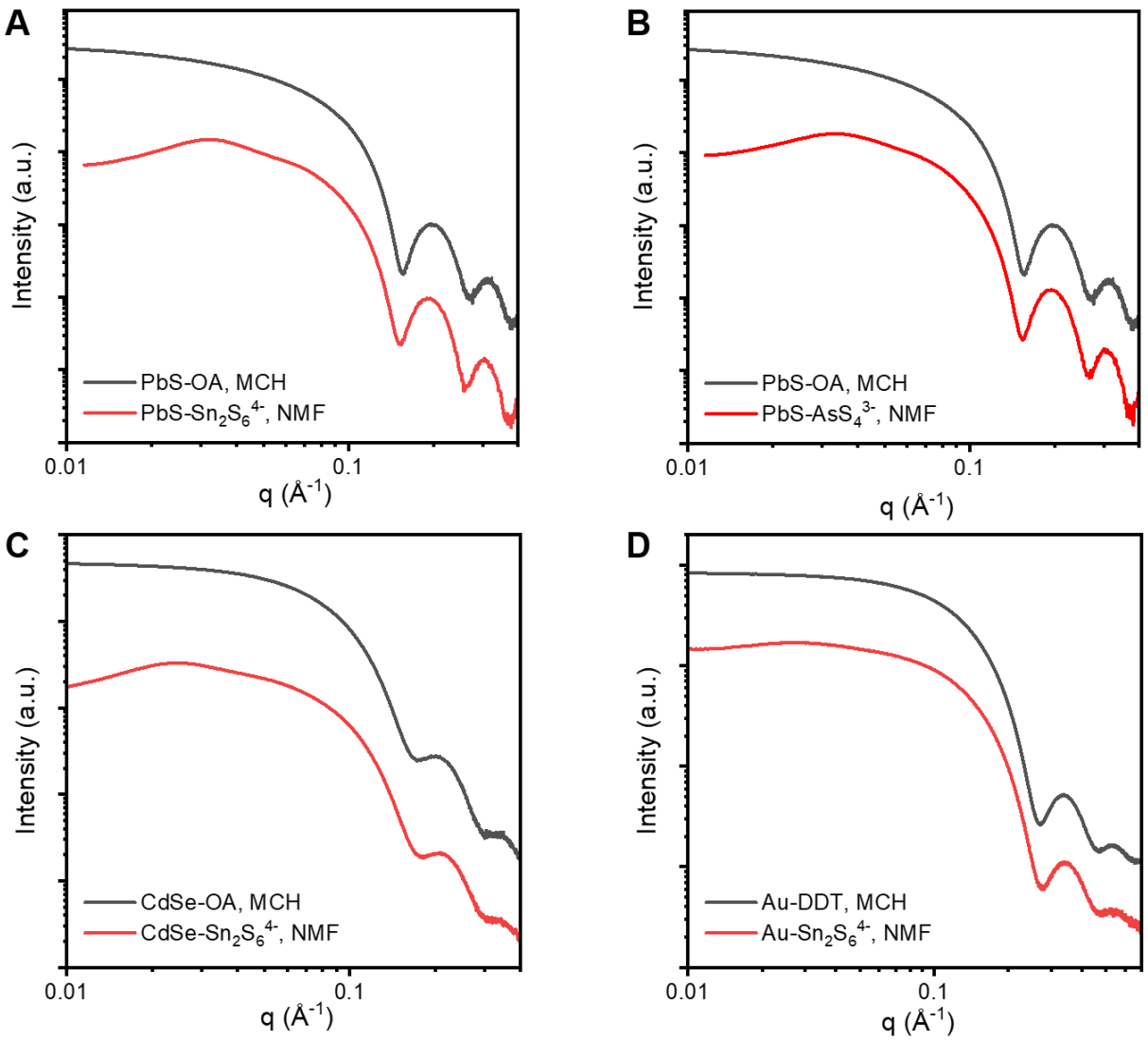

Figure 3.2.1: SAXS patterns of sterically and electrostatically stabilized nanocrystals. SAXS patterns of 10 mg/ml solutions of 5.8 nm PbS NCs with **(A)** OA and $Sn_2S_6^{4-}$ ligands, **(A)** PbS NCs with OA and AsS_4^{3-} ligands, **(C)** 5.2 nm CdSe NCs with OA and $Sn_2S_6^{4-}$ ligands, **(D)** 3.3 nm Su NCs with OA and $Sn_2S_6^{4-}$ ligands.

Across all materials examined, sterically stabilized NCs exhibit well-defined Bessel-type oscillations in the high-q region ($q > 0.1$ Å^{-1}). These oscillations arise from the form factor of monodisperse spherical particles and indicate narrow size and shape distributions.[11] Importantly, these oscillations remain preserved after ligand exchange to MCC ligands, demonstrating that the

inorganic ligand exchange process does not significantly alter the NC core size or morphology. At low q ($q < 0.1$ Å^{-1}), both sterically and electrostatically stabilized NCs display intensities that approach a constant value, consistent with well-dispersed, colloidally stable NCs in solution.

Despite these similarities, the low-q regions of the SAXS patterns reveal clear differences between the two stabilization mechanisms. In sterically stabilized NCs, the scattering intensity in the Guinier regime approaches a horizontal line on a log–log plot, consistent with ideal gas-like behavior and minimal interparticle correlations. In contrast, electrostatically stabilized NCs show pronounced deviations from this behavior, indicating the presence of significant interparticle interactions. Similar trends are observed for CdSe and Au NCs, confirming that this distinction is general across different material systems.

Extraction of structure factors

To investigate the origin of the unusual low-q features in electrostatically stabilized NCs, we extracted the structure factor S(q) from the measured SAXS intensity.[11] The total scattering intensity can be expressed as:

$$I(q) = A\,P(q)\,S(q)$$

Where A is a scaling factor determined by experimental conditions (X-ray flux, concentration, and NC composition), $P(q)$ is the form factor describing size, shape and polydispersity of the NCs, and $S(q)$ is the structure factor describing interparticle correlations.

The form factor $P(q)$ was obtained by fitting the high-q Porod region ($qR \gg 1$, where R is the NC radius) to the spherical form factor model using the Irena package in Igor Pro 9. The scaling factor A was determined by least-squares fitting of the form factor to the measured SAXS intensity in the region $2.0 < qR < 4.5$. Representative fits of the form factor and SAXS intensity

are shown in Figure 3.2.2. The structure factor was then calculated by dividing the measured intensity ($I(q)$) by the product $A\,P(q)$.

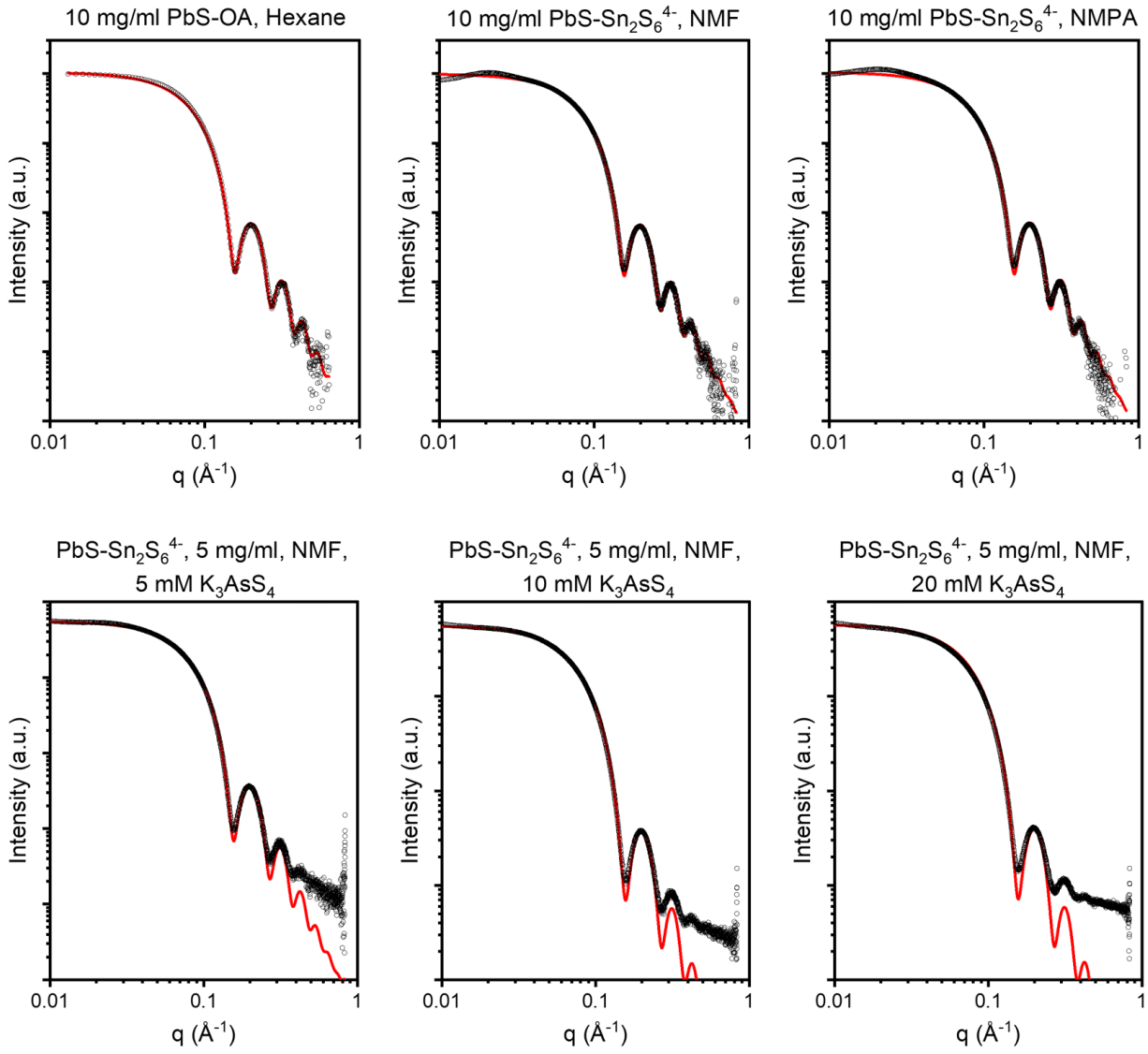

Figure 3.2.2: Fitting form factor of the SAXS patterns of colloidal nanocrystals.
Background subtracted SAXS patterns (black circles) and fitted form factors (red lines) of 5.7 nm PbS NCs.

Comparison of structure factors

Figure 3.2.3A compares the structure factors of 50 mg/mL PbS-OA NCs in hexane and PbS-$Sn_2S_6^{4-}$ NCs in NMF. For PbS-OA, S(q) exhibits only weak oscillations, consistent with a nearly random distribution of particles in solution, as illustrated in Figure 3.2.3B. This behavior reflects the short-range nature of steric stabilization, where interparticle interactions are limited to van der Waals attraction and steric repulsion.[12–14] Such behavior is characteristic of many sterically stabilized colloidal systems.

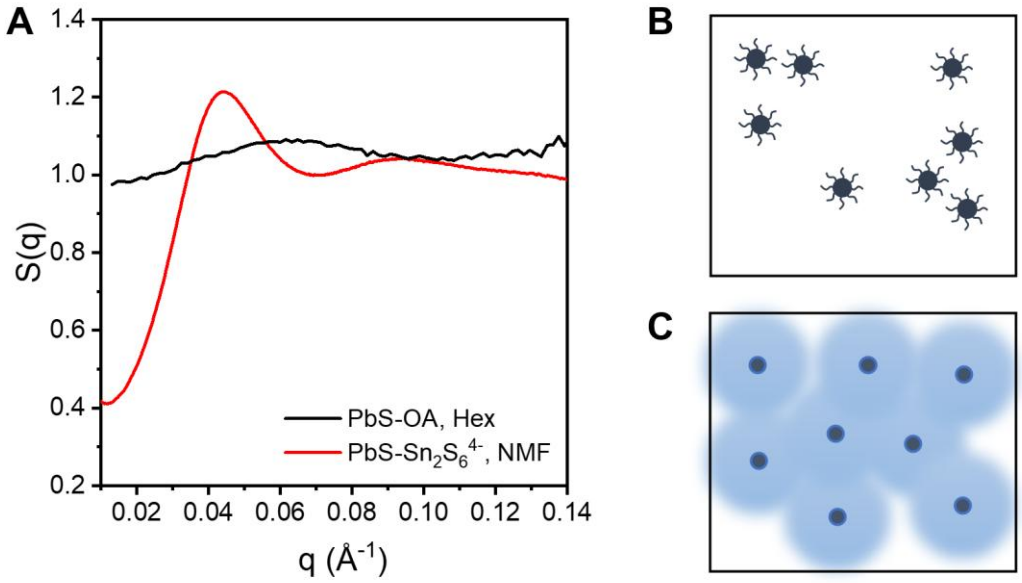

Figure 3.2.3: Spatial arrangements of sterically and electrostatically stabilized NCs in solution.

(A) The structure factors of colloidal dispersions of 50 mg/ml of 5.7 nm PbS NCs with different surface ligands: PbS-$Sn_2S_6^{4-}$ NCs in NMF (red) and PbS-OA in hexane (black). **(B)** Illustration of random arrangements of PbS-OA NCs in hexane, and the **(B)** illustration of a uniform arrangement of PbS-$Sn_2S_6^{4-}$ NCs in NMF.

In contrast, the structure factor of PbS-$Sn_2S_6^{4-}$ NCs displays pronounced oscillatory features, indicating strong deviations from ideal gas-like behavior. Two key features are observed:

1. S(q) < 1 at low q, indicating suppressed long-wavelength density fluctuations. This behavior is characteristic of systems with long-range repulsive interactions.
2. A pronounced peak at q ≈ 0.045 $Å^{-1}$, corresponding to a characteristic interparticle spacing of:

$$d \approx \frac{2\pi}{q_{\max}} \approx 14 \text{ nm}.$$

These features resemble the Percus–Yevick structure factor commonly used to describe liquids or amorphous aggregates.[15] In this analogy, electrostatically stabilized NCs behave like atoms in a dense liquid: each particle is "caged" by its neighbors, maintaining a well-defined separation distance but lacking long-range crystalline order. This behavior reflects the presence of long-range electrostatic repulsion between MCC-capped NCs, which enforces uniform spacing and produces the spatial arrangement illustrated in Figure 3.2.3C.

3.3. Concentration-dependent interactions of nanocrystals in solution

The structure factor of electrostatically stabilized nanocrystals (NCs) is highly sensitive to particle concentration, reflecting changes in interparticle correlations as the dispersion becomes more crowded. Figure 3.3.1A shows the structure factors of 5.7 nm PbS-$Sn_2S_6^{4-}$ NCs measured at concentrations ranging from 1 mg/mL to 300 mg/mL. As the concentration increases, the oscillatory features in *S(q)* become increasingly pronounced, indicating a transition toward more uniform spatial arrangements. This behavior is consistent with the concept of "caging", in which

each NC becomes confined by its neighbors at high volume fractions, leading to more well-defined interparticle separations (Figure 3.3.1B and C).

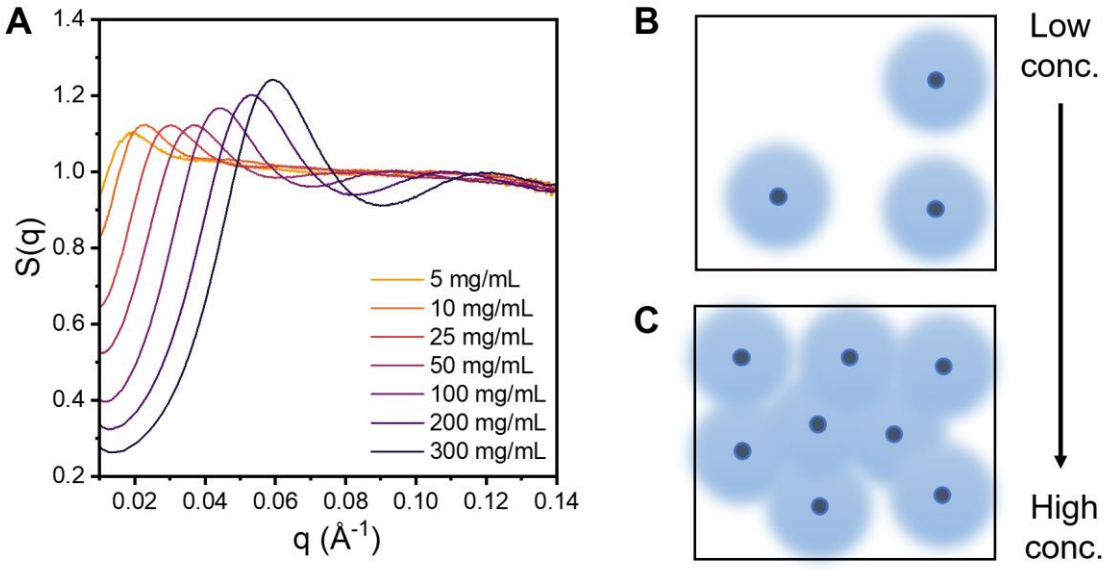

Figure 3.3.1: Concentration-dependent spatial arrangements of NCs in solution.
(A) The structure factor of 5.7 nm PbS-$Sn_2S_6^{4-}$ NCs in NMF at different concentrations. Illustration of transition from **(B)** random arrangement PbS-$Sn_2S_6^{4-}$ NCs to **(C)** uniform arrangement as the concentration of NCs increase.

Concentration-dependent characteristic distance between the NCs

A key signature of increasing interparticle correlations is the shift of the first maximum in *S(q)*. As the NC concentration increases from 1 mg/mL to 300 mg/mL, the first peak position ($q_{\max}$) shifts from $q = 0.012$ Å^{-1} to $q = 0.060$ Å^{-1}. The corresponding center-to-center distance (D_{NC-NC}) between neighboring NCs is given by:[16]

$$D_{NC-NC} = \frac{2\pi}{q_{\max}}$$

A log–log plot of $D_{\mathrm{NC-NC}}$ versus concentration (Figure 3.3.2) reveals a systematic decrease in interparticle spacing from ~52 nm at 1 mg/mL to ~10 nm at 300 mg/mL in a solution

of 5.7 nm PbS-$Sn_2S_6^{4-}$ NCs in NMF (Figure 3.3.1). A linear fit yields the empirical scaling relationship:

$$D_{NC-NC} = 448\, n^{-0.267}$$

$$q_{\max} = 0.0140\, n^{0.267}$$

where c is the NC concentration in mg mL^{-1}. This power-law dependence reflects the progressive compression of the electrostatic repulsion shell surrounding each NC as the dispersion becomes more concentrated.

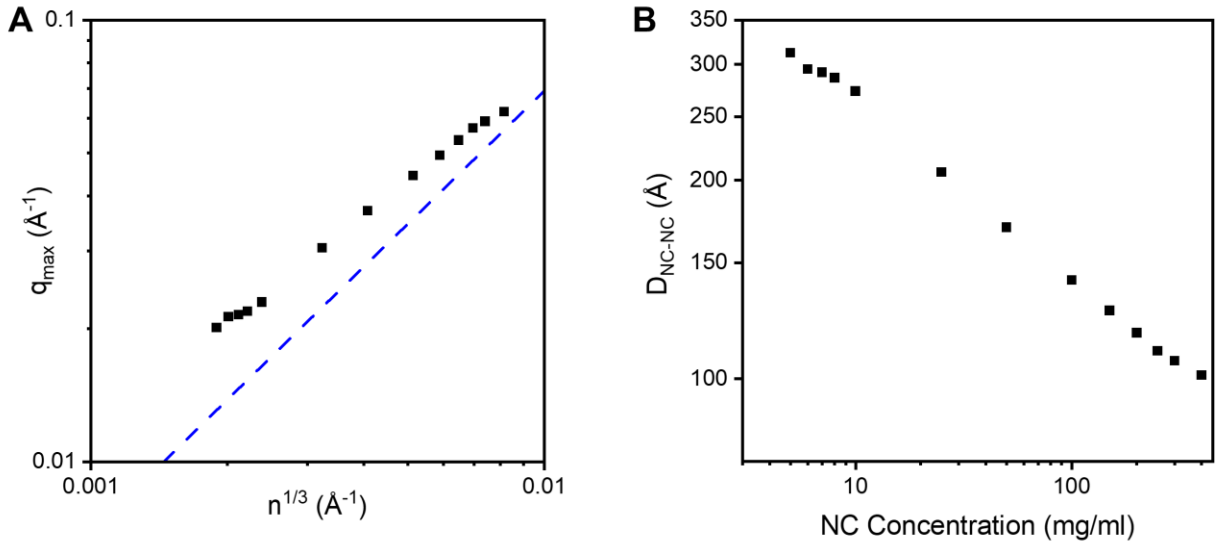

Figure 3.3.2: Concentration-dependent characteristic distance of NCs in solution.
Log-log plot of **(A)** q_{max} against NC concentration and **(B)** D_{NC-NC} against NC concentration (right). The NCs are 5.7 nm PbS-$Sn_2S_6^{4-}$ NCs. The black squares are experimental values, and blue dashed line is $q_{\max} \approx 2.2\pi n^{1/3}$, which represents strongly repulsive system.

These results deviate significantly from the well-known scaling for strongly repulsive systems with infinitely long-range interactions:

$$q_{\max} \approx 2.2\pi n^{1/3}$$

where *n* is the particle number density. The deviation (Figure 3.3.2A) indicates that the interparticle potential between PbS-$Sn_2S_6^{4-}$ NCs cannot be described by an infinitely long-range, strongly repulsive interaction.

Comparison to hard-sphere interactions using Percus-Yevick model

To further probe the nature of interparticle interactions, we compared the experimental structure factors to those predicted by the Percus–Yevick (PY) model for hard spheres.[15] The analytical PY structure factor is:

$$S_{PY}(q) = \frac{(1+2\eta)^2}{A^2(1-\eta)^4}(\sin A - A\cos A) - \frac{6\eta\left(1+\frac{\eta}{2}\right)}{A^3(1-\eta)^4}(2A\sin A + (2-A^2)\cos A - 2)$$

$$+ \frac{\eta(1+2\eta)^2}{2A^5(1-\eta)^4}\left((-A^4+12A^2-24)\cos A + 4A(A^2-6)\sin A + 24\right)$$

Where:

$$A = 2qR$$

$$q = \frac{4\pi}{\lambda}\sin\theta$$

And: η = volume fraction, R = radius of the hard sphere, λ = incident wavelength, θ = scattered angle. For comparison with the previous method, D_{NC-NC} is equivalent to $2R$.

Figure 3.3.3 shows the experimental structure factors alongside PY fits, and Table 3.1 presents the fitted parameters obtained from PY model. The extracted parameters (Table 3.1) reveal two trends : (i) effective volume fraction increases with concentration, as expected, and (ii) characteristic interparticle distance decreases with concentration, also expected as NCs are more crowded.

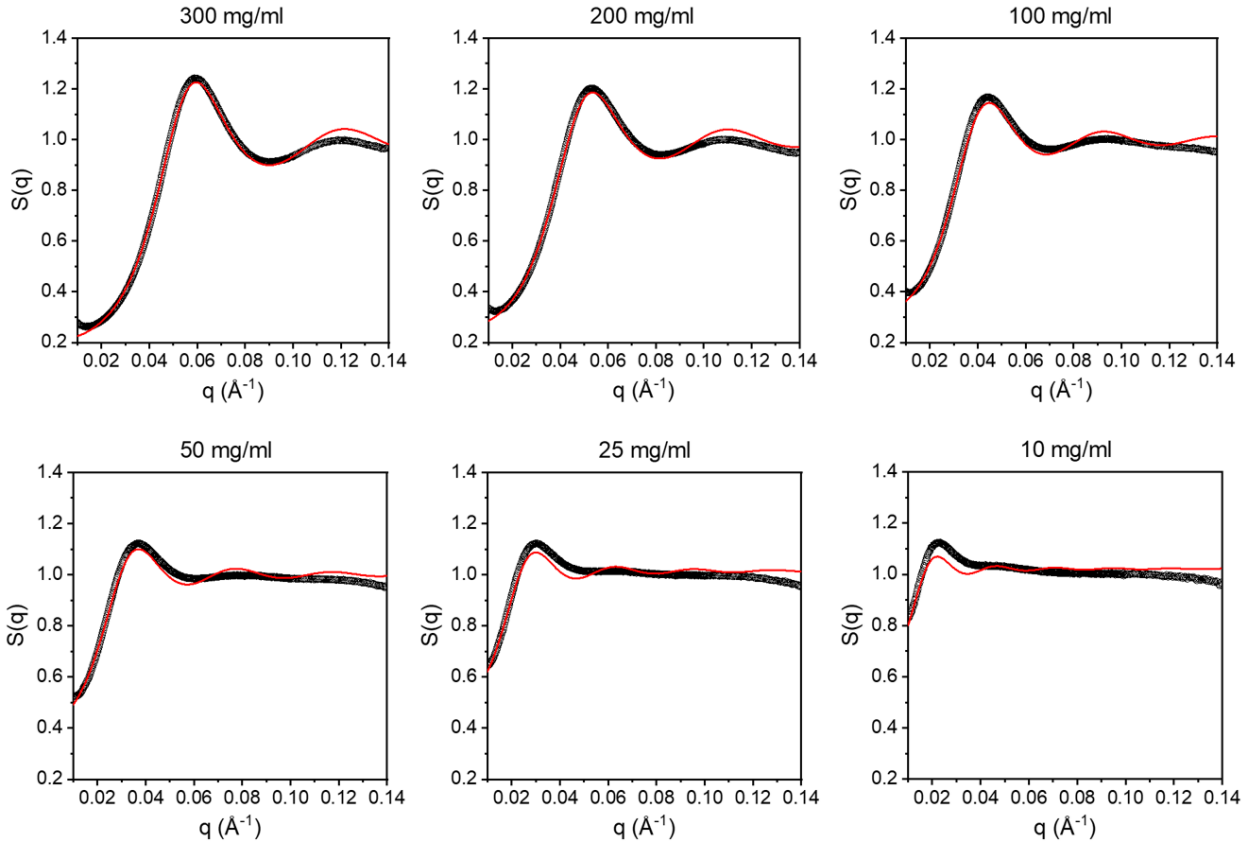

Figure 3.3.3: Fitting structure factor with Percus-Yevick model.

Experimentally obtained structure factors of 5.7 nm PbS-$Sn_2S_6^{4-}$ NCs (black circles) and fits from Percus-Yevick model, which assumes that NCs are hard spheres (red lines).

Table 3.1: List of characteristic distance and volume fraction of 5.7 nm PbS-$Sn_2S_6^{4-}$ NCs, determined by fitting the structure factor with Percus-Yevick model.

Concentration	Characteristic distance (D_{NC-NC})	Volume fraction (η)
300 mg/ml	10.2 nm	19.9%
200 mg/ml	11.3 nm	17.1%
100 mg/ml	13.4 nm	14.4%
50 mg/ml	16.0 nm	10.8%
25 mg/ml	19.6 nm	8.4%
10 mg/ml	26.4 nm	5.8%

However, the PY model fits well only at high concentrations. At lower concentrations (1–5 mg mL^{-1}), the fits become unphysical (e.g., negative η), indicating that the hard-sphere model fails to capture the long-range, soft repulsive interactions present in dilute dispersions. This is expected: at high concentration, NCs behave more like hard spheres due to strong short-range repulsion, whereas at low concentration, the interactions are dominated by soft, long-range electrostatic forces.

Comparison of structure factor to structure factor from Yukawa-type interactions

To take the long-range soft repulsive forces into account, we attempt to interpret the concentration-dependent structure factor with Yukawa (screened Coulomb) potential, where k_B is the Boltzmann constant, T is the temperature, k is $\kappa\sigma$ and x is r/σ. κ^{-1} the Debye screening length, σ is the diameter of the particle and r is the center-to-center distance.[17]

$$\frac{U(x)}{k_B T} = \begin{cases} \frac{\gamma \exp(-kx)}{x}, & x > 1 \\ \infty, & x < 1 \end{cases}$$

The value of γ is the contact potential, defined as:

$$\gamma = \frac{Z^*}{\pi \varepsilon \varepsilon_0 R(2 + \kappa R)}$$

where Z^* is the effective surface charge, ε is the relative dielectric constant, ε_0 is the vacuum permittivity and R is the radius of the particle.

Analytical structure factors for Yukawa-interacting particles were computed using an open-source code. Figure 3.3.4 compares the experimental structure factors with Yukawa-based fits.

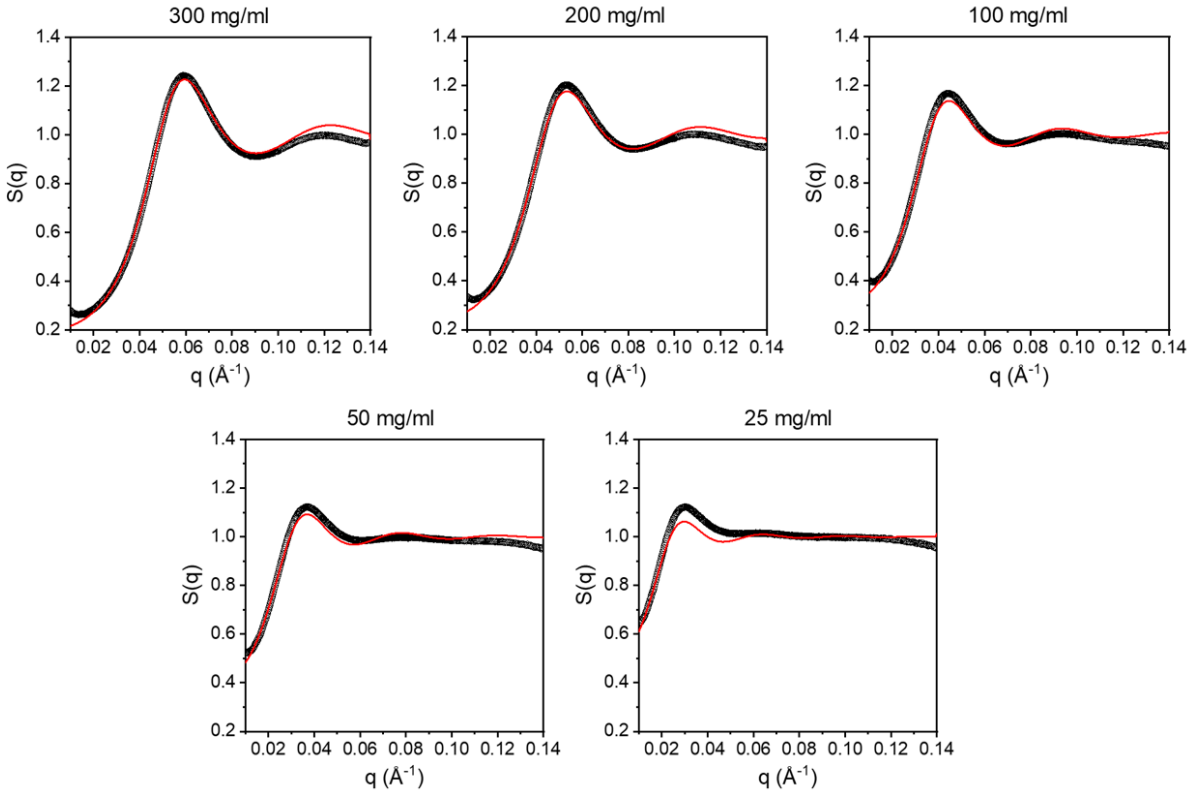

Figure 3.3.4: Fitting structure factor with Yukawa model.
Experimentally obtained structure factors of 5.7 nm PbS-$Sn_2S_6^{4-}$ NCs (black circles) and fits from Yukawa model (red lines).

The extracted Debye lengths and contact potentials (Figure 3.3.5) show intuitive qualitative trends: (i) Debye length decreases with increasing concentration, consistent with increasing counterion (K^+) concentration, and (ii) contact potential shows no systematic dependence on concentration, consistent with unchanged surface chemistry. However, the numerical values are unphysical (Debye length ~1–2 nm; γ ~10^5 k_BT), likely due to the fitting algorithm becoming trapped in local minima, which is common for complex structure-factor models.

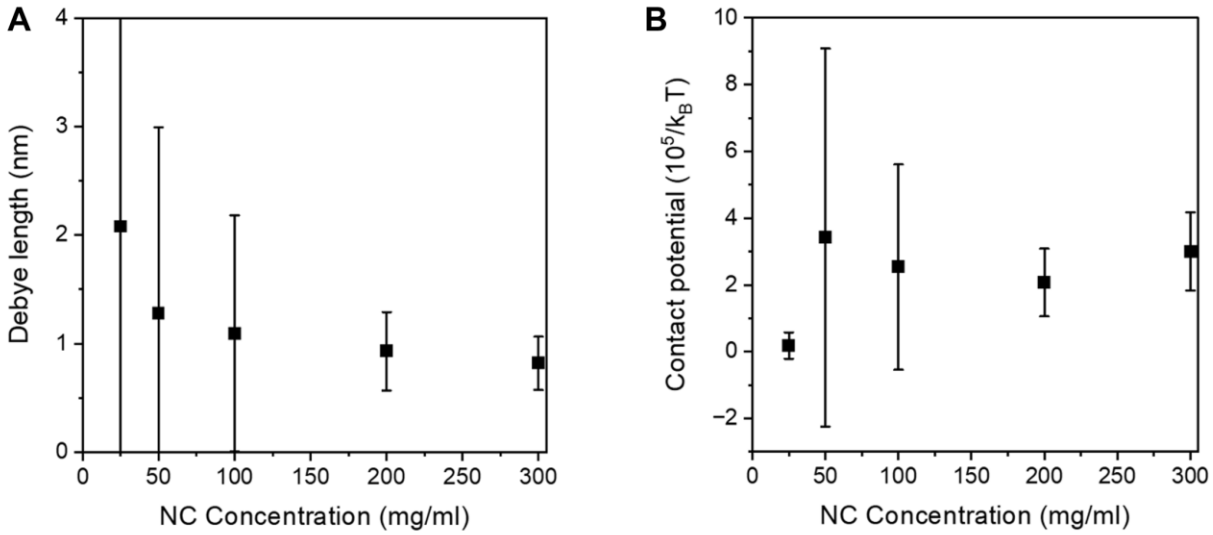

Figure 3.3.5: Parameters from fitting structure factor with Yukawa model.
Concentration-dependent **(A)** Debye lengths and **(B)** contact potentials of 5.7 nm PbS-$Sn_2S_6^{4-}$ NCs determined by fitting the structure factor with Yukawa model.

Because of this, I compared the experimental $q_{\max}$vs. $n^{1/3}$ to theoretical Yukawa predictions, instead of directly fitting the experimental structure factor to the Yukawa model. Figure 3.3.6 presents the plots of experimentally obtained overlaid with calculated trends from Yukawa model. The Yukawa model best matches the experimental results when the contact potential is 10 – 20 k_BT.

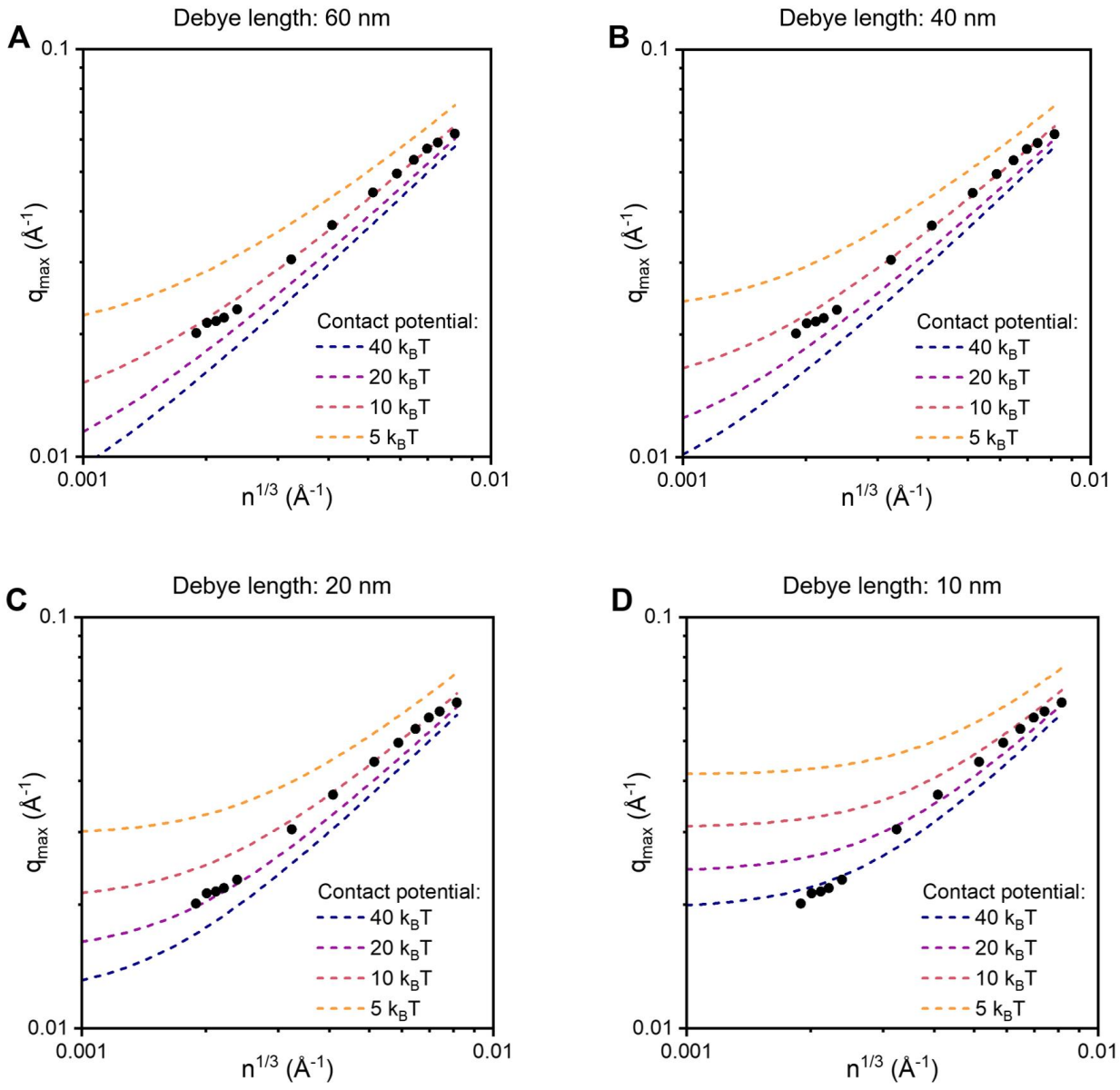

Figure 3.3.6: Characteristic distance from Yukawa model for constant Debye lengths.

Plot of $q_{\max}$ against $n^{1/3}$ of 5.7 nm PbS-$Sn_2Sn_6^{4-}$ NCs in NMF (black circles). The dashed lines indicate the simulated correlation between q_{max} and $n^{1/3}$ of 5.7 nm particles interacting via a Yukawa potential with the Debye length of **(A)** 60 nm, **(B)** 40 nm, **(C)** 20 nm, and **(D)** 10 nm and varying contact potential.

Figure 3.3.7 presents a similar plot, except that I present calculated trends with fixed contact potentials and varying Debye length.

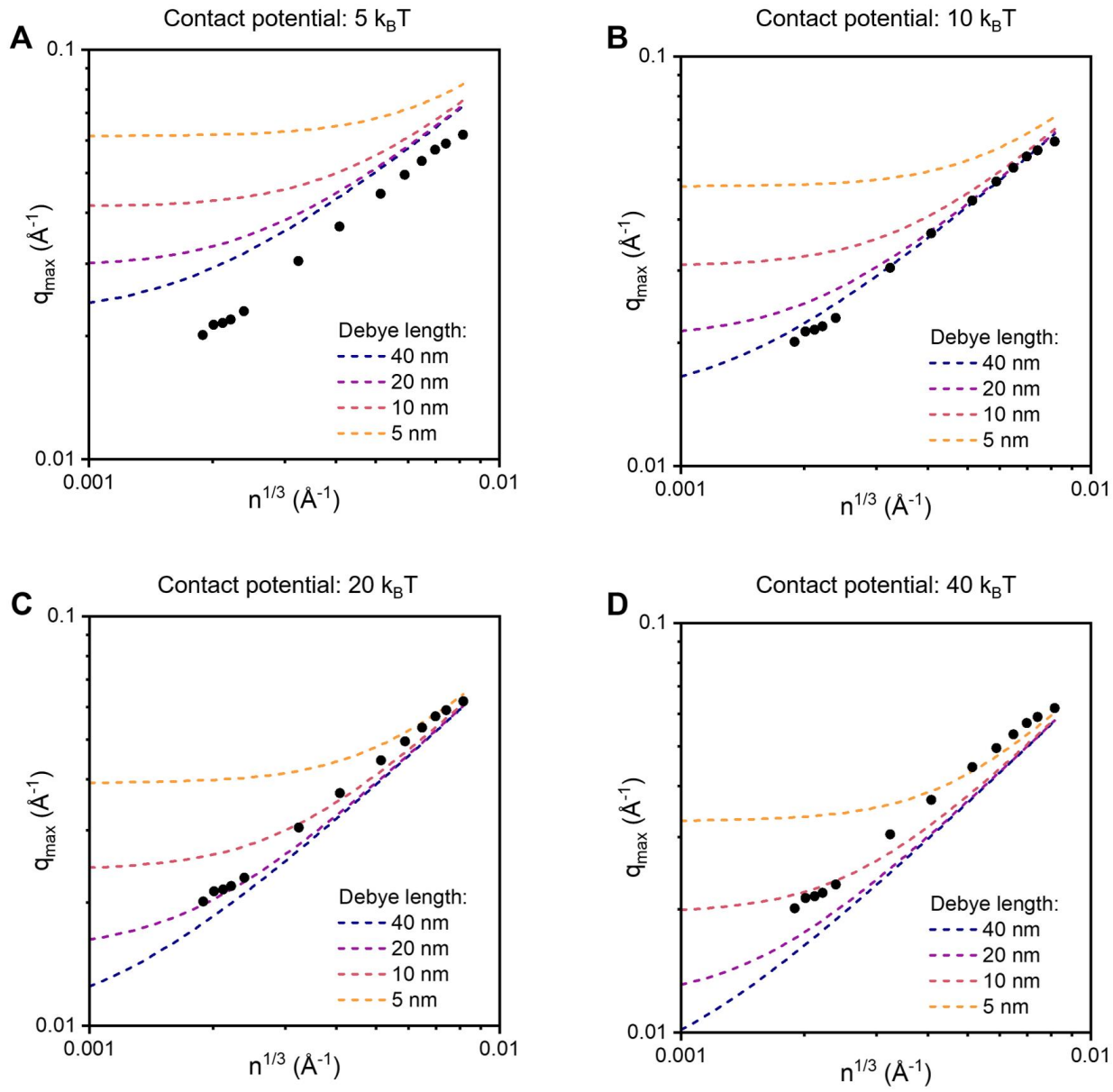

Figure 3.3.7: Characteristic distance from Yukawa model for constant contact potentials. Plot of $q_{\max}$ against $n^{1/3}$ of 5.7 nm PbS-$Sn_2Sn_6^{4-}$ NCs in NMF (black circles). The dashed lines indicate the simulated correlation between q_{max} and $n^{1/3}$ of 5.7 nm particles interacting via a Yukawa potential with the contact potential of **(A)** 5 k_BT, **(B)** 10 k_BT, **(C)** 20 k_BT, and **(D)** 40 k_BT and varying Debye lengths.

To qualitatively interpret the results, we assume that the contact potential remains constant across concentrations. When comparing the experimental trend to Yukawa-type predictions, contact potentials of 5 $k_{\mathrm{B}}T$ and 40 $k_{\mathrm{B}}T$ clearly fail to reproduce the observed behavior, further indicating that the contact potential falls within 10 – 20 $k_{\mathrm{B}}T$. The best agreement is obtained when the contact potential is set to approximately 10 $k_{\mathrm{B}}T$. Under this condition, the calculated q_{max} values align well with the experimental data when the Debye length is about 40 nm at low concentrations (~1 mg mL^{-1}) and about 5 nm at high concentrations (~300 mg mL^{-1}). This concentration-dependent evolution of the Debye length is qualitatively consistent with our experimental observations.

Estimating the Debye length using DLVO theory

To evaluate whether the inferred Debye lengths are physically reasonable, we estimated the concentration-dependent Debye length using the Derjaguin–Landau–Verwey–Overbeek (DLVO) theory.[18,19] The Debye length (κ^{-1}) is given by:

$$\kappa^{-1} = \sqrt{\frac{\varepsilon_0 \varepsilon_{\mathrm{sol}} k_B T}{2e^2 I_{\mathrm{sol}}}}$$

where ε_0 is the vacuum permittivity, $\varepsilon_{\mathrm{sol}}$ is the relative dielectric constant of the solvent, k_B is the Boltzmann constant, T is the temperature and I_{sol} is the ionic strength of the solvent. The ionic strength is defined as the following, where z_j is the charge of an ion in the solution, and ρ_j is the number density of the corresponding ion.

$$I_{\mathrm{sol}} = \frac{1}{2}\sum_{j=1}^{N} \rho_j z_j^2$$

Using a ligand grafting density of 0.55 nm^{-2} for 5.7 nm PbS-$Sn_2S_6^{4-}$ NCs, we estimate that a 1 mg mL^{-1} dispersion contains ~0.13 mM $Sn_2S_6^{4-}$ ligands. Density functional theory studies indicate that two terminal sulfur atoms form X-type bonds to the NC surface, while the bridging sulfur may form an L-type bond. Thus, each ligand is expected to be counterbalanced by approximately two K^+ ions, giving ~0.26 mM K^+ at 1 mg mL^{-1}. The temperature (T) was assumed to be 300 K, and the dielectric constant of NMF was assumed to be $\varepsilon_{\mathrm{sol}} = 170$ for this calculation.

Table 3.2 summarizes the Debye lengths calculated using DLVO theory, which predict that the screening length decreases dramatically, from roughly 40 nm at 1 mg mL^{-1} to about 2 nm at 300 mg mL^{-1}, as the concentration of PbS nanocrystals increases. These calculated values agree remarkably well with the Debye lengths inferred from the Yukawa-type analysis. In particular, when the contact potential is set to 10 $k_{\mathrm{B}}T$, the experimentally observed q_{max}values are best reproduced by a Debye length of approximately 40 nm at low concentration (~1 mg mL^{-1}) and by a Debye length of about 5 nm at high concentration (~300 mg mL^{-1}). The consistency between the two approaches supports the interpretation that the range of electrostatic repulsion decreases as the dispersion becomes more concentrated.

Table 3.2: Concentration-dependent Debye lengths of 5.7 nm PbS-$Sn_2S_6^{4-}$ NCs from DLVO theory.

Concentration	Debye length
1 mg/ml	39.4 nm
10 mg/ml	12.5 nm
100 mg/ml	4.0 nm
300 mg/ml	2.3 nm

It is important to note, however, that DLVO theory relies on assumptions that break down in concentrated electrolytes. The theory does not account for strong ion–ion correlations, which are expected for multivalent species such as $Sn_2S_6^{4-}$, nor does it capture counterion condensation effects. In fact, the presence of K^+ ions Coulombically bound to multiple thiostannate ligands at the nanocrystal surface is likely to reduce the effective ionic strength, leading DLVO theory to underestimate the true Debye length. Such counterion condensation has also been observed in numerical simulations. Despite these limitations, the DLVO-derived Debye lengths align closely with the values inferred from the Yukawa analysis, reinforcing the conclusion that the electrostatic screening length decreases substantially with increasing nanocrystal concentration.

3.4. Concentration-dependent uniformity of nanocrystals in solution

The concentration-dependent structure factors shown in Figure 3.3.1A reveal that the peak-to-valley ratio of *S(q)* increases with nanocrystal concentration, indicating that the spatial arrangement of electrostatically stabilized NCs becomes more uniform as the dispersion becomes

denser. This trend can be quantified using the hyperuniformity index, h, defined as the ratio of the structure factor at $q = 0$ to the height of the primary peak:

$$h = \frac{S(0)}{S_{\max}}$$

The hyperuniformity index provides a measure of large-scale density fluctuations within a material.[20,21] A perfectly hyperuniform system has $h = 0$, whereas a completely random arrangement (i.e. ideal gas) has $h = 1$. Materials with $h < 10^{-3}$ are typically classified as "effectively hyperuniform," reflecting a strong suppression of long-wavelength density fluctuations. Examples include perfect crystals, jammed hard-sphere packings, and systems dominated by long-range soft repulsive interactions.[20,21]

Figure 3.4.1 shows the hyperuniformity index of 5.7 nm PbS-$Sn_2S_6^{4-}$ NCs in NMF across a range of concentrations. At low concentrations, the electrostatic repulsion between NCs decays rapidly with distance, allowing the particles to adopt nearly random configurations. This is reflected in hyperuniformity indices close to unity. As the concentration increases, however, the stronger and more frequent electrostatic interactions force the NCs to adopt more uniform separations, leading to a reduction in h. At 300 mg mL^{-1}, the hyperuniformity index reaches a minimum value of 0.17. Although this indicates a significant increase in uniformity relative to dilute dispersions, the system remains far from the threshold for effective hyperuniformity. The NCs are not sufficiently "jammed," and the repulsive forces are not strong enough at these volume fractions to fully suppress density fluctuations.

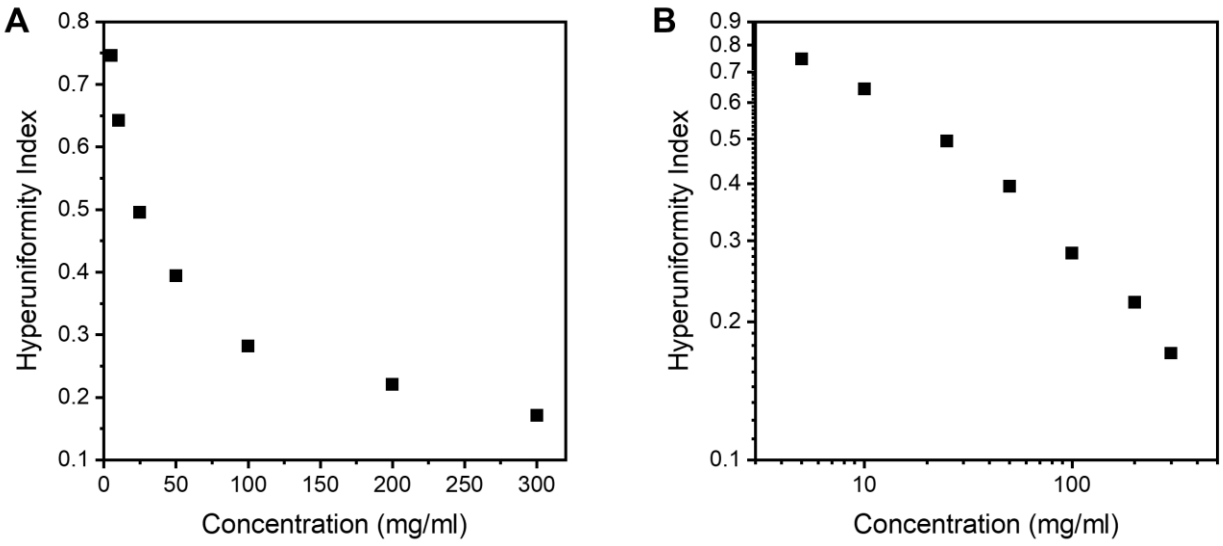

Figure 3.4.1: Concentration-dependent hyperuniformity index of NC solutions.
The **(A)** lin-lin and **(B)** log-log plot of the hyperuniformity index against concentration of 5.7 nm PbS-$Sn_2S_6^{4-}$ NCs in NMF.

Disordered hyperuniform materials have attracted considerable interest due to their defect tolerance, thermal stability, and isotropic optical properties, which make them promising for applications such as isotropic waveguides and thermal emitters.[20,21] Motivated by this, I explored whether lowering the temperature of the NC dispersion could enhance hyperuniformity, as reduced thermal motion generally promotes more uniform particle arrangements. For this experiment, approximately 30 µL of a 100 mg mL^{-1} dispersion of 7.2 nm PbS-$Sn_2S_6^{4-}$ NCs was prepared in a solvent mixture of 70% NMF and 30% DMF. This composition was chosen to lower the freezing point while maintaining colloidal stability. The sample was loaded into a capillary and cooled using a liquid-nitrogen flow system. SAXS measurements were collected as the temperature was varied from –60 °C to 30 °C in 10 °C increments. The collected structure factors and hyperuniformity index from the measurements are shown in Figure 3.4.2.

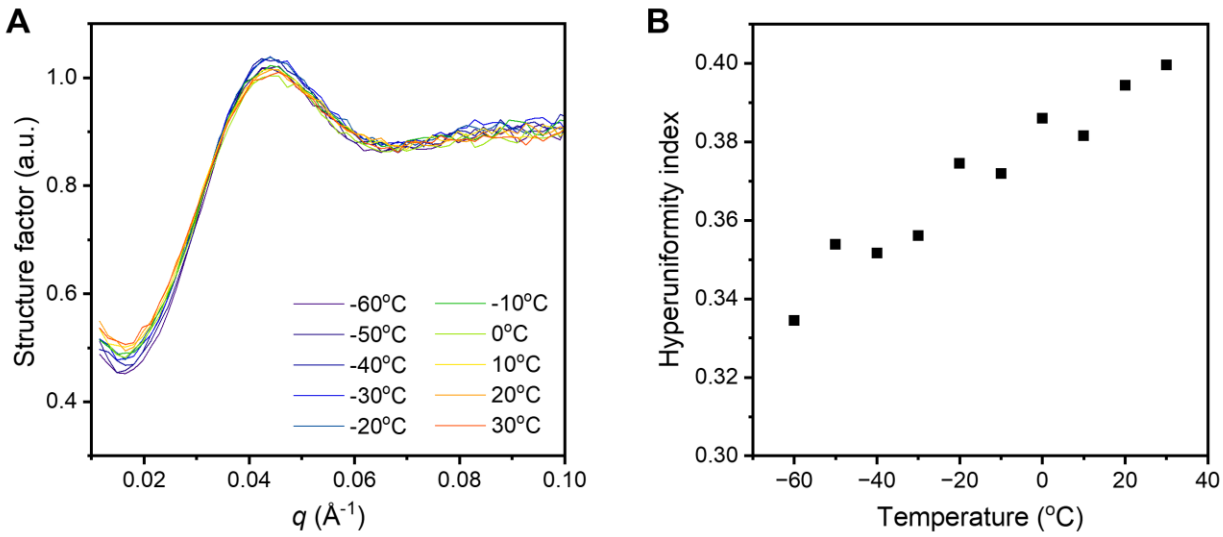

Figure 3.4.2: Temperature-dependent hyperuniformity index of NC solutions.
(A) Temperature-dependent structure factor of 7.2 nm PbS-$Sn_2S_6^{4-}$ NCs in a solvent mixture of 70% NMF and 30% DMF. **(B)** Temperature-dependent hyperuniformity index of the NC system.

The hyperuniformity index decreased modestly as the temperature was lowered, dropping from 0.40 at 30 °C to 0.34 at –60 °C. Although this trend is consistent with enhanced uniformity at lower temperatures, the magnitude of the change is small, and even at –60 °C the system remains far from the effectively hyperuniform regime ($h < 10^{-3}$). These preliminary results suggest that PbS-$Sn_2S_6^{4-}$ NCs in their current solvent environment are not strong candidates for forming hyperuniform glasses.

Interestingly, the hyperuniformity indices measured in the NMF/DMF mixture are noticeably higher than those obtained in pure NMF. This observation suggests that achieving hyperuniformity may require a solvent system that combines high polarity with a low freezing point. Such a solvent would preserve strong electrostatic interactions while allowing measurements at temperatures where hyperuniformity is more likely to emerge.

3.5. Cluster fluid formation of nanocrystals in formamide

An unusual structure factor was observed for 5.7 nm PbS-$Sn_2S_6^{4-}$ NCs dispersed in formamide (FA). As shown in Figure 3.5.1A, the SAXS profile exhibits two broad maxima at 0.041 $Å^{-1}$ and 0.116 $Å^{-1}$. The intensity of the second peak is too large to be interpreted as a simple higher-order feature of a single Percus-Yevick structure factor. Instead, the data are more consistent with a superposition of two Percus-Yevick-type structure factors, each with its own primary peak at 0.041 $Å^{-1}$ and 0.116 $Å^{-1}$. These peak positions correspond to characteristic real-space distances of approximately 15.3 nm and 5.4 nm, respectively.

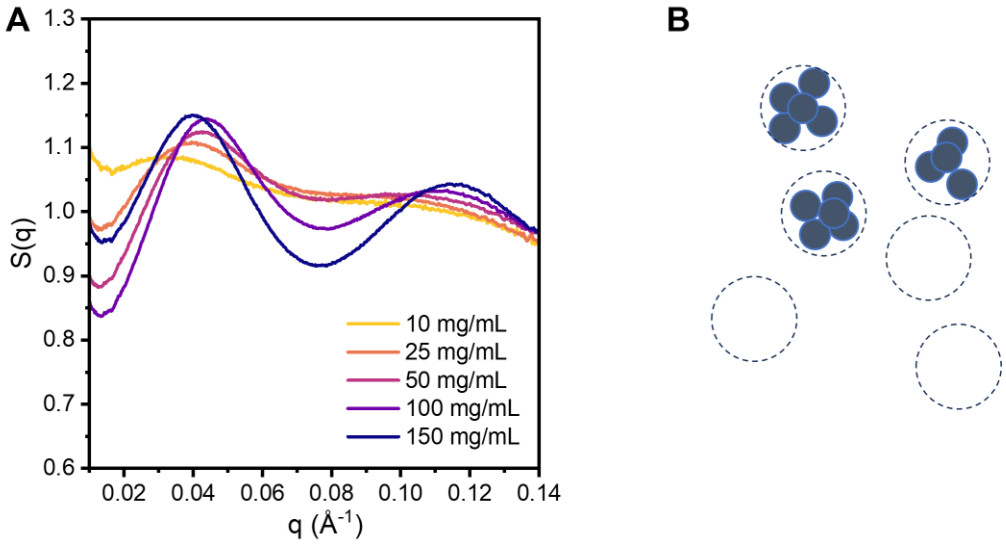

Figure 3.5.1: Cluster fluids from NCs in formamide.
(A) Structure factor of 5.7 nm PbS-$Sn_2S_6^{4-}$ NCs dissolved in formamide (FA). **(B)** Illustration of cluster fluid.

Such dual-length-scale scattering signatures are characteristic of cluster fluids, in which individual particles form dense clusters that remain dispersed within the solvent (Figure 3.5.1B).[16] In this scenario, the shorter length scale (5.4 nm) reflects the inter-NC spacing within clusters, indicating that the NCs are essentially in contact. The longer length scale (15.3 nm) corresponds to the average separation between clusters themselves. Thus, 5.7 nm PbS-$Sn_2S_6^{4-}$

NCs in formamide appear to adopt a hierarchical organization: tightly packed NC clusters that remain suspended and spatially separated within the continuous phase.

3.6. Effect of electrolytes on interparticle interactions

The addition of free ions to an electrostatically stabilized PbS-$Sn_2S_6^{4-}$ NCs solution is expected to reduce the screening length of electrostatic repulsion.[22] Consequently, the long-range repulsion of NCs is reduced, resulting in the reappearance of a colloidal gas-like configuration (Figure 3.6.1C). This phenomenon is corroborated by the structure factors shown in Figure 3.6.1A, where the oscillatory features of structure factor are suppressed by the addition of K_3AsS_4 salt. The addition of 10 mM K_3AsS_4 results in near-unity $S(q)$, similar to the case of sterically stabilized PbS-OA NCs.

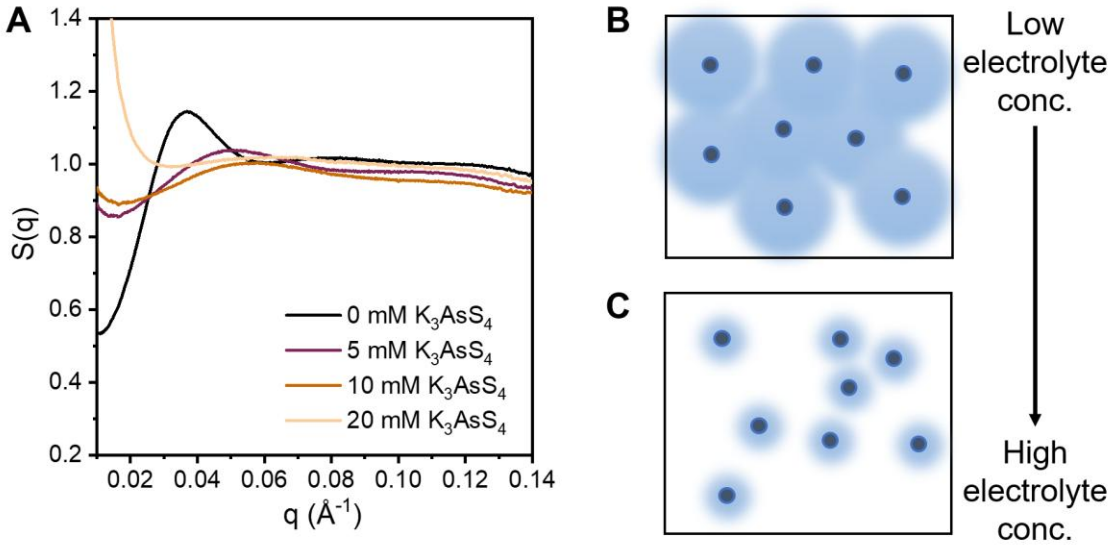

Figure 3.6.1: Spatial arrangements of screened NCs in solution.

(A) The structure factors of 50 mg/ml of 5.7 nm PbS-$Sn_2S_6^{4-}$ NCs in NMF at different concentrations of added K_3AsS_4 salt. Illustration of transition from **(B)** uniform arrangements of NCs to **(C)** random arrangements as the concentration of added K_3AsS_4 salts increases.

Notably, the rise of structure factors in the low-*q* region may be attributed to transient aggregation of PbS NCs, which can give rise to local clusters or voids and gives rise to strong X-ray scattering in this range (Figure 3.6.2). This may be due to the competing effects of short-range attraction that promotes clustering of the NCs and the long-range repulsion that prevents the growth of the aggregates into macroscopic size, similar to features discussed in Section 3.5.[16,23]

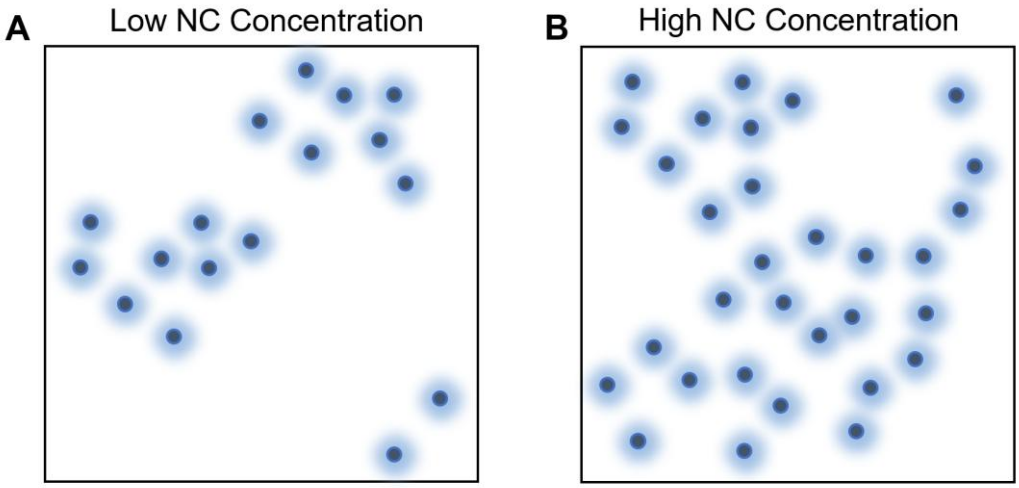

Figure 3.6.2: Cluster and void formations of in NC solution.
Illustration of **(A)** cluster formation at low concentrations of NCs, and **(B)** void formation at high concentrations of NCs. Both cases can give rise to low-*q* upturn in SAXS patterns.

3.7. Film-forming properties of sterically and electrostatically stabilized nanocrystals

Given the importance of colloidal NCs for thin-film optoelectronic devices, we aim to compare the films of PbS NCs prepared from colloidal solutions of sterically and electrostatically stabilized colloidal dispersions and evaluate what characteristics of the pair potentials are most favorable for the formation of dense and uniform layers desirable for LEDs, photodetectors, solar cells, and other thin-film devices.[24]

Drop-casting or spin-coating of colloidal solutions of sterically stabilized PbS-OA NCs typically results in ordered films containing multiple superlattice domains. The domain size is defined by solvent evaporation rate and is smaller for spin-coated films compared to that in films made by slow solvent evaporation (Figure 3.7.1). Our films of 7.2 nm PbS-OA NCs deposited from methylcyclohexane have *fcc* structure. In several theoretical studies which related pair potentials and phase diagrams of colloidal spheres, it has been shown that *fcc* phase is more favorable for particles that interact by hard sphere-like potentials, due to the higher packing density. Thus, very similar 7 nm PbS-OA NCs in toluene formed *fcc* superlattices upon slow addition of ethanol, which increased solvent polarity and gradually changed repulsive pair potentials to attractive.[25]

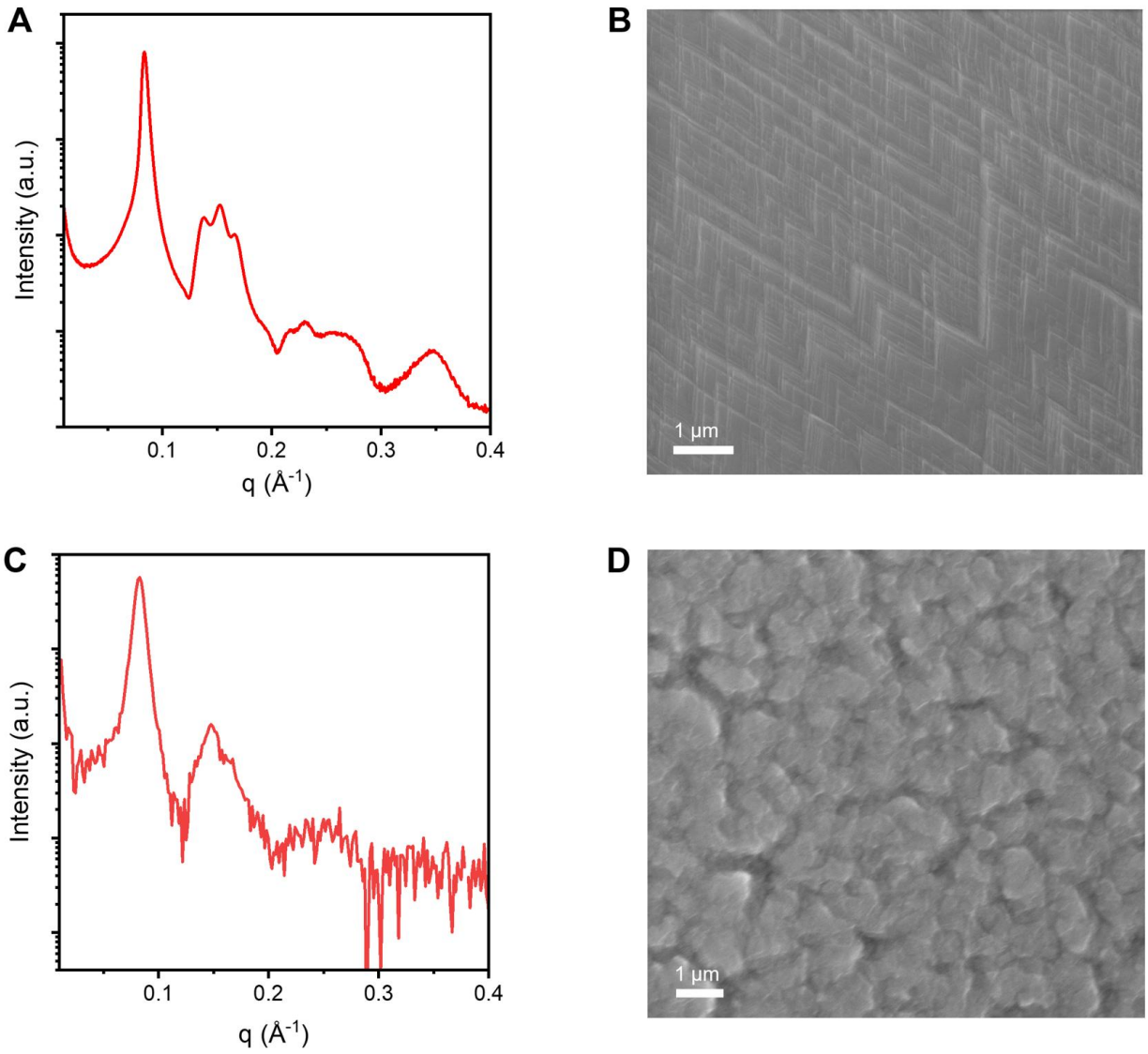

Figure 3.7.1: Crystalline films from PbS-OA NCs.

(A) SAXS pattern and **(B)** SEM image of films of 7.2 nm PbS-OA NCs drop-casted on a thin Si wafer. **(C)** SAXS pattern and **(D)** SEM image of films of 7.2 nm PbS-OA NCs spin-coated on a thin Si wafer.

In contrast, electrostatically stabilized PbS-$Sn_2S_6^{4-}$ NCs show more complex behavior. In the absence of added ions, spin-coated or drop-cast colloidal dispersions of PbS-$Sn_2S_6^{4-}$ NCs in NMF yield glassy films with no NC ordering (Figure 3.7.2).[24] The formation of disordered films is consistent with theoretical predictions for particles interacting through short-range attractive and

long-range repulsive potentials.[26] The randomly packed glassy NC layers are expected to have more isotropic properties compared to crystalline superlattices (Figure 3.7.1), which could be useful for applications in optoelectronic devices.

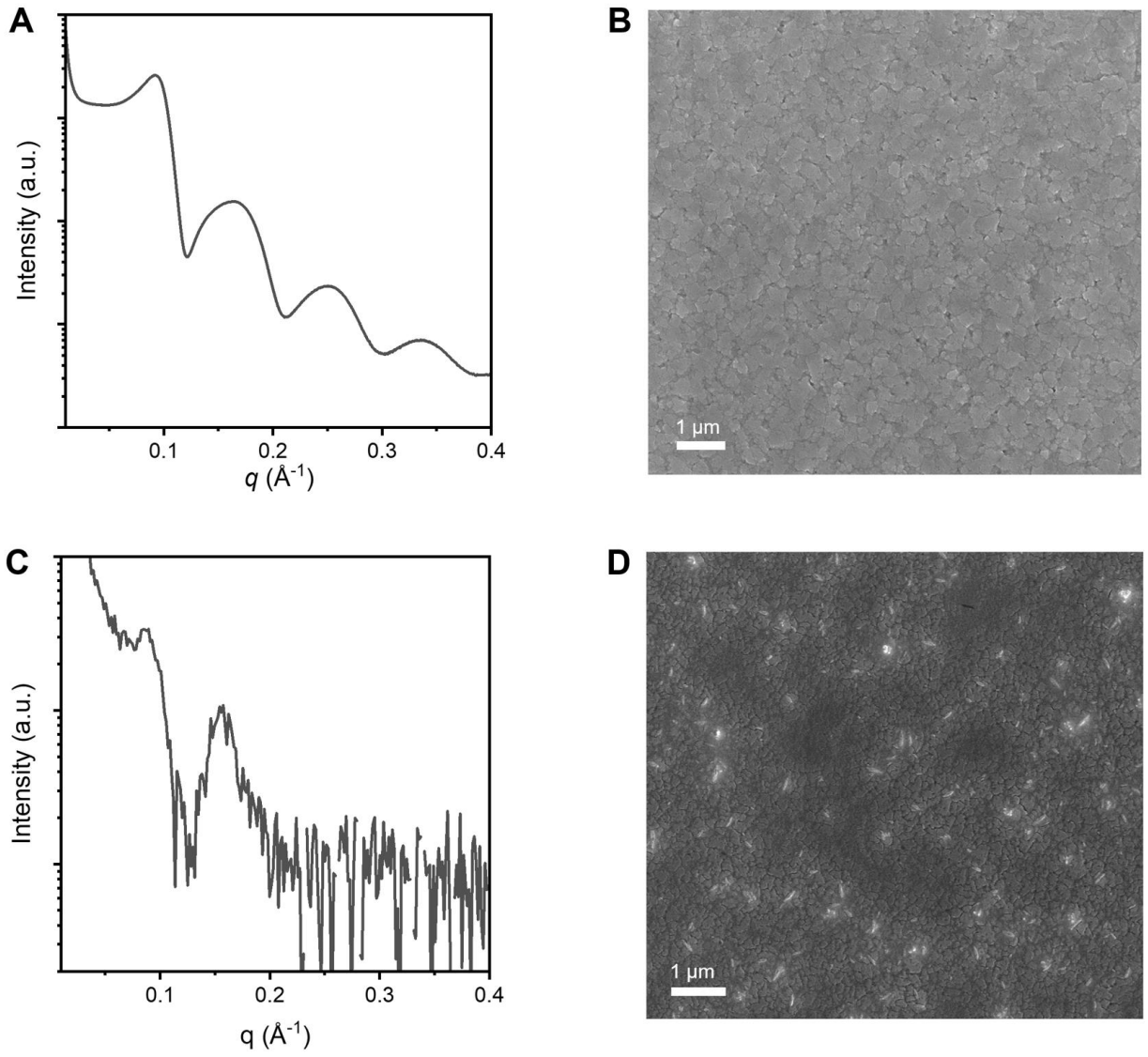

Figure 3.7.2: Amorphous films from PbS-$Sn_2S_6^{4-}$ NCs.

(A) SAXS pattern and **(B)** SEM image of films of 7.2 nm PbS-$Sn_2S_6^{4-}$ NCs drop-casted on a thin Si wafer. **(C)** SAXS pattern and **(D)** SEM image of films of 7.2 nm PbS-$Sn_2S_6^{4-}$ NCs spin-coated on a thin Si wafer.

The inability to self-assembly electrostatically stabilized PbS-$Sn_2S_6^{4-}$ NCs is due to the long-range repulsive potentials. In such systems, when the NC concentration increases due to solvent evaporation, the narrow attractive well promotes the formation of NC clusters which cannot grow further into superlattices due to the repulsive term.[27,28] Upon further increase of NC concentration, these clusters coalesce forming percolated networks of NCs and even microphases.[29] Computational studies also predict that NC colloids with short-range attraction and long-range repulsive potentials are prone to gelation, also leading to disordered NC layers.[28] In contrast, sterically stabilized PbS-OA NCs do not experience such long-range repulsive forces. Their interactions are dominated by short-range van der Waals attraction and steric repulsion, enabling them to readily self-assemble into well-ordered superlattices. The self-assembly of PbS-OA NCs and PbS-$Sn_2S_6^{4-}$ NCs are illustrated in Figure 3.7.3.

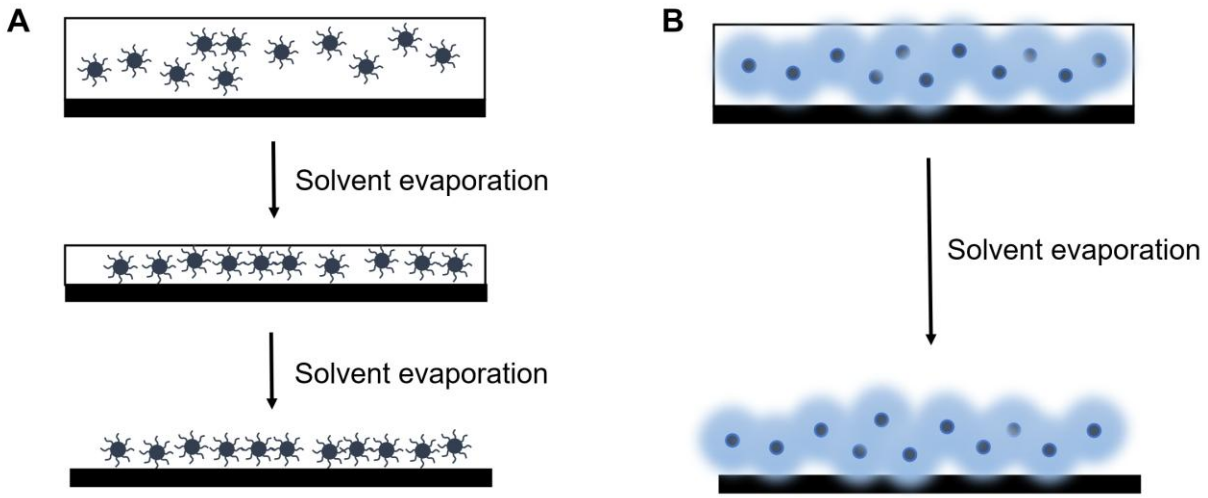

Figure 3.7.3: Film-forming properties of sterically and electrostatically stabilized NCs. Illustration of self-assembly of **(A)** sterically stabilized PbS-OA NCs, and **(B)** PbS-$Sn_2S_6^{4-}$ NCs. The short-range repulsive forces allow PbS-OA NCs to readily self-assemble into superlattice, whereas the long-range repulsive forces of PbS-$Sn_2S_6^{4-}$ NCs prevent self-assembly.

3.8. Film-forming properties of nanocrystals with screened electrostatic potential

To further investigate how the range of interparticle interactions influences self-assembly, we reduced the electrostatic repulsion between PbS-$Sn_2S_6^{4-}$ NCs by adding electrolytes. Within the framework of DLVO theory, the range of the repulsive forces is defined by the Debye screening length, and addition of an electrolyte into colloidal dispersion increases ionic strength and reduces Debye length.[18,19] Although DLVO-type theory does not perfectly depict the NC pair potential, many theoretical work demonstrated that the behavior of PbS-$Sn_2S_6^{4-}$ NCs at high ionic strengths resembles the behavior of spheres with a pair potential consisting of a narrow attractive well with the width less than 20% of NC diameter and depth of several k_BT.[6,30] At low ionic strength, the interparticle interactions can be modeled as a combination of short-range attractive and longer-range repulsive potentials, with the possibility of changing the contributions of attractive and repulsive components by varying the concentration of free ions added to a colloidal dispersion (Figure 3.8.1).[30] The DLVO theory and how it relates to our understanding of the interparticle forces between electrostatically stabilized NCs are further discussed in Chapter 4.

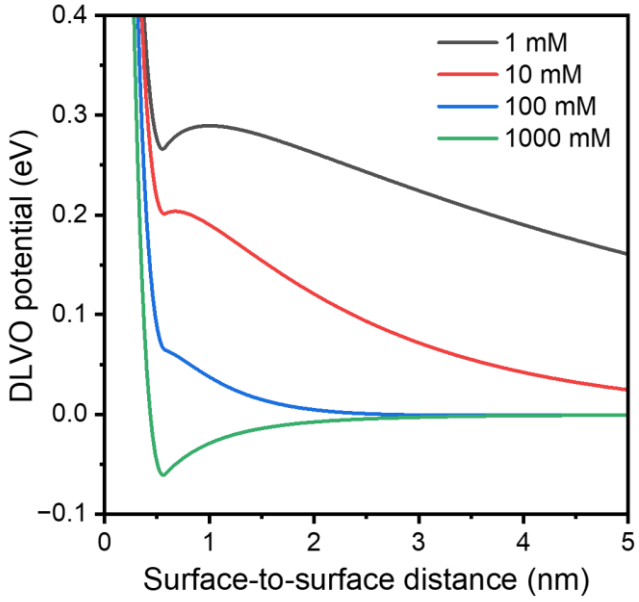

Figure 3.8.1: DLVO potential of NC solutions with varying electrolyte concentration.
DLVO potentials for 7.2 nm PbS-$Sn_2S_6^{4-}$ NCs in NMF with varying concentrations of added 1:3 electrolyte, e.g., K_3AsS_4 salt.

The addition of free ions, e.g., by adding K_3AsS_4 salt to the colloidal dispersion, whose concentration is gradually increasing upon solvent evaporation, is expected to suppress both the height and the range of repulsive component as shown in Figure 3.8.1. As it was shown in our previous study, elimination of the repulsive term is favorable for self-assembly of NCs into long-range ordered *fcc* superlattices,[6] because nucleated clusters of NCs can keep growing indefinitely. Figure 3.8.2 shows that the addition of K_3AsS_4 salt to 7.2 nm PbS-$Sn_2S_6^{4-}$ NCs increases ordering of NCs in both drop-casted and spin-coated films.

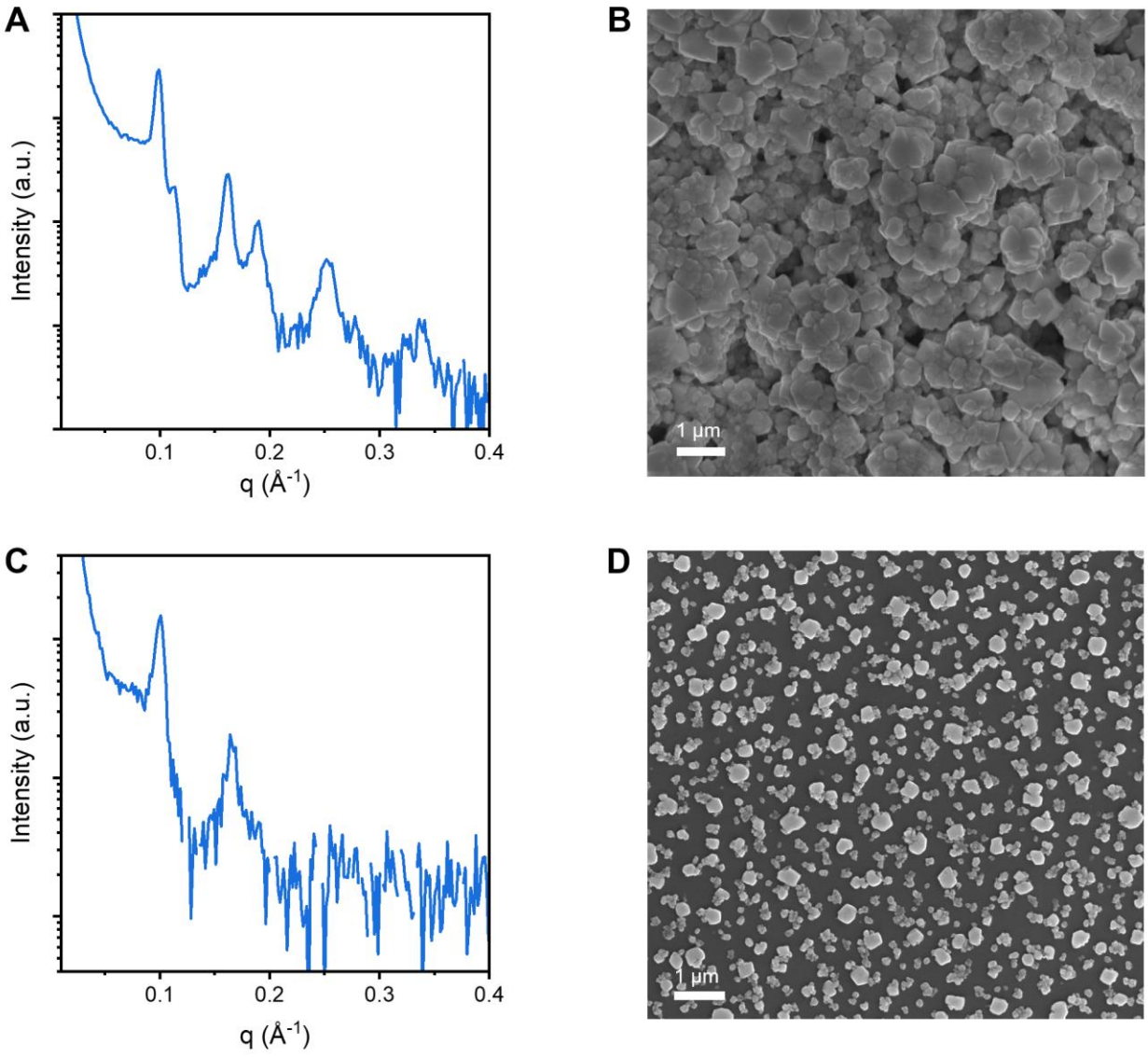

Figure 3.8.2: Crystalline powders from screened PbS-$Sn_2S_6^{4-}$ NCs.

(A) SAXS pattern and **(B)** SEM image of films of 7.2 nm PbS-$Sn_2S_6^{4-}$ NCs with added K_3AsS_4 drop-casted on a thin Si wafer. **(C)** SAXS pattern and **(D)** SEM image of films of 7.2 nm PbS-$Sn_2S_6^{4-}$ NCs with added K_3AsS_4 spin-coated on a thin Si wafer.

Figure 3.8.3 illustrates the transition from amorphous to crystalline nanocrystal solids as the concentration of K_3AsS_4 is increased in dispersions of 7.2 nm PbS-$Sn_2S_6^{4-}$ NCs. In Figure 3.8.3A, SAXS patterns were obtained by preparing 62 mg/mL NC dispersions containing 0–20 mM K_3AsS_4, drop-casting the solutions onto thin Si wafers, and collecting data in

transmission mode. The added electrolyte concentrations of 5, 10, and 20 mM correspond to 0.805, 1.610, and 2.320 μmol of K_3AsS_4 per milligram of PbS NCs, respectively. As the electrolyte concentration increases, the Bragg peaks sharpen and intensify, indicating that self-assembly is progressively enhanced and that the resulting superlattices become more ordered. The corresponding SEM images in Figures 3.8.3B–D show that the superlattice grain size increases with electrolyte concentration and that the grains become more faceted, consistent with improved crystallinity. These films were prepared by drop-casting NC dispersions containing 0.403, 1.208, and 2.013 μmol of K_3AsS_4 per milligram of PbS NCs, respectively. It should be noted that the SEM image of Figure 3.8.3B is imaged from a different region of the same film as Figure 3.8.2B.

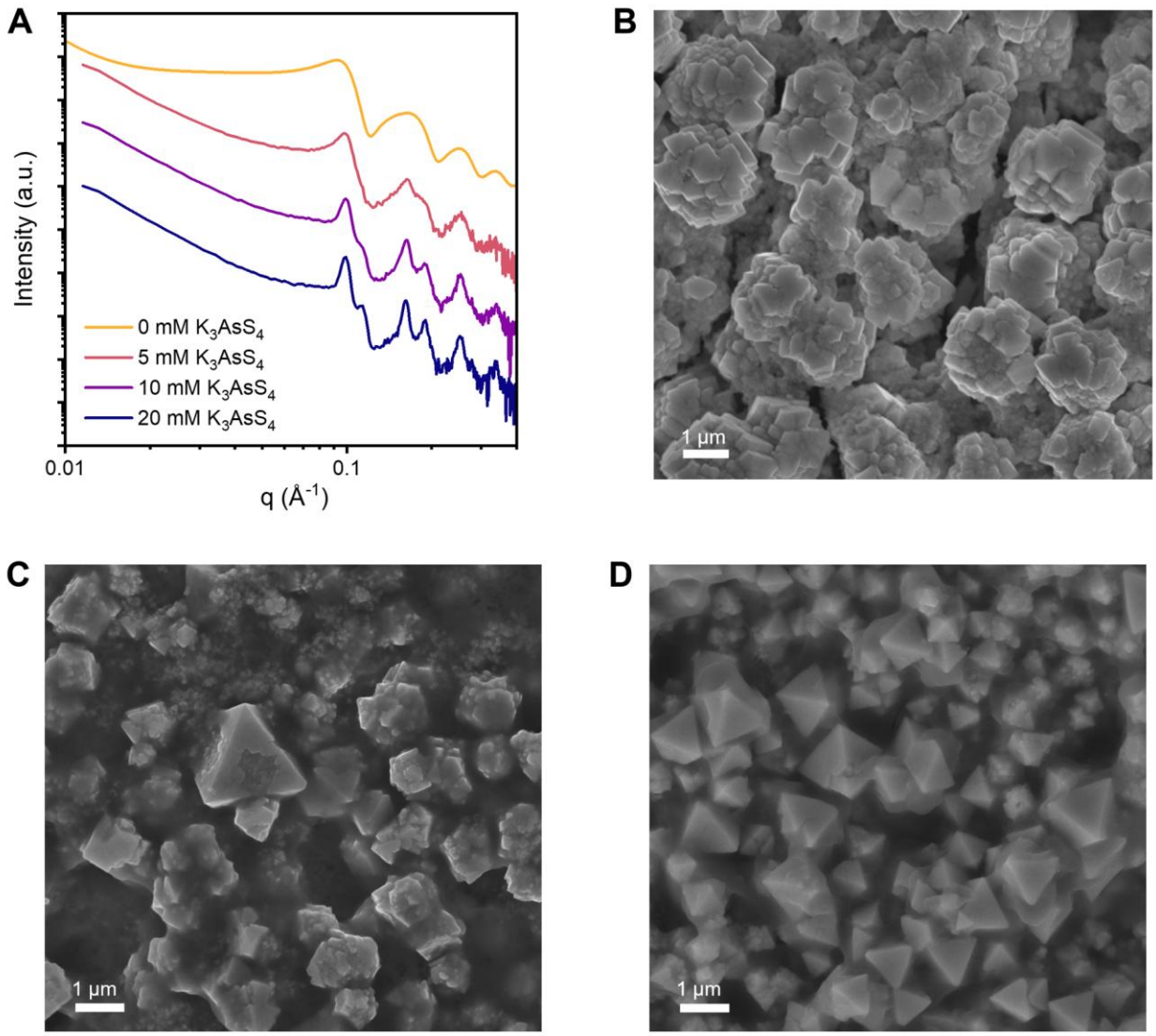

Figure 3.8.3: Films of PbS-$Sn_2S_6^{4-}$ NCs with increasing concentration of electrolytes.

(A) SAXS pattern of 7.2 nm PbS-$Sn_2S_6^{4-}$ NC film prepared by drop-casting a solution of NCs with increasing concentration of K_3AsS_4. **(B, C, D)** SEM images of 7.2 nm PbS-$Sn_2S_6^{4-}$ NC film prepared by drop-casting a solution of NCs with increasing concentration of K_3AsS_4.

Individual superlattices have nearly perfect octahedral faceting, corresponding to the Wulff construction with low energy facets with $(111)_{SL}$ Miller indices. The formation of such structures is expected if NCs have strong tendency to self-assemble into crystalline superlattices, while maximization of total cohesive energy through densification of NC layer is not happening. In one

plausible scenario, superlattices of PbS-$Sn_2S_6^{4-}$ NCs nucleate and grow at the early stage of film drying, and the precipitation of micron-size superlattices results in a pile of faceted superlattices (Figure 3.8.4). Naturally, the long-range electronic connectivity for such film morphology is relatively weak, and, despite the possibility for interesting physics (*e.g.* miniband formation) within superlattices of strongly electronically coupled NCs,[24] the utility for such layers for optoelectronic applications is questionable.

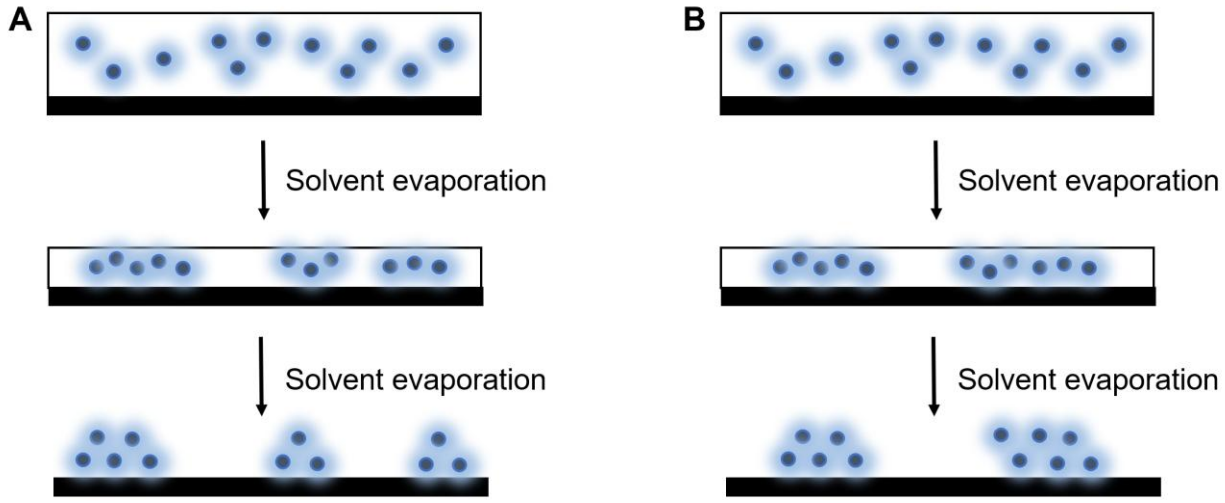

Figure 3.8.4: Film-forming properties of screened and unscreened NCs.
Illustration of self-assembly of PbS-$Sn_2S_6^{4-}$ NCs that are screened by **(A)** a low concentration and **(B)** a high concentration of K_3AsS_4. The short-range repulsive forces allow PbS-$Sn_2S_6^{4-}$ NCs to self-assemble, but their clustering results in non-uniform films that consist of superlattice grains.

Varying the concentration and nature of free ions in solution allows tuning of the pair potentials from long-ranged strongly repulsive, resulting in amorphous NC films, to short-range attractive that yields perfect but loosely packed NC superlattices. In between these limiting cases, there exists a "sweet spot" where NCs self-assemble into ordered domains that are shaped to connect with neighboring NC superlattices without gaps. Such a morphology maximizes packing

density and electronic coupling both within and between superlattice domains and enables good electronic connectivity across the entire NC film. A optical morphology is shown in Figure 3.8.5, where the NCs are overall amorphous but are well-covered, enabled by the trace amount of unbound $K_4Sn_2S_6$ ligands in the solution (see the reference for the estimate of the concentration of unbound ligands in solution).[31] It demonstrates that electrostatically stabilized colloidal dispersions of semiconductor NCs can be used as "inks" for making NC layers with packing density and structural quality comparable to those in films prepared from colloids of sterically stabilized NCs.

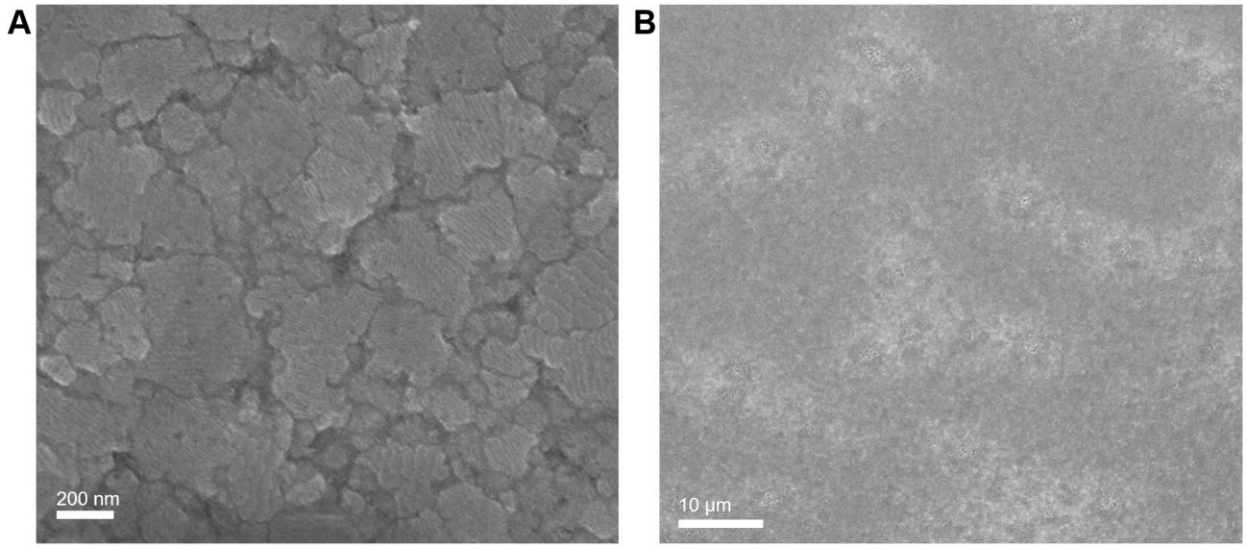

Figure 3.8.5: Well-covered amorphous film of PbS-$Sn_2S_6^{4-}$ NCs.

SEM images of a film of PbS-$Sn_2S_6^{4-}$ NCs showing **(A)** localized and **(B)** overview of complete coverage with NCs.

3.9. Chapter 3 bibliography

(1) Ye, X.; Zhu, C.; Ercius, P.; Raja, S. N.; He, B.; Jones, M. R.; Hauwiller, M. R.; Liu, Y.; Xu, T.; Alivisatos, A. P. Structural Diversity in Binary Superlattices Self-Assembled from Polymer-Grafted Nanocrystals. *Nat Commun* **2015**, *6* (1), 10052. https://doi.org/10.1038/ncomms10052.

(2) Boles, M. A.; Talapin, D. V. Many-Body Effects in Nanocrystal Superlattices: Departure from Sphere Packing Explains Stability of Binary Phases. *J. Am. Chem. Soc.* **2015**, *137* (13), 4494–4502. https://doi.org/10.1021/jacs.5b00839.

(3) Coropceanu, I.; Boles, M. A.; Talapin, D. V. Systematic Mapping of Binary Nanocrystal Superlattices: The Role of Topology in Phase Selection. *J. Am. Chem. Soc.* **2019**, *141* (14), 5728–5740. https://doi.org/10.1021/jacs.8b12539.

(4) Shevchenko, E. V.; Talapin, D. V.; Murray, C. B.; O'Brien, S. Structural Characterization of Self-Assembled Multifunctional Binary Nanoparticle Superlattices. *J. Am. Chem. Soc.* **2006**, *128* (11), 3620–3637. https://doi.org/10.1021/ja0564261.

(5) Talapin, D. V.; Lee, J.-S.; Kovalenko, M. V.; Shevchenko, E. V. Prospects of Colloidal Nanocrystals for Electronic and Optoelectronic Applications. *Chem. Rev.* **2010**, *110* (1), 389–458. https://doi.org/10.1021/cr900137k.

(6) Coropceanu, I.; Janke, E. M.; Portner, J.; Haubold, D.; Nguyen, T. D.; Das, A.; Tanner, C. P. N.; Utterback, J. K.; Teitelbaum, S. W.; Hudson, ¸ Margaret H.; Sarma, N. A.; Hinkle, A. M.; Tassone, C. J.; Eychmüller, A.; Limmer, D. T.; Olvera De La Cruz, M.; Ginsberg, N. S.; Talapin, D. V. Self-Assembly of Nanocrystals into Strongly Electronically Coupled All-Inorganic Supercrystals. *Science* **2022**, *375* (6587), 1422–1426. https://doi.org/10.1126/science.abm6753.

(7) Nag, A.; Kovalenko, M. V.; Lee, J.-S.; Liu, W.; Spokoyny, B.; Talapin, D. V. Metal-Free Inorganic Ligands for Colloidal Nanocrystals: S^{2-} , HS^{-} , Se^{2-} , HSe^{-} , Te^{2-} , HTe^{-} , TeS_3^{2-} , OH^{-} , and NH_2^{-} as Surface Ligands. *J. Am. Chem. Soc.* **2011**, *133* (27), 10612–10620. https://doi.org/10.1021/ja2029415.

(8) Talapin, D. V.; Murray, C. B. PbSe Nanocrystal Solids for N- and p-Channel Thin Film Field-Effect Transistors. *Science* **2005**, *310* (5745), 86–89. https://doi.org/10.1126/science.1116703.

(9) Kovalenko, M. V.; Scheele, M.; Talapin, D. V. Colloidal Nanocrystals with Molecular Metal Chalcogenide Surface Ligands. *Science* **2009**, *324* (5933), 1417–1420. https://doi.org/10.1126/science.1170524.

(10) Weidman, M. C.; Smilgies, D.-M.; Tisdale, W. A. Kinetics of the Self-Assembly of Nanocrystal Superlattices Measured by Real-Time in Situ X-Ray Scattering. *Nature Mater* **2016**, *15* (7), 775–781. https://doi.org/10.1038/nmat4600.

(11) Li, T.; Senesi, A. J.; Lee, B. Small Angle X-Ray Scattering for Nanoparticle Research. *Chem. Rev.* **2016**, *116* (18), 11128–11180. https://doi.org/10.1021/acs.chemrev.5b00690.

(12) Bishop, K. J. M.; Wilmer, C. E.; Soh, S.; Grzybowski, B. A. Nanoscale Forces and Their Uses in Self-Assembly. *Small* **2009**, *5* (14), 1600–1630. https://doi.org/10.1002/smll.200900358.

(13) Ofosu, C. K.; Kang, J.; Truskett, T. M.; Milliron, D. J. Effective Hard-Sphere Repulsions between Oleate-Capped Colloidal Metal Oxide Nanocrystals. *J. Phys. Chem. Lett.* **2022**, *13* (48), 11323–11329. https://doi.org/10.1021/acs.jpclett.2c02627.

(14) Holade, Y.; Sahin, N.; Servat, K.; Napporn, T.; Kokoh, K. Recent Advances in Carbon Supported Metal Nanoparticles Preparation for Oxygen Reduction Reaction in Low Temperature Fuel Cells. *Catalysts* **2015**, *5* (1), 310–348. https://doi.org/10.3390/catal5010310.

(15) Sirota, E. B.; Ou-Yang, H. D.; Sinha, S. K.; Chaikin, P. M.; Axe, J. D.; Fujii, Y. Complete Phase Diagram of a Charged Colloidal System: A Synchro- Tron x-Ray Scattering Study. *Phys. Rev. Lett.* **1989**, *62* (13), 1524–1527. https://doi.org/10.1103/PhysRevLett.62.1524.

(16) Stradner, A.; Sedgwick, H.; Cardinaux, F.; Poon, W. C. K.; Egelhaaf, S. U.; Schurtenberger, P. Equilibrium Cluster Formation in Concentrated Protein Solutions and Colloids. *Nature* **2004**, *432* (7016), 492–495. https://doi.org/10.1038/nature03109.

(17) Hayter, J. B.; Penfold, J. An Analytic Structure Factor for Macroion Solutions. *Molecular Physics* **1981**, *42* (1), 109–118. https://doi.org/10.1080/00268978100100091.

(18) Derjaguin, B.; Landau, L. Theory of the Stability of Strongly Charged Lyophobic Sols and of the Adhesion of Strongly Charged Particles in Solutions of Electrolytes. *Progress in Surface Science* **1993**, *43* (1–4), 30–59. https://doi.org/10.1016/0079-6816(93)90013-L.

(19) Verwey, E. J. W. Theory of the Stability of Lyophobic Colloids.

(20) Chremos, A.; Douglas, J. F. Hidden Hyperuniformity in Soft Polymeric Materials. *Phys. Rev. Lett.* **2018**, *121* (25), 258002. https://doi.org/10.1103/PhysRevLett.121.258002.

(21) Chremos, A.; Douglas, J. F. Particle Localization and Hyperuniformity of Polymer-Grafted Nanoparticle Materials. *Annalen der Physik* **2017**, *529* (5), 1600342. https://doi.org/10.1002/andp.201600342.

(22) Kohonen, M. M.; Karaman, M. E.; Pashley, R. M. Debye Length in Multivalent Electrolyte Solutions. *Langmuir* **2000**, *16* (13), 5749–5753. https://doi.org/10.1021/la991621c.

(23) Chremos, A.; Douglas, J. F. Influence of Solvation on the Structure of Highly Charged Nanoparticles in Salt-Free Solutions. *Polymer* **2019**, *170*, 107–112. https://doi.org/10.1016/j.polymer.2019.03.005.

(24) Kagan, C. R.; Murray, C. B. Charge Transport in Strongly Coupled Quantum Dot Solids. *Nature Nanotech* **2015**, *10* (12), 1013–1026. https://doi.org/10.1038/nnano.2015.247.

(25) Rupich, S. M.; Shevchenko, E. V.; Bodnarchuk, M. I.; Lee, B.; Talapin, D. V. Size-Dependent Multiple Twinning in Nanocrystal Superlattices. *J. Am. Chem. Soc.* **2010**, *132* (1), 289–296. https://doi.org/10.1021/ja9074425.

(26) Bini, M.; Brancolini, G.; Tozzini, V. Aggregation Behavior of Nanoparticles: Revisiting the Phase Diagram of Colloids. *Front. Mol. Biosci.* **2022**, *9*, 986223. https://doi.org/10.3389/fmolb.2022.986223.

(27) Ruiz-Franco, J.; Zaccarelli, E. On the Role of Competing Interactions in Charged Colloids with Short-Range Attraction. *Annu. Rev. Condens. Matter Phys.* **2021**, *12* (1), 51–70. https://doi.org/10.1146/annurev-conmatphys-061020-053046.

(28) Ioannidou, K.; Kanduč, M.; Li, L.; Frenkel, D.; Dobnikar, J.; Del Gado, E. The Crucial Effect of Early-Stage Gelation on the Mechanical Properties of Cement Hydrates. *Nat Commun* **2016**, *7* (1), 12106. https://doi.org/10.1038/ncomms12106.

(29) Zhuang, Y.; Charbonneau, P. Recent Advances in the Theory and Simulation of Model Colloidal Microphase Formers. *J. Phys. Chem. B* **2016**, *120* (32), 7775–7782. https://doi.org/10.1021/acs.jpcb.6b05471.

(30) Tanner, C. P. N.; Utterback, J. K.; Portner, J.; Coropceanu, I.; Das, A.; Tassone, C. J.; Teitelbaum, S. W.; Limmer, D. T.; Talapin, D. V.; Ginsberg, N. S. In Situ X-Ray Scattering Reveals Coarsening Rates of Superlattices Self-Assembled from Electrostatically Stabilized Metal Nanocrystals Depend Nonmonotonically on Driving Force. *ACS Nano* **2024**, acsnano.3c12186. https://doi.org/10.1021/acsnano.3c12186.

(31) Jeong, A.; Portner, J.; Tanner, C. P. N.; Ondry, J. C.; Zhou, C.; Mi, Z.; Tazoui, Y. A.; Lee, B.; Wall, V. R. K.; Ginsberg, N. S.; Talapin, D. V. Colloidal Dispersions of Sterically and Electrostatically Stabilized PbS Quantum Dots: Structure Factors, Second Virial Coefficients, and Film-Forming Properties. *ACS Nano* **2024**, *18* (50), 33864–33874. https://doi.org/10.1021/acsnano.4c06033.

4. Chapter 4: Second virial coefficients of electrostatically stabilized nanocrystals

Reprinted with permission from *ACS Nano* 2024, 18, 50, 33864–33874. Copyright © 2024 American Chemical Society.

4.1. Introduction

A comprehensive understanding of the NC-NC interactions in colloidal solutions is essential for making nanocrystal devices by solution processing methods or for developing bottom-up self-assembly techniques, as the interparticle interactions exert a profound impact on colloidal stability and NC assembly. Previous studies have utilized scattering and microscopy methods to experimentally study the NC-NC interactions in sterically stabilized NCs, revealing the influence of size, surface, solvent conditions on the colloidal stability and assembly.[1–6] However, our understanding of NC-NC interactions in colloidal dispersions of electrostatically stabilized NCs remains limited. To develop functional materials that harness the useful properties of electrostatically stabilized NCs, a thorough understanding of how the NC size, surface chemistry and solvent influence the interactions between electrostatically stabilized NCs will be necessary to advance the field.

To quantitatively analyze how the size, surface, and solvent of NCs impact the extent of deviation from the ideal behavior, we measured the second virial (B_2) coefficients of colloidal dispersions of electrostatically stabilized PbS NCs.[1] Various physical properties of non-ideal solution can be defined through virial coefficients. Thus, the osmotic pressure (Π) of a dispersion of interacting particles can be expressed as a power series of particle number density (n), where

k_B is the Boltzmann constant, T is the temperature, B_2 is the second virial coefficient and B_3 is the third virial coefficient:[7]

$$\frac{\Pi}{k_B T} = n + B_2\, n^2 + B_3\, n^3 + \ \ldots$$

A positive or negative B_2 coefficient indicates a net repulsive or a net attractive pairwise interaction between the particles, respectively. Quantitatively, B_2 can be directly related to the pair potentials $u(r)$ between NCs that are separated by the distance r:[8]

$$B_2 = -2\pi \int_0^\infty \left(\exp\left(-\frac{u(r)}{k_B T} \right) - 1 \right) r^2 \, \mathrm{d}r$$

When comparing B_2 coefficients of different NC samples, it is often convenient to calculate the normalized second virial coefficients (b_2), which provide more direct insights into colloidal stability and self-assembly behavior. For spherical or nearly spherical particles, a dimensionless b_2 can be calculated as $b_2 = B_2/B_{2,HS}$, where $B_{2,\,HS}$ is the second virial coefficient of an equivalent colloid of hard spheres. In turn, $B_{2,\,HS}$ can be calculated as $B_{2,HS} = 2\pi(d + 2\delta)^3/3$, where d is the diameter of the NC core and δ is the length of the surface ligands.[8] A positive b_2 value implies an overall repulsive interactions between NCs, leading to high colloidal stability. In contrast, a negative b_2, especially $b_2 < -10$, typically leads to uncontrolled aggregation into an amorphous structure.[52] Weakly attractive particles with a small b_2 coefficient ($-10 < b_2 < -1$) can self-assemble into ordered structures, such as protein crystals or NC superlattices.[9]

In this section, we experimentally determine the B_2 coefficients for PbS NCs from concentration-dependent SAXS data. Then, we compare our results with predictions from DLVO theory, which provides a minimalistic framework to describe the interparticle interactions of charged colloidal particles.[10,11]

4.2. Extraction of second virial coefficients from SAXS measurements

Concentration-dependent SAXS measurements

The second virial coefficient (B_2) was experimentally determined using concentration-dependent SAXS measurements. The value of B_2 is related to the structure factor at zero scattering vector, *S(0)*, through the virial expansion:

$$\frac{1}{S(0)} = 1 + 2B_2 n + \mathcal{O}(n^2)$$

where *n* is the number density of nanocrystals in solution.[8] Rearranging this expression shows that B_2 can be obtained from one-half of the slope of a plot of $1/S(0) - 1$versus *n*. The number density was calculated using:

$$n = \frac{c}{\rho V_{NC}}$$

where *c* is the NC concentration in mg/mL, ρ is the density of the nanocrystal material, and $V_{\mathrm{NC}}$is the nanocrystal volume.

To perform this analysis, a series of NC dispersions with different concentrations was prepared. The concentration of each stock solution was first measured by ICP-OES, and the dispersions were then diluted to the desired values. The samples were loaded into glass capillaries for SAXS measurements. For electrostatically stabilized PbS-$Sn_2S_6^{4-}$ NCs, concentrations between 6 and 14 mg/mL were used. In contrast, sterically stabilized PbS-OA NCs required much higher concentrations (50–300 mg/mL), because deviations of the structure factor from unity were too small to quantify at lower concentrations.

Figure 4.2.1 shows the experimental setup and representative concentration-dependent SAXS patterns for 7.2 nm PbS-$Sn_2S_6^{4-}$ NCs in NMF. This sample serves as the model system for demonstrating the extraction of the second virial coefficient throughout this section.

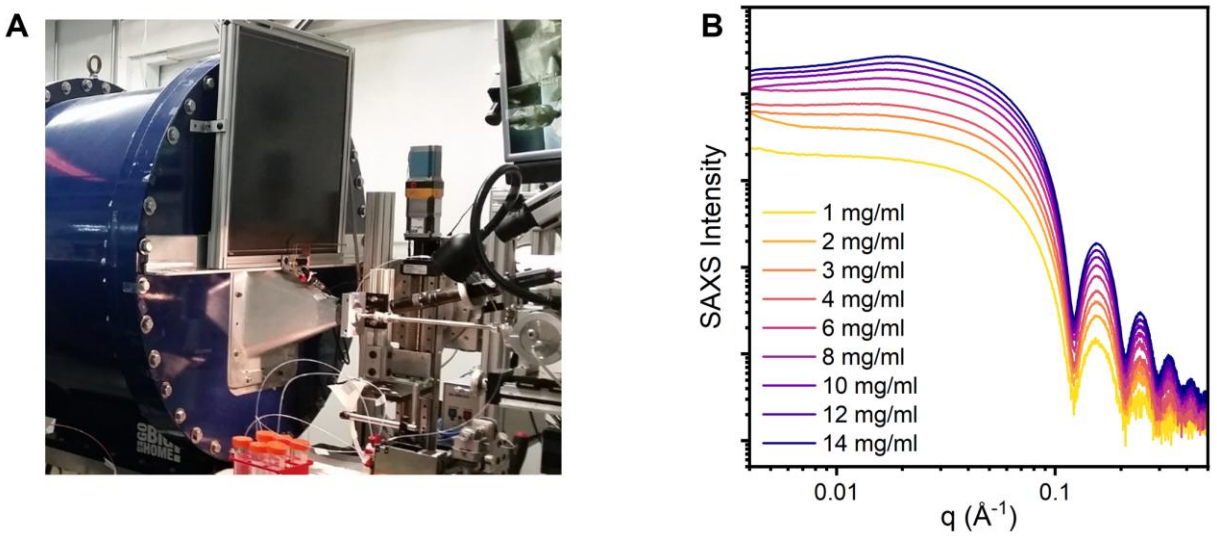

Figure 4.2.1: Concentration-dependent SAXS measurement.

(A) Experimental setup for concentration-dependent SAXS measurement for B_2 coefficient analysis. **(B)** Concentration-dependent SAXS patterns of 7.2 nm PbS-$Sn_2S_6^{4-}$ NCs in NMF.

Extraction of the structure factor

The next step in the analysis is to extract the concentration-dependent structure factors from the corresponding SAXS patterns. As a reminder, the measured SAXS intensity is related to the form factor and structure factor through:

$$I(q) = A\,P(q)\,S(q)$$

where A is a scaling constant, $P(q)$ is the form factor, and $S(q)$ is the structure factor. We approximated the form factor using the SAXS pattern of a dilute (1 mg mL^{-1}) NC dispersion, under the assumption that such a dilute sample exhibits negligible interparticle interactions and therefore has a structure factor close to unity. The scaling factor A was then obtained by fitting the product $A\,P(q)$ to the measured SAXS intensity in the region $3 < qR < 5$.

The intermediate-q window was chosen deliberately. At low q (the Guinier regime), the structure factor deviates from unity due to interparticle interactions, and including this region would distort the fit. At very high q (deep in the Porod regime), the scattering intensity becomes

weak and noisy, making the fit unreliable. The region between these two limits provides sufficiently strong signal while remaining minimally affected by structure-factor contributions, allowing an accurate determination of the scaling factor.

Figure 4.2.2. illustrates this fitting procedure. In Figure 4.2.2A, the SAXS patterns of 14 mg mL^{-1} and 1 mg mL^{-1} dispersions of 7.2 nm PbS-$Sn_2S_6^{4-}$ NCs in NMF are shown. The dilute 1 mg mL^{-1} pattern is treated as the form factor. The orange-highlighted region marks the q-range used to determine the scaling factor. Figure 4.2.2B shows the measured SAXS intensity overlaid with the fitted product $A\,P(q)$, demonstrating the quality of the fit prior to extracting the structure factor.

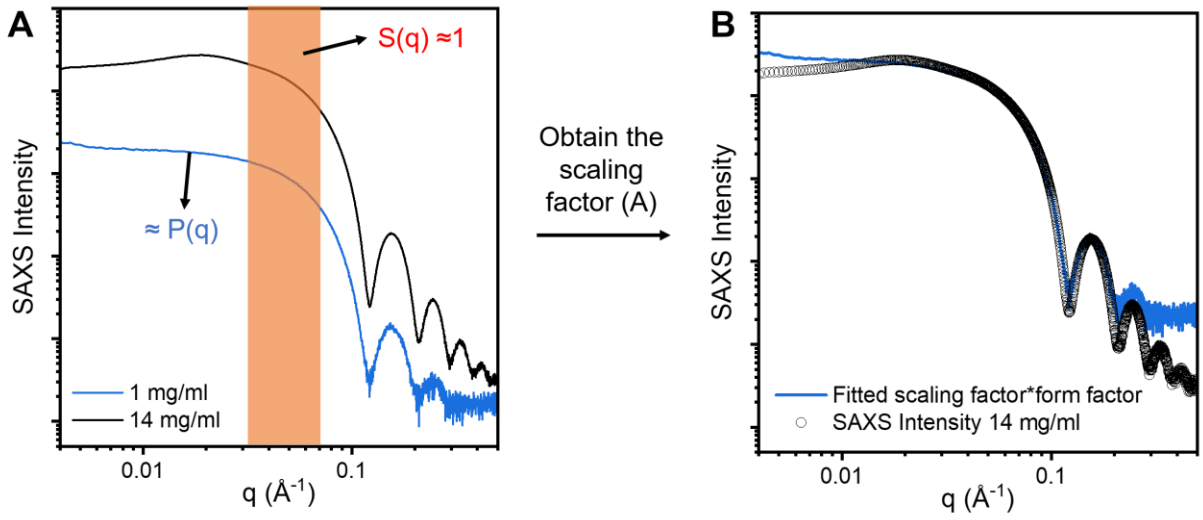

Figure 4.2.2: Extraction of scaling factor and form factor.
(A) SAXS intensity of 14 mg/ml (black) and 1 mg/ml (blue) 7.2 nm PbS-$Sn_2S_6^{4-}$ NCs in NMF. The form factor of the NC is assumed to be identical to the SAXS pattern of 1 mg/ml NC solution. Scaling factor was obtained by fitting the region highlighted in orange. **(B)** Plot of SAXS intensity (black circles) and the product of scaling factor and form factor ($A\,P(q)$).

Once the scaling factor and form factor were determined, the structure factor for each concentration was obtained by dividing the measured SAXS intensity by the product $AP(q)$. Figure 4.2.3 shows the resulting concentration-dependent structure factors for 7.2 nm PbS-$Sn_2S_6^{4-}$ NCs in NMF. Data from the most dilute samples (1–4 mg mL^{-1}) were excluded because the structure-factor features were too weak to distinguish from noise.

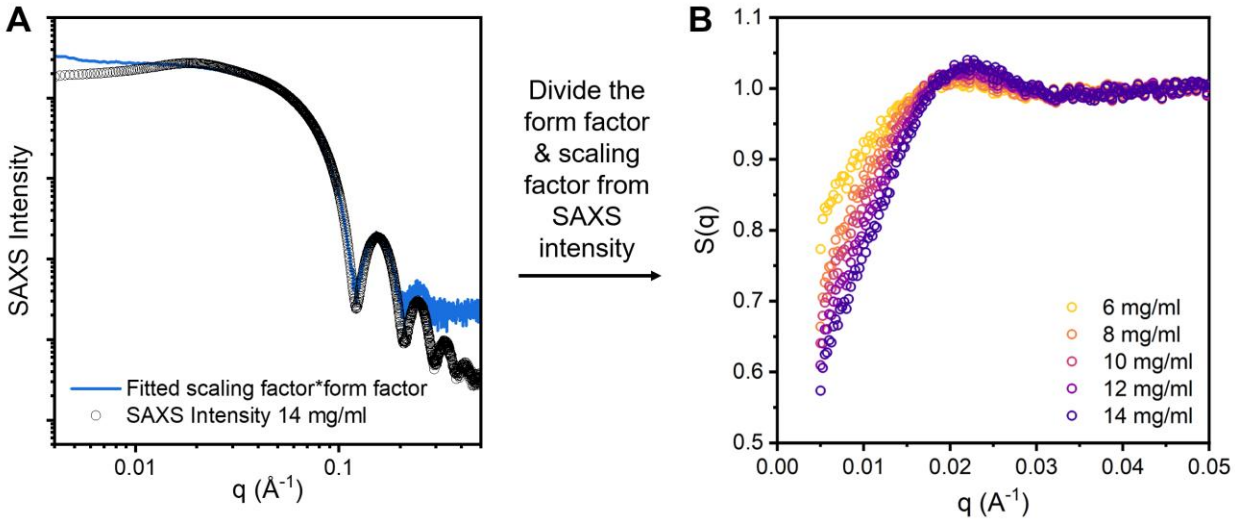

Figure 4.2.3: Extraction of structure factor.
(A) Plot of SAXS intensity (black circles) and the product of fitted scaling factor and form factor ($A\,P(q)$). **(B)** Concentration-dependent structure factor of 7.2 nm PbS-$Sn_2S_6^{4-}$ NCs in NMF.

It is important to note that we did not use the analytical form factor for spherical particles in this analysis. Although we attempted to construct an analytical form factor by fitting the SAXS pattern of a 10 mg/mL dispersion using the Irena package in Igor Pro 9 to obtain the number-weighted size distribution, and then summing the individual form factors accordingly, this approach produced unphysical results. Specifically, structure factors derived from the analytical form factor did not level off to unity at high q, which is inconsistent with physical expectations. This deviation propagated into later steps of the analysis, yielding non-zero intercepts in plots of $1/S(0) - 1$ versus number density, which is an unphysical outcome for

dilute systems. These discrepancies likely arise from anisotropy of the NC shape and other experimental uncertainties that are not fully captured by idealized analytical form-factor expressions.

Figure 4.2.4 illustrates this issue by comparing the measured SAXS intensity (black circles) with the fitted product $AP(q)$ obtained using the analytical form factor, along with the resulting structure factor. The extracted structure factors clearly fail to approach unity at high q, confirming that the analytical form factor is unsuitable for this system and validating our choice to use the experimentally measured dilute-solution form factor instead.

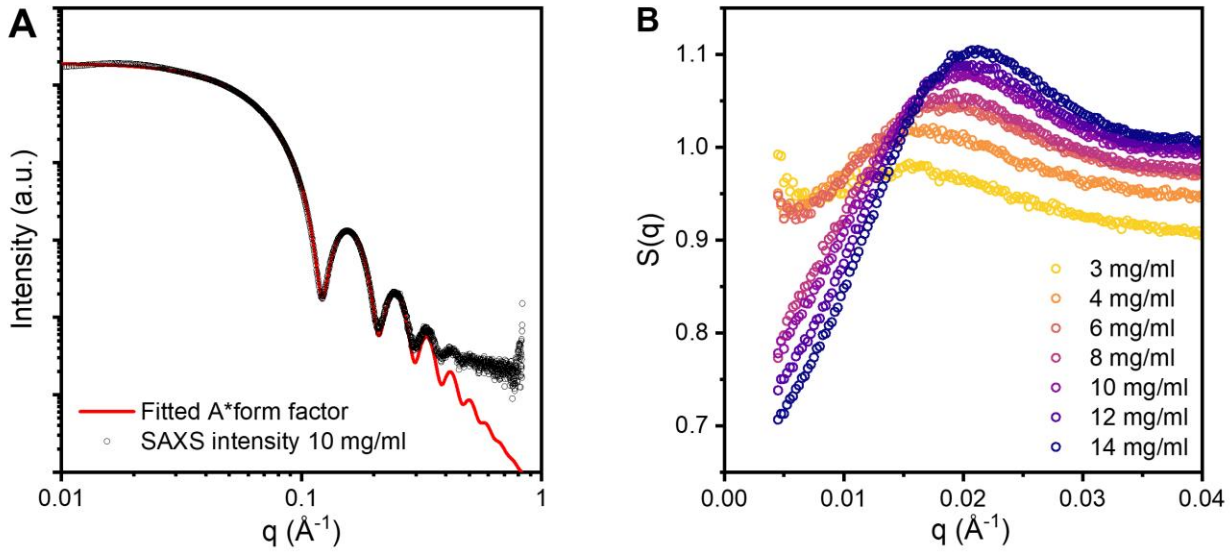

Figure 4.2.4: Unphysical structure factor extracted from analytical form factor.
(A) Plot of SAXS intensity (black circles) and the product of fitted scaling factor and form factor ($A\ P(q)$), where form factor was obtained using analytical equation. **(B)** Concentration-dependent structure factor of 7.2 nm PbS-$Sn_2S_6^{4-}$ NCs in NMF. The obtained structure factors are unphysical.

Extrapolation of S(0)

To extract $S(0)$ from the measured structure factors, we must adopt a model describing the interparticle interactions. In our system, the nanocrystals interact through a DLVO-type potential consisting of a short-range hard-sphere repulsion and a longer-range electrostatic term. The analytical expression for $S(q)$ under the DLVO potential is known but spans several pages and is not practical to apply directly. In the limit of small scattering vectors, this expression reduces to:[12]

$$\lim_{q\to 0} S(q) = -\frac{1}{A}$$

where A is another lengthy expression derived from the DLVO framework. When the surface charge is small, the DLVO solution approaches the hard-sphere model, meaning that the structure factor of charged particles converges toward that of hard spheres as the surface potential decreases. Thus, the hard-sphere model provides a reasonable and greatly simplified approximation for extrapolating $S(0)$ in our system.

Under the hard-sphere approximation, the low-q behavior of the structure factor can be expressed as:[13]

$$S(q) = S(0)\exp(aq^2)$$

where a is an empirical constant. This functional form has been successfully applied to systems analogous to hard spheres, including monoatomic liquids and polymer colloids. Because our nanocrystals are well described by a DLVO potential whose structure factor reduces to the hard-sphere form at low q, we use this relationship to extrapolate $S(0)$.

Practically, $S(0)$was obtained by plotting $\ln[S(q)]$versus $q^2$and fitting the linear region according to:

$$\ln[S(q)] = aq^2 + \ln[S(0)]$$

The ultra-low-q region ($qR < 0.50$) was excluded from the fit because it frequently exhibited anomalous upturns or downturns (Figure 4.2.7). These deviations arise from background scattering originating from the glass capillary, the solvent, or incomplete beam-stop coverage. Background contributions are strongest at very low q, and even small variations in beam intensity or capillary alignment can produce noticeable distortions. As $q$increases, the background intensity rapidly diminishes and becomes negligible. The high-q region ($qR > 0.75$) was also excluded due to the onset of non-linear behavior in the structure factor. Representative linear fits used to extract $S(0)$are shown in Figure 4.2.5.

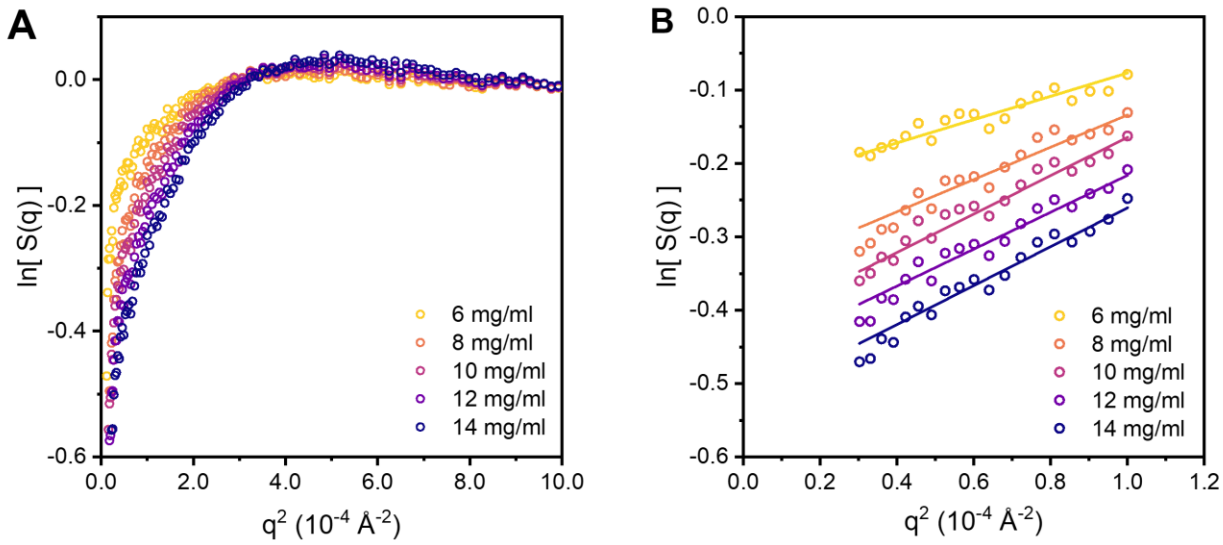

Figure 4.2.5: Extrapolation of S(0).

(A) A representative plot of $\ln[S(q)]$ against q^2. This plot was obtained from the experimentally determined structure factor of 7.2 nm PbS-$Sn_2S_6^{4-}$ NCs in NMF. **(B)** The linear fit of this plot. The solid line represents the fit, and the circles represent the experimental results that are within the fitting range.

Linear fit of $1/S(0) - 1$ *against number density to obtain* B_2 *coefficient*

Figure 4.2.6A shows the structure factor ($S(q)$) of 7.2 nm PbS NCs with $Sn_2S_6^{4-}$ ligands in NMF. The dashed lines are fits of $S(q)$ to $S(q) = A\exp(kq^2)$ in the low-q region using the method described above. The circles are experimentally determined $S(q)$ values.

After extracting the $S(0)$ for each concentration, $1/S(0) - 1$ was plotted against the number density. Figure 4.2.6B the plot of $1/S(0) - 1$ against the number density from 7.2 nm PbS-$Sn_2S_6^{4-}$ NCs in NMF, and the plots for all other NCs are shown in Figure 4.2.7. Finally, the B_2 coefficient was obtained by halving the slope of the plot of $1/S(0) - 1$ against the number density. The slope was obtained by fitting the plot of $1/S(0) - 1$ against the number density with a straight line through the origin.

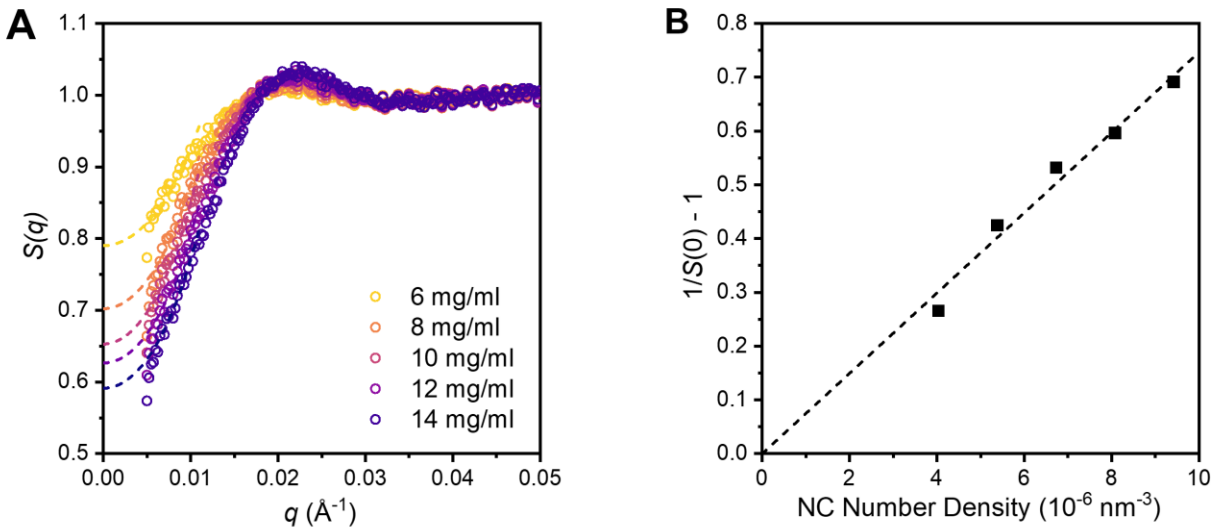

Figure 4.2.6: Extraction of B_2 coefficient.

(A) Structure factor ($S(q)$) of 7.2 nm PbS NCs with $Sn_2S_6^{4-}$ ligands in NMF. The dashed lines are fits of $S(q)$ to $S(q) = A\exp(kq^2)$ in the low-q region. The circles are experimentally determined $S(q)$ values. **(B)** The corresponding plot of $1/S(0) - 1$ against the number density of PbS NCs.

Extraction of B_2 coefficients for all other NCs

The structure factor and the plots of $1/S(0) - 1$ against number density for all other NCs are shown in Figure 4.2.7.

Figure 4.2.7:

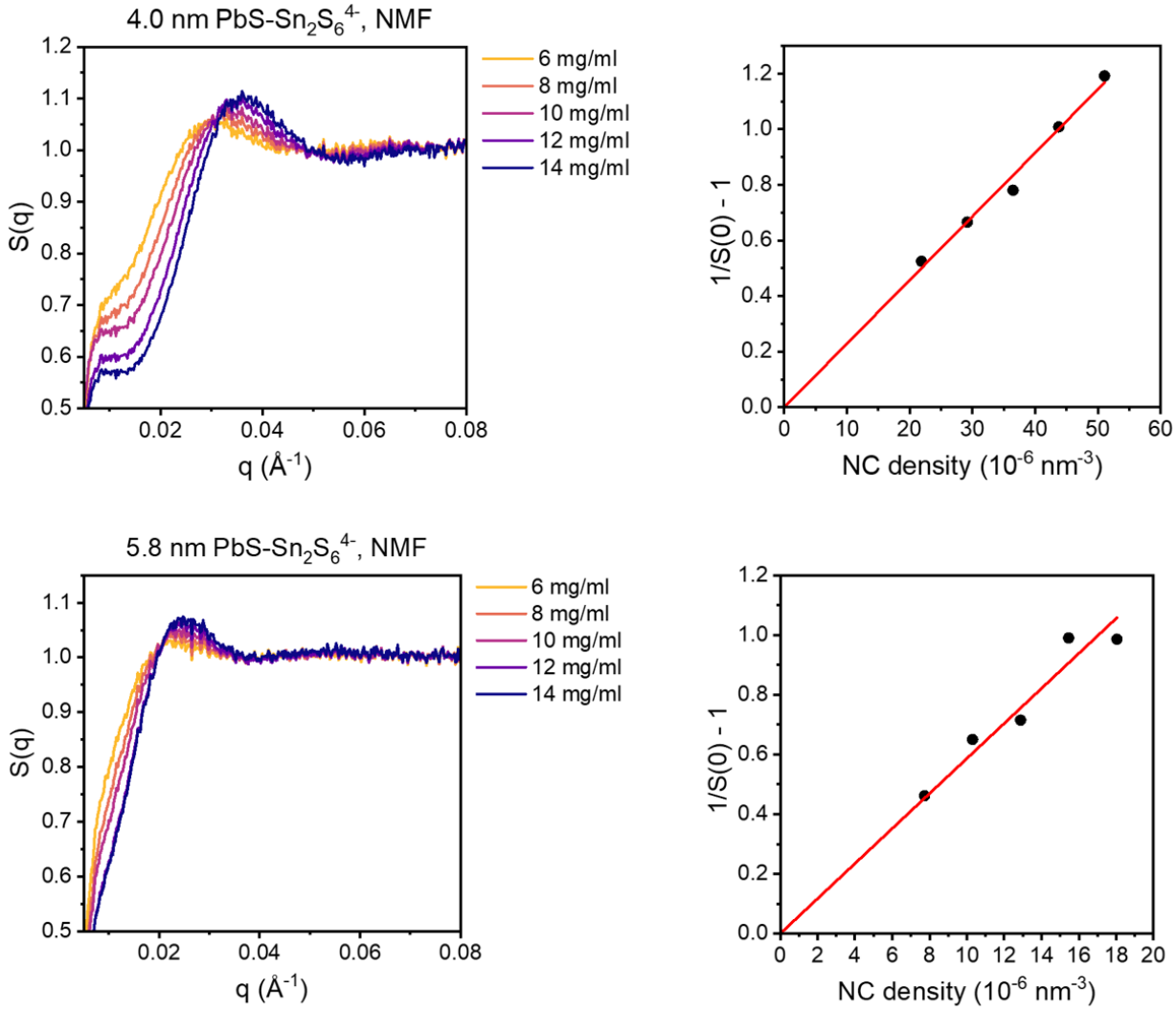

Figure 4.2.7 continued:

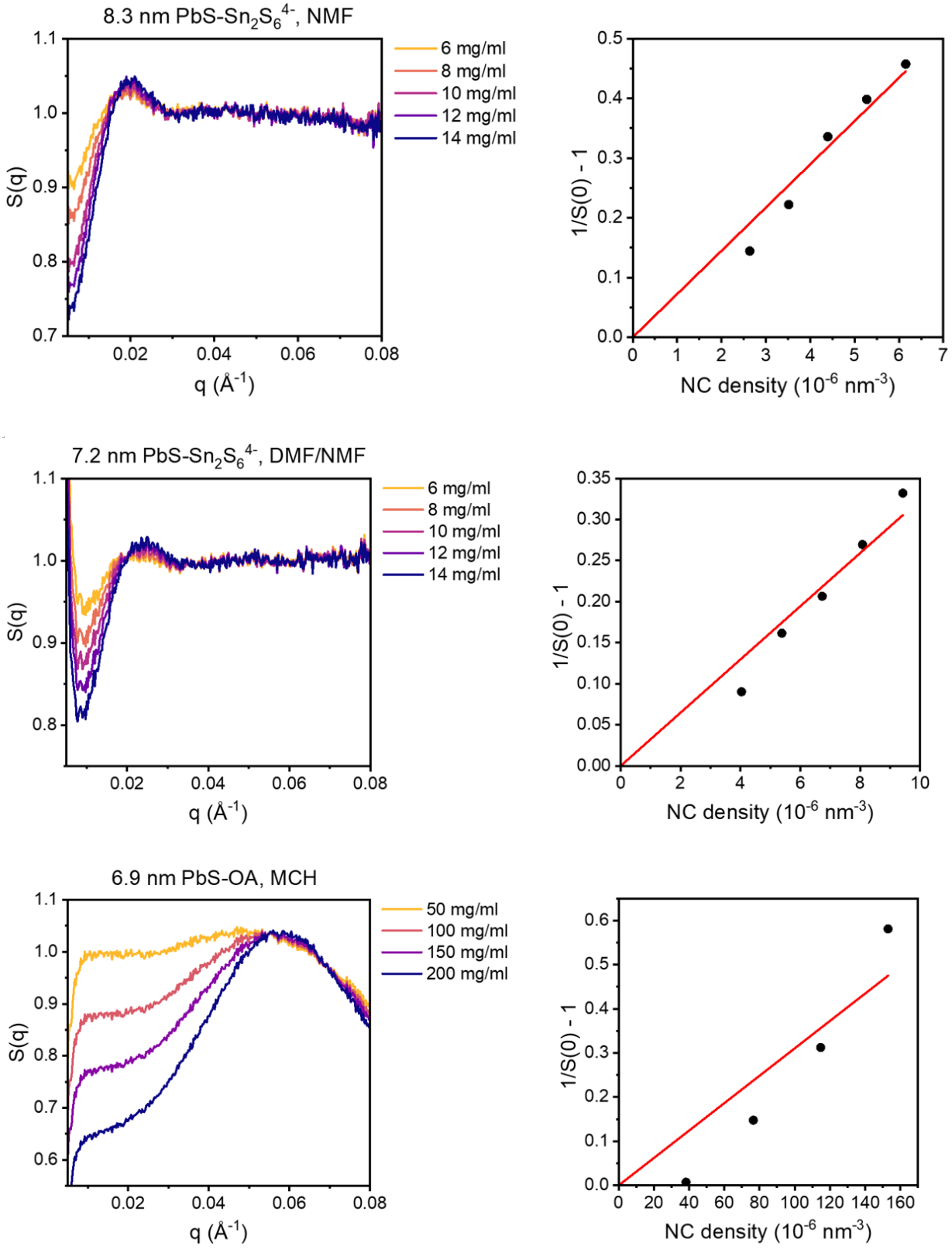

Figure 4.2.7 continued:

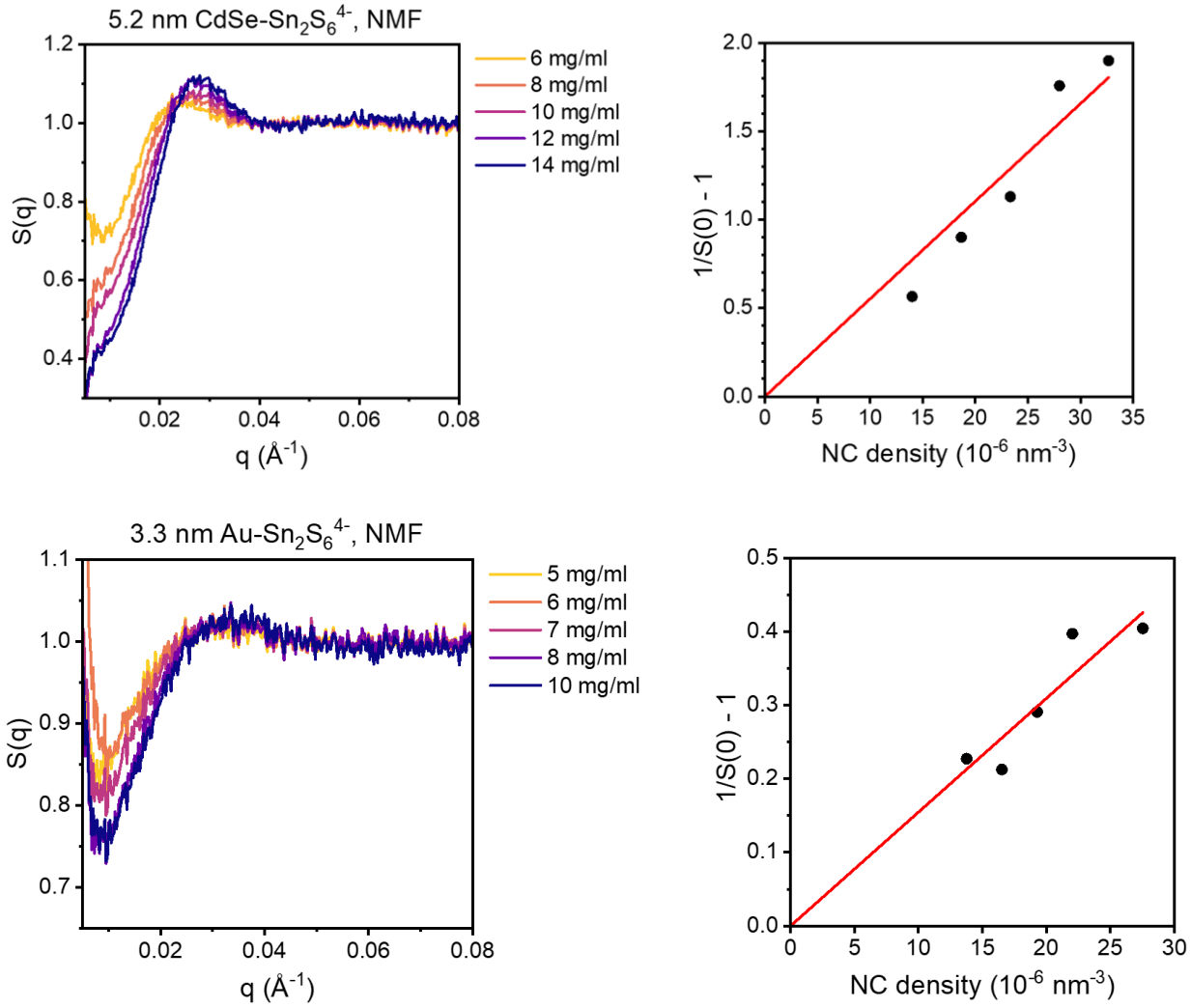

Figure 4.2.7: Structure factor and B_2 coefficients of all NCs.

Plots of the structure factors (left) and the values of $1/S(0) - 1$ against the number density of NCs (right).

Calculation of normalized B_2 coefficients

Normalized second virial coefficients were calculated using $b_2 = B_2/B_{2,\mathrm{HS}}$, where the hard-sphere reference value is given by:[8]

$$B_{2,HS} = \frac{2\pi}{3}(d + 2\delta)^3$$

In this expression, d is the diameter of the core-only quantum dot and $\delta$is the ligand length. The core diameters were obtained experimentally by fitting the SAXS intensity of the corresponding PbS-OA nanocrystals to extract the number-weighted size distribution, following the procedure described in Chapter 2. The resulting distributions were fit to a normal distribution, and the mean value was taken as the core diameter.

Ligand lengths were estimated by subtracting the core diameter from the nearest-neighbor distance in the superlattice. As established in Chapter 2, 7.2 nm PbS-OA nanocrystals form an FCC superlattice with a lattice constant of 13.2 nm, while 7.2 nm PbS-$Sn_2S_6^{4-}$ NCs also adopt an FCC structure but with a smaller lattice constant of 11.0 nm. Because the nearest-neighbor distance in an FCC lattice is $a\sqrt{3}/2$, where a is the lattice constant, and the core diameter is 7.2 nm, we estimate ligand lengths of approximately 1.1 nm for oleate and 0.29 nm for $Sn_2S_6^{4-}$. These values are consistent with previously reported measurements.

4.3. Influence of nanocrystal size, surface chemistry, and composition on B_2 coefficients

List of values of B_2 and b_2 coefficients

The list of experimentally extracted B_2 and b_2 coefficients of colloidal nanocrystals (NCs) are presented in Table 4.1.

Table 4.1: List of experimentally determined B_2 coefficients.

Sample	Exp. B_2 coefficient (10^7 Å^3)	Exp. b_2 coefficient
6.9 nm PbS-OA, MCH	0.155	0.76
4.0 nm PbS-$Sn_2S_6^{4-}$, NMF	1.02	50.8
5.8 nm PbS-$Sn_2S_6^{4-}$, NMF	2.93	53.9
7.2 nm PbS-$Sn_2S_6^{4-}$, NMF	3.73	37.8
8.3 nm PbS-$Sn_2S_6^{4-}$, NMF	3.62	24.7
7.2 nm PbS-$Sn_2S_6^{4-}$, NMF/DMF	1.62	16.4
5.2 nm CdSe-$Sn_2S_6^{4-}$, NMF	2.76	68.2
3.3 nm Au-$Sn_2S_6^{4}$, NMF	0.773	63.2

Effect of surface chemistry and solvent on B_2 coefficients

Figure 4.3.1 presents the B_2 and b_2 coefficients of ~7 nm PbS-OA and PbS-$Sn_2S_6^{4-}$ NCs. Notably, all NCs exhibit positive b_2 coefficients, indicating the presence of repulsive interactions among the particles. The 7.2 nm PbS NCs that are electrostatically stabilized by $Sn_2S_6^{4-}$ ligands ($b_2 > 16$) demonstrate significantly larger b_2 coefficients compared to the sterically stabilized 6.9 nm PbS-OA NCs ($b_2 = 0.76$) in methylcyclohexane (MCH). This observation is consistent with

the finding that the electrostatically stabilized NCs deviate far more from the ideal gas behavior compared to sterically stabilized NCs due to their long-range interactions.

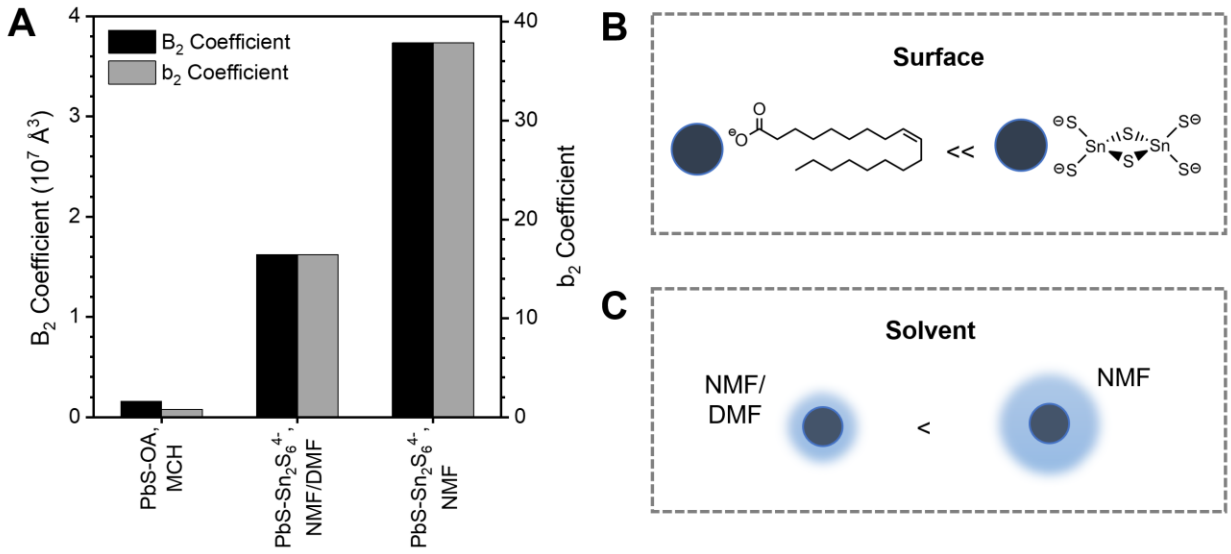

Figure 4.3.1: Surface- and solvent-dependent B_2 coefficients.

(A) The B_2 and b_2 coefficients of ~7 nm PbS NCs with different surface chemistries and solvent conditions. The diameters of PbS-OA and PbS-$Sn_2S_6^{4-}$ NCs are 6.9 nm and 7.2 nm, respectively. NMF/DMF indicates a mixture of NMF and DMF in a 7:3 volume ratio. **(B)** Illustration showing that $Sn_2S_6^{4-}$-capped NCs exhibit stronger repulsive forces than OA-capped NCs. **(C)** Illustration showing that $Sn_2S_6^{4-}$-capped NCs are more repulsive in polar solvent than less polar solvent.

The b_2 coefficients of PbS-$Sn_2S_6^{4-}$ NCs were measured in NMF and a mixture of NMF and *N,N*-dimethylformamide (DMF) in a 7:3 volume ratio (Figure 4.3.1). The b_2 coefficient of 7.2 nm PbS-$Sn_2S_6^{4-}$ NCs in the NMF/DMF mixture ($b_2 = 16.4$) is significantly lower than that in NMF ($b_2 = 37.8$). This is because the dielectric constant of NMF (ε_{NMF}~170) is much larger than that of the NMF/DMF mixture ($\varepsilon_{NMF/DMF}$~130),[54, 55] resulting in stronger ion-dipole interactions between the surface ligands of the PbS-$Sn_2S_6^{4-}$ NCs and the solvent molecules. These interactions contribute to the enhanced colloidal stability of the NCs in solvents with high dielectric constant.

Effect of composition on B_2 coefficients

Figure 4.3.2 compares thiostannate-capped nanocrystals of similar size but different compositions. The large normalized b_2 coefficients measured for 5.2 nm CdSe-$Sn_2S_6^{4-}$ NCs ($b_2 = 68.2$) and 3.3 nm Au-$Sn_2S_6^{4-}$ NCs ($b_2 = 63.2$) demonstrate that thiostannate-capped, electrostatically stabilized NCs exhibit strong interparticle repulsion largely independent of the underlying NC material. Notably, the different compositions do not lead to substantial differences in the measured B_2values. In principle, composition could influence interparticle interactions in two ways: (i) by altering the surface chemistry, where the ligand coverage and therefore surface charge is changed, or (ii) by modifying the van der Waals attraction, since more polarizable materials exhibit stronger dispersion forces. The experimental results suggest that both effects are minor. Variations in surface charge appear to be largely screened by the electrostatic double layer, whose thickness saturates once the surface potential exceeds a modest threshold. Likewise, differences in van der Waals attraction do not significantly affect the overall interparticle potential, likely because these forces are weak at the separations relevant to stable colloids. As long as the nanocrystals remain dispersed and do not aggregate, the long-range electrostatic repulsion dominates, effectively masking any composition-dependent differences in van der Waals interactions.

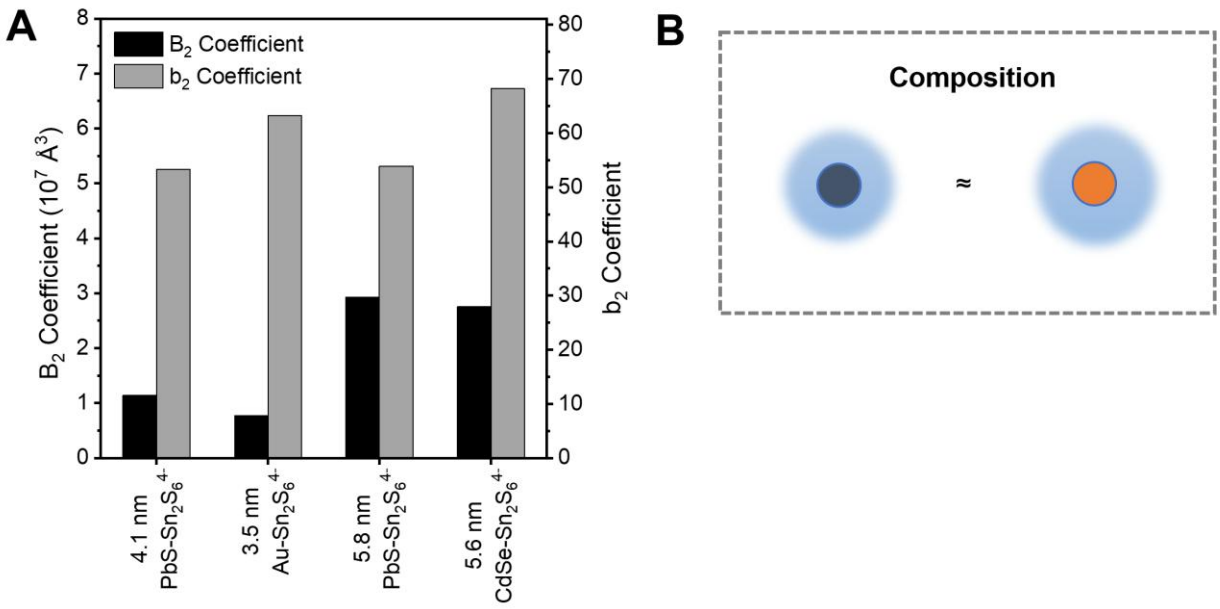

Figure 4.3.2: Composition-dependent B_2 coefficients.

(A) The B_2 and b_2 coefficients of $Sn_2S_6^{4-}$-capped PbS, Au and CdSe NCs. **(B)** Illustration showing that the composition has little impact on the repulsive forces of $Sn_2S_6^{4-}$-capped NCs.

In Figure 4.3.3, we present the B_2 and b_2 coefficients of four different PbS-$Sn_2S_6^{4-}$ NCs in NMF, ranging in size from 4.0 nm to 8.3 nm. Notably, the B_2 coefficient generally increases with NC diameter. This can be attributed to increased surface area of the NCs that exhibit repulsive forces, as well as increased volume of space that each NC occupies. Conversely, the b_2 coefficient shows generally decreases with the increasing NC diameter. In general, independence of b_2 and NC diameter suggests that interparticle interaction range scales with the NC size, implying a Debye length that scales linearly with NC radius (R). A decreasing b_2 trend, though, indicates that the Debye length either grows more slowly than linearly in the NC diameter, remains independent of NC diameter, or even decreases with increasing NC diameter. If no additional electrolyte is added and ligand grafting density is independent of NC size,[14] the Debye length, κ^{-1}, defined by the concentration of counter ions required for charge neutrality, should

scale as $\kappa^{-1} \propto \sqrt{R}$. If the ionic concentration in solution is set by added electrolyte, κ^{-1} should be independent of NC diameter. Both these limiting cases result in decreasing b_2 with increasing NC size, in agreement with the experimental data.

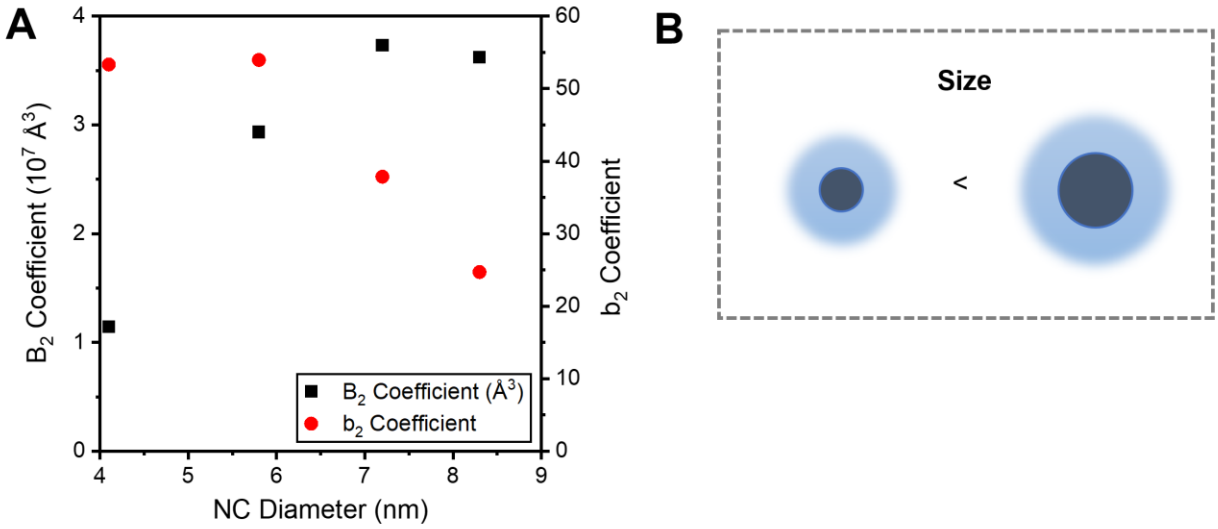

Figure 4.3.3: Size-dependent B_2 coefficients.

(A) B_2 and b_2 coefficients of PbS-$Sn_2S_6^{4-}$ NCs in NMF with NC diameters ranging from 4.0 nm to 8.3 nm. **(B)** Illustration showing larger NCs tend to have stronger repulsive forces.

4.4. Calculation of B_2 coefficients from DLVO theory

The DLVO potentials of the nanocrystals (NCs) were calculated to gain qualitative insights into how the interparticle potential is affected by factors such as NC size, composition, surface chemistry and solvent conditions.

DLVO theory

The NC-NC interaction of electrostatically stabilized NCs can be modelled using Derjaguin-Landau-Verwey-Overbeek (DLVO) theory. A DLVO potential (U_{DLVO}) consists of a repulsive screened double layer (Yukawa) potential (U_{ES}), an attractive Van der Waals potential (U_{VdW}) and a repulsive steric potential (U_{steric}).[15]

$$U_{DLVO} = U_{ES} + U_{VdW} + U_{steric}$$

The electrostatic potential can be expressed as the following, where k_B is the Boltzmann constant, T is the temperature, κ^{-1} is the Debye length, R is the radius of the particle, ρ_∞ is the bulk number density of 1:1 electrolyte and r is the surface-to-surface distance between the particles:[15]

$$U_{ES}(r) = \frac{32\pi k_B T g^2 \rho_\infty R}{\kappa^2} \cdot e^{-\kappa r}$$

The g in the above equation is described by:

$$g = \tanh\left(\frac{ze\varphi}{4k_B T}\right)$$

where z is the valency of the added salt, e is electron charge and φ is the surface potential of the particle. The value g approaches 1 for large surface potential, so it is assumed to be 1 throughout the calculations.

The Debye length (κ^{-1}) can be approximated with the following equation:

$$\kappa^{-1} = \sqrt{\frac{\varepsilon_0 \varepsilon_{\text{sol}} k_B T}{2e^2 I_{\text{sol}}}}$$

where ε_0 is the vacuum permittivity, ε_{sol} is the relative dielectric constant of the solvent and I_{sol} is the ionic strength of the solvent. The ionic strength is defined as the following, where z_j is the charge of an ion in the solution, and ρ_j is the number density of the corresponding ion.

$$I_{\text{sol}} = \frac{1}{2}\sum_{j=1}^{N} \rho_j z_j^2$$

The Van der Waals potential of two spherical particles can be described by:

$$U_{VdW} = -\frac{A}{6}\left(\frac{2R^2}{r^2+4rR} + \frac{2R^2}{r^2+4rR+4R^2} + \ln\left(\frac{r^2+4rR^2}{r^2+4rR+4R^2}\right)\right)$$

where A is the Hamaker constant, R is the radius of the particle, r is the surface-to-surface distance between the particles.[15]

In addition to the Van der Waals and electrostatic component, steric potential was added ($U_{steric}(r)$) to take the account of hard-sphere interactions. An arbitrary function shown below was used to model the interactions, where σ is the length of the ligand.

$$U_{steric}(r) = \begin{cases} \left(\ln\left(-\frac{r}{2\sigma}\right)\right)^2, & r < 2\sigma \\ 0, & r \geq 2\sigma \end{cases}$$

Parameters for calculation

The parameters required for calculating the interaction potentials, including the Hamaker constants of PbS, CdSe, and Au nanocrystals and the dielectric constants of the relevant solvents, were obtained from previously reported literature values. The following constants were used in all calculations:

- Hamaker constant of PbS: $A = 0.311$ eV
- Hamaker constant of CdSe: $A = 0.219$ eV
- Hamaker constant of Au: $A = 1.56$ eV
- Dielectric constant of NMF: $\varepsilon_{\text{sol}} = 173$
- Dielectric constant of 70% NMF, 30% DMF mixture: $\varepsilon_{\text{sol}} = 131$

All calculations were performed at $T = 298$ K. Unless otherwise specified, the nanocrystal diameter was fixed at 7.2 nm to enable direct comparison across different systems.

To estimate the ionic strength, we assumed the presence of 1 mM unbound ligand in solution. For example, dispersions of PbS-$Sn_2S_6^{4-}$ NCs were treated as containing 1 mM $K_4Sn_2S_6$ in ~10 mg/mL PbS NC dispersions. This estimate originates from the ICP-OES measurement of PbS-$Sn_2S_6^{4-}$ NC solution before and after the removal of excess unbound ligands by dialysis cycle. The experimental detail on the determination of the unbound ligand concentration can be found in the first section of the referenced paper.[14] Additional assumptions were required to determine the bulk ion number density (ρ_∞), because DLVO theory is formally defined for simple z:z electrolytes (e.g., NaCl, $CuSO_4$). To apply the model, we approximated the nanocrystal dispersion as a solution of a symmetric electrolyte with ionic strength equivalent to that produced by 0.5 mM unbound ligand. Under this assumption, a 1 mM $K_4Sn_2S_6$ solution corresponds to a bulk ion number density of $\rho_\infty = 0.0006023$ nm^{-3}.

Calculation of B_2 coefficients

The B_2 coefficient can be calculated from the following equation, where $u(r)$ is the interparticle potential. The interparticle potential is modelled using the DLVO potential (U_{DLVO}).[8]

$$B_2 = -2\pi \int_\sigma^\infty \left(\exp\left(-\frac{u(r)}{k_B T} \right) - 1 \right) r^2 \, \mathrm{d}r$$

The normalized b_2 coefficient can be calculated as:

$$b_2 = B_2 / B_{2,HS}$$

where:

$$B_{2,HS} = \frac{2\pi}{3}(d + 2\delta)^3$$

In this equation, d is the diameter of the core-only NC and δ is the length of the ligand. σ is an arbitrary value that is close to 0. For our integral, we set it as $\sigma = 0.001$ nm, which is a sufficiently small value for a reasonable estimation of the B_2 coefficient yet large enough to ensure the convergence of the integral. Below is the list of B_2 coefficients that were obtained experimentally and from the DLVO potentials.

List of B_2 coefficients from DLVO theory

The results of the calculations are listed in Table 4.2.

Table 4.2: List of theoretically calculated B_2 coefficients.

Sample	DLVO B_2 coefficient (10^7 Å^3)	DLVO b_2 coefficient
6.9 nm PbS-OA, MCH	N/A	N/A
4.0 nm PbS-$Sn_2S_6^{4-}$, NMF	0.45	15.69
5.8 nm PbS-$Sn_2S_6^{4-}$, NMF	0.61	8.56
7.2 nm PbS-$Sn_2S_6^{4-}$, NMF	0.71	5.83
8.3 nm PbS-$Sn_2S_6^{4-}$, NMF	0.79	4.47
7.2 nm PbS-$Sn_2S_6^{4-}$, NMF/DMF	0.38	3.10
5.2 nm CdSe-$Sn_2S_6^{4}$, NMF	0.56	10.3
3.3 nm Au-$Sn_2S_6^{4}$, NMF	0.38	20.7

4.5. Comparison of experimentally and theoretically determined B_2 coefficients

The DLVO interaction potentials calculated for PbS-$Sn_2S_6^{4-}$ NCs in two solvent systems (pure NMF and a mixed NMF/DMF solvent) show that higher-dielectric-constant solvents produce stronger electrostatic repulsion. In the DLVO framework, repulsive forces originate from the osmotic pressure of counterions surrounding the charged NC surface. In low-dielectric solvents, counterions are poorly solvated and remain tightly bound to the NC surface, forming a compact ionic layer. In contrast, high-dielectric solvents better disperse counterions, producing a more diffuse ("fluffier") ionic atmosphere that extends the range of NC–NC interactions and increases the overall repulsive potential. This trend is fully consistent with the experimental SAXS results presented in Figure 4.5.1, where increased solvent polarity correlates with larger B_2 values.

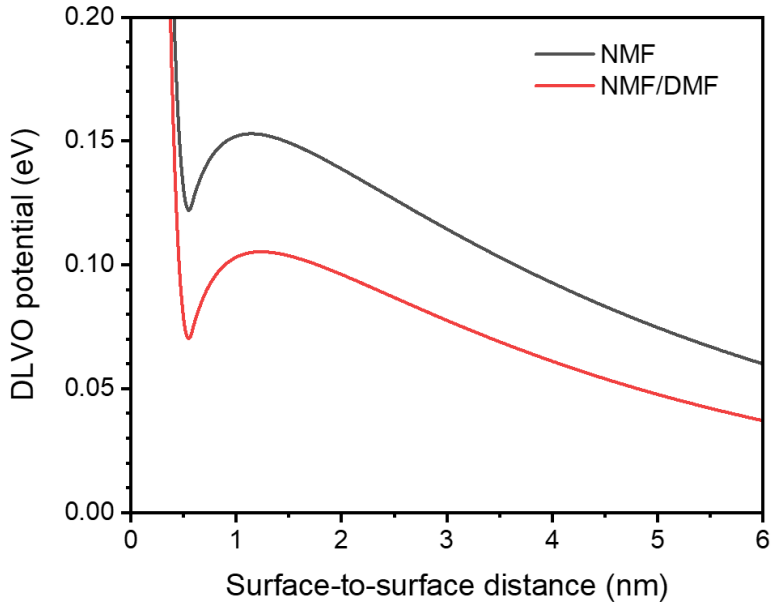

Figure 4.5.1: Solvent-dependent DLVO potential.

DLVO potentials for 7.2 nm PbS-$Sn_2S_6^{4-}$ NCs in NMF ($\varepsilon_{sol} = 173$) and a 70% NMF, 30% DMF mixture ($\varepsilon_{sol} = 131$). All solutions are assumed to contain 1 mM of $K_4Sn_2S_6$.

Figure 4.5.2 compares the DLVO potentials of 7.2 nm PbS-$Sn_2S_6^{4-}$ and 7.2 nm CdSe-$Sn_2S_6^{4-}$ NCs dispersed in NMF. Although CdSe has a lower Hamaker constant than PbS, the resulting reduction in attractive forces leads to only a minimal change in the overall repulsive potential. This is because van der Waals forces, while strong, operate only at short range and become relevant primarily during aggregation. At the longer NC–NC distances characteristic of stable colloidal dispersions, electrostatic repulsion dominates. This agrees with our experimental observation that nanocrystal composition has little influence on the measured B_2coefficients for thiostannate-capped systems.

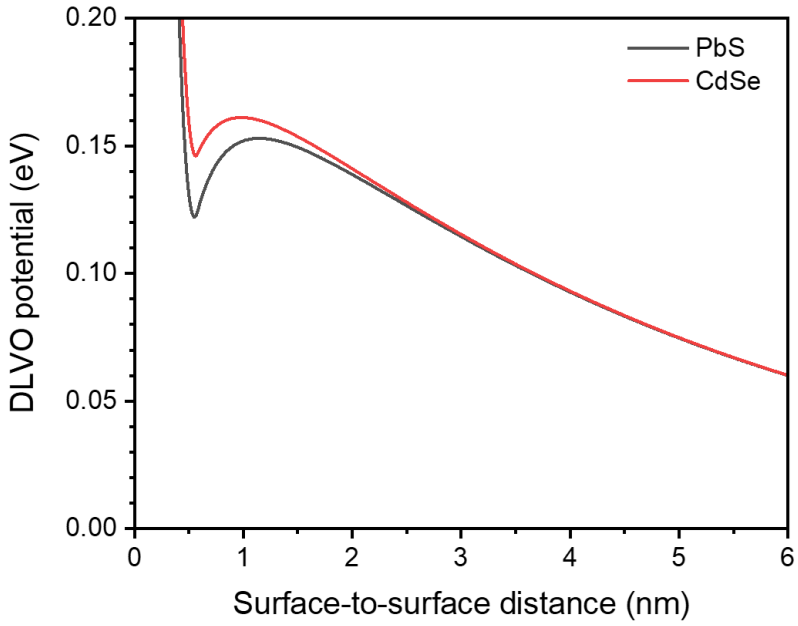

Figure 4.5.2: Composition-dependent DLVO potential.
DLVO potentials for 7.2 nm PbS-$Sn_2S_6^{4-}$ NCs ($A = 0.311$ eV) and 7.2 nm CdSe-$Sn_2S_6^{4-}$ NCs ($A = 0.219$ eV) in NMF. All solutions are assumed to contain 1 mM of $K_4Sn_2S_6$.

The calculated DLVO potentials for PbS-$Sn_2S_6^{4-}$ NCs with diameters between 4.0 and 8.3 nm show that repulsive interactions strengthen with increasing particle size. Larger NCs experience (i) greater hard-sphere steric repulsion due to their increased physical volume, and (ii) higher total surface charge arising from their larger surface area. This size-dependent trend mirrors the experimental results in Figure 4.5.3, where larger nanocrystals exhibit higher B_2values.

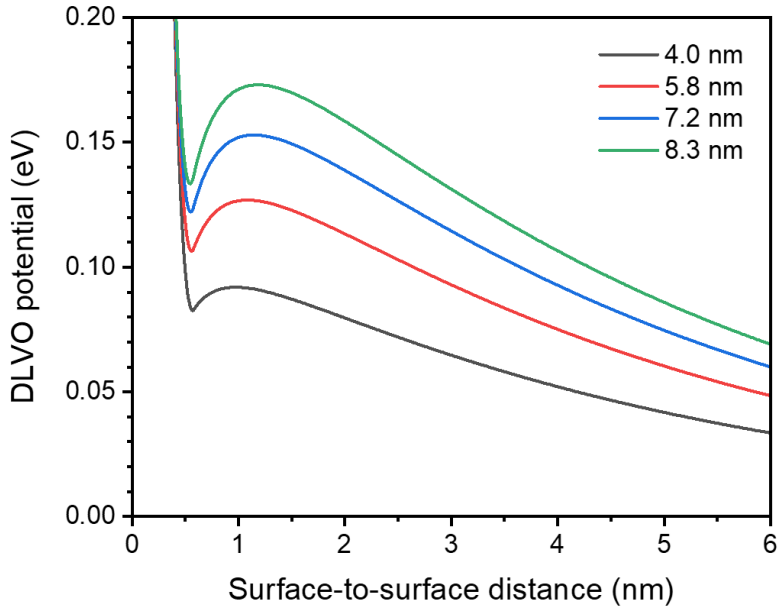

Figure 4.5.3: Size-dependent DLVO potential.
DLVO potential of PbS-$Sn_2S_6^{4-}$ NCs in NMF with the diameter ($2R$) of 4.0 nm, 5.8 nm, 7.2 nm and 8.3 nm. All solutions are assumed to contain 1 mM of $K_4Sn_2S_6$.

Overall, the experimentally observed size- and solvent-dependent variations in $B_2$are broadly consistent with DLVO theory, indicating that DLVO provides a useful framework for modeling electrostatically stabilized nanocrystals. However, the theory systematically underestimates the magnitude of the repulsion, leading to B_2values smaller than those measured experimentally (Table 4.2). This discrepancy likely arises from two key assumptions in DLVO

theory that do not hold for our system. First, DLVO theory is most accurate for dilute 1:1 electrolytes, whereas our nanocrystals are dispersed in solutions containing concentrated, multivalent ligands that introduce ion–ion correlations not captured by the classical model. Second, DLVO theory relies on the Derjaguin approximation, which treats curved surfaces as locally flat. While this approximation is reasonable for micron-scale colloids, it becomes inaccurate for nanocrystals whose radii of curvature are comparable to the interaction range.

These limitations are consistent with recent findings by Coropceanu and co-workers, who showed that electrostatically stabilized nanocrystals can undergo flocculation and even self-assembly in highly concentrated multivalent electrolytes, which is behavior that cannot be explained by DLVO theory alone. Their work highlights the need for more advanced models that incorporate ion-correlation effects and nanoscale curvature to accurately describe interparticle interactions in charged nanocrystal systems.

4.6. Chapter 4 Bibliography

(1) Saunders, A. E.; Korgel, B. A. Second Virial Coefficient Measurements of Dilute Gold Nanocrystal Dispersions Using Small-Angle X-Ray Scattering. *J. Phys. Chem. B* **2004**, *108* (43), 16732–16738. https://doi.org/10.1021/jp047153j.

(2) Monego, D.; Kister, T.; Kirkwood, N.; Mulvaney, P.; Widmer-Cooper, A.; Kraus, T. Colloidal Stability of Apolar Nanoparticles: Role of Ligand Length. *Langmuir* **2018**, *34* (43), 12982–12989. https://doi.org/10.1021/acs.langmuir.8b02883.

(3) Doblas, D.; Kister, T.; Cano-Bonilla, M.; González-García, L.; Kraus, T. Colloidal Solubility and Agglomeration of Apolar Nanoparticles in Different Solvents. *Nano Lett.* **2019**, *19* (8), 5246–5252. https://doi.org/10.1021/acs.nanolett.9b01688.

(4) Kister, T.; Monego, D.; Mulvaney, P.; Widmer-Cooper, A.; Kraus, T. Colloidal Stability of Apolar Nanoparticles: The Role of Particle Size and Ligand Shell Structure. *ACS Nano* **2018**, *12* (6), 5969–5977. https://doi.org/10.1021/acsnano.8b02202.

(5) Van Rijssel, J.; Peters, V. F. D.; Meeldijk, J. D.; Kortschot, R. J.; Van Dijk-Moes, R. J. A.; Petukhov, A. V.; Erné, B. H.; Philipse, A. P. Size-Dependent Second Virial Coefficients of Quantum Dots from Quantitative Cryogenic Electron Microscopy. *J. Phys. Chem. B* **2014**, *118* (37), 11000–11005. https://doi.org/10.1021/jp5056182.

(6) Monego, D.; Kister, T.; Kirkwood, N.; Doblas, D.; Mulvaney, P.; Kraus, T.; Widmer-Cooper, A. When Like Destabilizes Like: Inverted Solvent Effects in Apolar Nanoparticle Dispersions. *ACS Nano* **2020**, *14* (5), 5278–5287. https://doi.org/10.1021/acsnano.9b03552.

(7) Bonneté, F.; Finet, S.; Tardieu, A. Second Virial Coefficient: Variations with Lysozyme Crystallization Conditions. *J. Cryst. Growth* **1999**, *196* (2–4), 403–414. https://doi.org/10.1016/S0022-0248(98)00826-4.

(8) Ofosu, C. K.; Kang, J.; Truskett, T. M.; Milliron, D. J. Effective Hard-Sphere Repulsions between Oleate-Capped Colloidal Metal Oxide Nanocrystals. *J. Phys. Chem. Lett.* **2022**, *13* (48), 11323–11329. https://doi.org/10.1021/acs.jpclett.2c02627.

(9) Haxton, T. K.; Whitelam, S. Design Rules for the Self-Assembly of a Protein Crystal. *Soft Matter* **2012**, *8* (13), 3558. https://doi.org/10.1039/c2sm07436b.

(10) Derjaguin, B.; Landau, L. Theory of the Stability of Strongly Charged Lyophobic Sols and of the Adhesion of Strongly Charged Particles in Solutions of Electrolytes. *Prog. Surf. Sci.* **1993**, *43* (1–4), 30–59. https://doi.org/10.1016/0079-6816(93)90013-L.

(11) Verwey, E. J. W. Theory of the Stability of Lyophobic Colloids.

(12) Hayter, J. B.; Penfold, J. An Analytic Structure Factor for Macroion Solutions. *Mol. Phys.* **1981**, *42* (1), 109–118. https://doi.org/10.1080/00268978100100091.

(13) Tanabe, Y.; Müller, N.; Fischer, E. W. Density Fluctuation in Amorphous Polymers by Small Angle X-Ray Scattering. *Polym. J.* **1984**, *16* (6), 445–452. https://doi.org/10.1295/polymj.16.445.

(14) Jeong, A.; Portner, J.; Tanner, C. P. N.; Ondry, J. C.; Zhou, C.; Mi, Z.; Tazoui, Y. A.; Lee, B.; Wall, V. R. K.; Ginsberg, N. S.; Talapin, D. V. Colloidal Dispersions of Sterically and Electrostatically Stabilized PbS Quantum Dots: Structure Factors, Second Virial Coefficients, and Film-Forming Properties. *ACS Nano* **2024**, *18* (50), 33864–33874. https://doi.org/10.1021/acsnano.4c06033.

(15) Coropceanu, I.; Janke, E. M.; Portner, J.; Haubold, D.; Nguyen, T. D.; Das, A.; Tanner, C. P. N.; Utterback, J. K.; Teitelbaum, S. W.; Hudson, ¸ Margaret H.; Sarma, N. A.; Hinkle, A. M.; Tassone, C. J.; Eychmüller, A.; Limmer, D. T.; Olvera De La Cruz, M.; Ginsberg, N. S.; Talapin, D. V. Self-Assembly of Nanocrystals into Strongly Electronically Coupled All-Inorganic Supercrystals. *Science* **2022**, *375* (6587), 1422–1426. https://doi.org/10.1126/science.abm6753.

5. Chapter 5: Self-assembly of all-inorganic nanocrystals into atomically aligned superlattice

Reprinted with permission from *J. Am. Chem. Soc.* 2026, 148, 25, 25480–25490. Copyright © 2026 American Chemical Society.

5.1. Introduction

Self-assembly of colloidal nanocrystals (NCs) provides a powerful bottom-up strategy for constructing complex materials from modular, atomically defined building blocks.[1,2] By selecting NCs with tailored compositions, shapes, and surface chemistries, it becomes possible to engineer a vast library of ordered structures with programmable optical, electronic, and mechanical properties.[1,2] Importantly, some self-assembled NC materials can be disassembled back into their colloidal components, enabling stimuli-responsive, dynamic, and reconfigurable architectures that are difficult to achieve through traditional solid-state synthesis.[3,4]

Among the various modes of NC assembly, oriented attachment is particularly attractive because it allows discrete nanocrystals to fuse into bulk-like solids with coherent crystallographic alignment.[5] This process offers a route to single-crystal-like materials with customized architectures, all accessible through solution-processable methods.[6,7] However, oriented attachment is typically irreversible: NCs often meet in a face-to-face geometry that creates large contact areas and strong, permanent necks.[7] Once fused, the NCs cannot detach or rearrange, which prevents error correction and often leads to significant structural defects.[8] Achieving atomic precision in oriented attachment therefore remains a major challenge, as irreversibility limits the system's ability to anneal misaligned interfaces.

Metal chalcogenide complex (MCC) ligands offer a promising path forward. These inorganic ligands are only a few atoms long, enabling exceptionally short interparticle distances and high packing densities in NC superlattices.[9] Their compact size and ionic nature promote long-range order while maintaining strong electronic coupling between NCs.

In this study, we demonstrate the self-assembly of PbS NCs with metal chalcogenide complex (MCC) ligands (e.g. $Sn_2S_6^{4-}$, AsS_4^{3-}) into "all-inorganic" superlattices exhibiting both long-range translational *and* orientational order, with individual NCs bridged with epitaxial "necks". We show that the self-assembly of these NCs exhibits controllable reversibility, a counterintuitive feature for orientationally attached NC superlattices with atomic-lattice alignment. Structural characterizations reveal that the NCs adopt an edge-to-edge alignment, a unique configuration facilitated by strong ionic correlations in the dense electrolyte. The formation of densely packed and oriented superlattices with controlled reversibility offers possibilities to utilize the benefits of reversible self-assembly in dynamic and adaptive material systems.

5.2. Parameter screening for self-assembly of all-inorganic PbS nanocrystals

Experimental procedure

Self-assembly of PbS-$Sn_2S_6^{4-}$ NCs dispersed in N-methylformamide (NMF) was induced by adding a non-solvent together with a multivalent flocculant that screens the surface charge of the NCs, thereby reducing long-range electrostatic repulsion.[10] As flocculants, we used K_3AsS_4, K_4GeS_4, $K_4Sn_2Se_6$, all of which dissociate readily in polar solvents and substantially increase the ionic strength. In parallel, addition of a non-solvent such as DMF or MeCN lowers the effective dielectric constant of the medium, decreasing NC solubility and further promoting assembly. Upon

addition of both components, a black solid precipitated from the dispersion, while unassembled NCs remained in the brown supernatant.

To wash the resulting PbS-$Sn_2S_6^{4-}$ NC superlattices, the precipitate was resuspended in acetonitrile and centrifuged to remove the solvent. The residual acetonitrile was allowed to evaporate, yielding a free-flowing black powder. SAXS measurements of the precipitated solids revealed sharp Bragg peaks, confirming the formation of highly ordered superlattices. A schematic overview of the self-assembly workflow is shown in Figure 5.2.1.

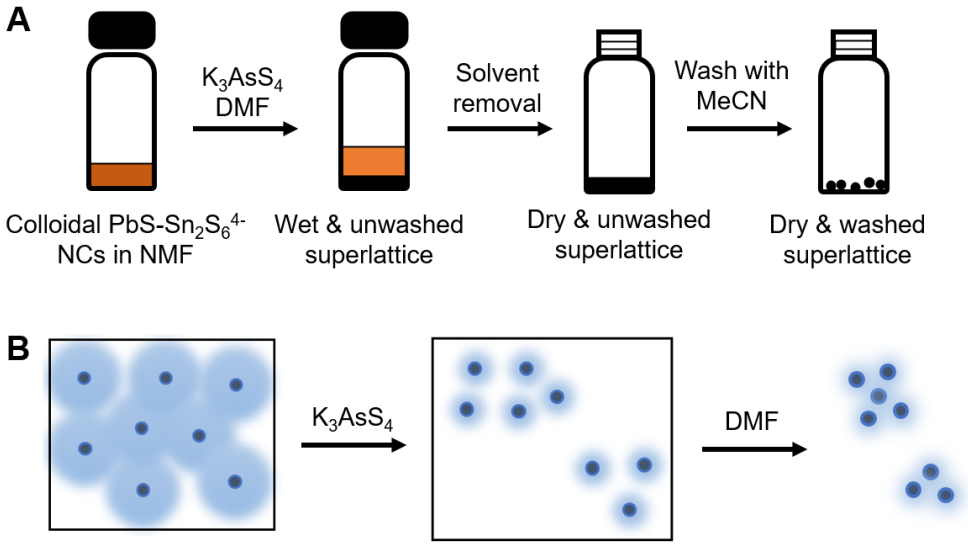

Figure 5.2.1: Self-assembly of all-inorganic nanocrystals.

(A) Schematics of self-assembly procedure. **(B)** Schematics presenting the roles of flocculant (K_3AsS_4) and non-solvent (DMF). Flocculant screens the electrostatic potential, and non-solvent promotes precipitation.

In this section, we examine how non-solvents, flocculants, nanocrystal surface chemistry, and nanocrystal size influence the self-assembly of all-inorganic PbS-$Sn_2S_6^{4-}$ NCs. All SAXS patterns presented here were collected from *wet, unwashed* superlattices. For each measurement, the self-assembled solids that are still suspended in their reaction medium were transferred directly into glass capillaries without any washing or drying steps, ensuring that the SAXS data reflect the structures formed under the native assembly conditions.

Effect of solvent on self-assembly

We evaluated a range of solvents miscible with NMF and possessing lower polarity to determine their suitability as non-solvents. Figure 5.2.2 shows SAXS patterns of superlattices formed by adding 8 µL of 0.50 M K_3AsS_4 in NMF and 8 µL of various non-solvents to 4 µL of stock dispersion of 5.8 nm PbS-$Sn_2S_6^{4-}$ NCs in NMF. The final mixture contained ~10 mg mL^{-1} NCs, 200 mM K_3AsS_4, and a 60:40 ratio of NMF to non-solvent. Tested non-solvents included N-methylpropionamide (NMPA), dimethyl sulfoxide (DMSO), acetonitrile (MeCN), *N,N*-dimethyl formamide (DMF), ethanol (EtOH), and toluene. All produced superlattices with sharp Bragg peaks, indicating that the choice of non-solvent does not significantly affect the assembly outcome under these conditions.

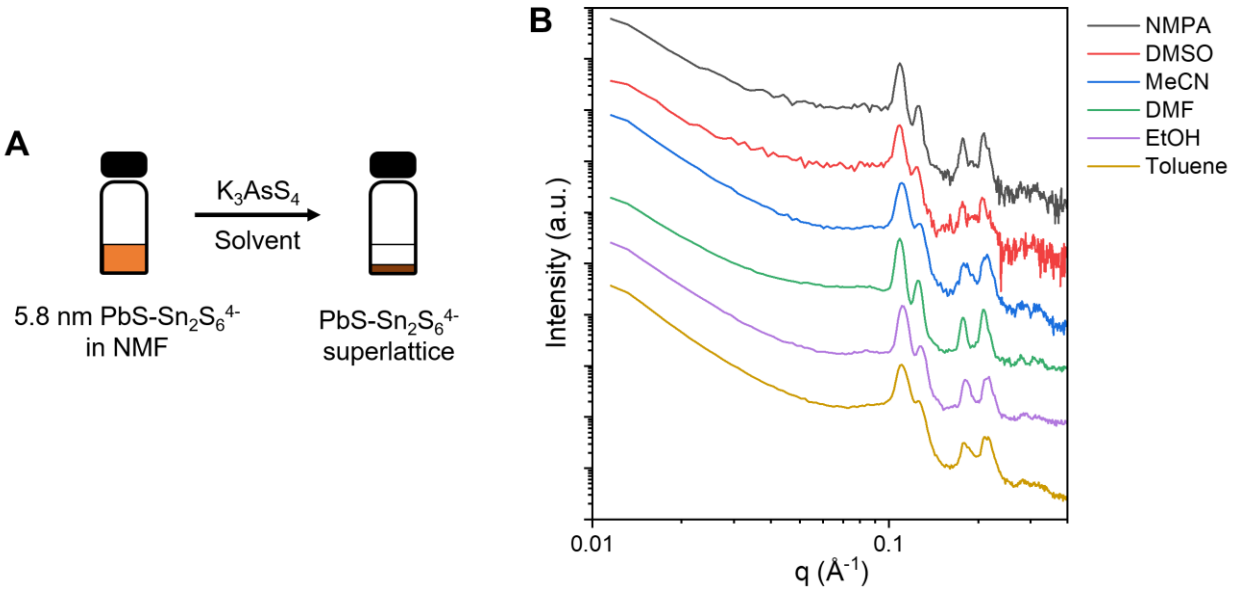

Figure 5.2.2: Effect of solvents on self-assembly.

(A) Illustration of self-assembly test with various solvents. **(B)** SAXS patterns of 5.8 nm PbS-$Sn_2S_6^{4-}$ NCs that were self-assembled by adding 200 mM of K_3AsS_4 as flocculant and 40% volume fraction of various organic solvents as non-solvents.

Effect of flocculant on self-assembly

Figure 5.2.3 shows the influence of K_3AsS_4 concentration on self-assembly. Mixtures were prepared by combining 4 µL of stock NC solution with 8 µL MeCN and 8 µL of K_3AsS_4 solutions of varying concentration, yielding ~10 mg mL^{-1} NCs, 60% NMF / 40% MeCN, and a varying K_3AsS_4 concentration. The NCs remained colloidally stable up to ~100 mM K_3AsS_4; above this threshold, ordered superlattices formed. The Bragg peak positions and shapes were invariant with respect to flocculant concentration, while the relative peak intensities changed, indicating that the amount of precipitated superlattice increased but the structural quality remained constant.

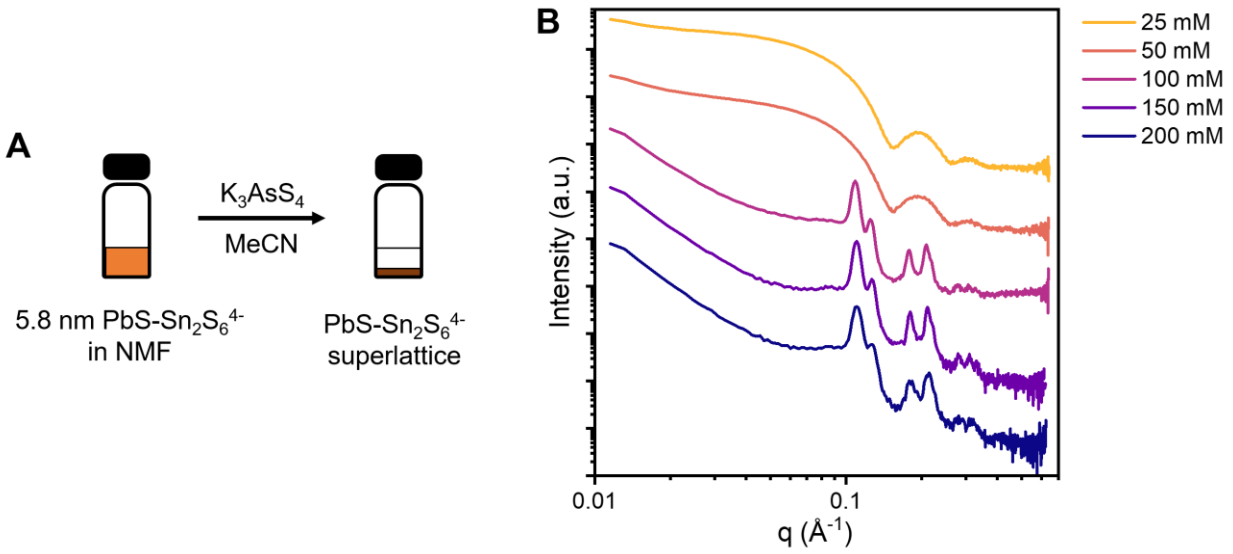

Figure 5.2.3: Effect of electrolyte concentration on self-assembly.

(A) Illustration of self-assembly test with various concentrations of K_3AsS_4. **(B)** SAXS patterns of 5.8 nm PbS-$Sn_2S_6^{4-}$ NCs that were self-assembled by adding various concentrations of K_3AsS_4 as flocculant and 40% volume fraction of acetonitrile (MeCN) as non-solvents.

We next compared different multivalent salts (Figure 5.2.4). Mixtures contained ~10 mg mL^{-1} NCs, 60% NMF / 40% non-solvent, and the maximum soluble concentration of each salt. K_3AsS_4, K_4GeS_4, $K_4Sn_2Se_6$ all produced superlattices with strong, well-defined Bragg peaks, indicating that the identity of the multivalent anion does not alter the resulting crystal structure. The use of K_3AsS_4 as the flocculant consistently yielded the sharpest peaks, suggesting it is the most effective flocculant. In contrast, K_3AsS_3 produced disordered aggregates, and $MAPbI_3$ only partially screened the NCs, reducing colloidal stability without inducing ordered assembly. These results highlight the importance of selecting an appropriate multivalent salt.

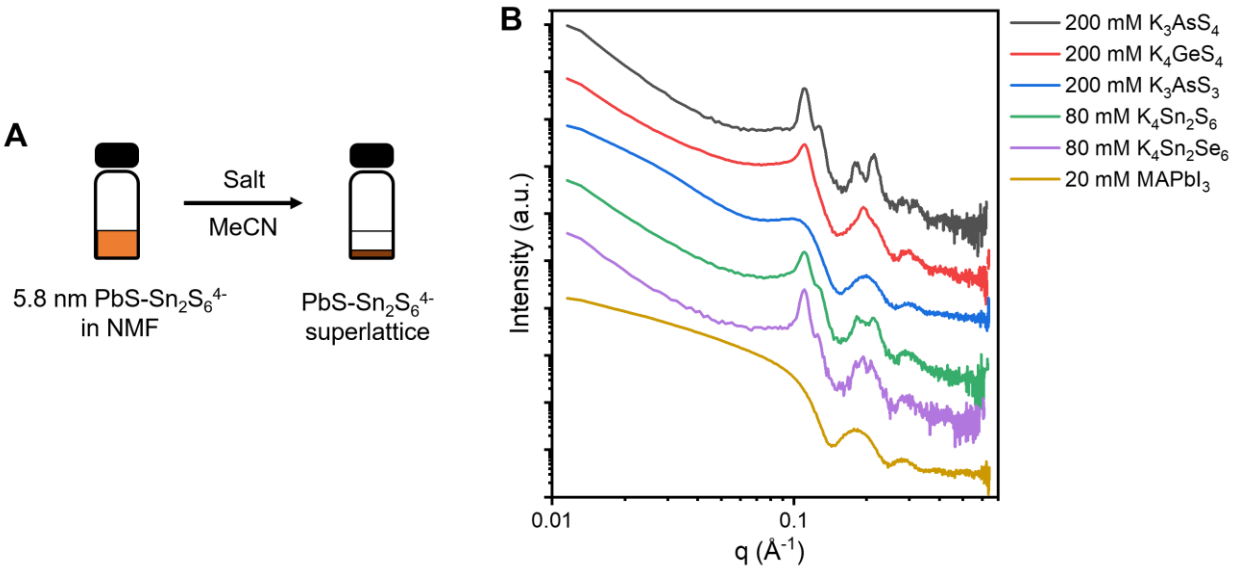

Figure 5.2.4: Effect of electrolytes on self-assembly.

(A) Illustration of self-assembly test with various salts as flocculants. **(B)** SAXS patterns of 5.8 nm PbS-$Sn_2S_6^{4-}$ NCs that were self-assembled by adding various salts as flocculant and 40% volume fraction of acetonitrile (MeCN) as non-solvents.

Effect of surface ligands of NCs on self-assembly

We examined the self-assembly behavior of PbS NCs capped with various inorganic ligands ($Sn_2S_6^{4-}$, AsS_4^{3-}, GeS_4^{4-}, AsS_3^{3-}, and S^{2-}), using K^+ as the counterion. For each ligand type, 4 µL of stock NC solution was mixed with 8 µL DMF or MeCN and 8 µL of 0.50 M K_3AsS_4, yielding ~10 mg mL^{-1} NCs and 200 mM K_3AsS_4. SAXS patterns of the colloidal dispersions (Figure 5.2.5B) showed that PbS NCs capped with $Sn_2S_6^{4-}$, AsS_4^{3-}, and GeS_4^{4-} exhibited nearly identical Bessel oscillations, indicating similar size and shape distributions. In contrast, SAXS patterns of NCs capped with AsS_3^{3-} or S^{2-} displayed broadened oscillations and smeared Guinier-to-Porod transitions, consistent with aggregation into dimers, trimers, or larger clusters.

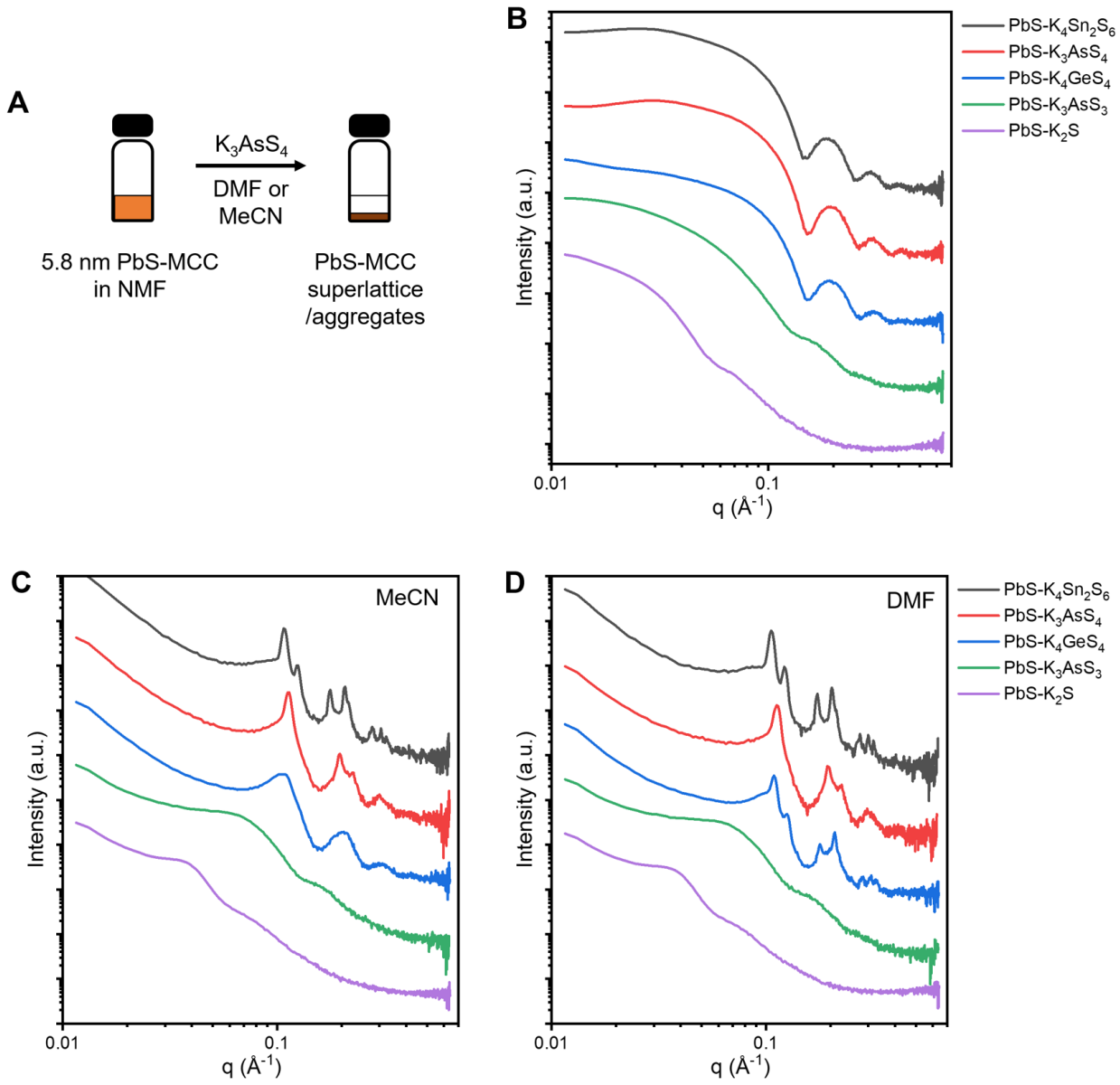

Figure 5.2.5: Effect of NC surface on self-assembly.

(A) Illustration of self-assembly test of PbS NCs with various MCC surface ligands. **(B)** SAXS patterns of 5.8 nm PbS-MCC NCs that were self-assembled by adding 200 mM K_3AsS_4 as flocculant and 40% volume fraction of **(C)** acetonitrile (MeCN) or **(D)** *N,N*-dimethylforamide (DMF) as non-solvents.

Self-assembly experiments revealed that PbS NCs capped with $Sn_2S_6^{4-}$, AsS_4^{3-}, and GeS_4^{4-} readily formed ordered superlattices, whereas those capped with AsS_3^{3-} or S^{2-} did not assemble. Among the assembling systems, PbS-$Sn_2S_6^{4-}$ NCs produced the sharpest Bragg peaks, while PbS-AsS_4^{3-} and PbS-GeS_4^{4-} NCs yielded weaker peaks. Interestingly, the choice of non-solvent (DMF vs MeCN) had little effect on PbS-$Sn_2S_6^{4-}$ and PbS-AsS_4^{3-} NC assembly, but PbS-GeS_4^{4-} NCs produced noticeably sharper peaks in DMF than in MeCN, suggesting ligand-dependent solvent effects.

Effect of size of the NCs on self-assembly

Next, the effect of NC diameter on the self-assembly was explored. PbS-$Sn_2S_6^{4-}$ NCs with diameters from 5.4 to 8.1 nm were tested for self-assembly by mixing 4 μL stock NC solution with 8 μL DMF and 8 μL 0.50 M K_3AsS_4, yielding ~10 mg/mL NCs, 200 mM K_3AsS_4, and 60% NMF / 40% DMF solution mixture. All NCs in this size range formed ordered superlattices (Figure 5.2.6), with Bragg peaks shifting to lower q as NC diameter increased, consistent with larger lattice constants.

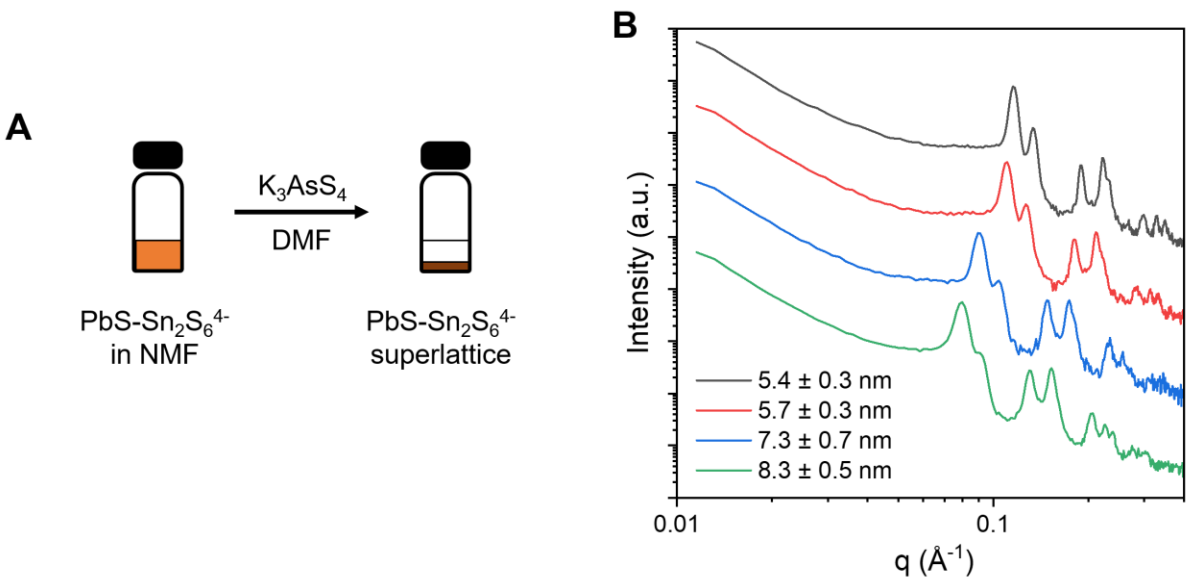

Figure 5.2.6: Effect of NC size on self-assembly.

(A) Illustration of self-assembly test of PbS-$Sn_2S_6^{4-}$ NCs with various NC diameters. **(B)** SAXS patterns of 5.8 nm PbS-$Sn_2S_6^{4-}$ NCs that were self-assembled by adding various concentrations of K_3AsS_4 as flocculant and 40% volume fraction of *N,N*-dimethylforamide (DMF) as non-solvents.

To probe smaller sizes, PbS NCs were synthesized via hot-injection of $(TMS)_2S$ (See Chapter 2 for synthetic details). SAXS patterns of the PbS-OA precursors and the corresponding PbS-$Sn_2S_6^{4-}$ NCs after ligand exchange are shown in Figures 5.2.7A and 5.2.7B. These NCs were tested for self-assembly using the same condition as above: ~10 mg/mL NCs, 200 mM K_3AsS_4, and 60% NMF / 40% DMF solution mixture. As shown in Figures 5.2.7C–D, NCs of 5.0 and 5.4 nm assembled into ordered superlattices in DMF, whereas 4.5 nm and 3.5 nm NCs formed disordered aggregates. In MeCN, all sizes showed some degree of ordering, but the Bragg peaks broadened progressively as NC size decreased. Overall, NCs smaller than ~5.4 nm exhibited reduced assembly propensity, with a clear dependence on the choice of non-solvent. This behavior likely reflects the size-dependent shape transition from truncated octahedra to more

spherical cuboctahedra near 4–5 nm, as the increased sphericity of cuboctahedral NCs enables denser packing within the superlattice.[11–13]

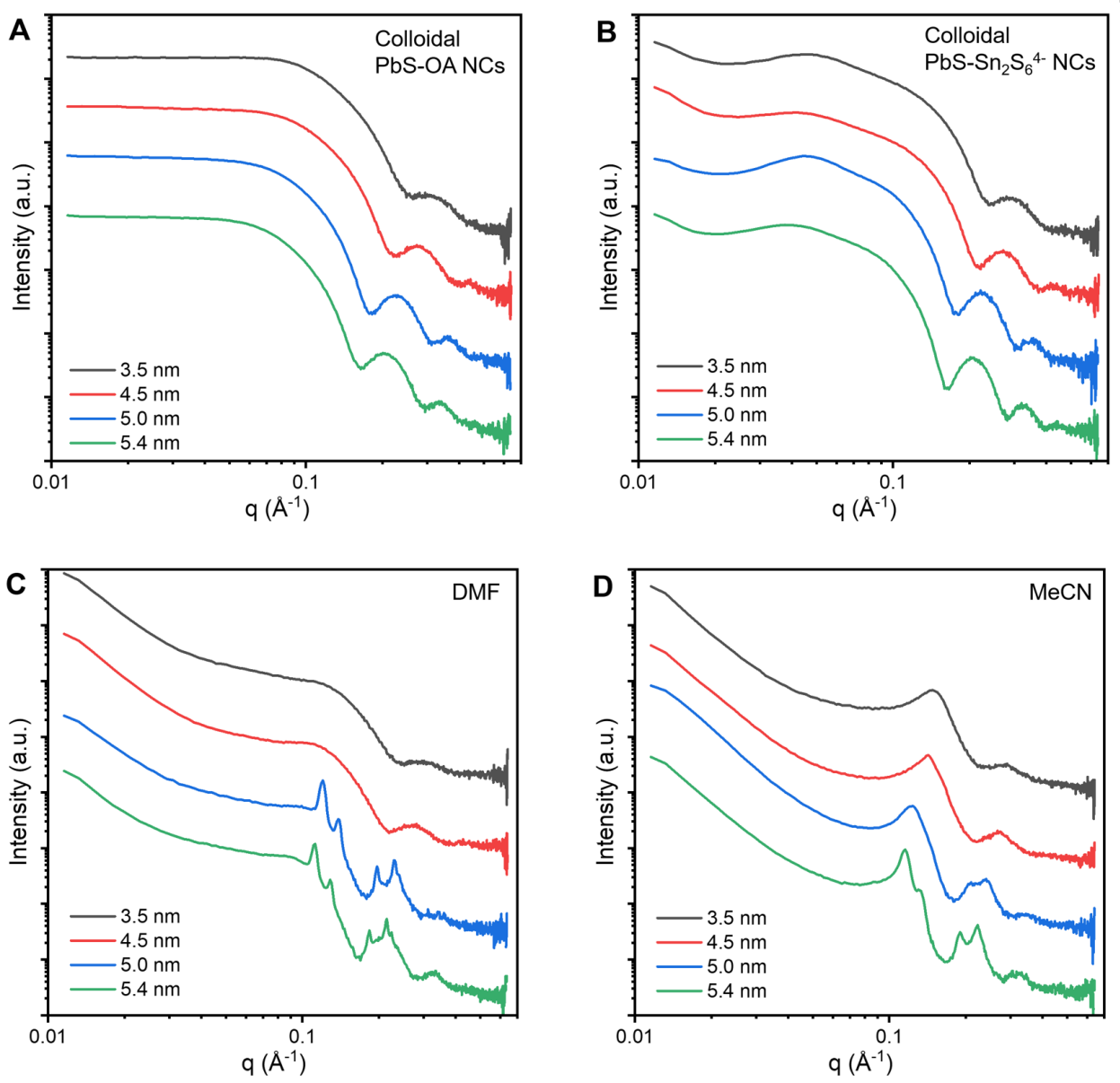

Figure 5.2.7: Self-assembly of smaller PbS NCs.

SAXS patterns of colloidal **(A)** PbS-OA NCs and **(B)** PbS-$Sn_2S_6^{4-}$ NCs with various diameters. SAXS patterns of 5.8 nm PbS-$Sn_2S_6^{4-}$ NCs that were self-assembled by adding 200 mM K_3AsS_4 as flocculant and 40% volume fraction of **(C)** *N,N*-dimethylforamide (DMF) or **(D)** acetonitrile (MeCN) as non-solvents.

5.3. Atomic alignment of all-inorganic superlattices

In this section, we take a closer look into the superlattice through electron microscopy imaging. Experimental results show that MCC-capped PbS nanocrystals exhibit not only long-range translational order but also long-range orientational order within their superlattices. Remarkably, this orientational coherence is so precise that the atomic lattices of neighboring PbS NCs align seamlessly across the entire superlattice domain, producing continuous atomic lattice fringes. In this section, we present the experimental evidence demonstrating this atomically precise alignment and discuss its implications for the structural coherence of all-inorganic nanocrystal superlattices.

All nanocrystal superlattices discussed in this section were prepared using the following procedure. First, 20 µL of a stock dispersion of 5.7 nm PbS-$Sn_2S_6^{4-}$ NCs was transferred into a 2 mL vial containing a stir bar, followed by the addition of 40 µL of DMF. A 0.50 M K_3AsS_4 solution was then added in 5 µL increments every 60 s until a total of 40 µL had been introduced. The mixture was stirred for an additional 30 min, during which a suspension of superlattice precipitate formed. The suspension was subsequently centrifuged, and the supernatant was removed. The collected solid was washed once by resuspending it in 1 mL of acetonitrile, centrifuging, and discarding the solvent. The washed superlattice powder was then resuspended in ~20 µL of acetonitrile and drop-cast onto TEM grids for imaging.

All 5.7 nm PbS-$Sn_2S_6^{4-}$ NC superlattices presented in this section correspond to *dried, washed* samples (see Figure 5.2.1), enabling high-resolution TEM characterization under high-vacuum conditions.

TEM and SAED images showing continuous crystal lattices

Figure 5.3.1 presents representative TEM images of washed 5.7 nm PbS-$Sn_2S_6^{4-}$ NC superlattices. The low-magnification image in Figure 5.3.1A provides an overview of the superlattice powder, where the presence of straight, well-defined grain boundaries indicates that the majority of the material forms highly ordered superlattice domains. Higher-magnification images (Figures 5.3.1B and 5.3.1C) reveal clear periodic contrast throughout the grains, confirming that the solids consist of well-ordered nanocrystals arranged in a superlattice.

The high-resolution TEM image in Figure 5.3.1D shows atomic lattice fringes with sufficient clarity to resolve individual atomic planes. Remarkably, these fringes are continuous across multiple NCs. In other words, the nanocrystals are not merely positioned on a periodic lattice, but they are atomically aligned with one another. This demonstrates that the superlattice exhibit not only long-range translational order but also precise orientational alignment of the individual NCs. This behavior was consistently observed across more than fifty TEM images, indicating that such atomic-level coherence is a robust and reproducible feature of these superlattices.

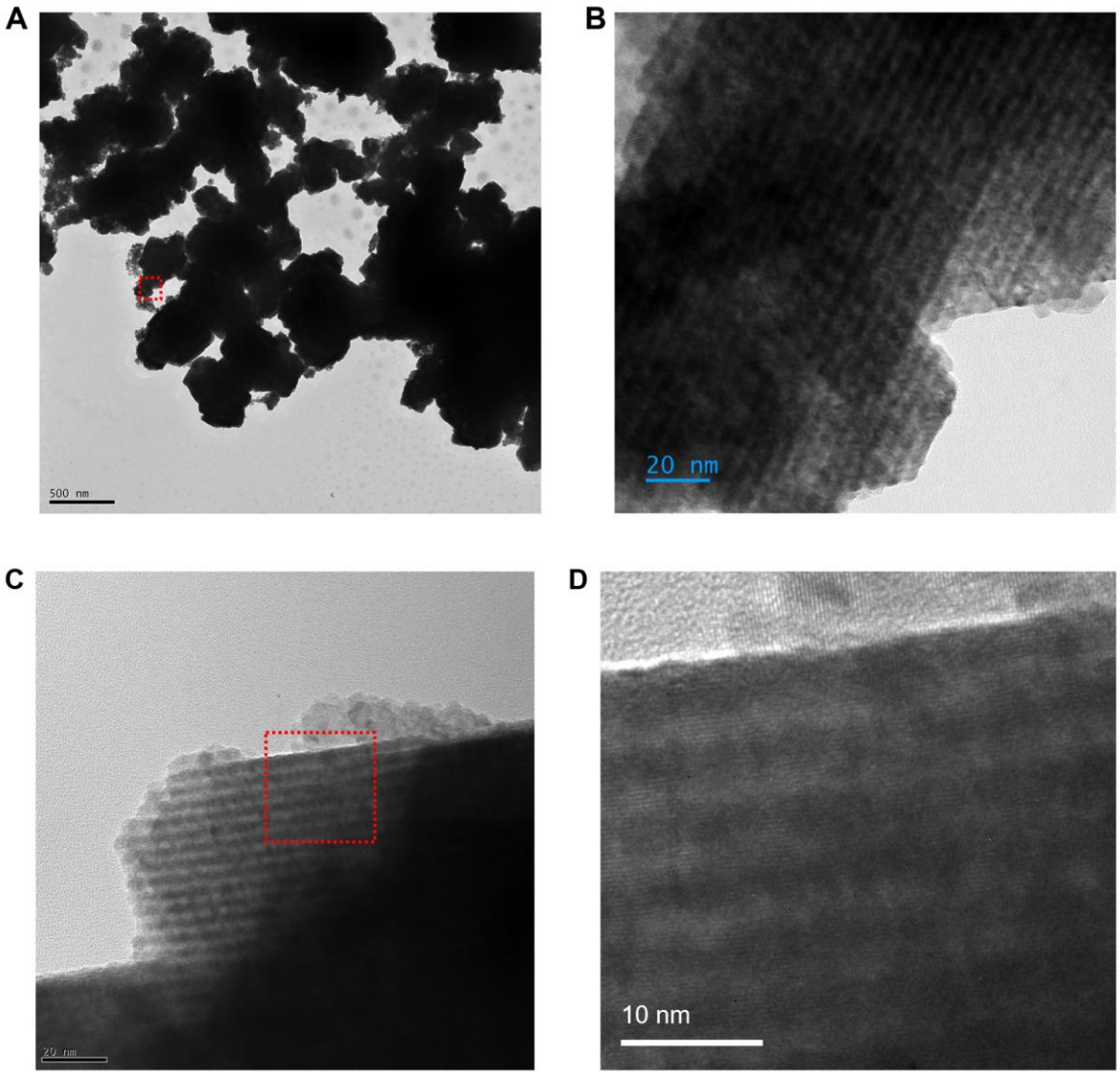

Figure 5.3.1: Atomic alignment of PbS-$Sn_2S_6^{4-}$ NC superlattices.

(A) Low-magnification TEM images of 5.7 nm PbS-$Sn_2S_6^{4-}$ NC superlattices. **(B)** corresponds to the region in **(A)** that is highlighted with a red dashed square. **(D)** corresponds to the region in **(C)** that is highlighted with a red dashed square.

We identified a superlattice grain exceeding 1 μm in width that consists of a single, continuous superlattice domain, shown in Figure 5.3.2. The TEM image in Figure 5.3.2A captures the entire grain, while Figures 5.3.2B and 5.3.2C reveal, at higher magnification, that the domain is composed of well-ordered nanocrystals and a highly periodic crystal lattice. The corresponding

selected-area electron diffraction (SAED) pattern in Figure 5.3.2D displays sharp, well-defined diffraction spots characteristic of an FCC atomic lattice viewed along the [110] zone axis.[14,15] The absence of diffraction rings or extraneous reflections indicates that the PbS nanocrystals maintain uniform orientational alignment across the entire >1 μm grain, confirming long-range orientational coherence throughout the superlattice.

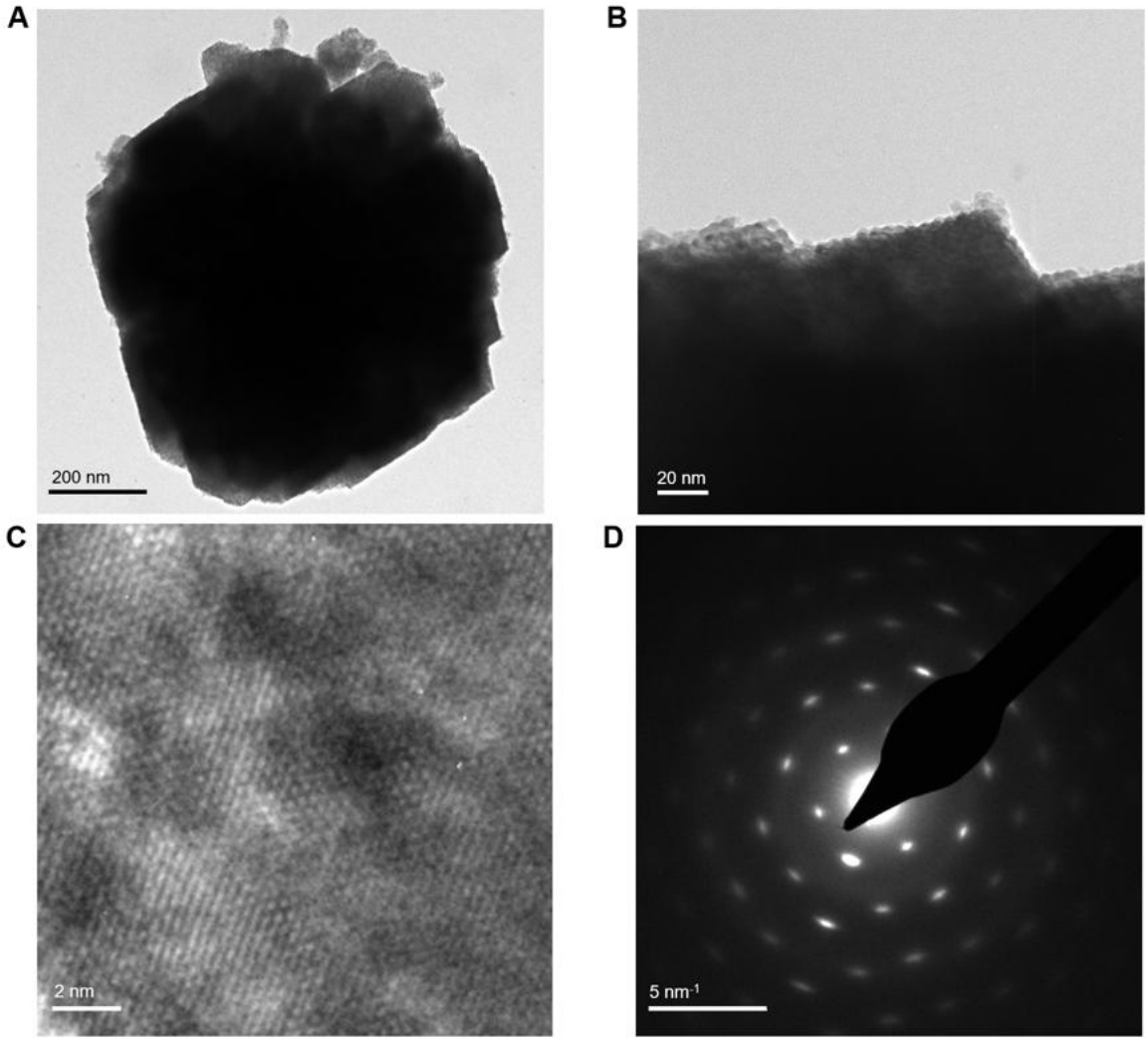

Figure 5.3.2: Atomic alignment of a single crystal superlattice grain.

(A) TEM image of a single crystal superlattice grain. **(B)** TEM image of the same grain at a higher magnification, showing NCs with long-range translational order. **(C)** High-resolution TEM of the same grain, showing that NCs are atomically aligned. **(D)** SAED image of the entire grain shown in (A).

STEM images showing continuous crystal lattices

High-angle annular dark-field scanning transmission electron microscopy (HAADF-STEM) imaging with atomic resolution (Figures 5.3.3) reveals the crystalline necks between NCs formed across the superlattice.

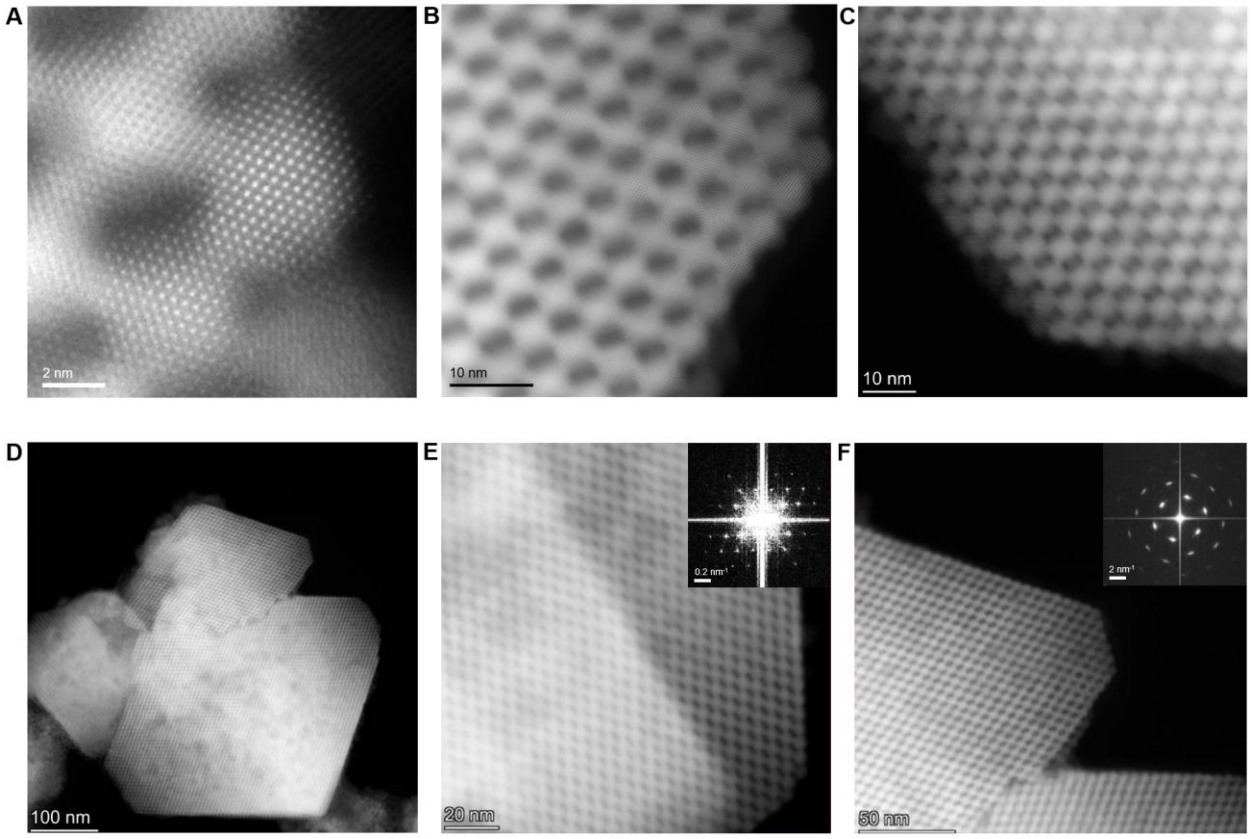

Figure 5.3.3: STEM images of atomically aligned all-inorganic superlattices.
(A-F) HAADF-STEM images of 5.7 nm PbS-$Sn_2S_6^{4-}$ NC superlattices. Insets: Fourier transformed image of the corresponding STEM images.

TEM images of superlattices of other NCs

TEM images in Figure 5.3.4 of the superlattices show that spontaneous oriented self-assembly occurs for PbS-$Sn_2S_6^{4-}$ NCs of different sizes, and similar behavior can be found from PbS-AsS_4^{3-} NCs and PbSe-$Sn_2S_6^{4-}$ NCs. The distinct spot patterns in wide-angle FT-TEM images

shown in the inset indicate that there is a strong preference for the NCs to be orientationally aligned within the superlattice.

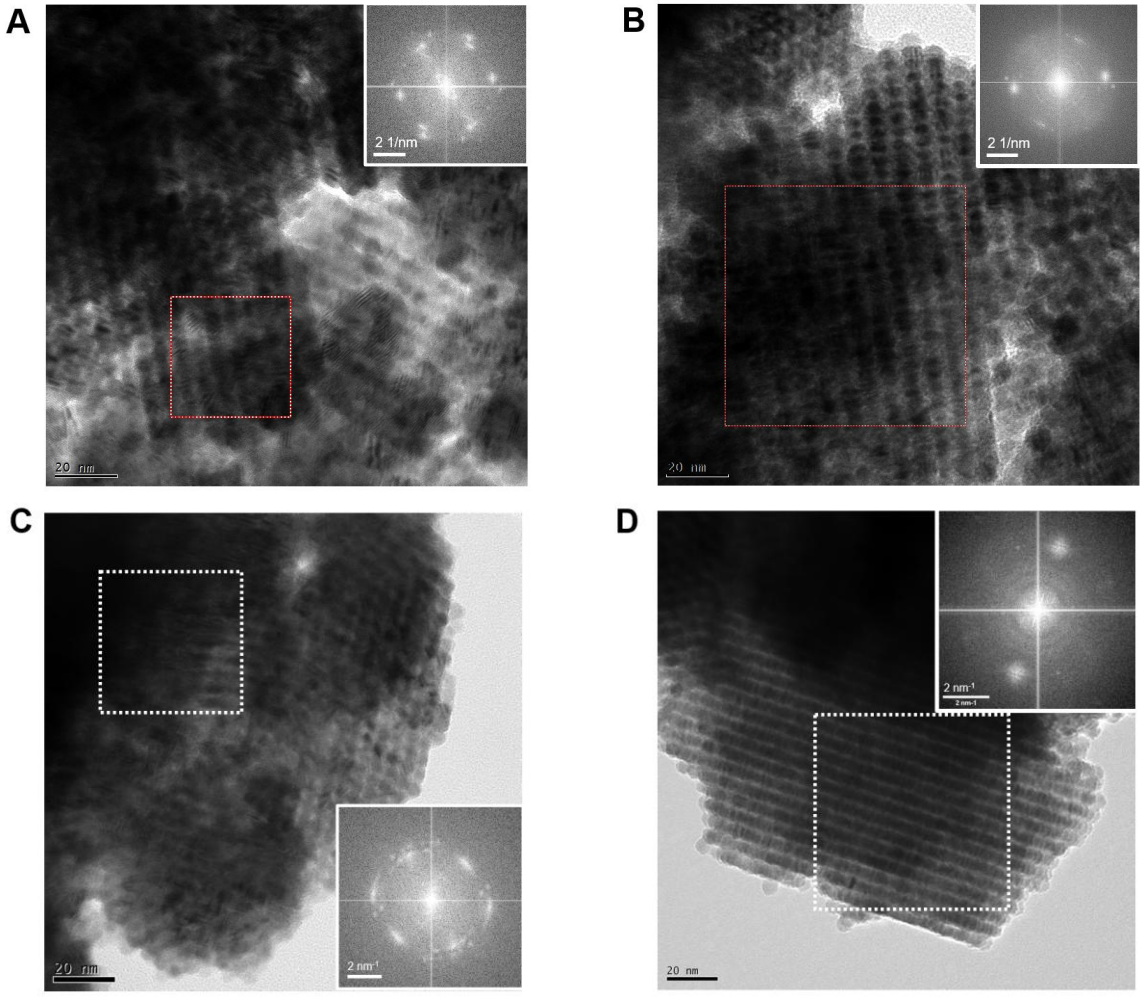

Figure 5.3.4: Atomically aligned superlattices from various all-inorganic NCs.
TEM images of **(A)** 7.3 nm PbS-$Sn_2S_6^{4-}$ NC, **(B)** 8.3 nm PbS-$Sn_2S_6^{4-}$ NC, **(C)** 5.7 nm PbS-AsS_4^{3-} NC and **(D)** 6.4 nm PbSe-$Sn_2S_6^{4-}$ NC superlattices. Inset: Fourier transformed image of the region enclosed by red dashed box.

TEM image of a grain boundary of superlattices

A twinning grain boundary, a frequently seen grain boundary in *fcc* lattice (Figure 5.3.5),[16] further support the formation of well-ordered *fcc* superlattice. Even at grain boundary, we find that

the PbS lattice fringes change angle but are still continuous, further supporting the strong tendency for formation of orientational alignment.

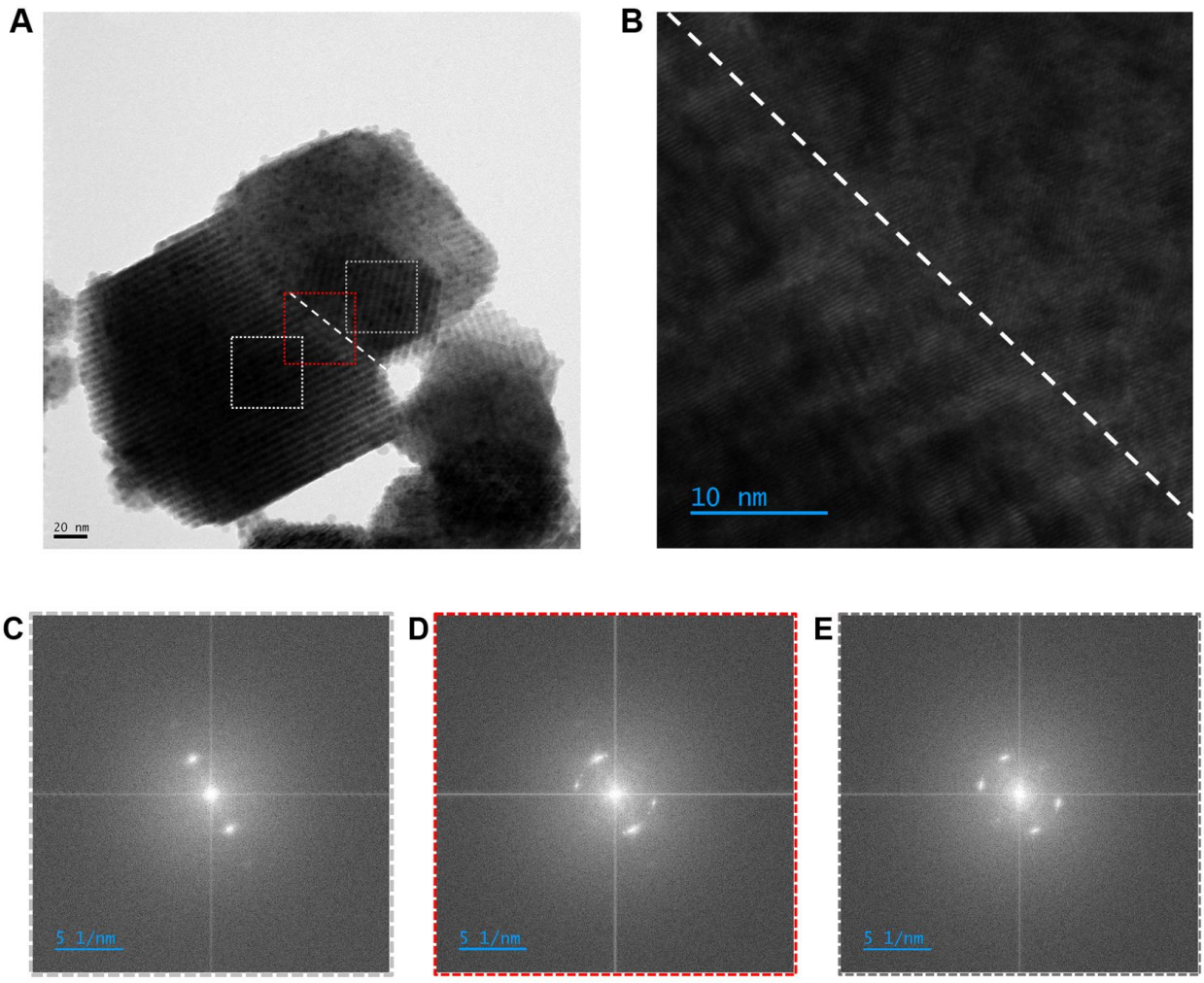

Figure 5.3.5: Grain boundary of atomically aligned superlattices.

(A) TEM image of 5.8 nm PbS-$Sn_2S_6^{4-}$ NCs with a grain boundary. The grain boundary is marked with a white dashed line. **(B)** HRTEM image of the grain boundary. Atomic lattice fringes are continuous, even though there is a change in the zone axis. **(C)** Fourier transformed image of TEM image shown in (A). The regions where the FT image are from are labelled with grey and red dashed cubes.

Scherrer analysis showing lattice expansion

The selected area electron diffraction (SAED) pattern shown in Figure 5.3.3D was analyzed to estimate the Scherrer diameter of the washed PbS-$Sn_2S_6^{4-}$ NC superlattice. Owing to the orientational alignment of the superlattice, an extension of Scherrer analysis to the assembled structure was anticipated. The center of the diffraction pattern was first determined using the DiffTools plugin in Gatan DigitalMicrograph software. A linear intensity profile passing through the center of the pattern (Figure 5.3.6A) was then extracted to identify diffraction peaks. Scherrer analysis was performed on the sharpest peak in the linear profile, as indicated in Figure 5.3.6B.

The Scherrer diameter (D) is calculated from the full-width half-maximum (FWHM) of the selected peak. The classical Scherrer equation is given by:

$$D = \frac{K\lambda}{\beta \cos(\theta)}$$

Where K is the shape factor, λ is wavelength of the incident beam, β is the FWHM of scattering angle in radians and θ is the Bragg angle.[17] Since our measurement is in reciprocal space in $1/d$ scale rather than in angular space, a modified form of the equation was employed, where Δq is the FWHM in the reciprocal space. The shape factor, K, can be estimated as 0.93 for spherical particles.

$$D = \frac{K}{\Delta q}$$

From this analysis, a Scherrer diameter of 6.1 nm was obtained for the washed PbS-$Sn_2S_6^{4-}$ NC superlattice. This value is larger than the estimated diameter of individual PbS-$Sn_2S_6^{4-}$ NCs derived from powder X-ray diffraction shown in Figure 5.4.2 (PXRD) (5.4 nm). The increase in Scherrer diameter upon self-assembly supports the presence of oriented attachment of NCs within the superlattice. The relatively small Scherrer diameter compared to the estimated superlattice size

(on the order of microns) may be attributed to instrumental broadening, e-beam convergence, and to the emergence of satellite peaks due to the periodic superlattice structure.[18]

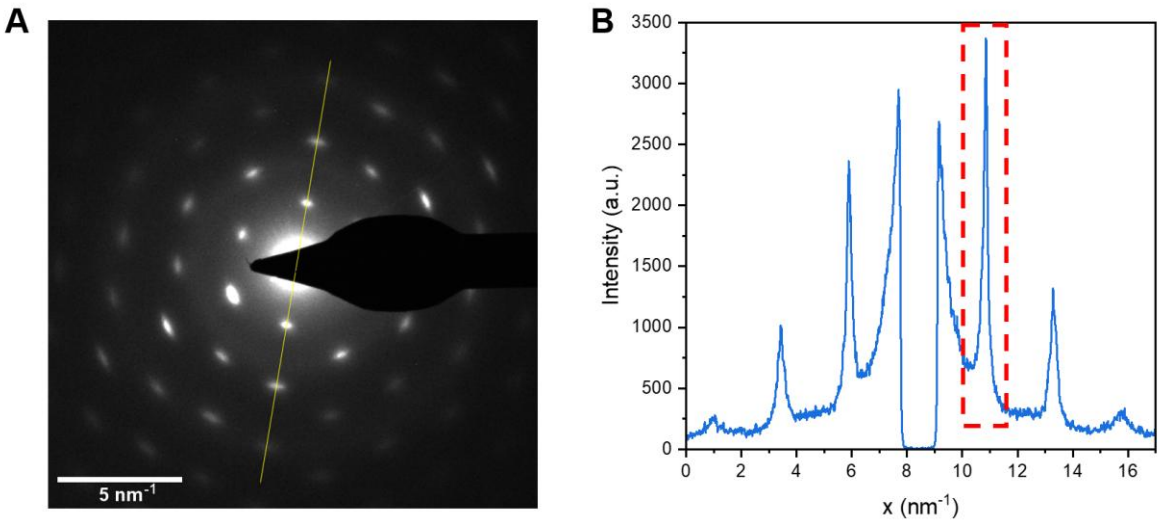

Figure 5.3.6: Scherrer analysis of superlattice using SAED.

(A) SAED image of the 5.7 nm PbS-$Sn_2S_6^{4-}$ NC superlattice. The yellow line indicates the location where the linear profile shown in (B) is obtained. The peak indicated by the dashed red box in **(B)** is the peak where the full-width half-maximum (FWHM) was obtained for the Scherrer analysis. The detailed description of the Scherrer analysis is given in Section 4.3.

5.4. Shape analysis of thiostannate-capped PbS nanocrystals

Now that we have established that the superlattices exhibit long-range orientational order, the next question is *how* the nanocrystals are oriented within the lattice. To address this, we must first determine the shape of the individual PbS nanocrystals. It is well established that very small PbS NCs (<3 nm) adopt an octahedral morphology dominated by {111} facets. As the NCs grow larger, {100} facets begin to appear, producing truncated-octahedral shapes that eventually evolve toward cuboctahedra. In this section, we perform a detailed analysis to confirm the morphology of the PbS-$Sn_2S_6^{4-}$ NCs used in our study.

Wulff construction analysis using HRTEM

We begin by applying Wulff construction analysis to high-resolution TEM (HRTEM) images. The Wulff ratio is defined as the ratio of the surface energy of a given facet ($\gamma_{(hkl)}$) to that of the {100} facet (γ_{100}).[19] This ratio can be obtained directly from the ratio of the perpendicular distances from the nanocrystal center to the corresponding facets (h_{hkl}/h_{100}), which can be measured from HRTEM images:

$$\frac{\gamma_{hkl}}{\gamma_{100}} = \frac{h_{hkl}}{h_{100}}$$

Figures 5.4.1A and 5.4.1B show the HRTEM image of 5.7 nm PbS–$Sn_2S_6^{4-}$ NCs and the corresponding Fourier-transformed (FT) image. Samples were prepared by drop-casting a dilute NC dispersion in NMF and evaporating the solvent under vacuum. The FT image displays several diffraction rings corresponding to different Miller indices, which are labeled accordingly.

Figures 5.4.1C–H present HRTEM images of individual NCs oriented along the [110] zone axis. Using the FT-TEM patterns, we measured the perpendicular distances associated with the (111) and (002) reflections to determine the Wulff ratio. The extracted h_{111}/h_{100} values were 0.979, 0.981, and 1.002, giving an average of 0.99.

According to established criteria, NCs exposing both {100} and {111} facets are:

- octahedral when $h_{111}/h_{100} = 1/\sqrt{3}$,
- truncated octahedral when $1/\sqrt{3} < h_{111}/h_{100} < 2/\sqrt{3}$,
- cuboctahedral when $h_{111}/h_{100} = 2/\sqrt{3}$.

Our measured ratio of ~0.99 falls squarely within the truncated-octahedral regime, indicating that the PbS-$Sn_2S_6^{4-}$ NCs adopt a truncated octahedral morphology.

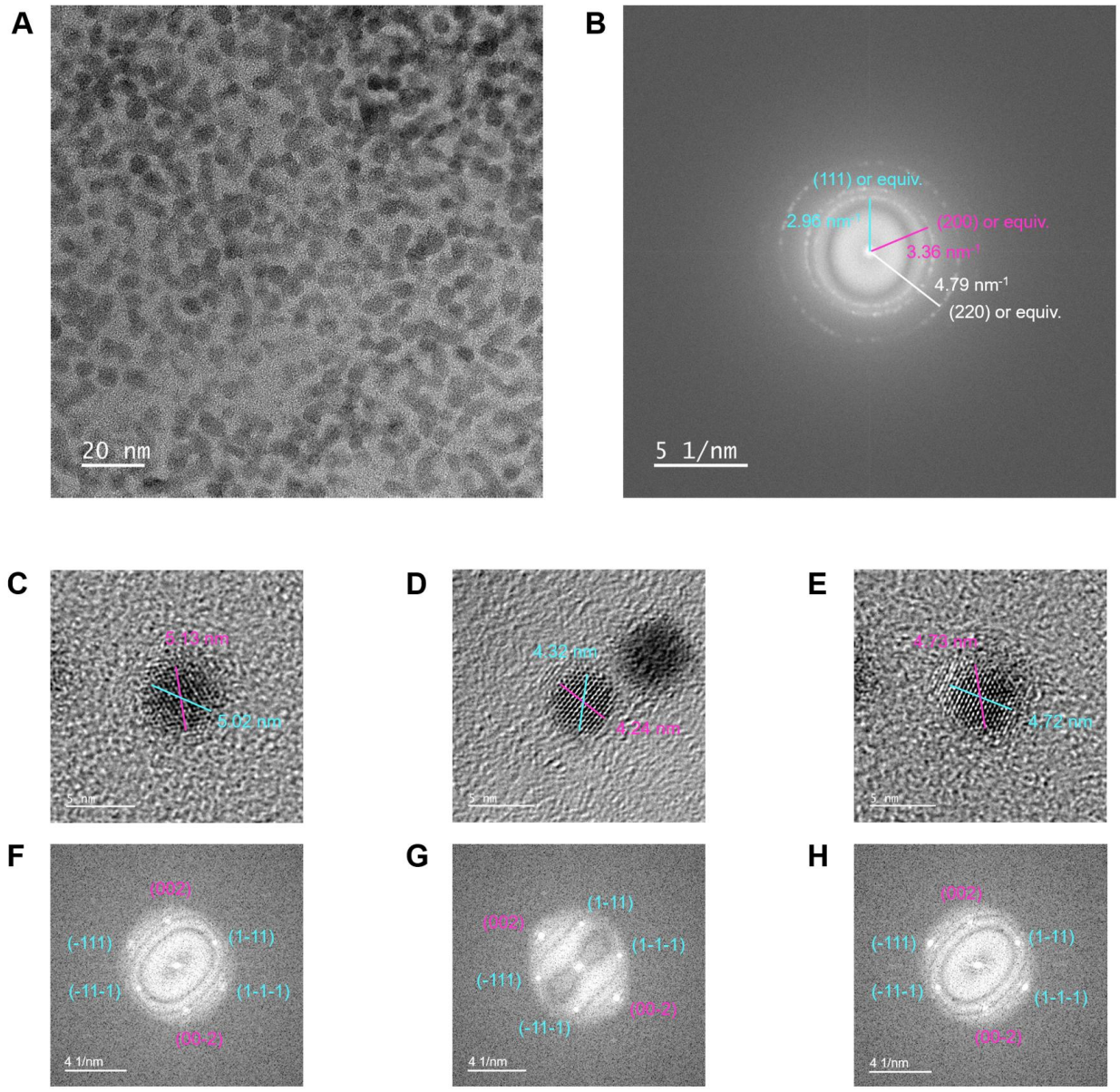

Figure 5.4.1: Wulff construction analysis using TEM.

(A) HRTEM image and **(B)** corresponding Fourier transformed image of 5.7 nm PbS-$Sn_2S_6^{4-}$ NCs. **(C-E)** HRTEM and **(F-H)** corresponding Fourier transformed image of individual NCs that are in (110) zone axis.

Wulff construction analysis using PXRD

The Wulff construction ratio $h(111)/h(100)$ for 5.7 nm PbS-$Sn_2S_6^{4-}$ NCs was determined from the Scherrer size of the (111) and (200) peaks in the PXRD pattern (Figure 5.4.2), calculated using SmartLab Studio II (Rigaku). The Scherrer sizes were 55.7 Å and 54.4 Å, respectively, yielding a Wulff ratio of 1.02, which is well-aligned with the value obtained from HRTEM method. This indicates that these NCs exhibit a truncated octahedral shape ($0.58 < h(111)/h(100) < 1.15$),[20] consistent with previous experimental and computational studies.[19,20] TEM images of colloidal PbS-$Sn_2S_6^{4-}$ NCs show that the NCs are nearly spherical, which further supports this.

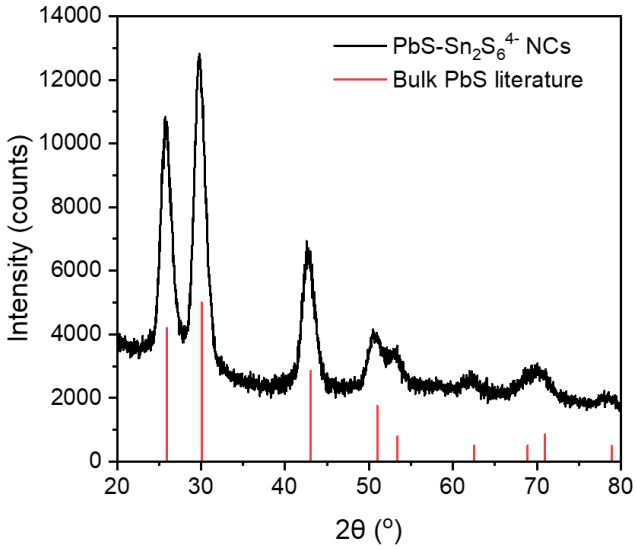

Figure 5.4.2: PXRD pattern of PbS-$Sn_2S_6^{4-}$ NCs.

PXRD pattern of 5.8 nm PbS-$Sn_2S_6^{4-}$ NCs. The red lines are the PXRD pattern of bulk PbS obtained from the literature (rock-salt structure, unit cell length 5.9 Å).

5.5. Structural analysis of all-inorganic superlattices

The translational and orientational ordering of the 5.7 nm PbS-$Sn_2S_6^{4-}$ NCs was further examined using real and reciprocal space analysis of TEM images of NC superlattices. Figure 5.5.1 presents TEM and Fourier-transformed (FT) TEM images of washed 5.7 nm PbS-$Sn_2S_6^{4-}$ NC superlattice. Figures 5.5.1B and C are the low-magnification TEM and high-resolution TEM (HRTEM) images of the resulting superlattice, while Figures 5.5.1E and F display the corresponding FT-TEM images, respectively. The FT-TEM image in Figure 5.5.1E reflects the periodicity of NC packing in the superlattice, showing six spots arranged in an elongated hexagonal pattern, where two adjacent spots form a 54° angle. This arrangement is characteristic of the reciprocal-space representation of a face-centered cubic (*fcc*) crystal viewed along the (110) zone axis, which is consistent with the SAXS pattern.[21] The four innermost spots arise from the (-111), (1-11), (-11-1), and (1-1-1) sets of superlattice planes, while the two outer spots correspond to the (002) and (00-2) planes. The calculation of the *d*-spacing from the spot-to-center distances yields a superlattice unit cell length of 8.7 nm, which is consistent with the SAXS measurement of 8.5 nm. The FT-TEM image in Figure 5.5.1F indicates a PbS atomic unit cell lattice constant of 6.1 Å, which is in good agreement with the powder X-ray diffraction (PXRD) measurement (5.9 Å, Figure 5.4.2).

The FT-TEM images in Figure 5.5.1 demonstrate that both the NC superlattice and the atomic lattices of individual NC are simultaneously oriented along the (110) zone axis. This alignment is only achievable if the PbS NCs are assembled edge-to-edge, with the closest nearly touching edges being parallel to the <110> set of equivalent lattice directions of the superlattice and NC atomic lattices, as depicted in Figures 5.5.1A and D.

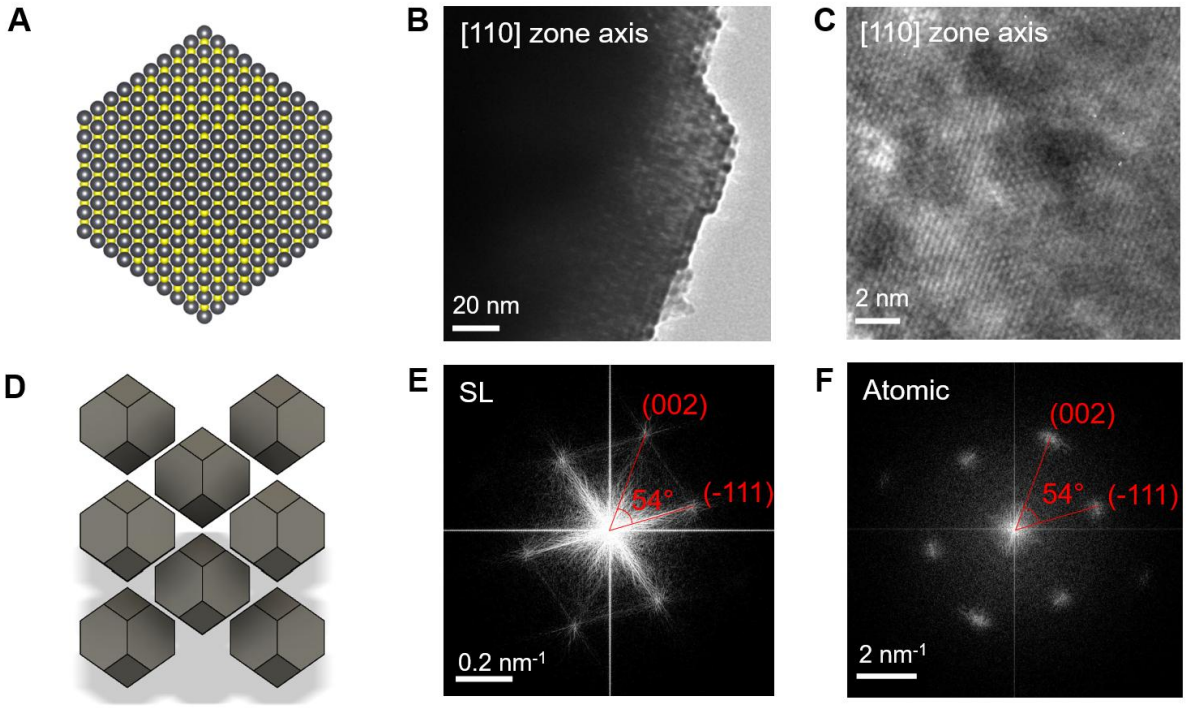

Figure 5.5.1: Superlattice viewed along (110) zone axis.

(A) Illustration of 5.7 nm PbS-$Sn_2S_6^{4-}$ NC viewed along (110) zone axis and. **(B)** Transmission electron microscopy (TEM) and **(C)** High-resolution TEM (HRTEM) image of the superlattice of 5.7 nm PbS-$Sn_2S_6^{4-}$ NCs, viewed along the (110) zone axis. **(D)** Illustration of 5.7 nm PbS-$Sn_2S_6^{4-}$ NC superlattice viewed along (110) zone axis and. **(E, F)** Fourier-transformed TEM (FT-TEM) images of the superlattice viewed along the (110) zone axis, with the distinct spots indicating highly ordered *fcc* structures at both nanometer and atomic scales.

The TEM, HRTEM, and the corresponding FT-TEM images of the washed 5.7 nm PbS-$Sn_2S_6^{4-}$ NC superlattice viewed along (100) zone axis are shown in Figures 5.5.2, respectively. The matching spot patterns in the FT-TEM images in Figures 5.5.2 for the superlattice viewed along the (100) zone axis further confirm the edge-to-edge alignment of NCs within the superlattice, as depicted in Figures 5.5.2A and D.

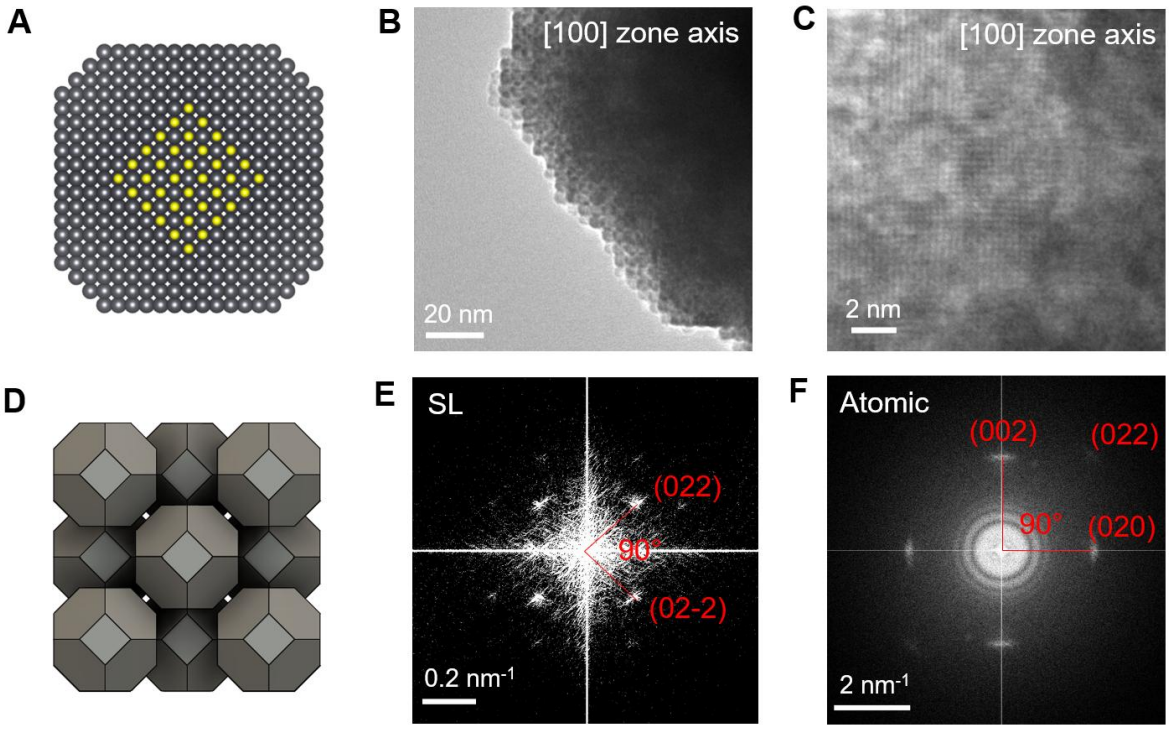

Figure 5.5.2: Superlattice viewed along (100) zone axis.

(A) Illustration of 5.7 nm PbS-$Sn_2S_6^{4-}$ NC viewed along (100) zone axis and. **(B)** Transmission electron microscopy (TEM) and **(C)** High-resolution TEM (HRTEM) image of the superlattice of 5.7 nm PbS-$Sn_2S_6^{4-}$ NCs, viewed along the (100) zone axis. **(D)** Illustration of 5.7 nm PbS-$Sn_2S_6^{4-}$ NC superlattice viewed along (100) zone axis and. **(E, F)** Fourier-transformed TEM (FT-TEM) images of the superlattice viewed along the (100) zone axis, with the distinct spots indicating highly ordered *fcc* structures at both nanometer and atomic scales.

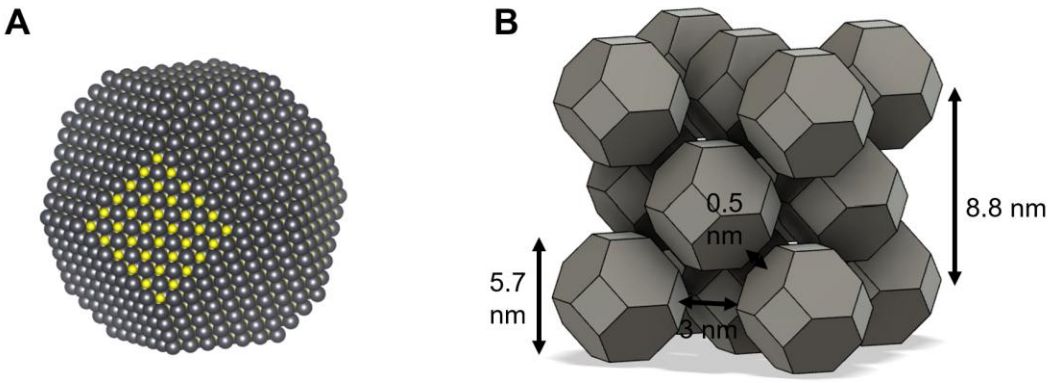

Figure 5.5.3: Nanocrystal and superlattice.

Illustration of **(A)** 5.7 nm PbS-$Sn_2S_6^{4-}$ NC and **(B)** its superlattice.

Other orientations, such as face-to-face *fcc* or *bcc* were excluded, because the spot patterns of FT-TEM do not align with the experimental results. Figure 5.5.4 presents simulated FT-TEM spot patterns of the PbS superlattice and atomic lattice generated using CrysTBox.[15] The superlattice spot patterns for *fcc* and *bcc* structures were simulated using solid Ar and α-Fe as model systems, which adopt *fcc* and *bcc* crystal structures, respectively. While these model systems differ in lattice constant, they reproduce the same qualitative diffraction features (i.e., reflection indices, angular relationships, and relative spot positions). The atomic lattice of PbS was simulated using the PbS crystal structure.

The simulated spot patterns for an *fcc* superlattice with edge-to-edge alignment viewed along the ⟨110⟩ zone axis (Figure 5.5.4A) are in good agreement with the experimental patterns shown in Figures 5.5.1. Similarly, simulations along the ⟨100⟩ zone axis (Figure 5.5.4B) match well with Figures 5.5.2. In contrast, none of the simulated patterns corresponding to alternative configurations (Figures 5.5.4C-L), including *fcc* and *bcc* superlattices with face-to-face alignment, were observed experimentally, allowing us to rule out these packing motifs.

Figure 5.5.4:

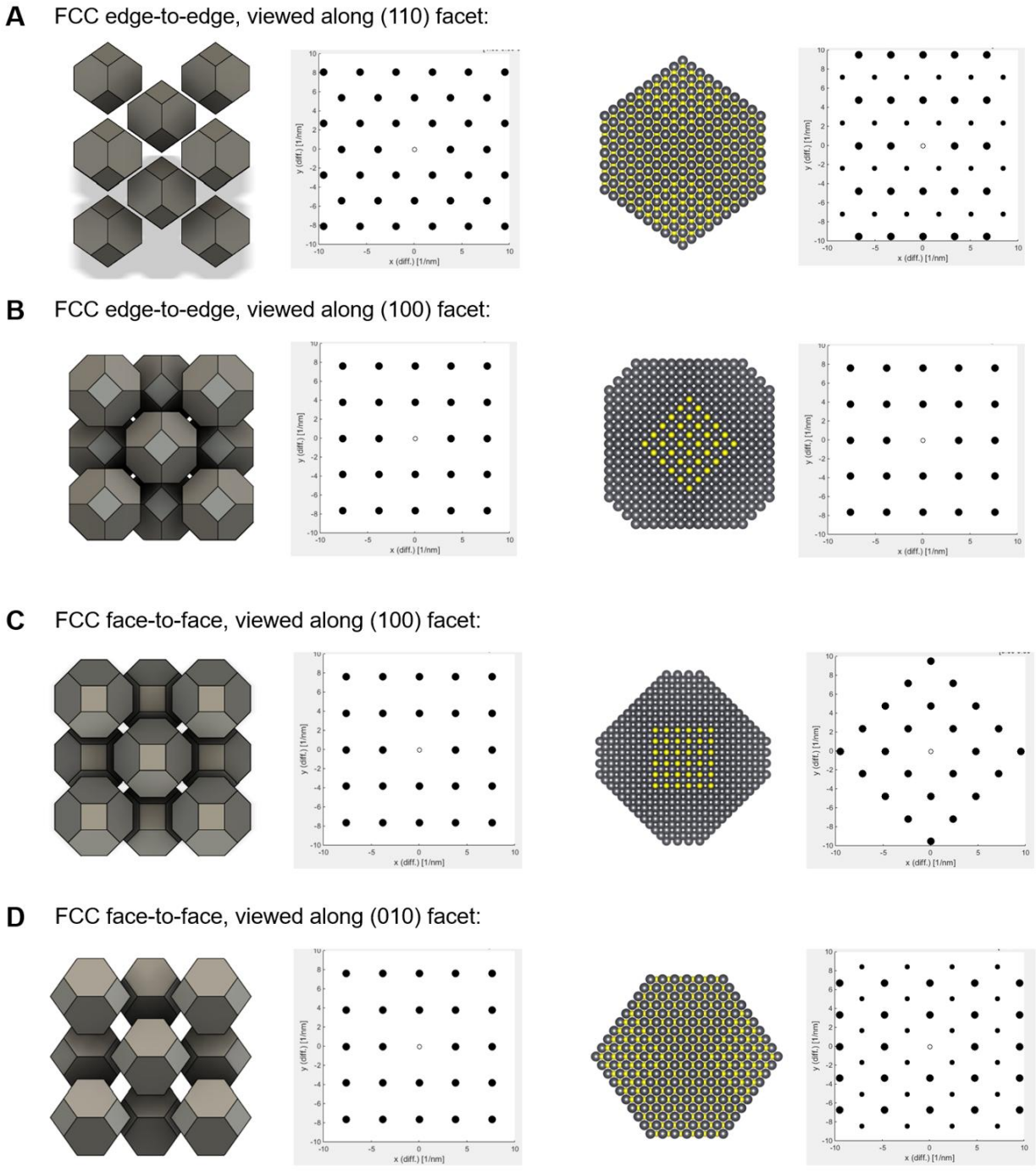
A FCC edge-to-edge, viewed along (110) facet:
B FCC edge-to-edge, viewed along (100) facet:
C FCC face-to-face, viewed along (100) facet:
D FCC face-to-face, viewed along (010) facet:
x (diff.) [1/nm]
y (diff.) [1/nm]

Figure 5.5.4 continued:

E FCC face-to-face, viewed along (110) facet:

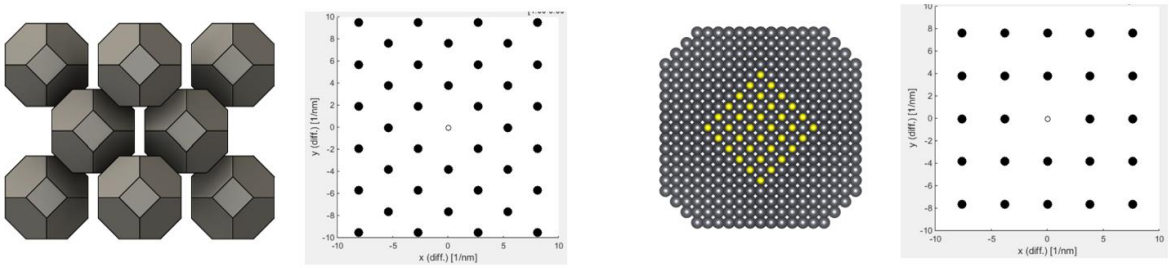

F FCC face-to-face, viewed along (101) facet:

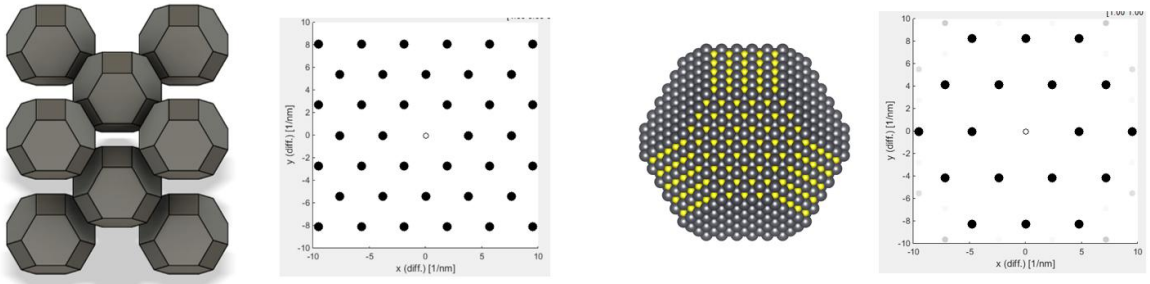

G FCC face-to-face, viewed along (111) facet:

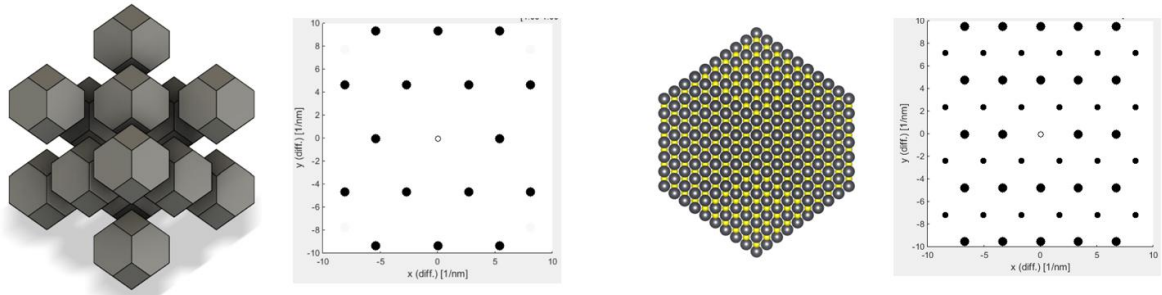

H BCC face-to-face, viewed along (100) facet:

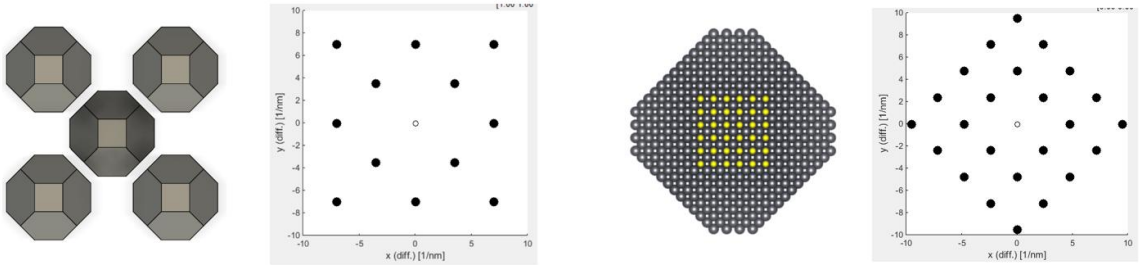

Figure 5.5.4 continued:

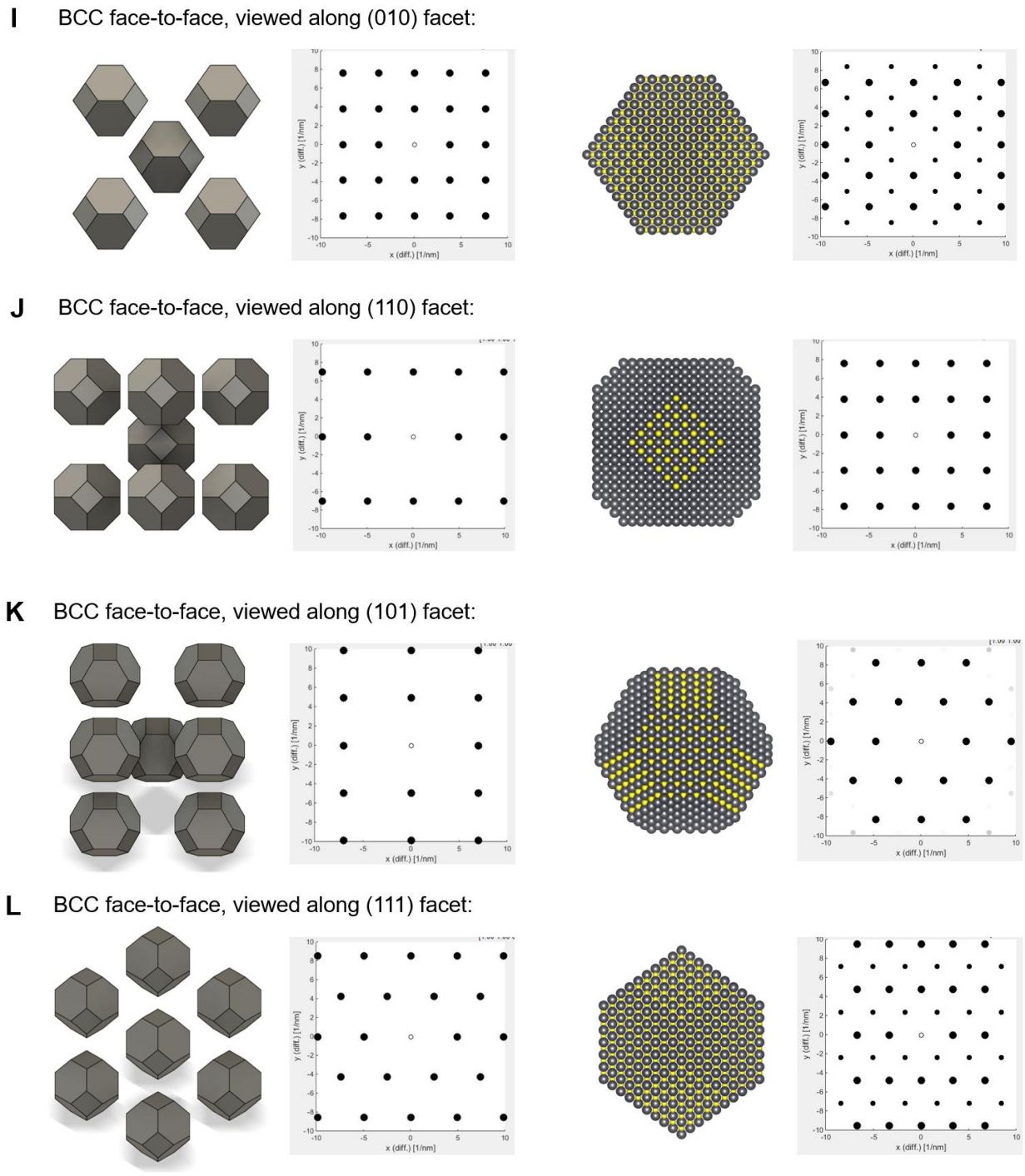

Figure 5.5.4: Simulated FT-TEM spot patterns.

(A-L) Simulation of FT-TEM spot patterns for different structures and orientational alignments.

Figure 5.5.4 continued: Each row presents illustration of superlattice unit cell, simulated spot pattern of the superlattice, illustration of PbS nanocrystal and simulated spot pattern of the crystal lattice from left to right. Further details can be found in Section 4.5.

This edge-to-edge alignment is highly unusual for NC assemblies, which typically favor face-to-face orientations to maximize the cohesive energy from van der Waals interactions. For NCs with steric colloidal stabilization provided by ligands with long hydrocarbon chains, there are only a few reported examples of superlattices supported by vertex-to-vertex contacts,[22] but such examples are far rarer compared to the face-to-face assemblies.[23–25] We propose that this unique superlattice configuration plays a key role in enabling the reversible nature of self-assembly processes in the absence of bulky organic surface ligands, where the traditional face-to-face packing would be more prone to irreversible aggregation under strong van der Waals forces.[26] Furthermore, the narrow connecting NC edges may be instrumental in establishing epitaxial necks with atomically precise order.

5.6. Structural evolution of superlattices during drying and washing

In this section, we examine how post-assembly processing, specifically drying and washing, modifies the structural and compositional properties of PbS-$Sn_2S_6^{4-}$ NC superlattices. As illustrated in Figure 5.6.1, the initial superlattice is generated by adding K_3AsS_4 and DMF to a colloidal dispersion of PbS NCs, producing a suspension of precipitated solids referred to as the *wet & unwashed* superlattice. Removing the solvent yields a *dry & unwashed* superlattice, which initially forms a dense black paste and can be converted into a powder after extended vacuum drying. Washing is performed by resuspending the solids in acetonitrile, producing a *wet & washed*

superlattice, which is then isolated as a *dry & washed* superlattice after centrifugation and brief evaporation.

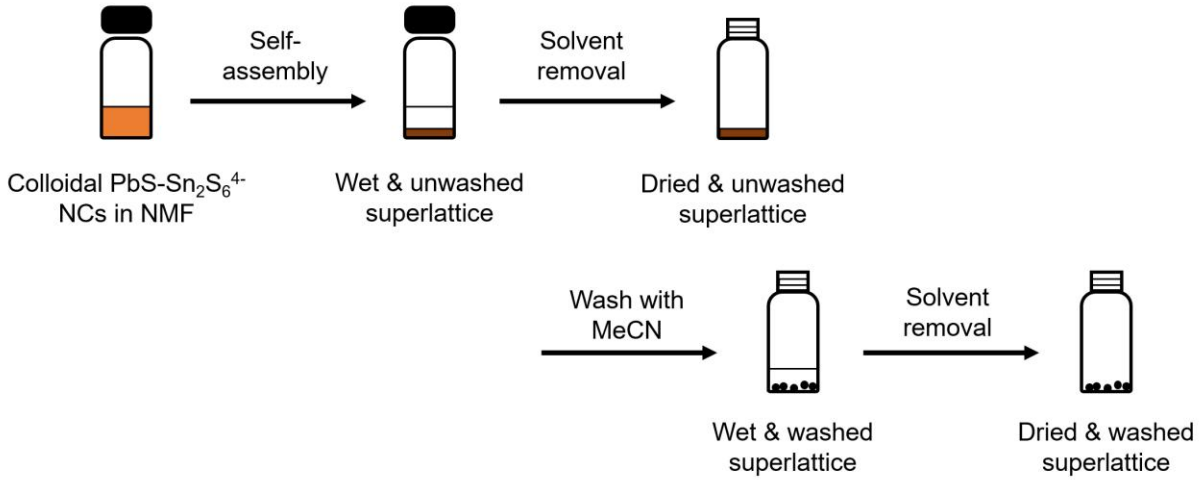

Figure 5.6.1: Washing and drying superlattice.
Schematics of washing and drying procedure of self-assembled superlattice.

Lattice contraction revealed by SAXS

SAXS measurements collected at each processing stage reveal systematic lattice contraction (Figure 5.6.2). The wet & unwashed superlattice exhibits a lattice constant of 10.0 nm. Drying this material reduces the lattice constant to 9.3 nm, indicating that solvent removal alone induces significant contraction. Subsequent washing produces an additional contraction to 8.5 nm, as evidenced by the shift of Bragg peaks to higher q. These results demonstrate that both solvent removal and salt extraction contribute to densification of the superlattice lattice.

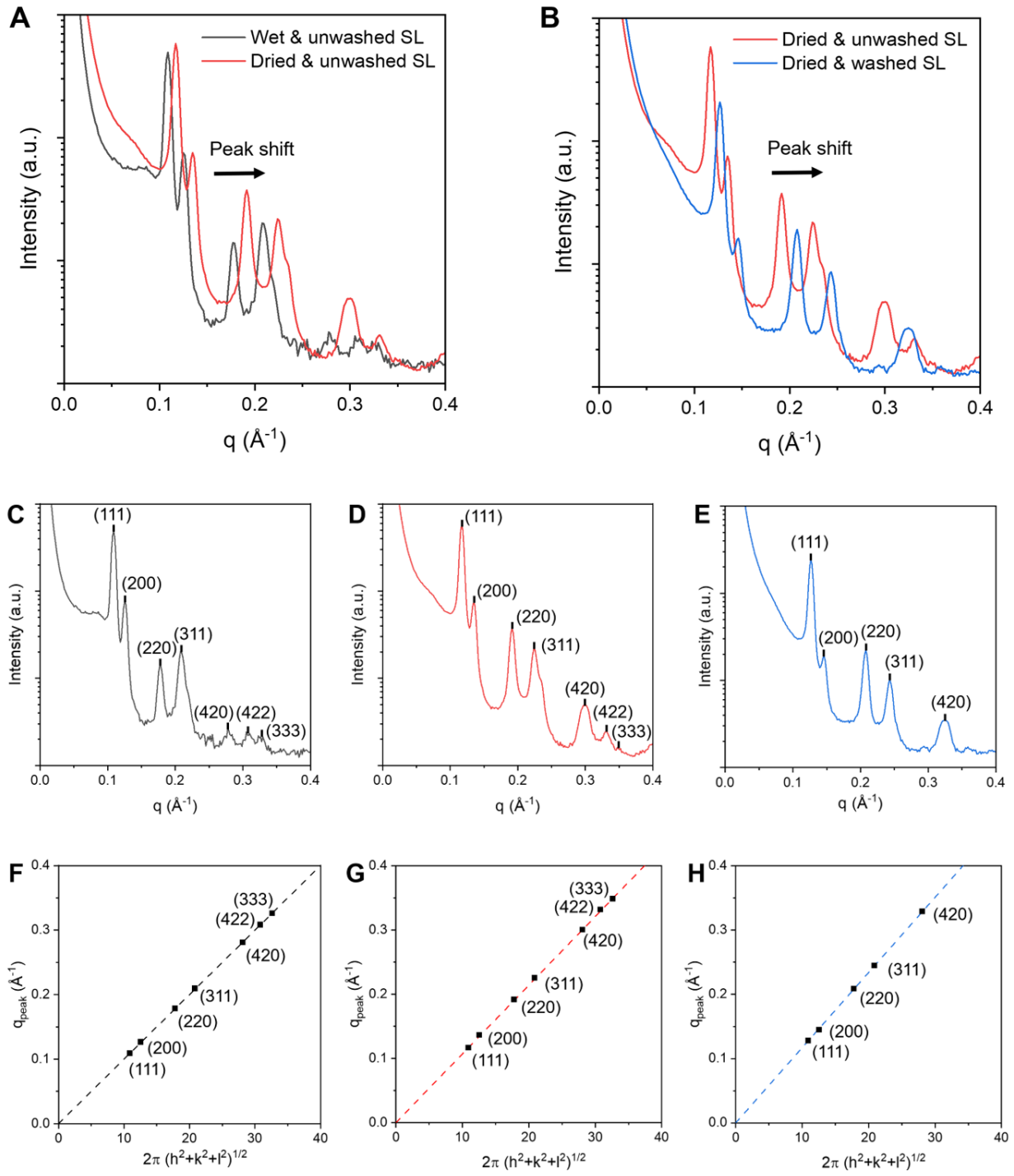

Figure 5.6.2: Lattice contraction of washed and dried superlattices.

(A) SAXS patterns of unwashed 5.7 nm PbS-$Sn_2S_6^{4-}$ NC superlattices, comparing wet & dried states. **(B)** SAXS patterns of dried 5.7 nm 5.7 nm PbS-$Sn_2S_6^{4-}$ NC superlattices, comparing unwashed & washed states.

Figure 5.6.2 continued: **(C-E)** SAXS patterns and **(F-H)** and the plot of q_{peak} versus $2\pi(h^2+k^2+l^2)^{1/2}$ of wet unwashed (black), dried unwashed (red) and dried washed (blue) 5.7 nm PbS-$Sn_2S_6^{4-}$ NC superlattices. The superlattice was deposited on Kapton tape and dried before the SAXS measurement. The assigned Miller indices satisfy the selection rule for an *fcc* crystal structure (where *h*, *k*, and *l* are either all odd or all even). The data points align closely with a straight line passing through the origin, confirming that the superlattices exhibit an *fcc* structure.

Orientational alignment of washed & unwashed superlattices

TEM and HRTEM imaging show that both unwashed and washed superlattices retain long-range orientational alignment, with continuous atomic lattice fringes extending across multiple nanocrystals (Figure 5.6.3). Fourier-transformed images further confirm the presence of well-defined diffraction spots in both cases. However, unwashed samples often contain fewer intact superlattice grains and are more susceptible to electron-beam-induced disruption, suggesting that the contracted, washed superlattices are mechanically more robust.

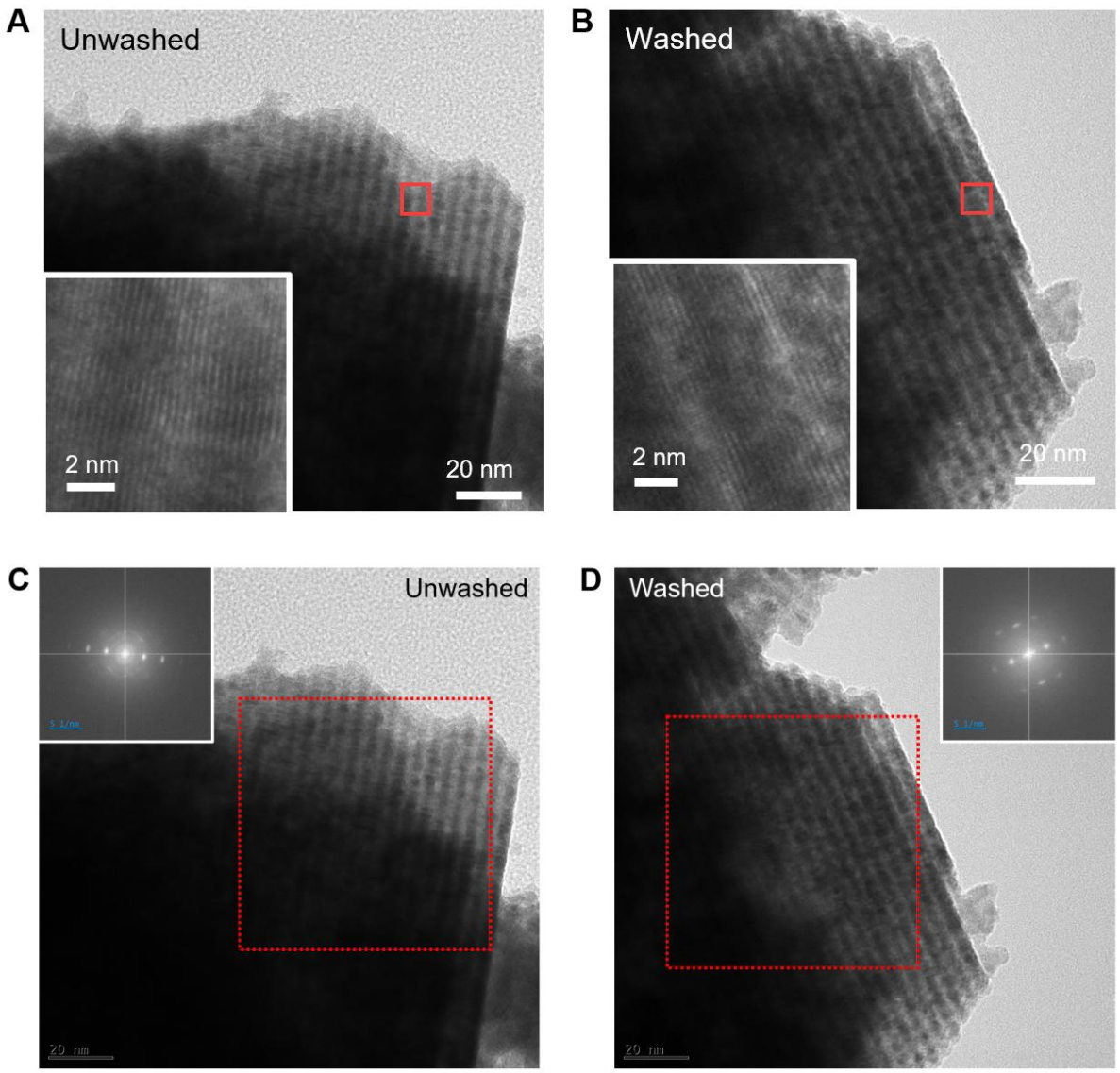

Figure 5.6.3: Atomic alignment of unwashed and washed superlattices.

TEM images of unwashed and washed 5.7 nm PbS-$Sn_2S_6^{4-}$ NC superlattices. **(A, B)** Insets: magnified images of the regions highlighted by red squares. **(C, D)** Insets: Fourier transformed images of the regions highlighted by red squares.

Although both washed and unwashed superlattices exhibit clear orientational alignment in TEM and HRTEM images, we consistently observed that unwashed samples contained far fewer intact superlattice grains. Most of the material appeared as disordered aggregates, despite the

SAXS patterns showing sharp Bragg peaks indicative of a substantial fraction of ordered superlattice in the bulk solid. This discrepancy suggests that the unwashed superlattices are significantly more fragile and may partially disassemble under external stimuli, such as electron-beam exposure during TEM imaging. In contrast, the washed superlattices appear mechanically more robust and retain their structural integrity more reliably during imaging.

Compositional origin of lattice contraction

Elemental analysis provides insight into the origin of the observed lattice contraction (Table 5.1). During self-assembly, substantial amounts of K and As are incorporated into the solid, consistent with the inclusion of K_3AsS_4 within the superlattice. Washing removes a significant fraction of this salt, leading to a measurable reduction in K and As content. Importantly, Sn levels remain unchanged, indicating that the $Sn_2S_6^{4-}$ surface ligands remain bound to the NCs throughout assembly and washing. The removal of incorporated K_3AsS_4 therefore accounts for the contraction of the superlattice lattice.

Table 5.1: Relative mole ratio of five elements (Pb, S, K, Sn, As) in 5.7 nm PbS-$Sn_2S_6^{4-}$ NC superlattices before and after washing with MeCN, obtained through the ICP-OES measurements.

Element	NC solution	Before wash	After wash
Pb	1.000	1.000	1.000
S	1.131	1.190	1.122
K	0.137	0.277	0.222
Sn	0.094	0.074	0.072
As	None	0.086	0.065

STEM-EDS measurements further confirm the presence and spatial distribution of the incorporated salt. In unwashed superlattices, K_3AsS_4 is broadly distributed throughout the structure (Figure 5.6.4), though excess salt complicates detailed analysis.

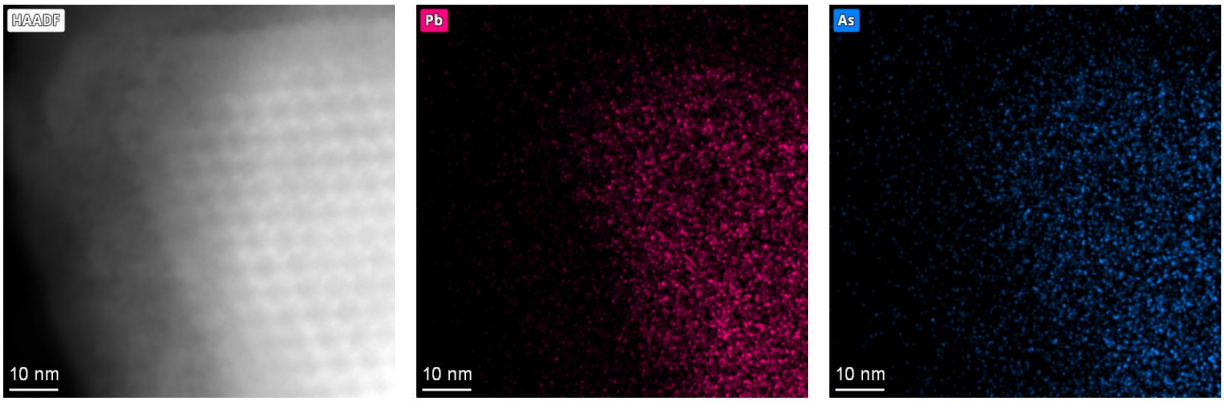

Figure 5.6.4: Elemental analysis of unwashed superlattice.
HAADF-STEM image and STEM-EDS images of unwashed 5.9 nm PbS-$Sn_2S_6^{4-}$ NC superlattices.

Figure 5.6.5 presents STEM-EDS elemental mapping within a 5.9 nm PbS-$Sn_2S_6^{4-}$ NC superlattice, along with the corresponding elemental line scan across the superlattice. The bright regions in the HAADF-STEM image correspond to superlattice planes formed by PbS NCs, while the darker regions represent the interparticle gaps with necks connecting adjacent NCs. The STEM-EDS Pb signal intensity is higher in the brighter regions of the HAADF-STEM image, confirming this correspondence. Notably, the spatial distribution of tin (Sn) exhibits an anti-phase relationship with that of lead (Pb), clearly indicated by the plot of Sn/Pb ratio. This indicates that the interparticle regions are enriched in Sn, suggesting that the epitaxial bridging of PbS NCs involves $Sn_2S_6^{4-}$ surface ligands.

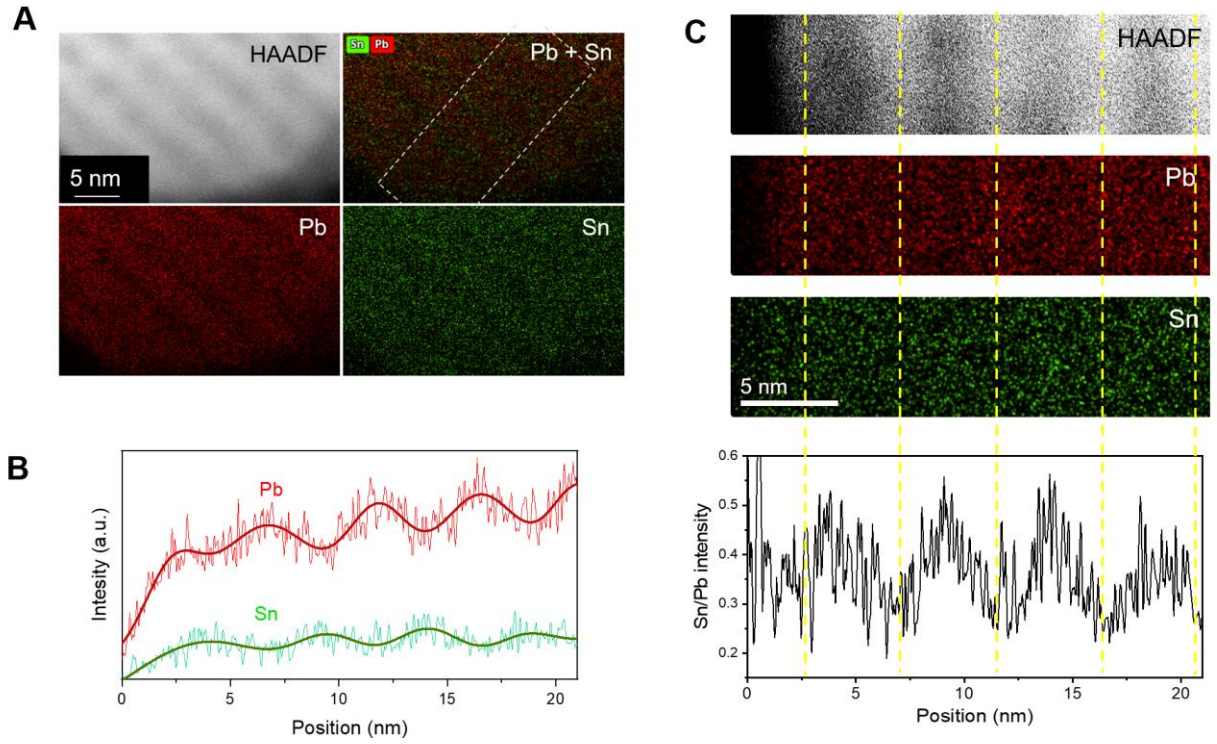

Figure 5.6.5: Elemental analysis of washed superlattice.

(A) HAADF-STEM image and STEM-EDS mapping of 5.9 nm PbS-$Sn_2S_6^{4-}$ NC superlattice. **(B)** Line scan of the STEM-EDS mapping. The area where the line scan was carried out is marked with a dashed grey box. **(C)** HAADF-STEM image and STEM-EDS elemental mapping of the superlattice. The plot below presents the ratio of the Sn and Pb signal counts across the superlattice.

5.7. Reversible oriented attachment of edge-to-edge nanocrystal assemblies

Reversible self-assembly of PbS NCs

A striking and counterintuitive feature of PbS-$Sn_2S_6^{4-}$ NC superlattices is their ability to fully revert to the colloidal state. Figure 5.7.1A shows the SAXS pattern of the original 5.8 nm PbS-$Sn_2S_6^{4-}$ NC colloid (black). The corresponding unwashed, dried superlattice exhibits sharp Bragg peaks (red), confirming long-range order. Remarkably, this superlattice can be completely disassembled by adding highly polar NMF. The SAXS pattern of the redispersed NCs (blue) displays Bessel oscillations identical to those of the original colloid at high q (>0.1 $Å^{-1}$), demonstrating that the NCs are fully recovered without changes in size or shape distribution. Similar reversible behavior is observed for PbS-AsS_4^{3-} NCs of the same size and for PbS-$Sn_2S_6^{4-}$ NCs of different sizes (Figure 5.7.1B–D).

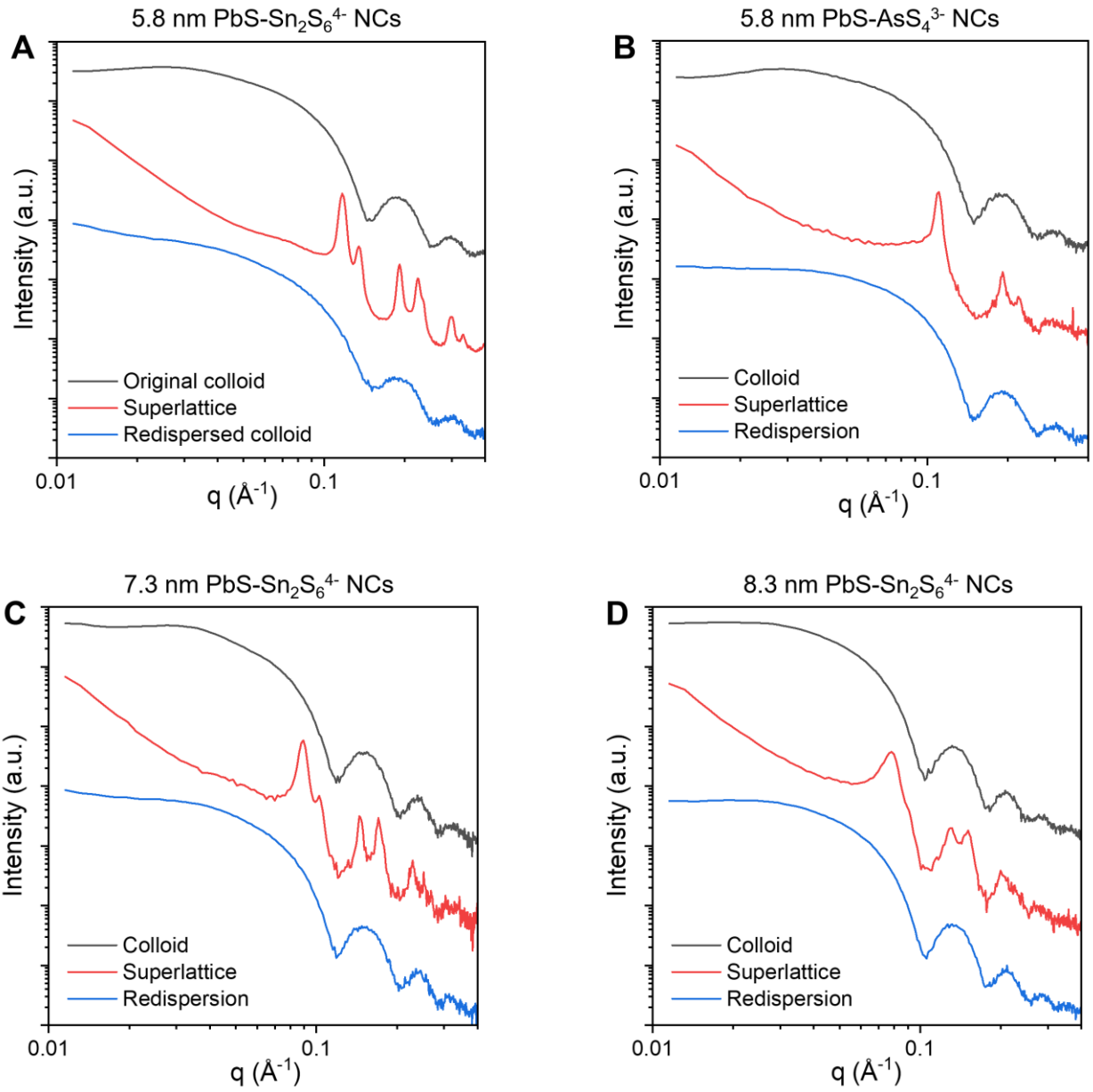

Figure 5.7.1: Redispersion test of superlattices of various all-inorganic NCs.

Small-angle X-ray scattering (SAXS) patterns of the original colloid solution, unwashed superlattices (SL) and redispersed colloid of: **(A)** 5.7 nm PbS-$Sn_2S_6^{4-}$ NCs (dried), **(B)** 5.8 nm PbS-AsS_4^{3-} NCs (wet), **(C)** 7.3 nm PbS-$Sn_2S_6^{4-}$ NCs (wet) and **(D)** 8.3 PbS-$Sn_2S_6^{4-}$ NCs (wet). The y-axis is vertically offset for clarity. Absence of Bragg peaks from the SAXS pattern of redispersed PbS NCs indicates full disassembly of superlattices.

Photographs and TEM images of the redispersed colloids (Figure 5.7.2) further confirm complete recovery: the solutions appear indistinguishable from the original colloids, with no visible solids, and TEM images show fully separated NCs with no aggregated clusters.

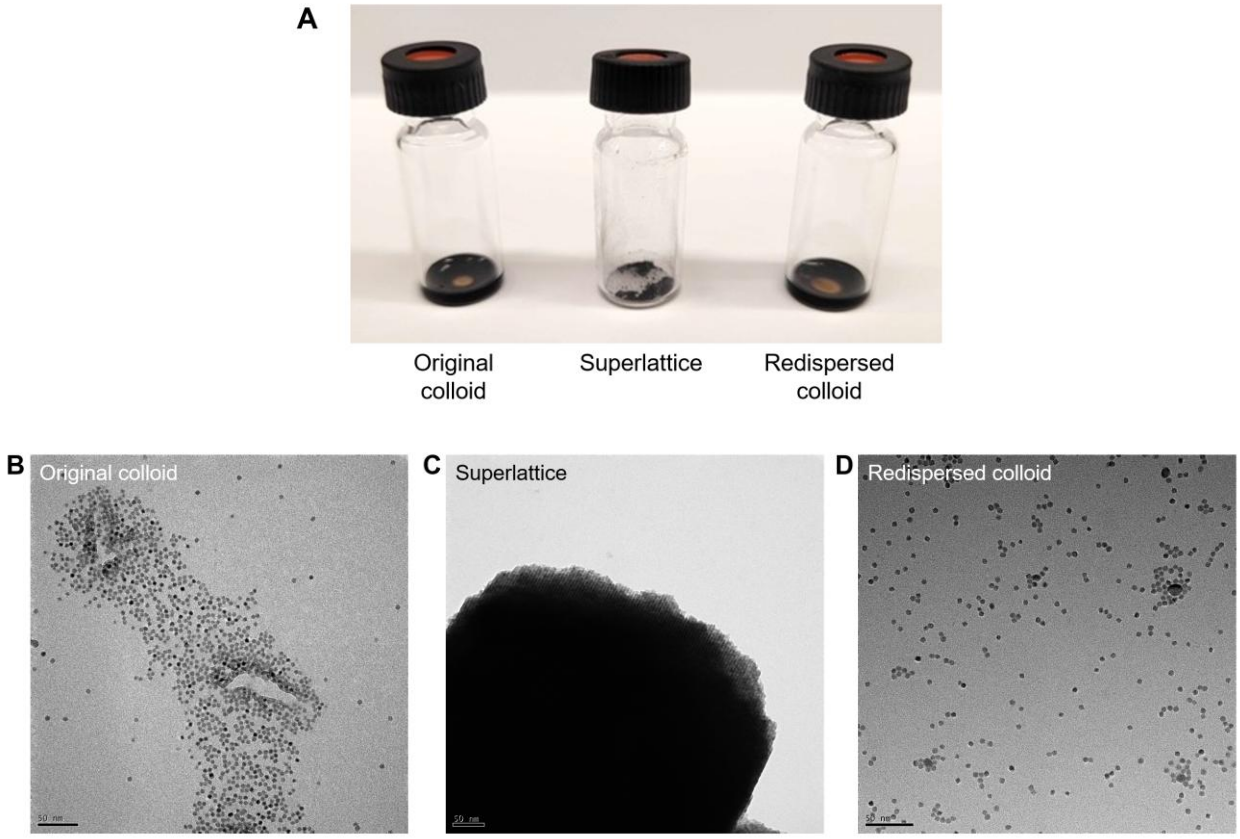

Figure 5.7.2: Complete redispersion of superlattices into colloidal NCs.
(A) Photograph of colloidal 5.7 nm PbS-$Sn_2S_6^{4-}$ NCs (left), washed superlattices in powdered form (center), and colloidal NCs that are recovered by redispersing superlattices in NMF (right). TEM images of **(B)** original colloid, **(C)** washed superlattice and **(D)** redispersed colloid of 5.7 nm PbS-$Sn_2S_6^{4-}$ NCs.

Influence of washing and drying on reversibility

Unwashed superlattices exhibit excellent redispersibility. Even after vacuum drying (house vacuum) or aging for more than two days, they can be fully redissolved in NMF, yielding SAXS patterns identical to the original colloid (Figure 5.7.3). This demonstrates that the oriented attachment in unwashed superlattices remains reversible.

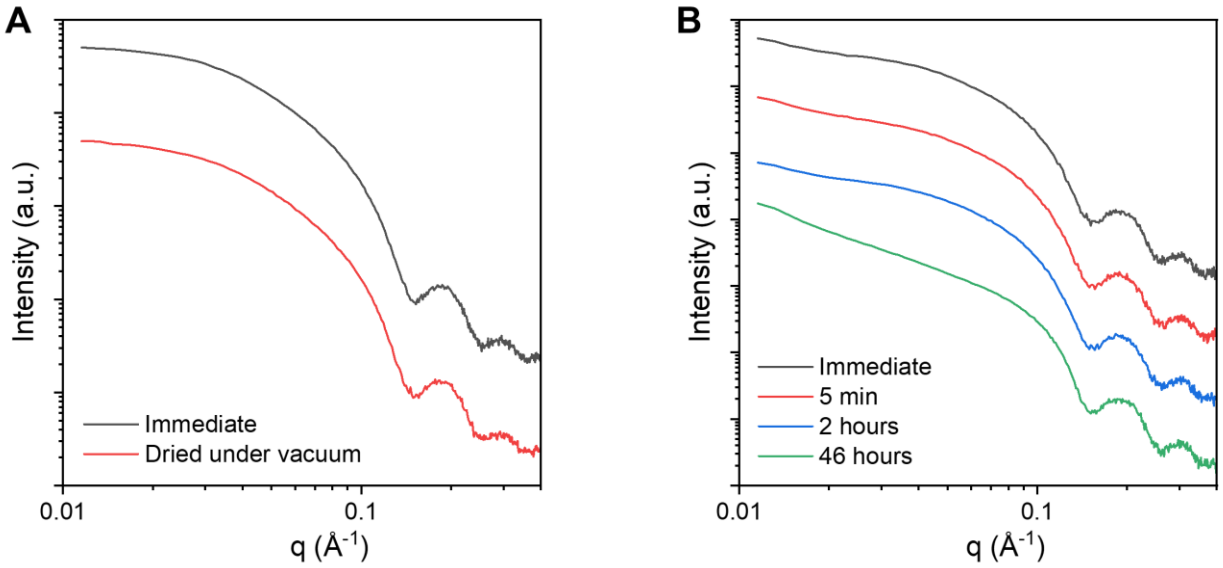

Figure 5.7.3: Redispersion of unwashed all-inorganic superlattices.
SAXS patterns of as-prepared 5.8 nm PbS-$Sn_2S_6^{4-}$ NC superlattices redispersed in NMF. **(A)** Superlattices were redispersed in NMF immediately after solvent removal or after drying under vacuum for 2 hours. **(B)** Superlattices were stored under a N_2 atmosphere for the indicated durations following solvent removal and subsequently redispersed in NMF.

In contrast, washing alters this behavior. Immediately after washing with acetonitrile, the superlattices can still be redispersed into individual NCs and subsequently reassembled (Figure 5.7.4). However, once the washed superlattice is allowed to dry, its reversibility is lost. Attempts to redisperse washed-and-dried superlattices result in SAXS patterns that retain Bragg peaks, indicating that the NCs remain attached and do not return to the colloidal state.

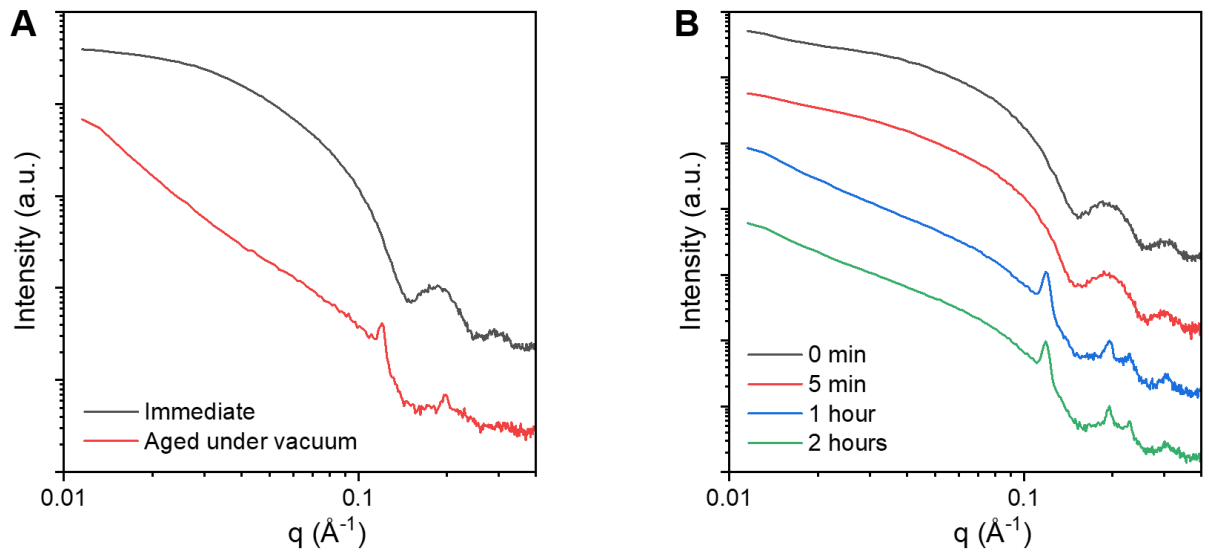

Figure 5.7.4: Redispersion of washed all-inorganic superlattices.
SAXS patterns of washed 5.7 nm PbS-$Sn_2S_6^{4-}$ NC superlattices redispersed in NMF. **(A)** Superlattices were redispersed in NMF immediately after solvent removal or after drying under vacuum for 2 hours. **(B)** Superlattices were stored under a N_2 atmosphere for the indicated durations following solvent removal and subsequently redispersed in NMF.

Photographs comparing the redispersed solutions of washed/unwashed and wet/dried 5.8 nm PbS-$Sn_2S_6^{4-}$ NC superlattices are shown in Figure 5.7.5. For this set of experiment, "dried" superlattices were prepared by allowing the solvent to evaporate in house vacuum for two hours. All samples except for the washed and dried superlattice readily redispersed in NMF without leaving any visible solid residue. In contrast, the washed and dried superlattice formed a suspension of black, insoluble powders, indicating that it can no longer be disassembled into individual NCs.

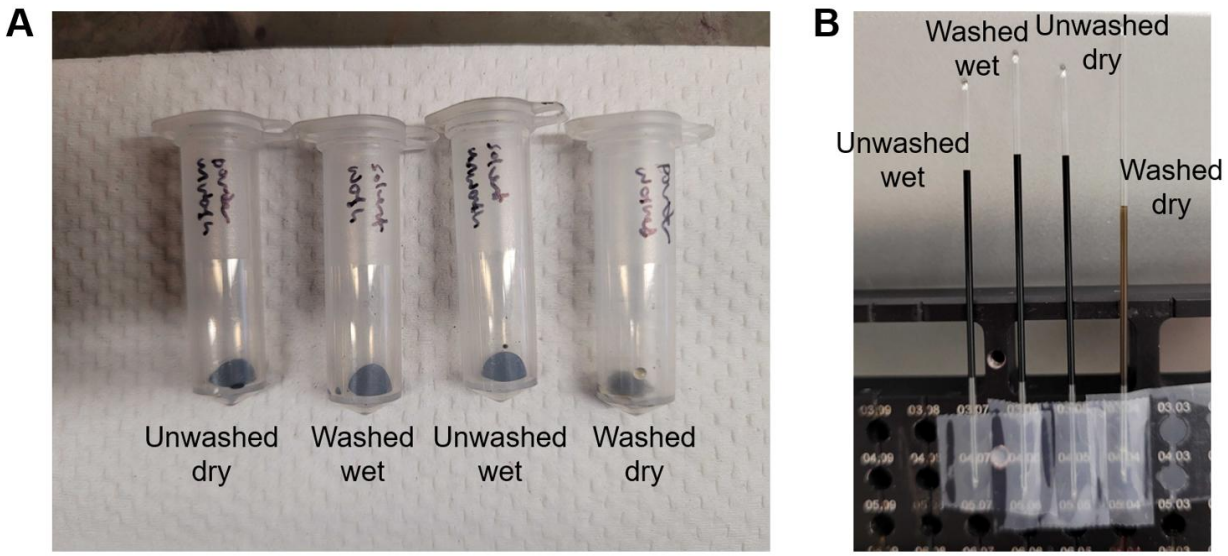

Figure 5.7.5: Influence of washing and drying on reversibility.

Photographs of 5.8 nm PbS-$Sn_2S_6^{4-}$ NC superlattices redispersed in NMF. Superlattices were redispersed either immediately after solvent removal or after drying under vacuum for 2 hours. Samples were transferred to **(A)** centrifuge tubes and **(B)** glass capillaries prior to imaging.

Furthermore, this washed and dried 5.8 nm PbS-$Sn_2S_6^{4-}$ NC superlattice did not redisperse even in a 50 mM K $K_4Sn_2S_6$ solution in NMF (Figure 5.7.6), confirming that the irreversibility is not due to insufficient salt but rather to permanent interparticle attachment (i.e. neck formation) within the superlattice.

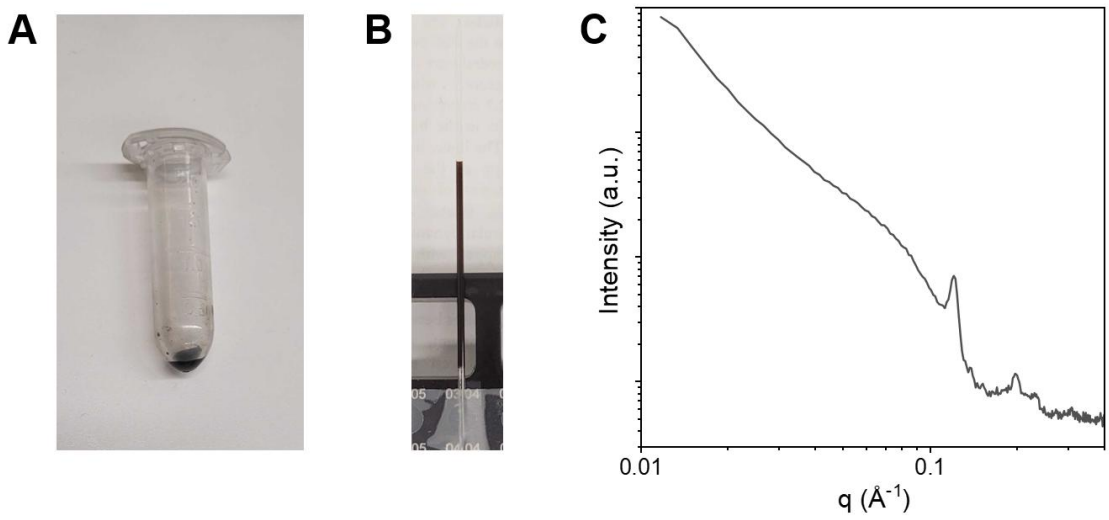

Figure 5.7.6: Redispersion of washed all-inorganic superlattices in $K_4Sn_2S_6$ solution

(A, B) Photographs and **(C)** SAXS pattern of 5.8 nm PbS-$Sn_2S_6^{4-}$ NC superlattices in 50 mM $K_4Sn_2S_6$ solution. Superlattices were redispersed after washing with acetonitrile, followed by drying under ambient pressure for 30 minutes. Samples were transferred to **(A)** centrifuge tubes and **(B)** glass capillaries prior to imaging.

Redispersion over multiple assembly-disassembly cycles

Unwashed superlattices can undergo multiple cycles of assembly and disassembly. Figure 5.7.7 shows SAXS patterns from repeated cycling of 5.8 nm PbS-$Sn_2S_6^{4-}$ NCs. Each redispersed sample shows no Bragg peaks, confirming complete dissolution, while each reassembled sample exhibits sharp peaks characteristic of well-formed superlattices. This demonstrates that reversibility is preserved over multiple cycles.

However, repeated cycling eventually leads to degradation: low-*q* scattering increases in the colloidal SAXS patterns, and Bragg peaks weaken in the superlattice patterns. This suggests gradual NC damage, likely due to partial ligand loss during repeated assembly-disassembly events.

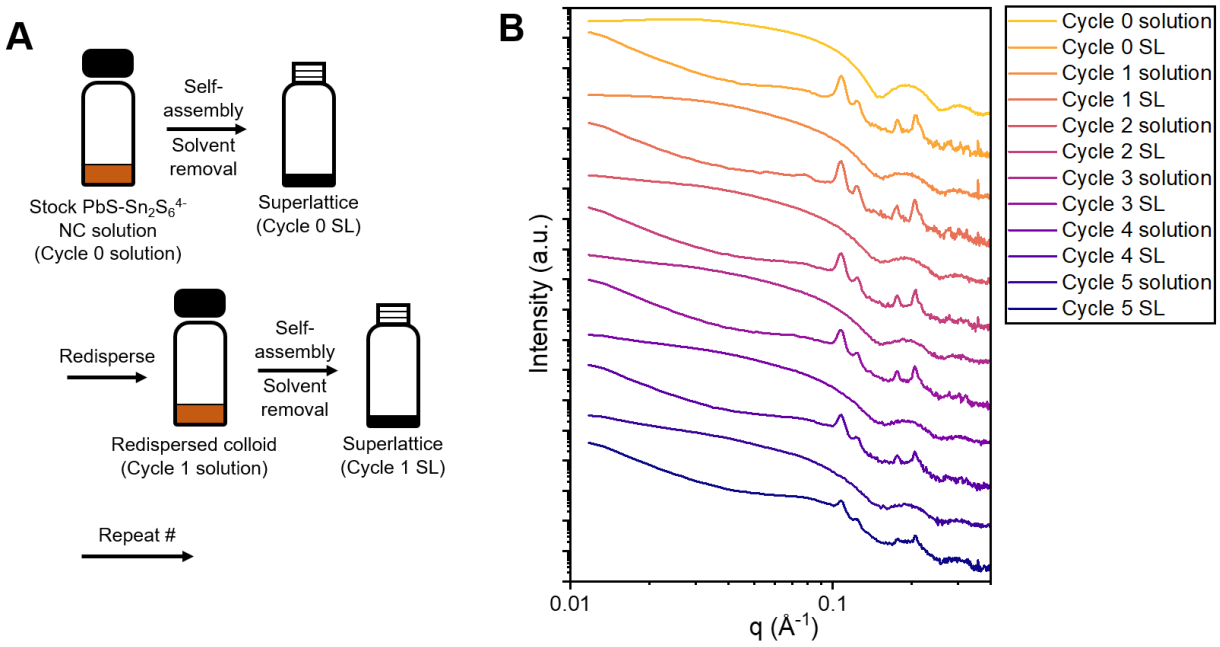

Figure 5.7.7: Assembly-disassembly cycle of unwashed all-inorganic superlattices.
(A) Schematics outlining the sample preparation procedure. **(B)** SAXS pattern of solutions of superlattice (SL) through assembly/disassembly cycles.

Washed superlattices can also undergo reversible cycling, but only if they are redispersed in NMF immediately after acetonitrile removal. If the washed solids are allowed to dry, they become irreversibly attached. Figure 5.7.8 shows that two cycles can be completed successfully, with minor degradation observed similar to the unwashed superlattices.

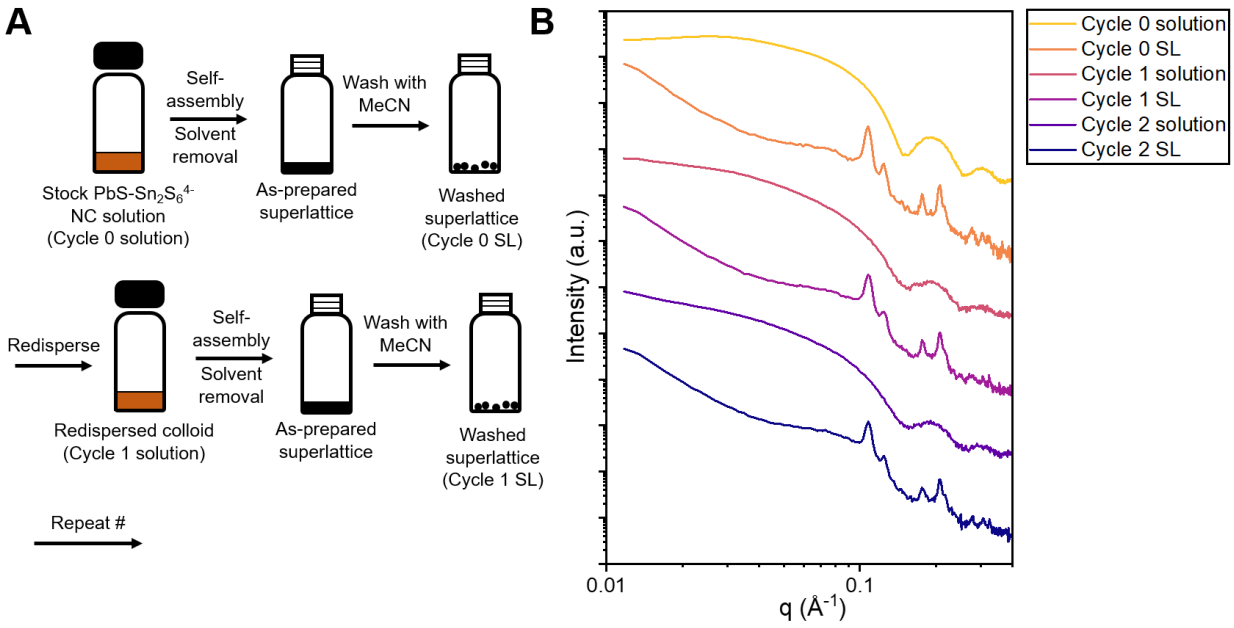

Figure 5.7.8: Assembly-disassembly cycle of washed all-inorganic superlattices.
(A) Schematics outlining the sample preparation procedure. **(B)** SAXS pattern of solutions of superlattice (SL) through assembly/disassembly cycles with washing in between each step.

Origin of reversible self-assembly of atomically aligned superlattice

To rationalize these observations, we consider the mechanism of reversible oriented attachment (ROA) in PbS-$Sn_2S_6^{4-}$ NC superlattices. Two key conditions must be satisfied for ROA to occur.

First condition is the minimization of contact area during oriented attachment. Large face-to-face contact areas (Figure 5.7.9A), typical of many superlattices, tend to produce irreversible necks and defect-prone attachment. In contrast, edge-to-edge alignment minimizes the initial contact area, allowing attachment to proceed through a narrow line of contact (Figure 5.7.9B). This geometry reduces the likelihood of irreversible bonding and facilitates reversibility. PbS-$Sn_2S_6^{4-}$ NC superlattices indeed exhibit this edge-to-edge configuration, stabilized by ion layering within the multivalent electrolyte.

Second, the dynamic nature of the surface ligands is necessary. The chemical nature of the inorganic ligands is equally important. $Sn_2S_6^{4-}$ ligands appear to mediate epitaxial bridging between NCs, as indicated by the Sn-rich interparticle regions observed in STEM-EDS (Figure 5.6.5). Their dynamic Sn–S–Sn bonding in polar solvents allows local rearrangements, enabling both attachment and detachment of NCs.

The flocculant K_3AsS_4 further contributes to reversibility. AsS_4^{3-} ions cannot epitaxially integrate into the PbS lattice, preventing premature formation of irreversible necks. Elemental analysis (Table 5.1) shows that large amounts of K_3AsS_4 are incorporated into unwashed superlattices. Washing removes much of this salt, triggering lattice contraction and promoting irreversible oriented attachment. As AsS_4^{3-} ion is removed, $Sn_2S_6^{4-}$ ligands reorganize and form stable epitaxial bridges, locking the NCs into place and preventing redispersion.

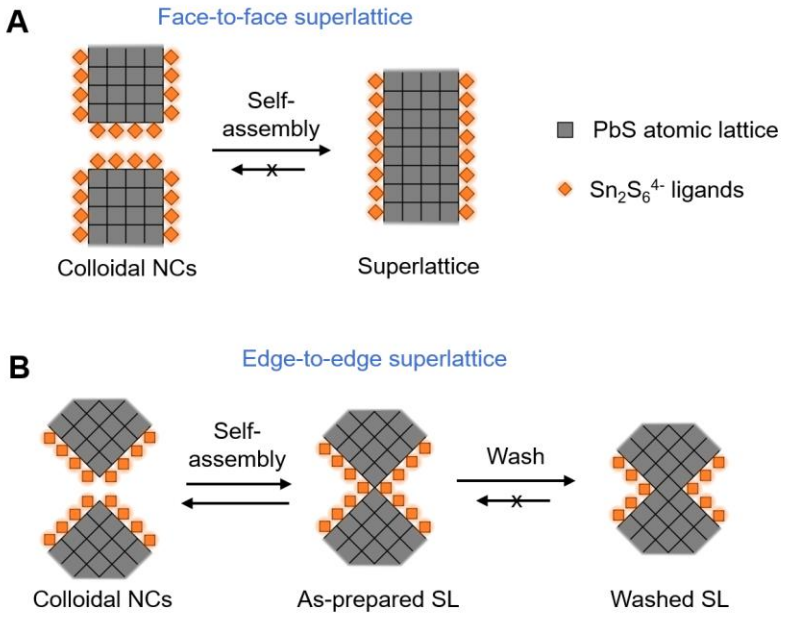

Figure 5.7.9: Face-to-face and edge-to-edge orientated attachment.

(A) Schematic of face-to-face oriented attachment. **(B)** Schematic of edge-to-edge oriented attachment of superlattice.

In summary, our results demonstrate that PbS NCs capped with compact and highly charged $Sn_2S_6^{4-}$ inorganic ligands can self-assemble into superlattices that exhibit exceptionally high translational and orientational order, approaching single-crystal precision. Structural and compositional analyses reveal that the NCs adopt a distinctive edge-to-edge orientation, promoted by the ionic layering in the electrolyte containing multi-charged ions. We further reveal that the reversibility of this self-assembly is influenced by the incorporation and partial removal of K_3AsS_4 salts during the washing process. The superlattices with incorporated K_3AsS_4 can be completely disassembled into their original colloidal state, whereas the partial removal of salts results in permanent lattice contraction and epitaxial oriented attachment of NCs. These findings highlight the interplay between ligand chemistry, lattice stability, and reversibility, offering a tunable strategy for control of NC assemblies. This ability to reversibly assemble colloidal nanocrystals with atomic-level alignment opens exciting opportunities for creating dynamic, reconfigurable materials with single-crystal-like properties, holding potential for applications in adaptive optoelectronics, self-healing materials, and nanostructured devices.

5.8. Chapter 5 bibliography

(1) Boles, M. A.; Engel, M.; Talapin, D. V. Self-Assembly of Colloidal Nanocrystals: From Intricate Structures to Functional Materials. *Chem. Rev.* **2016**, *116* (18), 11220–11289. https://doi.org/10.1021/acs.chemrev.6b00196.

(2) Bassani, C. L.; Van Anders, G.; Banin, U.; Baranov, D.; Chen, Q.; Dijkstra, M.; Dimitriyev, M. S.; Efrati, E.; Faraudo, J.; Gang, O.; Gaston, N.; Golestanian, R.; Guerrero-Garcia, G. I.; Gruenwald, M.; Haji-Akbari, A.; Ibáñez, M.; Karg, M.; Kraus, T.; Lee, B.; Van Lehn, R. C.; Macfarlane, R. J.; Mognetti, B. M.; Nikoubashman, A.; Osat, S.; Prezhdo, O. V.; Rotskoff, G. M.; Saiz, L.; Shi, A.-C.; Skrabalak, S.; Smalyukh, I. I.; Tagliazucchi, M.; Talapin, D. V.; Tkachenko, A. V.; Tretiak, S.; Vaknin, D.; Widmer-Cooper, A.; Wong, G. C. L.; Ye, X.; Zhou, S.; Rabani, E.; Engel, M.; Travesset, A. Nanocrystal Assemblies:

Current Advances and Open Problems. *ACS Nano* **2024**, *18* (23), 14791–14840. https://doi.org/10.1021/acsnano.3c10201.

(3) Grzelczak, M.; Liz-Marzán, L. M.; Klajn, R. Stimuli-Responsive Self-Assembly of Nanoparticles. *Chem. Soc. Rev.* **2019**, *48* (5), 1342–1361. https://doi.org/10.1039/C8CS00787J.

(4) Bian, T.; Gardin, A.; Gemen, J.; Houben, L.; Perego, C.; Lee, B.; Elad, N.; Chu, Z.; Pavan, G. M.; Klajn, R. Electrostatic Co-Assembly of Nanoparticles with Oppositely Charged Small Molecules into Static and Dynamic Superstructures. *Nat. Chem.* **2021**, *13* (10), 940–949. https://doi.org/10.1038/s41557-021-00752-9.

(5) Li, D.; Chen, Q.; Chun, J.; Fichthorn, K.; De Yoreo, J.; Zheng, H. Nanoparticle Assembly and Oriented Attachment: Correlating Controlling Factors to the Resulting Structures. *Chem. Rev.* **2023**, *123* (6), 3127–3159. https://doi.org/10.1021/acs.chemrev.2c00700.

(6) Whitham, K.; Yang, J.; Savitzky, B. H.; Kourkoutis, L. F.; Wise, F.; Hanrath, T. Charge Transport and Localization in Atomically Coherent Quantum Dot Solids. *Nat. Mater.* **2016**, *15* (5), 557–563. https://doi.org/10.1038/nmat4576.

(7) Abelson, A.; Qian, C.; Salk, T.; Luan, Z.; Fu, K.; Zheng, J.-G.; Wardini, J. L.; Law, M. Collective Topo-Epitaxy in the Self-Assembly of a 3D Quantum Dot Superlattice. *Nat. Mater.* **2020**, *19* (1), 49–55. https://doi.org/10.1038/s41563-019-0485-2.

(8) Ondry, J. C.; Philbin, J. P.; Lostica, M.; Rabani, E.; Alivisatos, A. P. Resilient Pathways to Atomic Attachment of Quantum Dot Dimers and Artificial Solids from Faceted CdSe Quantum Dot Building Blocks. *ACS Nano* **2019**, *13* (11), 12322–12344. https://doi.org/10.1021/acsnano.9b03052.

(9) Coropceanu, I.; Janke, E. M.; Portner, J.; Haubold, D.; Nguyen, T. D.; Das, A.; Tanner, C. P. N.; Utterback, J. K.; Teitelbaum, S. W.; Hudson, ¸ Margaret H.; Sarma, N. A.; Hinkle, A. M.; Tassone, C. J.; Eychmüller, A.; Limmer, D. T.; Olvera De La Cruz, M.; Ginsberg, N. S.; Talapin, D. V. Self-Assembly of Nanocrystals into Strongly Electronically Coupled All-Inorganic Supercrystals. *Science* **2022**, *375* (6587), 1422–1426. https://doi.org/10.1126/science.abm6753.

(10) Jeong, A.; Portner, J.; Tanner, C. P. N.; Ondry, J. C.; Zhou, C.; Mi, Z.; Tazoui, Y. A.; Lee, B.; Wall, V. R. K.; Ginsberg, N. S.; Talapin, D. V. Colloidal Dispersions of Sterically and Electrostatically Stabilized PbS Quantum Dots: Structure Factors, Second Virial Coefficients, and Film-Forming Properties. *ACS Nano* **2024**, *18* (50), 33864–33874. https://doi.org/10.1021/acsnano.4c06033.

(11) Kessler, M. L.; Dempsey, J. L. Mapping the Topology of PbS Nanocrystals through Displacement Isotherms of Surface-Bound Metal Oleate Complexes. *Chem. Mater.* **2020**, *32* (6), 2561–2571. https://doi.org/10.1021/acs.chemmater.0c00014.

(12) Choi, H.; Ko, J.-H.; Kim, Y.-H.; Jeong, S. Steric-Hindrance-Driven Shape Transition in PbS Quantum Dots: Understanding Size-Dependent Stability. *J. Am. Chem. Soc.* **2013**, *135* (14), 5278–5281. https://doi.org/10.1021/ja400948t.

(13) Beygi, H.; Sajjadi, S. A.; Babakhani, A.; Young, J. F.; Van Veggel, F. C. J. M. Surface Chemistry of As-Synthesized and Air-Oxidized PbS Quantum Dots. *Appl. Surf. Sci.* **2018**, *457*, 1–10. https://doi.org/10.1016/j.apsusc.2018.06.152.

(14) Klinger, M.; Jäger, A. *Crystallographic Tool Box* (*CrysTBox*): Automated Tools for Transmission Electron Microscopists and Crystallographers. *J. Appl. Crystallogr.* **2015**, *48* (6), 2012–2018. https://doi.org/10.1107/S1600576715017252.

(15) Klinger, M. More Features, More Tools, More *CrysTBox*. *J. Appl. Crystallogr.* **2017**, *50* (4), 1226–1234. https://doi.org/10.1107/S1600576717006793.

(16) Rupich, S. M.; Shevchenko, E. V.; Bodnarchuk, M. I.; Lee, B.; Talapin, D. V. Size-Dependent Multiple Twinning in Nanocrystal Superlattices. *J. Am. Chem. Soc.* **2010**, *132* (1), 289–296. https://doi.org/10.1021/ja9074425.

(17) Smilgies, D.-M. Scherrer Grain-Size Analysis Adapted to Grazing-Incidence Scattering with Area Detectors. *J. Appl. Crystallogr.* **2009**, *42* (6), 1030–1034. https://doi.org/10.1107/S0021889809040126.

(18) Toso, S.; Baranov, D.; Altamura, D.; Scattarella, F.; Dahl, J.; Wang, X.; Marras, S.; Alivisatos, A. P.; Singer, A.; Giannini, C.; Manna, L. Multilayer Diffraction Reveals That Colloidal Superlattices Approach the Structural Perfection of Single Crystals. *ACS Nano* **2021**, *15* (4), 6243–6256. https://doi.org/10.1021/acsnano.0c08929.

(19) Choi, H.; Ko, J.-H.; Kim, Y.-H.; Jeong, S. Steric-Hindrance-Driven Shape Transition in PbS Quantum Dots: Understanding Size-Dependent Stability. *J. Am. Chem. Soc.* **2013**, *135* (14), 5278–5281. https://doi.org/10.1021/ja400948t.

(20) Beygi, H.; Sajjadi, S. A.; Babakhani, A.; Young, J. F.; Van Veggel, F. C. J. M. Surface Chemistry of As-Synthesized and Air-Oxidized PbS Quantum Dots. *Appl. Surf. Sci.* **2018**, *457*, 1–10. https://doi.org/10.1016/j.apsusc.2018.06.152.

(21) Klinger, M. More Features, More Tools, More *CrysTBox*. *J. Appl. Crystallogr.* **2017**, *50* (4), 1226–1234. https://doi.org/10.1107/S1600576717006793.

(22) Zhang, J.; Luo, Z.; Quan, Z.; Wang, Y.; Kumbhar, A.; Smilgies, D.-M.; Fang, J. Low Packing Density Self-Assembled Superstructure of Octahedral Pt_3 Ni Nanocrystals. *Nano Lett.* **2011**, *11* (7), 2912–2918. https://doi.org/10.1021/nl201386e.

(23) Weidman, M. C.; Smilgies, D.-M.; Tisdale, W. A. Kinetics of the Self-Assembly of Nanocrystal Superlattices Measured by Real-Time in Situ X-Ray Scattering. *Nat. Mater.* **2016**, *15* (7), 775–781. https://doi.org/10.1038/nmat4600.

(24) Choi, J. J.; Bealing, C. R.; Bian, K.; Hughes, K. J.; Zhang, W.; Smilgies, D.-M.; Hennig, R. G.; Engstrom, J. R.; Hanrath, T. Controlling Nanocrystal Superlattice Symmetry and Shape-Anisotropic Interactions through Variable Ligand Surface Coverage. *J. Am. Chem. Soc.* **2011**, *133* (9), 3131–3138. https://doi.org/10.1021/ja110454b.

(25) Li, R.; Bian, K.; Hanrath, T.; Bassett, W. A.; Wang, Z. Decoding the Superlattice and Interface Structure of Truncate PbS Nanocrystal-Assembled Supercrystal and Associated Interaction Forces. *J. Am. Chem. Soc.* **2014**, *136* (34), 12047–12055. https://doi.org/10.1021/ja5057032.

(26) Ondry, J. C.; Frechette, L. B.; Geissler, P. L.; Alivisatos, A. P. Trade-Offs between Translational and Orientational Order in 2D Superlattices of Polygonal Nanocrystals with Differing Edge Count. *Nano Lett.* **2022**, *22* (1), 389–395. https://doi.org/10.1021/acs.nanolett.1c04058.